

# Thermal fluid network model for a prismatic block in a gas-cooled reactor using FLOWNEX

**P Sambureni**  
**20991487**

Dissertation submitted in *partial* fulfillment of the requirements  
for the degree *Master of Engineering* in Nuclear at the  
Potchefstroom Campus of the North-West University

Supervisor: Prof C.G Du Toit  
Co-supervisor: Prof P.G Rousseau

October 2015

## ***Abstract***

Very High Temperature Reactors are complex reactors and various system codes have been developed to design different aspects such as neutronics, thermal hydraulics etc. Flownex is one of the system codes and it has been used to model the flow and heat transfer for a pebble fuel element and pebble-bed reactor. Although Flownex has been used to model the High Temperature Test Reactor, the prismatic block was modelled in a simplified manner. The aim of this study was to develop a more integrated model for a single block. A one sixth block was modelled in Flownex and the results were validated by comparing the results with results obtained using the Computational Fluid Dynamics (CFD) code STAR-CCM+.

The conduction heat transfer through the prismatic blocks containing the fuel elements in a Very High Temperature Reactor is of crucial importance for the proper operation of the reactor under normal operating conditions and upset conditions. In this study, a model developed in a system code, Flownex is discussed. The model comprised of a collection of 1-D solid conduction heat transfer, convection heat transfer and pipe elements that were arranged in such a manner to represent the heat transfer and fluid flow in the prismatic block using a network approach. The validity of the model was investigated by comparing the heat transfer and temperature distribution in the block for various scenarios with the corresponding values obtained using a detailed CFD model of one twelfth of a prismatic block.

Cubical and triangular block verification cases were conducted in Flownex and the results were validated by STAR-CCM+. The results were very comparable; however one issue has to be addressed. The one sixth integrated prismatic block was then modelled for a steady state and the results were also comparable. The outlet helium temperatures predicted by the STAR-CCM+ model was 542.94 ° C, at the same time the Flownex model predicted 542.98 ° C. Although the Flownex model did not provide the same detail as the STAR-CCM+ model the agreement between the results obtained with the two codes was satisfactory. Based on these findings it was concluded that Flownex could be used to build a representative integrated network model for a prismatic block reactor.

**Keywords:** VHTR, HTTR, Flownex, CFD, STAR-CCM+.

## ***Declaration***

I, Privilege Sambureni (Passport number: EN306136), hereby declare the work contained in this dissertation to be my own. All information which has been gained from various journal articles, text books or other sources has been referenced accordingly.

---

Privilege Sambureni

---

Date

## ***Acknowledgements***

First and above all, I praise God, the almighty for providing me this opportunity and granting me the capability to proceed successfully. This thesis appears in its current form due to the assistance and guidance of several people. I would therefore like to offer my sincere thanks to all of them.

- Prof C.G Du Toit and Prof P.G Rousseau, my esteemed promoters, my cordial thanks for accepting me as your Masters student, your warm encouragement, thoughtful guidance and correction of the dissertation.
- Mr L.A. le Grange for simulating the prismatic block in STAR-CCM+ and offering guidance in my verification studies. Without your hard work this project would not have been a success.
- My family, for being a source of encouragement.
- My friends for being there for me through the good and bad times.
- All my colleagues and staff members at the Nuclear Engineering Department.
- M-Tech Industrial (Pty) Ltd for providing the licence to use on their software package, Flownex.
- The North-West University (Potchefstroom Campus), the Department of Trade and Industry (DTI) and (National Research Foundation) NRF for their financial support.
- This work is based upon research supported by the South African Research Chairs Initiative of the Department of Science and Technology and National Research Foundation

## **Table of contents**

<b>Abstract</b> .....	<b>1</b>
<b>Declaration</b> .....	<b>2</b>
<b>Acknowledgements</b> .....	<b>3</b>
<b>Table of contents</b> .....	<b>4</b>
<b>List of Tables</b> .....	<b>7</b>
<b>List of Figures</b> .....	<b>8</b>
<b>Nomenclature</b> .....	<b>14</b>
<b>1. Introduction</b> .....	<b>19</b>
1.1 Introduction.....	19
1.1.1 Global energy outlook.....	19
1.1.2 A description of Generation IV future goals and reactors .....	19
1.2 High Temperature Reactors.....	20
1.2.1 Background of High Temperature Reactors (HTRs).....	20
1.2.2 Developments of HTR technology .....	21
1.3 Modelling of HTRs .....	22
1.3.1 The role of simulations.....	22
1.3.2 Numerical approaches used in thermal-fluid simulations .....	22
1.3.3 Flownex .....	23
1.3.4 CFD .....	23
1.4 Problem statement .....	24
1.5 Study objectives .....	24
1.6 Layout of dissertation.....	25
<b>2. Literature Survey</b> .....	<b>26</b>
2.1 Introduction.....	26
2.2 Principle of thermal-fluids network .....	26
2.3 Simulation of thermal systems .....	26
2.3.1 The network approach.....	27
2.3.2 CFD Approach.....	28
2.3.3 System CFD Approach .....	29
2.4 Numerical solution algorithms.....	30
2.4.1 Explicit vs. implicit numerical methods.....	30
2.4.2 The Stability Issue .....	31
2.4.3 The Accuracy Issue .....	31
2.5 Two dimensional steady state conduction.....	31
2.5.1 Analytical method (Method of separation of variables).....	32
2.5.2 Graphical method .....	32
2.5.3 Numerical method (Finite difference equations).....	34
2.6 Discretization schemes.....	34

2.6.1	The Finite volume method .....	35
2.6.2	Collocated arrangement .....	37
2.6.3	Staggered grid.....	38
2.7	Previous work on HTRs .....	39
2.7.1	Coolant flow analysis .....	39
2.7.2	Accident Conditions study .....	42
2.7.3	Modelling of flow and heat transfer .....	46
2.8	Summary .....	53
<b>3.</b>	<b>Implicit method for the solution of the thermal-fluid network.....</b>	<b>55</b>
3.1	Introduction.....	55
3.2	Governing equations.....	55
3.2.1	Conservation of mass .....	55
3.2.2	Conservation of momentum.....	55
3.2.3	Conservation of energy.....	56
3.2.4	Equation of state.....	57
3.3	Discretization of partial differential equations .....	57
3.3.1	Pipe flow.....	58
3.3.2	Equations for heat transfer .....	59
3.4	The conduction shape factor.....	63
3.4.1	Conduction between fuel rods and coolant channels in a prismatic fuel block ..	63
3.5	Heat transfer dimensionless parameters.....	66
3.5.1	Biot number .....	66
3.5.2	Fourier number .....	67
3.6	The Implicit Pressure Correction Method (IPCM) .....	69
3.6.1	Computational grid .....	69
3.6.2	Discretisation of governing equations for the IPCM .....	69
3.6.3	Solution procedure .....	71
3.7	Summary .....	71
<b>4.</b>	<b>Separate effects modelling and verification.....</b>	<b>72</b>
4.1	Introduction.....	72
4.2	Thermal fluid network code – Flownex.....	72
4.3	Different elements in Flownex.....	72
4.3.1	The pipe element.....	72
4.3.2	The conductive heat transfer element.....	74
4.3.3	The cross conductive heat transfer element .....	75
4.3.4	The convective heat transfer element .....	76
4.3.5	Nodes and boundary conditions .....	77
4.4	Cubical block test cases .....	78
4.4.1	Case 1 .....	79
4.4.2	Case 2.....	81

4.4.3	Case 3.....	83
4.4.4	Case 4.....	85
4.4.5	Case 5.....	87
4.5	Triangular block test cases.....	90
4.5.1	Effect of grid size in Flownex.....	90
4.5.2	Case 1.....	95
4.5.3	Case 2.....	100
4.5.4	Case 3.....	102
4.5.5	Conclusion.....	104
4.6	Summary.....	104
<b>5.</b>	<b>Prismatic block modelling methodology and results.....</b>	<b>106</b>
5.1	Introduction.....	106
5.2	Description of prismatic HTR core design.....	106
5.2.1	Fuel elements.....	107
5.3	Flow paths in an HTR.....	109
5.4	Modelling Approach.....	110
5.4.1	Flownex and the inputs.....	110
5.4.2	STAR-CCM+.....	125
5.5	Integrated prismatic block.....	141
5.5.1	Results and discussion.....	142
5.5.2	Conclusion.....	146
5.6	Summary.....	146
<b>6.</b>	<b>Conclusion and recommendations.....</b>	<b>148</b>
6.1	Introduction.....	148
6.2	Conclusions.....	148
6.3	Recommendations.....	149
<b>Appendix A</b>	<b>.....</b>	<b>155</b>
<b>Appendix B</b>	<b>.....</b>	<b>159</b>
<b>Appendix C</b>	<b>.....</b>	<b>164</b>
<b>Appendix D</b>	<b>.....</b>	<b>194</b>

**List of Tables**

Table 3-1: Transient, 2D finite difference equations (Incropera *et al.*, 2007). ..... 68

Table 4-1: Centreline temperatures for the different node models of heat conduction  
dominantly in the radial direction. .... 92

Table 4-2: Centreline temperatures for the different node models of heat conduction  
dominantly in the tangential direction. .... 94

Table 5-1: Graphite properties used in Flownex. .... 114

Table 5-2 : Helium material property correlations. .... 114

Table 5-3: Helium properties used in Flownex. .... 115

Table 5-4: Geometrical dimensions. .... 130

Table 5-5: Boundary layer increment relation to  $y+$  value. .... 138

Table 5-6: Parameters used to simulate the one sixth block in Flownex. .... 141

Table 5-7: Parameters used to simulate the one sixth block in STAR-CCM+. .... 142

Table 5-8: Inlet and outlet coolant temperatures. .... 146

## List of Figures

Figure 2-1: Conventional control volume for a CFD approach (Cruz & Monsivais, 2014).....	28
Figure 2-2: Conventional node element configuration for a systems-CFD approach (Rousseau, 2013) .....	29
Figure 2-3: Conduction in a square channel. (a) Symmetry planes. (b) Flux plot. (c) Typical curvilinear square (Incropera <i>et al.</i> , 2007).....	33
Figure 2-4: Section of a grid network in an x-y plane (Bejan, 1993).....	34
Figure 2-5: Steady state diffusion in a 1-D domain grid (Versteeg & Malalasekera, 2007).....	35
Figure 2-6: Basic unit cell types and examples of computational grids (Tak <i>et al.</i> , 2012).....	36
Figure 2-7: An example of computational grids developed for a standard fuel block (Tak <i>et al.</i> , 2012).....	36
Figure 2-8: Collocated arrangement of velocity and pressure components on a finite volume grid (Ferziger & Peric, 2013).....	37
Figure 2-9: Partially staggered arrangement of velocity and pressure components (Ferziger & Peric, 2013).....	38
Figure 2-10: Symmetric lines for the one twelfth fuel assembly model and the unit cell model (Tak <i>et al.</i> , 2008) .....	40
Figure 2-11: One half control fuel assembly CFD model (Kim <i>et al.</i> , 2010).....	41
Figure 2-12: Temperature distribution at the fuel hot spot plane for the three gap sizes (Sato <i>et al.</i> , 2010).....	42
Figure 2-13: Schematic for a $T_{1-M}$ (Maruyama <i>et al.</i> , 1994). .....	44
Figure 2-14: One fuel assembly surrounded by six half fuel assemblies (Cioni <i>et al.</i> , 2006)....	45
Figure 2-15: One fuel assembly surrounded by five half fuel assemblies and one half reflector block (Cioni <i>et al.</i> , 2006).....	45
Figure 2-16: Coolant flow path in the fuel block of the PMR200 (Tak <i>et al.</i> , 2012).....	47
Figure 2-17: Coolant flow path in the fuel block of the HTTR (Takamatsu <i>et al.</i> , 2006).....	47

Figure 2-18: (a) Schematic layout of the core (b) Schematic layout of the coolant flow path (Rousseau & Greyvenstein, 2002) .....	48
Figure 2-19: Thermal network schematic for the heat transfer for a single fuel assembly block control volume (Rousseau & Greyvenstein, 2002). .....	49
Figure 2-20: Completed flow element and solid thermal mass node network (Rousseau & Greyvenstein, 2002).....	50
Figure 2-21: Schematic for a simplified network of the solids in the pebble bed core structures (Du Toit & Rosseau, 2012). .....	51
Figure 2-22: Modelling procedure from basic unit cell to whole prismatic core (Tak <i>et al.</i> , 2014).....	52
Figure 2-23: Maximum predicted temperatures for a one sixth core of PMR600 (Tak <i>et al.</i> , 2014).....	53
Figure 3-1: Discretisation of a pipe section.....	58
Figure 3-2: Conduction to an interior node from its adjacent nodes (Incropera <i>et al.</i> , 2007). ...	60
Figure 3-3: Node at plane surface with convection (Incropera <i>et al.</i> , 2007).....	62
Figure 3-4: Schematic layout of fuel rods, coolant channels, Flownex solid nodal points and the associated Flownex CVs. ....	64
Figure 3-5: Coolant channel surrounded by fuel rods. ....	65
Figure 3-6: Unit cell for conduction between fuel rod and coolant channel. ....	65
Figure 3-7: Finite volume discretisation scheme (Greyvenstein, 2002).....	70
Figure 4-1: Node and element representation for two connected CHT elements.....	75
Figure 4-2: Node and element representation for two cross CHT elements.....	75
Figure 4-3: Node and element representation for a convection element.....	76
Figure 4-4: Schematic layout of heat transfer in a cubical block in Flownex.....	78
Figure 4-5: Schematic representation of the block and the boundary conditions for the first case. ....	79

Figure 4-6: Steady state temperature results from Flownex and STAR-CCM+ for the first case. ....	79
Figure 4-7: Transient temperature results from Flownex and STAR-CCM+ for the first case. ....	81
Figure 4-8: Schematic representation of the block and the boundary conditions for the second case. ....	81
Figure 4-9: Steady state temperature results from Flownex and STAR-CCM+ for the second case. ....	82
Figure 4-10: Transient temperature results from Flownex and STAR-CCM+ for the second case. ....	83
Figure 4-11: Schematic representation of the block and the boundary conditions for the third case. ....	84
Figure 4-12: Steady state temperature results from Flownex and STAR-CCM+ for the third case. ....	84
Figure 4-13: Transient temperature results from Flownex and STAR-CCM+ for the third case. ....	85
Figure 4-14: Schematic representation of the block and the boundary conditions for the fourth case. ....	86
Figure 4-15: Steady state temperature results from Flownex and STAR-CCM+ for the fourth case. ....	86
Figure 4-16: Transient temperature results from Flownex and STAR-CCM+ for the fourth case. ....	87
Figure 4-17: Schematic representation of the block and the boundary conditions for the fifth case. ....	88
Figure 4-18: Steady state temperature results from Flownex and STAR-CCM+ for the fifth case. ....	88
Figure 4-19: Transient temperature results from Flownex and STAR-CCM+ for the fifth case. ....	89

Figure 4-20: Discretisation of the block in the (a) radial and (b) tangential directions.....	90
Figure 4-21: Boundary temperature conditions for Flownex models. ....	91
Figure 4-22: Schematic layout for the simple 3 × 3 node model heat transfer network. ....	92
Figure 4-23: Comparison of n node systems in the radial direction.....	93
Figure 4-24: Comparison of n node systems in the tangential direction. ....	95
Figure 4-25: STAR-CCM+ triangular block model and the meshed cells. ....	96
Figure 4-26: Comparison between the 11 × 3, 11 × 5 and STAR-CCM+ models in the radial direction.....	97
Figure 4-27: Comparison between the 11 × 5, 11 × 3 and STAR-CCM+ models in the tangential direction. ....	98
Figure 4-28: Comparison between the 800 K and 900 K vertex Flownex models with the STAR-CCM+ model in the radial direction.....	99
Figure 4-29: Comparison between the 800 K and 900 K vertex Flownex models with the STAR-CCM+ model in the tangential direction. ....	99
Figure 4-30: Case 2 comparison between STAR-CCM+ and FLOWNEX at the centroid after dropping the temperature at the boundary BC.....	101
Figure 4-31: Case 2 comparison between STAR-CCM+ and Flownex at the centroid after dropping the temperature at the boundary AB.....	102
Figure 4-32: Case 3 comparison between STAR-CCM+ and Flownex for a steady state.....	103
Figure 4-33: Case 3 comparison between STAR-CCM+ and Flownex at the centroid after increasing the heat source. ....	104
Figure 5-1: PMR200 core internal structure and nominal flow (Tak <i>et al.</i> , 2012).....	106
Figure 5-2: Core radial layout (Tak <i>et al.</i> , 2012).....	107
Figure 5-3: Standard fuel element of PMR200 (Tak <i>et al.</i> , 2012).....	108
Figure 5-4: Control or reserved shutdown fuel element of PMR200 (Tak <i>et al.</i> , 2012).....	109
Figure 5-5: Flow paths in the prismatic HTR core (Yoon <i>et al.</i> , 2012).....	110

Figure 5-6: Isolated one sixth segment of a prismatic block and its dimensions. ....	111
Figure 5-7: Flownex network for heat transfer from the fuel rod surface to the coolant channel. ....	112
Figure 5-8: An illustration layout of a heat transfer and flow network for a 3 × 3 node model. ....	113
Figure 5-9: CHT element layout (M-Tech, 2013).....	117
Figure 5-10: CHT element property window. ....	118
Figure 5-11: Example of a 2D plate represented by CHT cross CHT elements. ....	119
Figure 5-12: Cross CHT connection in the width direction. ....	119
Figure 5-13: Cross CHT connection in the height direction. ....	120
Figure 5-14: Cross CHT element property window. ....	120
Figure 5-15: Convection from a solid node (M-Tech, 2013). ....	121
Figure 5-16: Convection element property window. ....	122
Figure 5-17: Boundary condition input property page layout. ....	123
Figure 5-18: Node property window. ....	124
Figure 5-19: Pipe property window. ....	125
Figure 5-20: A one twelfth fuel element block showing the fuel compacts, cooling channels and graphite structure (Tak <i>et al.</i> , 2012).....	126
Figure 5-21: Fine and coarse mesh point distribution. ....	127
Figure 5-22: Expanded CAD model showing graphite, fuel rods, cooling channels and by- pass gap. ....	128
Figure 5-23: Initial fine mesh and extrude coarse mesh representing the fuel element. ....	129
Figure 5-24: Flat boundary layer cells for fluid adjacent to solid walls. ....	129
Figure 5-25: (a) Turbulent and laminar velocity power-law empirical velocity profile (b) exponent n as a function of the Reynolds number (Morrison, 2013).....	131

Figure 5-26: (a) Flat boundary layer cells (b) $y^+$ values plotted on the walls of the cooling channel. ....	132
Figure 5-27: Boundary conditions for the fuel element.....	133
Figure 5-28: Fully developed turbulent velocity profiles at the cooling channel inlets.....	134
Figure 5-29: Solid temperature profiles for a coarse mesh. ....	135
Figure 5-30: Sensitivity of solid temperature to mesh density. ....	136
Figure 5-31: Boundary layer refinement for the cooling channel. ....	137
Figure 5-32: Sensitivity of solid temperature to $y^+$ value.....	137
Figure 5-33: Variation in maximum temperature versus cell size in the length direction.....	139
Figure 5-34: Convergence behaviour for a steady state solution of the fuel element. ....	140
Figure 5-35: Temperature contours for a steady state solution of the fuel element for the bottom/outlet side of the block.....	140
Figure 5-36: Schematic indicating the centreline and the outer edge in the Flownex and STAR-CCM+ models.....	143
Figure 5-37: Temperature distributions along the centreline for both STAR-CCM+ and Flownex for the integrated block.....	144
Figure 5-38: Temperature distributions along the outer margin for both STAR-CCM+ and Flownex for the integrated block.....	145

## **Nomenclature**

### **General**

$A$	Area.
$A_e$	Cross-sectional area at the control volume face, e.
$A_{fs}$	Equivalent surface area of the fuel rods.
$A_s$	Equivalent surface area.
$A_{sw}$	Surface area of the coolant channels.
$A_1$	Upstream Cross sectional area.
$A_2$	Downstream cross sectional area.
$A_m$	Average area between $A_1$ and $A_2$ .
$Bi$	Biot number.
$C_p$	Heat capacity.
$D$	Inside diameter of the pipe.
$D_H$	Hydraulic diameter.
$D_h^{CH}$	Hydraulic diameter of the coolant channel.
$\dot{E}_{in}$	Inflow of thermal and mechanical energy across the control surface.
$\dot{E}_{out}$	Outflow of thermal and mechanical energy across the control surface.
$\dot{E}_g$	Thermal energy generation.
$\dot{E}_{st}$	Stored mechanical and thermal energy.
$F$	Geometric view factor.
$F_{12}$	Geometric view factor from surface 1 to surface 2.
$f$	Friction factor.
$F_o$	Fourier number.
$g$	Acceleration due to gravity constant.
$h$	Convection heat transfer coefficient.
$h$	Specific static enthalpy.
$h_o$	Specific total enthalpy
$h_{0e}$	Total enthalpy of the eastern element.
$h_{0w}$	Total enthalpy of the western element.
$k$	Thermal conductivity.
$k_C$	Thermal conductivity of the coolant channel.
$k_{eff,rad(1)}$	Effective thermal conductivity of the fuel block in the radial direction.
$k_{eff,axial(1)}$	Effective thermal conductivity of the fuel block in the axial direction.
$k_f$	Thermal conductivity of the fuel compact.
$k_{gas}$	Thermal conductivity of helium.

$k_s$	Thermal conductivity of the graphite block.
$K_i$	Inlet loss coefficient.
$K_e$	Outlet loss coefficient.
$L$	Characteristic length.
$L$	Length of heat transfer path.
$L_c$	Conduction length.
$L_{fs}$	Distance from the fuel rod surface to the graphite node.
$L_{sw}$	Distance from the graphite node to the coolant channel wall.
$M$	Mach number.
$n_h$	Heating constant.
$n_c$	Cooling constant.
$N_1$	Upstream node.
$N_2$	Downstream node.
$Nu$	Nusselt number.
$Nu_{lam}$	Specified laminar Nusselt number.
$Nu_{turb}$	Nusselt number for turbulent flow.
$p$	Static pressure.
$p_o$	Total pressure.
$Pr$	Prandtl number.
$q$	Rate of heat transfer.
$Q$	Volumetric flow rate.
$Q$	Net heat added to the system.
$Q_{conv}$	Rate of convection heat transfer.
$Q_{rad}$	Rate of radiation heat transfer.
$R$	Gas constant.
$Re$	Reynolds number.
$R_{t,cond (2D)}$	Two dimensional conduction resistance.
$s$	Compressibility factor.
$S$	Conduction shape factor.
$S_{fs}$	Conduction shape factor (fuel rod surface to graphite).
$S_{sw}$	Conduction shape factor (graphite to coolant channel wall).
$t$	Time.
$T$	Static temperature.
$T_f$	Fuel rod surface temperature.
$T_o$	Total temperature.
$T_s$	Graphite mass averaged temperature.

$T_s$	Surface temperature.
$T_{surr}$	Surface absolute temperature of a larger (black) surface.
$T_w$	Coolant channel wall temperature.
$T_\infty$	Fluid temperature.
$T_{1-2}$	Temperature difference between boundaries.
$v$	Mean velocity.
$V$	Volume.
$v_i$	Velocity at the pipe inlet.
$v_e$	Velocity at the pipe outlet.
$W$	Net work done by the system.
$x$	Length in the direction of the flow.
$z$	Elevation.
$\Delta p_{or}$	Total pressure drop over an orifice.
$\Delta t$	Time step size.
$\Delta T_0$	Total temperature difference.
$\Delta x$	Distance between the nodes in the x –direction.
$\Delta y$	Distance between the nodes in the y-direction.
$\Delta z$	Height difference between the inlet and outlet.
$\sum K_s$	Sum of secondary loss components like bends, valves and junctions.

### Greek letters

$\varepsilon$	Surface emissivity.
$\varepsilon_1$	Upstream surface emissivity.
$\varepsilon_2$	Downstream surface emissivity.
$\sigma$	Stefan-Boltzmann constant.
$\forall$	Volume of the control volume.
$\alpha$	Weighting factor.
$\varepsilon$	Mean inside wall roughness.
$\rho$	Density.
$\rho_e$	Density of the eastern elements.
$\rho_w$	Density of the western elements
$\alpha_c$	Volume fraction of the coolant channel.
$\alpha_f$	Volume fraction of the fuel compact.

## Abbreviations

1-D	One dimensional.
2-D	Two dimensional.
3-D	Three dimensional.
ALE	Arbitrary Lagrangian Eulerian.
B <sub>4</sub> C	Boron Carbide.
CAD	Computer Aided Design.
CFD	Computational Fluid Dynamics.
CHT	Conductive Heat Transfer.
CORONA	Core Reliable Optimisation and thermo-Network Analysis.
CV	Control Volume.
FD	Finite Difference.
FE	Finite Element.
FV	Finite Volume.
GA	General Atomics.
GCR	Gas Cooled Reactor.
GIF	Generation IV International Forum.
GFR	Gas cooled Fast Reactor.
GT-MHR	Gas Turbine Modular Helium Reactor.
HENDEL	Helium Engineering Demonstration Loop.
HTGR	High Temperature Gas cooled Reactor.
HTTR	High Temperature Test Reactor.
HTR	High Temperature Reactor.
IEO	International Energy Outlook.
IPCM	Implicit Pressure Correction Method.
JAERI	Japan Atomic Energy Research Institute.
LFR	Lead cooled Fast Reactor.
LBP	Lumped Burnable Poison.
MINATOM	Russian Federation Ministry of Atomic Energy.
MSR	Molten Salt Reactor.
MWe	Megawatt electrical energy.
MWt	Megawatt thermal energy.
PBMR	Pebble Bed Modular Reactor.
SCR	Silicon Controlled Rectifiers.
SCWR	Supercritical Water Cooled Fast Reactor.
SFR	Sodium cooled Fast Reactor.
TRISO	Tristructural Isotopic.

VHTR

Very High Temperature Reactor.

USA

United States of America.

# 1. INTRODUCTION

---

## 1.1 Introduction

### 1.1.1 Global energy outlook

According to the International Energy Outlook 2013 (IEO, 2013), global energy consumption is expected to increase by a 56 percent margin over a 30 year period. The global net electricity generation is projected to increase from 20.2 trillion kilowatt-hours in 2010 to 39.0 trillion kilowatt-hours in 2040 (IEO, 2013). Coal is abundant in the most energy-consuming countries such as China, the USA, India, Australia and some parts Europe, and as a result coal is the main fuel for electricity production. However the carbon dioxide emissions are high and to counteract these high levels of emission, technologies such as carbon dioxide separation and sequestration, which are not yet commercially mature have to be implemented (Lior, 2008). Wind and solar photovoltaic power generation are not yet commercially viable at a large scale. Hydrogen production efficiency is low and challenges such as transportation and safety remain (Lior, 2008).

Nuclear is another significant non-renewable source of energy, mostly for power generation, which yields approximately 16 percent of the global electricity generation. The increasing concern of global warming from fossil fuels and the improved public perspective on nuclear power has led to the evolution of new government initiatives (Lior, 2008). However, concerns about safety, nuclear proliferation and nuclear waste disposal still linger.

### 1.1.2 A description of Generation IV future goals and reactors

The Generation IV International Forum (GIF) has identified the goals for future nuclear power into four categories namely: sustainability, economic competitiveness, safety and reliability and proliferation resistance and physical protection (Forum, 2002).

- Sustainability is the aptitude of meeting the energy needs of the present generation while reinforcing the energy needs for future generations indefinitely. The sustainability objectives for the GIF include waste management, resource utilization and extension of nuclear power into other energy sectors such as transportation and production of other energy products such as hydrogen from nuclear process heat.
- Economic competitiveness regards the competitive costs and financial risks that come with nuclear energy systems. The reduction of operating and capital costs by increasing the fuel cycle efficiency, design simplifications and plant sizes are also approaches to having competitive costs. The reduction of economic risk to nuclear systems can be

implemented by the development of plants built using innovative fabrication, construction techniques and modular designs.

- Safety and reliability goals encompass safe and reliable operations, investment security, reduced need for off-site emergency response, improved accident management and minimization of consequences.
- Proliferation resistance and physical protection goals comprise of techniques of controlling and safeguarding nuclear material and nuclear facilities against intentional and unintentional activities (Forum, 2002).

The Generation IV reactor systems which were selected by the GIF are:

- Gas-Cooled Fast Reactor systems (GFR).
- Lead-Cooled Fast Reactor systems (LFR).
- Molten Salt Reactor systems (MSR).
- Sodium-Cooled Fast Reactor systems (SFR).
- Supercritical-Water-Cooled Reactor systems (SCWR).
- Very –High –Temperature Reactor systems (VHTR).

## **1.2 High Temperature Reactors**

### **1.2.1 Background of High Temperature Reactors (HTRs)**

Gas-cooled reactors (GCRs) amongst many other types of reactors have been explored since the evolution of nuclear power. The main focus on gas cooled reactors centred on development rather than deployment, and as a result construction of a significant number of prototype and demonstration plants in Britain, Germany and the USA began. Increasing the coolant temperatures and plant efficiencies were the main objectives of these plants (Chapin *et al.*, 2004).

The development of helium gas cooled reactors dates back in 1959 when the construction of the DRAGON reactor started in Great Britain. This reactor was operated productively from 1966 to 1975 until it was closed due to political and financial inferences (Kugeler & Schulten, 1989). This reactor used ceramic fuel elements and was the first to use coated fuel particles.

The Peach Bottom and the Fort St. Vrain reactors were also developed in the United States. They operated from 1965 to 1988 and 1976 to 1989 respectively. The Peach Bottom reactor made an extensive contribution to fuel technology on the block type fuel elements. The Peach Bottom Reactor was stopped when the Fort St. Vrain Reactor came into operation.

In Germany, the AVR Reactor was developed in 1965 (Kugeler & Schulten, 1989). The AVR Reactor used pebble fuel elements. This reactor operated for more than 20 years. The HTR was operated soon after the AVR but was however closed due to financial and political motives after the Chernobyl accident in Ukraine (Kugeler & Schulten, 1989).

### **1.2.2 Developments of HTR technology**

Over the years new HTR concepts have been established. A few development projects in the GIF member states include:

#### **a) HTTR (Japan)**

The High Temperature Test Reactor (HTTR) Project began with preparatory design, research and development by the Japan Atomic Energy Research Institute (JAERI) (Chapin *et al.*, 2004). The HTTR uses a block type tubular fuel element (Kugeler & Schulten, 1989). The primary aims of the HTTR are to establish and improve the technological aspects for High Temperature gas-cooled Reactors (HTGR) and to carry out numerous irradiation tests for advanced high temperature basic researches. The HTTR construction was finalized in 1996. This test reactor reached its first criticality in 1998 and the first full power operation with an outlet coolant temperature of 850 °C was accomplished in 2001 (IAEA, 2003).

#### **b) HTR-10 (China)**

The construction of the 10 MW High Temperature gas-cooled Reactor-test module (HTR-10) in China started in 1995. The criticality of this reactor was reached in December 2000, and full power operation started in January 2003. The HTR-10 reactor is a graphite moderated helium gas cooled reactor which uses pebble bed fuel elements (Tsinghua, 2010). Approximately 100 commissioning checks have been finished and 6 safety test experiments have been conducted since 2003 (Tsinghua, 2010).

#### **c) GT-MHR (USA and Russia)**

In February 1995, the Russian Federation Ministry for Atomic Energy (MINATOM) and General Atomics (GA) signed an agreement for the development and design of the Gas Turbine Modular helium reactor (GT-MHR) (Kiryushin *et al.*, 1997). The core function of the GT-MHR is production of electricity, cogeneration of electricity and process heat and burning of weapon grade plutonium very effectively. The GT-MHR will use the block type fuel element with Tristructural-Isotropic (TRISO) particles embedded in fuel rods (Kugeler & Schulten, 1989).

#### **d) PBMR (South Africa)**

For some years, South Africa had been developing the Pebble Bed Modular Reactor (PBMR). The PBMR design comprised of a pebble-bed reactor merged with a Brayton cycle and a three-shaft-turbo-machine. A thermal power of approximately 260 MWt and a net electrical output estimate of 110 MWe were projected (Kugeler & Schulten, 1989). The PBMR reactor was designed to have add-on safety equipment and ceramic materials and thus eliminating the release of any radioactive substances in normal operation and accident conditions. Mr Juan le Roux, the power plant division software systems manager for PBMR recited that, “The beauty of the pebble bed modular nuclear Reactor (PBMR) technology is that it has intrinsically safe features. It cannot suffer a meltdown”. He went on to say that “The nuclear plant is easy to operate and you can regulate the power output. You couldn’t do that with the conventional reactors, which needed to run at 100 percent all the time. Also, the pebble bed design allows us to refuel the plant without shutting it down, which represents enormous cost savings.” (Intergraph, 2014).

The South African government stopped funding the PBMR project in 2010 due to a number of factors. At present, ESKOM is managing the PBMR assets and the main PBMR test facilities that include fuel development and helium test facility are secured and maintained (WNA, 2014).

### **1.3 Modelling of HTRs**

#### **1.3.1 The role of simulations**

Dependable flow and heat transfer simulations are of great importance in the next generation HTRs (Becker & Laurien, 2003). The advancement of computer capabilities has made the analysis of complex physical and chemical interrelations possible. The physical and chemical interrelations play a huge role in determining plant behaviour in both normal and accident conditions (Rohde *et al.*, 2012). The development of existing calculation techniques for HTRs has led to a new generation of simulation tools for both pebble-shaped and prismatic fuel assemblies (Rohde *et al.*, 2012).

Process simulators in the nuclear industry are used for various purposes which include: design verification and validation, understanding the designed system(s), monitoring and assessing operating systems and operator training. Numerical computer based simulation packages simulate several plant conditions thereby giving the plant operator an opportunity to practice on how to respond to normal or accident conditions (Jayanthi *et al.*, 2007).

#### **1.3.2 Numerical approaches used in thermal-fluid simulations**

Thermal-fluid simulations can be performed using a three-dimensional (3-D) CFD approach or a system CFD or thermal-fluid network approach.

A 3-D CFD approach will endeavour to simulate the full detail of the geometry and the thermal-fluid phenomena that occur in a HTR (Versteeg & Malalasekera, 2007). An example of code that is based on a 3-D CFD approach is STAR-CCM+ (Chung, 2002) which is the 3-D CFD code that was employed in this study.

A thermal-fluid network for an HTR articulates the complex behaviour of the thermal hydraulics in a HTR using a one dimensional (1-D) approach. An example of a system code is Flownex (M-Tech, 2013) which is the network code that was used in this study.

### **1.3.3 Flownex**

The development of the Flownex simulation software started in 1986. The Hardy Cross method which was used to solve for air distribution networks for aero belt conveyor systems sired the development of the code. Over the years, there were improvements on Flownex such as extending the code to deal with complete aircraft air-conditioning and fuel systems. In 1992, the code was called Flownet. In 1999, M-Tech Industrial was contracted by the PBMR (Pty) to re-develop Flownet. The code name Flownet was changed to Flownex in 2001.

Flownex has been successfully integrated into an engineering simulation environment to form part of an extensive plant simulation, analysis as well as optimization suite of tools. Flownex is being continually developed and improved to execute thermal-fluid analyses on many applications using an implicit approach. Looking closely at the PBMR, Flownex had been used to calculate mass flow rates, pressures and temperatures in the reactor core and the Brayton cycle during normal operation and accident conditions. Steady state as well as transient calculations are also accomplished using Flownex (M-Tech, 2013).

### **1.3.4 CFD**

CFD is the analysis of matter with a fluid like nature (something that is capable of flowing) by using computer based simulations (Versteeg & Malalasekera, 2007). CFD is a branch of mechanics that utilizes numerical algorithms to solve differential equations and evaluate fluid flows, heat transfer as well as chemical reactions.

All CFD commercial packages have sophisticated user interfaces which are used to input problem specifications and to evaluate the results. Three main components which are contained in all CFD codes are: a pre-processor, a solver and a post-processor (Versteeg & Malalasekera, 2007). Pre-processing includes the creation of surface meshes and setup of boundary conditions for thermal analysis and heat transfer modelling. A solver is a numerical technique used to solve the differential equations for a given problem. Three distinct numerical solution methods are used in CFD analysis namely: finite element (FE), finite difference (FD) and finite

volume (FV) methods. The code STAR-CCM+ is based on the FV method. The post-processing stage entails evaluating, visualising and estimating the accuracy of the solution. Some visualization tools include vector plots, two dimensional (2-D) and 3-D surface plots, colour postscript output and particle tracking (Versteeg & Malalasekera, 2007).

#### **1.4 Problem statement**

Advanced System CFD or network models for the flow and heat transfer for a pebble fuel element and pebble-bed reactor have been developed using Flownex. However, no advanced system CFD or network models for prismatic standard and control or reserved shutdown fuel assemblies using Flownex have been established. This thesis discusses a system CFD model that simulates the heat transfer and fluid flow in a prismatic block in a representative manner which could be extended to model the entire reactor and the associated thermal-flow systems. The model comprised of a collection of 1-D solid conduction, convection heat transfer and pipe elements that were arranged in a distinct manner to represent the heat transfer and fluid flow in the prismatic block using a network approach.

The development of a system CFD or network model for the flow and heat transfer for a prismatic block will aid in giving an insight to anyone who intends to perform an integrated thermal-hydraulic analysis for the prismatic high temperature reactor core and the associated plant.

#### **1.5 Study objectives**

The main objectives of this study included:

- Developing a thermal-fluid network model for an HTGR prismatic block reactor using Flownex.
- Analysing the heat transfer from the fuel to the coolant (helium) in two dimensions within a prismatic block and at the bypass gap.
- Verification of the Flownex model using the CFD code STAR-CCM+ by modelling different scenarios in both codes and comparing the results. The STAR-CCM+ code was used as an experimental set-up in this study.

The validity of the Flownex model was investigated by comparing the heat transfer and temperature distribution of the prismatic block with the corresponding values obtained using STAR-CCM+ model.

It is important to note that even though some phenomenological aspects of HTGRs are important, in this study they were not modelled. These aspects include:

- Heat transfer by radiation.
- Cross flows.
- Neutronics.

## 1.6 Layout of dissertation

This chapter gave a short description on the goals of the GIF and how the HTR is playing a part in achieving those goals. The evolution of the HTR from the 1950s up until now has been outlined. Numerical methods which are used in simulating thermal-fluid problems have been mentioned as well.

A short outline of the succeeding chapters in this dissertation is as follows:

**Chapter 2:** An overview of the literature survey is conducted. A background to modelling strategies and the relevant theory of HTRs are discussed in this chapter. The chapter concludes with previous studies conducted on HTRs particularly coolant flow analysis, accident scenarios and flow and heat transfer modelling.

**Chapter 3:** In this chapter an overview on the theoretical background required to simulate fluid and heat transfer in an HTR block is given. Some background on numerical modelling is also outlined.

**Chapter 4:** In this chapter, five cubical and three triangular blocks simple test cases that were modelled in Flownex are discussed and the results compared with the corresponding STAR-CCM+ results.

**Chapter 5:** This chapter demonstrates the modelling procedure, the assumptions, parameters and boundaries implemented in modelling an HTR prismatic block in both Flownex and CFD code StarCCM+. The Flownex and STAR-CCM+ results for the HTR block are compared.

**Chapter 6:** In this final chapter, conclusions of the findings of this study are drawn and recommendations for future work are made.

## 2. LITERATURE SURVEY

---

### 2.1 Introduction

In the preceding chapter, the position of the GIF reactors was outlined in the framework of sustainability, economic competitiveness, safety and reliability as well as proliferation resistance and physical protection. In this chapter, simulation of thermal systems will be discussed. The implicit and explicit numerical methods will also be discussed. Methods for solving 2-D conduction steady state problems are also dealt with in this chapter. This chapter will conclude with previous work done on HTRs. Three broad studies will be surveyed; coolant flow analysis, accident conditions studies and modelling of flow and heat transfer.

### 2.2 Principle of thermal-fluids network

In a thermal-hydraulic process, the flow and heat transfer phenomena can be comprehensively described by a thermal-fluid network. The thermal-fluid network comprises of a fluid network and a thermal network that are linked. The fluid network simulates the coolant flow in the fluid region while the thermal network simulates the heat transfer in the solid regions and also the interface between the fluid and solid regions (Yangping *et al.*, 2013). The coupling between the fluid and thermal networks is conducted through heat convection.

A thermal-fluid network consists of a representative of 1-D elements and components e.g. pipe flow networks. A thermal-fluid network is established by the fundamental component of a node and a branch (Yangping *et al.*, 2013). A node represents a specific region, and its temperature is a measure of the average temperature of the region (Incropera *et al.*, 2007). Branches are the elements of the flow network where flow conditions such as geometry and flow rate are known or calculated (Schallhorn & Popok, 1999).

### 2.3 Simulation of thermal systems

Modelling and simulation enables designers to assess whether design specifications are met by using computer-generated tests rather than physical experiments. The utilization of computer generated models significantly reduces the cost as well as the time spent on the design. The conventional methods used in design and simulation of engineering systems are manual calculations, spread-sheets and CFD. Manual calculations are very basic and spread-sheets are not compatible with other systems and time consuming to generate. The CFD analysis even though highly accurate is expensive in terms of pre-processing, solving, post processing, computational resources and time.

Nuclear reactors have simultaneous heat transfer mechanisms by conduction, convection and radiation in complex geometries. It is therefore necessary to build a lumped parameter network for the heat transfer. The network design consists of node arrays made up of individual nodes which can either be passive or attached with heat sources or sinks. The nodes are interconnected by resistances equivalent to numerous mechanisms of heat transfer (Zvizdić & Ružinski, 2000). This methodology incorporates existing theoretical and empirical heat transfer information as well as flexible network theory as building blocks for the network analogy model. The network analogy model is designed to demonstrate heat transfer occurrence at specific positions in a system (Van Der Merwe, 2003).

Thermal fluid systems can be regarded as networks of flow paths through various components such as pipes, valves, compressors, turbines, heat exchangers and power sources. Data such as pressure drop correlations and thermal behaviour of the components can be obtained from handbooks or vendor specifications. During the early stages of a design, it is impractical to use CFD for a large number of design alternatives. This is due to the time spent on setting up the model, solving and pre-processing the large amount of data. A thermal fluid approach ensures fast and accurate predictions of flow distribution and thermal efficiency of a system.

### **2.3.1 The network approach**

A thermal network is characterized by an array of nodes and conductances, and is similar to an electrical network. The network approach originates from the energy balance equations and corresponds to a particular finite difference discretization of the fundamental heat transfer equation (Milman & Petrick, 2000).

In order to develop a thermal network it is necessary to subdivide the thermal system into finite sub-volumes. These sub-volumes are the nodes. The thermal properties of each node are designed to be concentrated at the central nodal point of each sub-volume. Each node represents a temperature (potential) and a capacitance (thermal mass). A nodal temperature represents the average mass temperature of the sub-volume while a nodal capacitance is calculated from the thermo-physical properties of the sub-volume material evaluated at the temperature of the node. The nodal capacitance is also assumed to be concentrated at the nodal centre of the sub-volume. Since a node symbolizes a lumping of parameters to a single point in space through a sub-volume, it therefore implies that the nodal temperature is linear and not a step function. In a homogeneous material, the temperature of any point which is not a nodal point and is situated between two nodes can be approximated by interpolation between the two adjacent nodal points where the temperatures are known (NASA, 2000).

1-D network modelling has some restrictions which can be compensated for by 2-D or 3-D flow and thermal analyses. These can predict the flow parameters to the required level of detail.

### 2.3.2 CFD Approach

The CFD approach provides a numerical description of fluid flow behaviour. This is achieved by solving the governing equations which are the conservation of mass, momentum and energy on a per unit volume basis. The CFD approach uses the FV method discretisation technique for discretizing its domain. **Figure 2-1** displays a 2-D control volume implemented in the CFD approach.

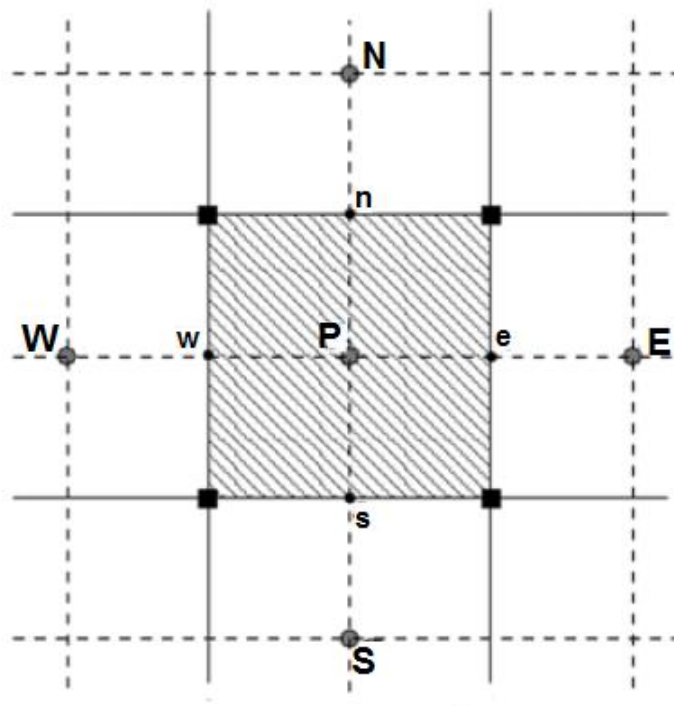


**Figure 2-1:** Conventional control volume for a CFD approach (Cruz & Monsivais, 2014).

Properties of the control volume (velocity, pressure and temperature) which are assumed to fluctuate smoothly over a control volume are averaged and represented at the central nodal point P. The velocities, pressures and temperatures of the control volume are related to its nearest neighbours (N, S, E and W) and the mass, momentum and energy fluxes across the boundaries of the control volume, after the differential forms of the conservation equations have been integrated in a distinct way. This facilitates the computation of velocity, pressure and temperature distributions throughout the flow field (Rousseau, 2013).

It is important to note that this approach utilises the staggered grid approach which will be explained more in section 2.6.3.

It is important to note that even though CFD requires a solution of the mass, momentum and energy equations, it usually involves a single component or a part of it. A CFD analysis is not suitable for a large system where the designer needs to adjust and optimize certain variables to reach an optimum design. This is because a CFD analysis requires a complex definition of the problem and may require extensive computational resources. It would therefore be recommended to conduct a 1-D analysis at an early stage of a design, if suitable, and then progress to a 3-D CFD analysis as the design/analysis process develops. This will serve as a guide on the design process.

**2.3.3 System CFD Approach**

The system CFD which is also named the network approach utilizes a collection of 1-D elements linking nodes in any unstructured way. Flownex is based on this approach. The circles represent the elements while the squares represent the nodes as illustrated in **Figure 2-2**. The elements can be any thermal fluid component for instance a pipe, fan, compressor, turbine, heat exchanger or a pump. The nodes can either represent a reservoir or tank by retaining a volume or just being a connection between two elements with no physical implication. An essential feature of the network approach is that thermal-fluid components although portrayed on the systems level as single elements or pairs of elements, can be discretized into sub-networks. Networks can thus be embedded inside networks thereby aiding the model to treat complex elements as distributed systems rather than lumped systems (Greyvenstein *et al.*, 2002)

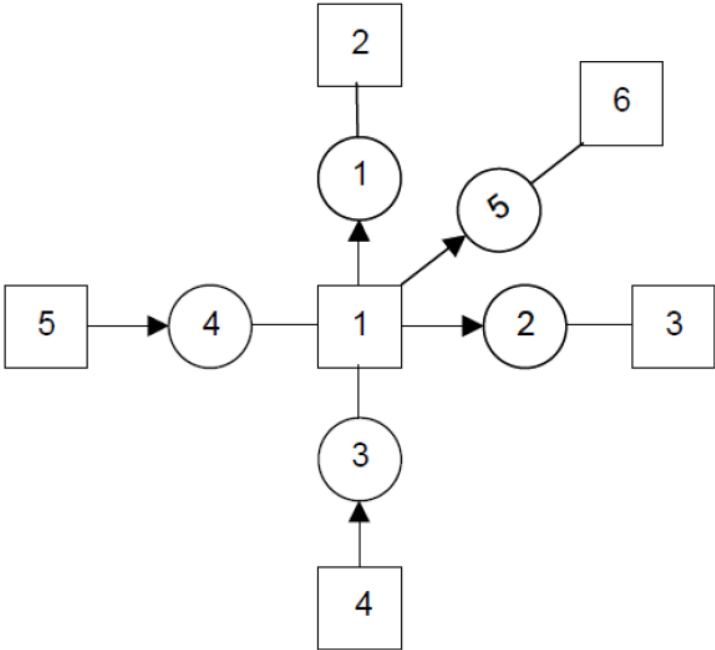


**Figure 2-2: Conventional node element configuration for a systems-CFD approach (Rousseau, 2013) .**

Analogous to the CFD approach, the system CFD approach assumes the properties of the fluid in a node to be represented by a single averaged value. The conservation of mass and energy are also written for a node while the conservation of momentum is written for elements that connect the nodes.

Despite the fact that 1-D flow may seem restrictive, it is imperative to note that any two or three dimensional flow field can be built up with the network approach by assembling the appropriate combination of elements for each coordinate system. This approach is used in the discretized heat exchangers and pebble bed reactor models (Rousseau, 2013).

## **2.4 Numerical solution algorithms**

### **2.4.1 Explicit vs. implicit numerical methods**

Explicit and implicit numerical methods are tactics used in numerical analysis for attaining numerical solutions of time dependent ordinary and partial differential equations. These methods are employed in computer simulations of physical processes. An explicit method is a direct computation as it calculates the state of a system at a later time from the state of the system at the current time by looking forward in time. An implicit method is an iterative method as it calculates the state of a system at the current time from the state of the system at the previous time by looking backward in time.

In CFD, the governing equations are non-linear and the number of unknown variables is usually very large. As a result, implicitly formulated equations are mostly solved using iterative techniques (Flow3D, 2014).

Iterations are utilized to advance a solution through a series of steps from the initial state to the final converged state. This is true even if the solution needed is either one step in a transient problem or a final steady state result. In either case, the iteration steps resemble a time-like process. The iteration steps typically do not correlate to a realistic time-dependent behaviour. This characteristic of an implicit method makes it more favourable for steady state computations because the number of iterations needed for a solution is mostly much smaller than the number of time steps needed for an accurate transient that asymptotically approaches steady conditions (Flow3D, 2014)

This “distorted transient” feature has led to the questioning of the consequences of using an explicit versus an implicit solution method for a time-dependent problem. The answer to this question has two parts. The numerical stability and accuracy of the chosen method comes into play (Flow3D, 2014).

Flownex is an implicit network solver, and was the primary code that was used in this study. Both the explicit and implicit methods yield satisfactory solutions provided the time step is small. However the behaviour of both explicit and implicit methods for a large time step size is essential to compute the slow long-term behaviour of solutions. The implicit method is therefore faster than the explicit method due to the large time step that can be used and less computing time. This aspect arouses the question of stability (Van Der Merwe, 2003).

#### 2.4.2 The Stability Issue

The prime reason for using implicit solution methods which are more complex to program and require more computational effort in each solution step, is to permit large time step sizes. Numerical stability has to do with the behaviour of the solution as the time step  $\Delta t$  is increased. If the solution remains well behaved after an arbitrary large value of the time step, the method is then termed to be unconditionally stable. This is the case with the implicit method, it is unconditionally stable and yields bounded solutions for any time steps. This situation never happens with explicit methods, which are constantly conditionally stable and requires a small ratio of time step  $\Delta t$  to the distance  $\Delta x$  (FlowScience, 2015).

#### 2.4.3 The Accuracy Issue

Numerical solutions of fluid flow and heat transfer problems are only approximate solutions. Besides the errors that might be introduced in the duration of the development of the solution algorithm, in programming or setting up the boundary conditions, numerical solutions always include three classes of systematic errors (Ferziger & Peric, 2013). These include:

- I. **Modelling errors** which are defined as the difference between the actual flow and the exact solution of the mathematical model.
- II. **Discretization errors** which are defined as the difference between the exact solution of the conservation equations and the exact solution of the algebraic system of equations acquired by discretizing these equations.
- III. **Iteration errors** which are defined as the difference between the iterative and exact solutions of the algebraic equations systems.

For a single small step, the Taylor series can be used to show that the explicit method is a first order accurate method. The implicit method is also a first order method (Van Der Merwe, 2003).

### 2.5 Two dimensional steady state conduction

In HTRs conduction is the main heat transfer mechanism from the fuel to the graphite and from the graphite to the coolant channel walls. If a 1-D conduction approach is used, it would grossly

oversimplify the heat transfer. Therefore there is a necessity to account for multidimensional conduction. In this section, three methods which are implemented in solving for 2-D steady state conduction are discussed.

### 2.5.1 Analytical method (Method of separation of variables)

The analytical method entails acquiring an exact mathematical solution from the heat equation. The heat equation for 2-D steady state conduction with no generation and a constant thermal conductivity is given by equation (2-1)

$$\frac{\partial^2 T}{\partial x^2} + \frac{\partial^2 T}{\partial y^2} = 0 \quad (2-1)$$

An analytical solution sets up a mathematical solution to equation (2-1). However equation (2-1) is very difficult to solve since it includes a partial instead of an ordinary differential equation. Although several methods which typically involve complicated mathematical series and functions are available for such kind of problems, they are however restricted to a set of simple geometries and boundary conditions. The method of separation of variables is one technique widely used to solve equation (2-1) analytically (Incropera *et al.*, 2007). However, analytical solutions are not always possible to solve and in most cases they are very cumbersome and difficult to implement. In these cases graphical and numerical techniques are often used to advantage (Incropera *et al.*, 2007).

### 2.5.2 Graphical method

The graphical method was mostly used before the era of computers. The graphical method was an effective technique of estimating the total heat transfer rate through a complex geometry. The graphic method still has a significance as it gives the problem solver a chance to develop a better feel for “how heat flows” through a complicated body (Incropera *et al.*, 2007).

The graphical method is based on the fact that lines of constant temperature are perpendicular to the lines denoting the direction of heat flow by conduction. Isotherms (lines of constant temperature) and heat flux lines (lines indicating the directions of heat flow) represent the lines of constant heat flow rate. These two sets of lines intersect at right angles and form a network of curvilinear squares termed a flux plot see (Figure 2-3). This flux plot is employed to deduce the temperature distribution and the heat flow rate through a system.

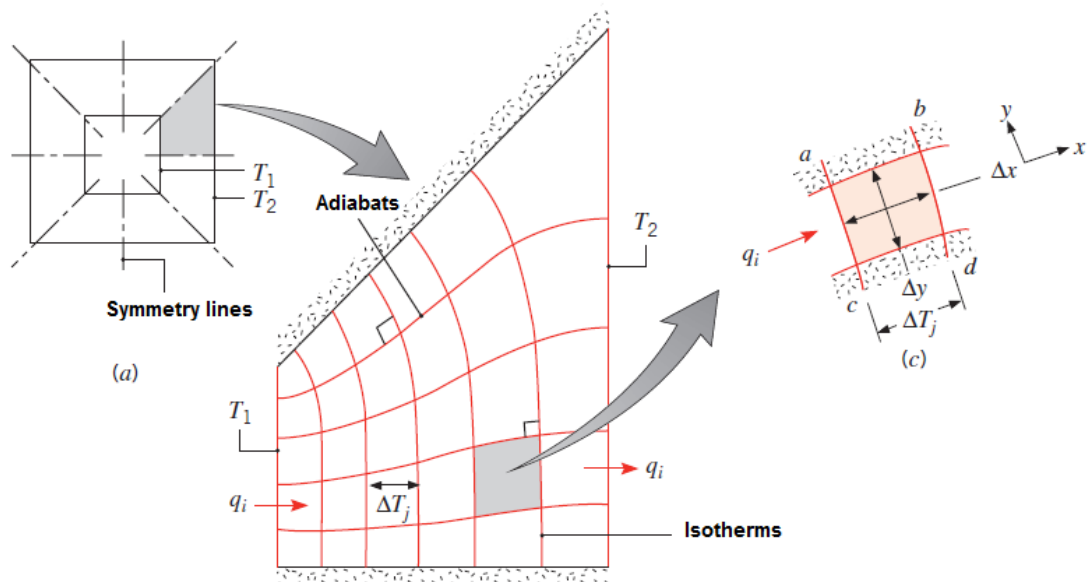


**Figure 2-3: Conduction in a square channel. (a) Symmetry planes. (b) Flux plot. (c) Typical curvilinear square (Incropera *et al.*, 2007).**

However, the graphical method is restricted to 2-D systems with isothermal and insulated boundaries. In spite of its restrictions, the graphical method generates sensible and satisfactory approximations of the temperature distribution and heat flow in a system (Incropera *et al.*, 2007).

The graphical method can also be implemented to estimate the conduction shape factors for 2-D geometries. The rate of heat transfer may be expressed as:

$$q = S k \Delta T_{1-2} \quad (2-2)$$

Where

$S$  = conduction shape factor,

$k$  = thermal conductivity and

$T_{1-2}$  = Temperature difference between boundaries.

Therefore a 2-D conduction resistance may also be expressed as:

$$R_{t,cond(2D)} = \frac{1}{Sk} \quad (2-3)$$

Where  $R_{t,cond(2D)}$  is a 2-D conduction resistance.

Conduction shape factors for some common configurations for numerous 2-D systems have been derived in literature. These derivations are beyond the scope of this study and will

therefore not be discussed. However in this study, the conduction shape factor in an HTGR reactor core will be discussed in the next chapter.

**2.5.3 Numerical method (Finite difference equations)**

It has already been established that analytical methods for a 2-D steady state conduction problem involves complex mathematical series and functions. Numerical methods however are much simpler and are flexible in its solution with respect to the geometry of the system and the boundary conditions. Numerical methods offer solutions that predict the values of the dependent variables at discrete points in the domain, called grid network. **Figure 2-4** below shows an example of a section of a grid network in an x-y plane.

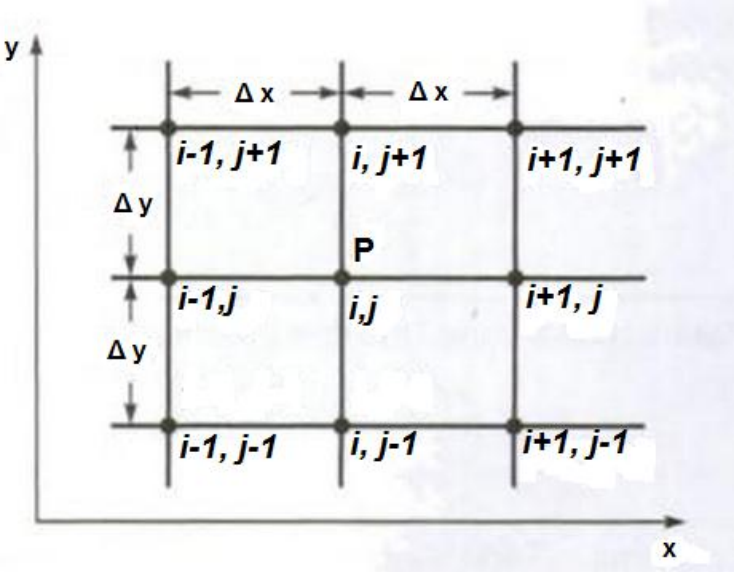


**Figure 2-4: Section of a grid network in an x-y plane (Bejan, 1993).**

In numerical methods the most effective approach is one that is based on finite-difference techniques (Incropera *et al.*, 2007). Some well-known finite difference techniques include the FV method, FE method and the FD method. Finite differences are used to estimate differential increments in the temperature and space coordinates. The smaller the finite increment, the more closely is the estimate temperature to the true temperature (Incropera *et al.*, 2007).

**2.6 Discretization schemes**

In the last section (section 2.5), numerical methods were briefly discussed. In order to attain an accurate temperature distribution within an HTGR core, there is a necessity to discretise the reactor core into a number of control volumes. It is well known that finite differences techniques are numerical methods that approximate a continuous temperature distribution with finite nodal

elements. The more the number of nodes the more comparable the approximation comes to the true temperature. An appropriate discretisation method should therefore be selected.

The FV discretisation scheme which transfers continuous models and equations into discrete counterparts is briefly discussed. Other known discretisation schemes such as the FE, FD, spectral schemes, boundary element methods and cellular automata will not be discussed in this study.

A numerical grid is defined as the discrete representation of the geometric domain for which the problem is to be solved. It divides the solution domain into a finite number of subdomains (elements, control volumes etc.). The two most common choices of arrangements of the numerical grid are the collocated and staggered arrangements (Ferziger & Peric, 2013). These two arrangements will be discussed briefly.

### 2.6.1 The Finite volume method

The FV method is a discretisation technique for partial differential equations. “Finite volume” refers to the utilisation of volume integral formulation of a problem with finite partitioning set of volumes to discretise equations. Generally the FV involves the following steps:

- 1) Grid generation.
- 2) Discretisation.
- 3) Solution of equations.

#### Step 1: Grid generation

The first step in the FV method is to set up a grid which mainly involves dividing the domain into discrete control volumes (Tak *et al.*, 2012). **Figure 2-5** shows a simple example of a grid.

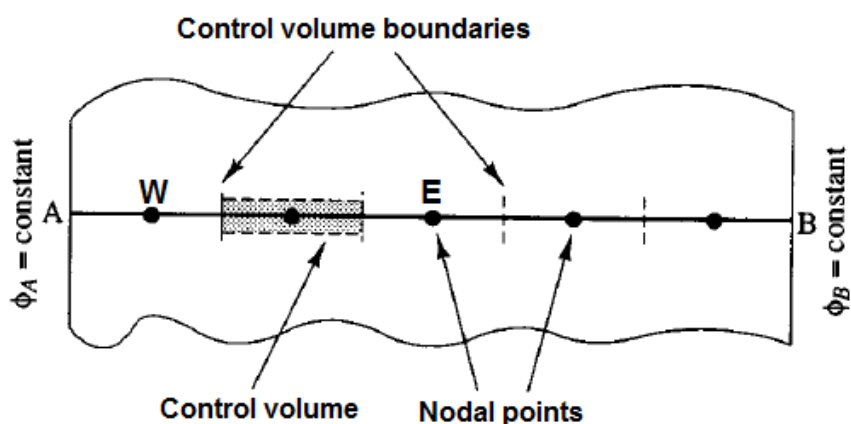


**Figure 2-5: Steady state diffusion in a 1-D domain grid (Versteeg & Malalasekera, 2007).**

The nodal points are placed between A and B as indicated. The boundaries of control volumes are situated midway between neighbouring nodes; therefore each node is surrounded by a control volume.

Tak et al. (2012) developed a simple method for grid generation using a basic unit cell concept. A unit cell model is made up of a coolant channel surrounded by six fuel holes (Tak *et al.*, 2008). **Figure 2-6** shows the basic unit cell types used to model the prismatic fuel blocks. The computational grids were defined in the basic unit cells. The perception of using unit cells facilitates the generation of unstructured computational grids for modelling the solid region of an entire fuel block.



**Figure 2-6: Basic unit cell types and examples of computational grids (Tak *et al.*, 2012).**

**Figure 2-7** illustrates the computational grids generated using basic unit cells for the standard fuel block.

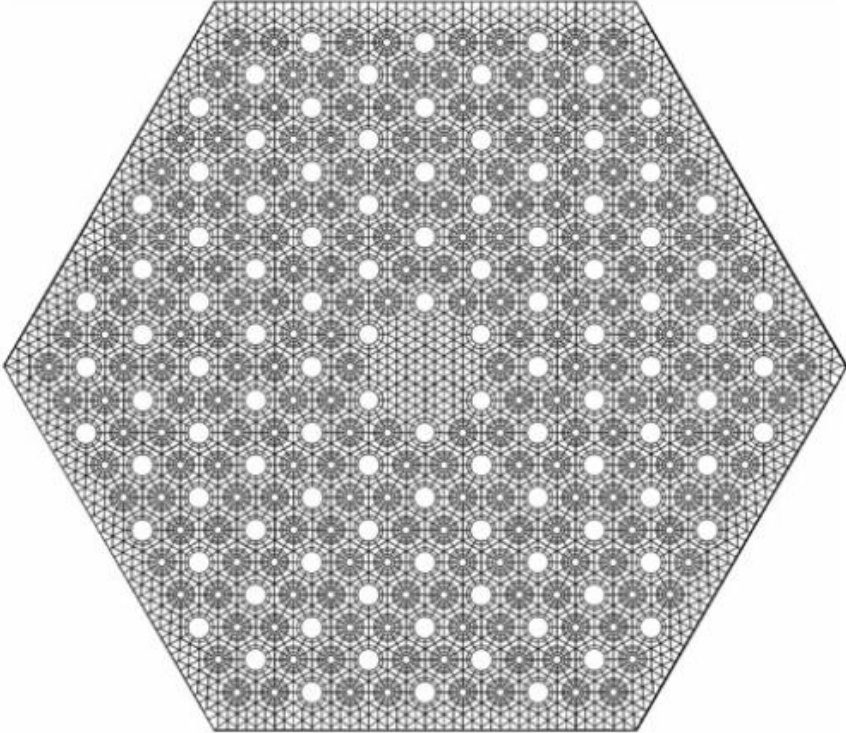


**Figure 2-7: An example of computational grids developed for a standard fuel block (Tak *et al.*, 2012).**

### Step 2: Discretisation

The important step of the FV method is the integration of the governing equation(s) over a control volume. This will produce discretised equation(s) at its nodal point (Versteeg & Malalasekera, 2007).

### Step 3: Solution of equations

A set of discretised equations from step 2 must be solved at each nodal point. The control volumes that are next to the domain boundaries should be modified to incorporate boundary conditions. The obtained set of equations can be solved matrix solution techniques such as Jacobi method, Gauss-Seidel method, Successive over-Relaxation method and Alternative Direction Implicit method.

#### **2.6.2 Collocated arrangement**

The collocated arrangement stores all the variables at the same set of grid points; it also uses the same control volumes for all variables as illustrated in **Figure 2-8**. Considering that many of the terms in each of the equations are fundamentally identical, the number of coefficients that must be solved and stored is minimized and the programming is simplified by this arrangement (Ferziger & Peric, 2013).

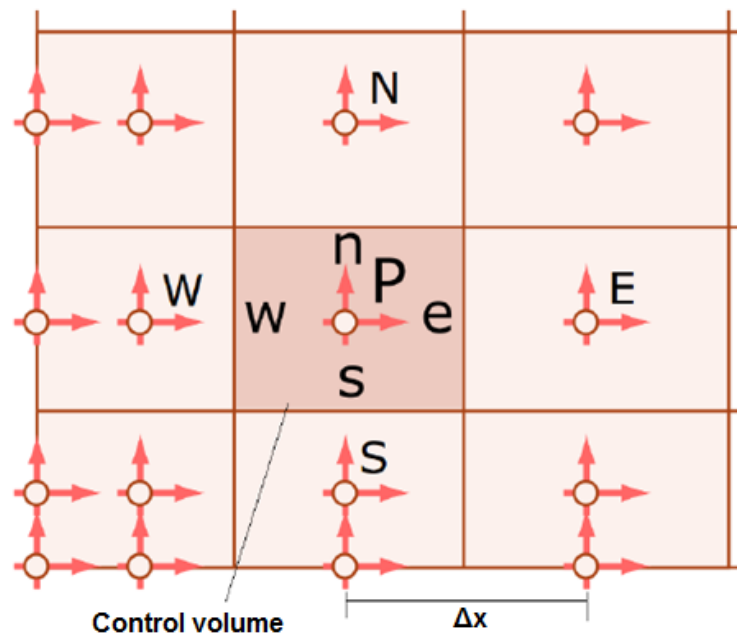


**Figure 2-8: Collocated arrangement of velocity and pressure components on a finite volume grid (Ferziger & Peric, 2013).**

Some advantages and disadvantages of a collocated arrangement are:

**Advantages:**

- All geometric coefficients are evaluated at the same points.
- It is easy to apply to multi-grid procedures (collocated refinements of the grid).

**Disadvantages:**

- It was not favourable and not used much until in the 1980s due to the manifestation of oscillations in the pressure and complications with pressure-velocity coupling (Ferziger & Peric, 2013).

**2.6.3 Staggered grid**

The staggered arrangement in Cartesian coordinates was first introduced by Harlow and Welsh in 1965. Several terms that have to be interpolated with the collated arrangement, can be calculated (to a second order approximation) without interpolation. This is illustrated in **Figure 2-9**. Pressure and diffusion terms are estimated by central difference approximations without interpolation; since the pressure nodes exist at control volume face centres and the velocity derivatives required for the diffusive terms are readily computed at the control volume faces (Ferziger & Peric, 2013).



**Figure 2-9: Partially staggered arrangement of velocity and pressure components (Ferziger & Peric, 2013).**

The staggered arrangement offers several advantages over the collocated arrangement; some of them are listed below:

#### **Advantages:**

- Many terms that need interpolation in collocated grids can be assessed without interpolation.
- Can be applied to the pressure term (situated at the control volume centres) and the diffusion term (first derivative needed at control surface centres), when employing central differences.
- Can be shown to directly conserve kinetic energy.
- It has many variations: partially staggered ALE (Arbitrary Lagrangian-Eulerian) method

#### **Disadvantages:**

- Higher order numerical schemes with order higher than 2<sup>nd</sup> will be difficult.
- Different variables are stored at different places; this in-turn makes it more difficult to handle different control volumes for different variables (Harlow & Welch, 1965).
- Requires special schemes to implement on grids that are non-orthogonal.

## **2.7 Previous work on HTRs**

Work that has been conducted on HTRs is discussed in this section, particularly coolant flow analysis, accident scenarios as well as flow and heat transfer modelling.

### **2.7.1 Coolant flow analysis**

Tak et al. (2008) investigated the heat transfer within a prismatic fuel assembly of a VHTR. The complex geometry of the hexagonal blocks in an HTR core compromises the accurate evaluation of the temperature profiles within a fuel assembly if detailed numerical analysis is not carried out. Tak et al. (2008) illustrated that a unit cell model does not consider heat transfer within a fuel assembly and coolant flow through the bypass gap and this will affect the maximum fuel temperatures within the core.

A one twelfth standard fuel assembly of a PMR600 reactor was set up using CFD and unit cell models with a bypass gap of 1 mm. The commercial code CFX11 was used for the CFD calculations. **Figure 2-10** illustrates the symmetric lines for both models.

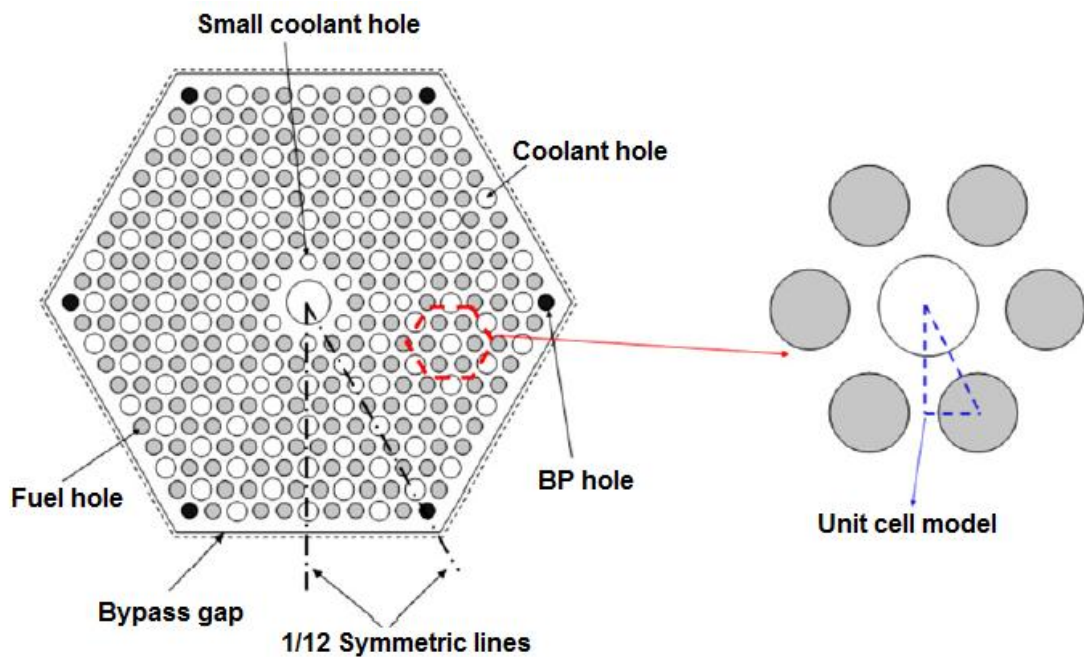


**Figure 2-10: Symmetric lines for the one twelfth fuel assembly model and the unit cell model (Tak et al., 2008)**

The results obtained for the average fuel temperature indicated that the unit cell model was reasonable with a difference of 3 °C. However, for the maximum fuel temperatures, the unit cell model result was lower by 20 °C. This was due to the inability of the unit cell model to consider heat transfer at the central and peripheral regions of the block as well as the bypass flow between neighbouring fuel assemblies.

The effect of the bypass flow was investigated by varying the bypass gap size. Bypass gap sizes of 1 mm, 3 mm and 5mm were investigated. Tak et al. (2008) found that the maximum fuel temperature increased with an increase in bypass gap size. This was due to a reduced coolant flow rate within the block. A wider bypass gap implied that a slightly higher fraction of the coolant would flow in the bypass gap and not within the block, and thereby decreasing the rate of heat transfer within the prismatic block thus higher temperatures within the block.

Two years later, Kim et al. (2010) conducted a CFD analysis on the hot spot fuel temperature in the control fuel block assembly of a PMR200. In this study, a CFD model for the control fuel block assembly was developed and applied for the analysis of the PMR200 hot spot. The bypass and the cross-flows were also included in the model development.

A computational domain which consisted of the active core with six layered control fuel rods and two reflector blocks for the top and bottom sides was modelled. The small gap between the fuel and the graphite moderator was modelled by effective conductivity. The fuel region had two

different types of heat sources, constant power density and an axial power distribution at the hottest fuel assembly attained from the core neutronics analysis (Kim *et al.*, 2010). **Figure 2-11** indicates a half control fuel assembly modelled.

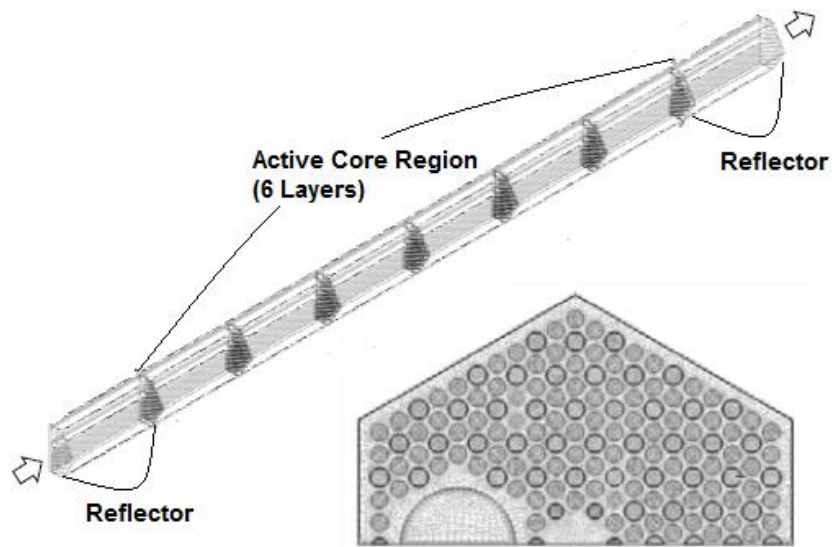


**Figure 2-11: One half control fuel assembly CFD model (Kim *et al.*, 2010).**

Two separate CFD analyses were conducted on the half control fuel assembly with the same average power density. One was simulated with no cross gaps and the other had cross gaps of 1 mm. Both models had a bypass flow which comprised of 3.1 % of the total flow of the assembly.

The model with a 1 mm cross gap had a higher temperature compared to the model with no cross gap. Basing on this finding Kim *et al.* (2010) concluded that the influence of the cross flows was large such that the integrity of the fuel performance would be compromised (Kim *et al.*, 2010).

Sato *et al.* (2010) also investigated the core bypass flow phenomena in a prismatic VHTR amongst other investigations. A one twelfth segment of a prismatic block was isolated. This is because a one twelfth segment is the smallest region that has symmetry boundaries on all edges (Sato *et al.*, 2010). Similar to the work conducted by Tak *et al.* (2008), three different bypass gap sizes were evaluated, 0 mm, 3 mm and 5 mm bypass gap sizes using the CFD commercial code FLUENT. These three gap sizes were modelled separately but they all had equal coolant inlet temperatures, equal mass flow rates and equal heat generation rate. **Figure 2-12** displays the temperature distribution obtained at the fuel hot spots plane for each gap width.

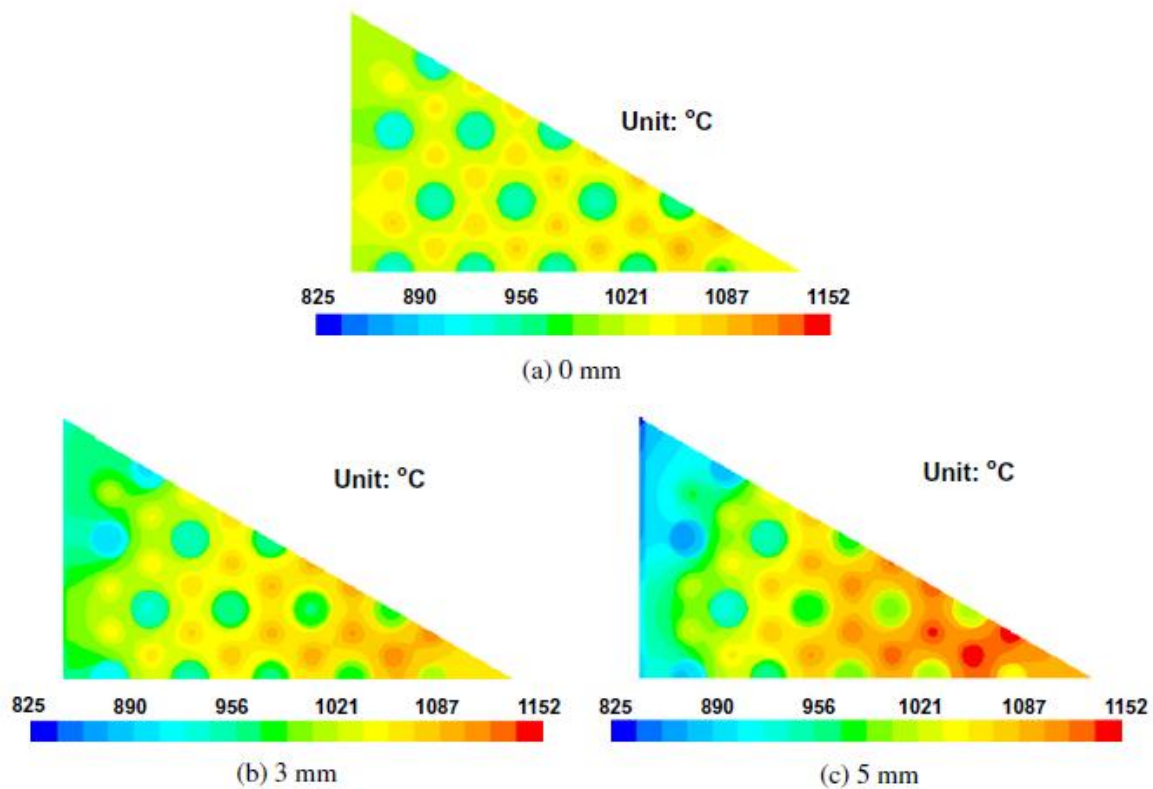


**Figure 2-12: Temperature distribution at the fuel hot spot plane for the three gap sizes (Sato *et al.*, 2010).**

From their findings, Sato *et al.* (2010) also established that an increase in the bypass gap results in increased fuel and coolant temperatures near the centre of the block. The hottest coolant temperatures were obtained at the small coolant channel located at near the centre of the block for all gap sizes. A maximum fuel temperature difference of 62 °C and maximum outlet coolant temperatures of 55 °C were obtained between the 0 mm and 5 mm gaps.

## 2.7.2 Accident Conditions study

Maruyama *et al.* (1994) investigated an accident scenario by blocking coolant channels of a fuel element. The maximum fuel temperatures in such a state were analysed and compared to the core damage limits. A thermal hydraulics code, FLOWNET/TRUMP was developed for this analysis. This code was validated by comparing the analytical results with the results of thermal and hydraulic tests of the Helium Engineering Demonstration Loop (HENDEL) multi-channel test rig. The HENDEL test rig comprised of twelve simulated fuel rods and eleven fuel graphite blocks. The validation of the code was executed by implementing a uniform and asymmetric power distribution tests and channel blockage simulation tests. These were performed in a helium environment at high temperatures up to 800 °C and a high pressure of 4 MPa.

The analytical model for the FLOWNET part of the code consisted of 1-D flow branches and pressure nodes which were the junctions of the branches. Branches model the flow paths while the nodes model the connections i.e. the intersections of the flow paths (Siemens, 2013). Each branch had an equivalent cross-section, length, hydraulic diameter and pressure-loss coefficients for the actual passages. Pressure loss coefficients used in the calculations for bypass and cross-flows was derived from experimental results. The analytical model for the TRUMP part of the code consisted of solid and fluid nodes. The nodes represent each region, for instance the fuel rods, graphite moderators and coolant. The boundary conditions were determined at the surfaces adjacent to the boundaries of each solid node (Maruyama *et al.*, 1994).

The HENDEL had been built so as to evaluate the thermal hydraulic design code system for the HTTR and also for the demonstration tests for high temperature components of the HTTR such as fuel stack, core support structures etc. The  $T_{1-M}$  is a multi-channel test rig and comprises of eleven graphite blocks and twelve simulated fuel rods. Helium coolant flows downward towards the internal cooler through the annular channel between the graphite blocks and the simulated fuel rods. **Figure 2-13** below shows the schematic for a  $T_{1-M}$ . The rate of heat generation for each simulated fuel rod was controlled by Silicon Controlled Rectifiers (SCRs) so as to obtain an arbitrary power distribution in the fuel stack model.

Some coolant channels of the fuel element were blocked as a design basis for an accident. The outlet coolant results from the HENDEL facility were slightly lower compared to the FLOWNET/TRUMP coolant outlet temperatures, giving conservative results. However the coolant flow rates for both cases in each fuel cooling channel were decreasing with an increase in the rate of heat generation of the simulated fuel rods.

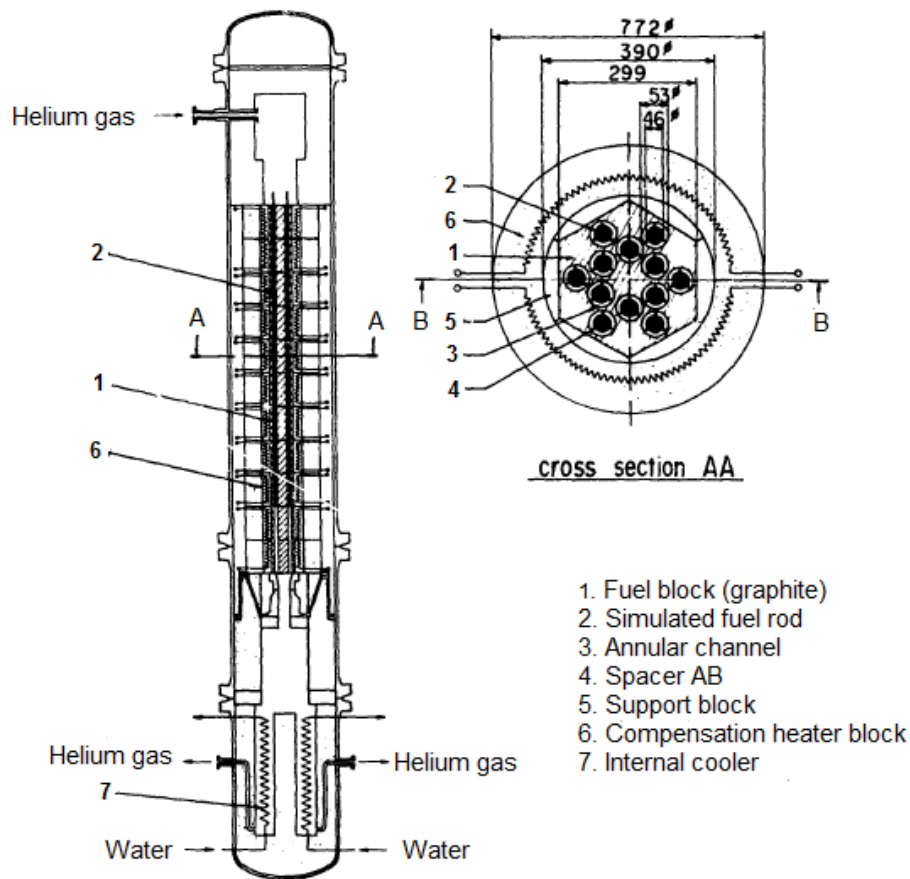


**Figure 2-13: Schematic for a T<sub>1-M</sub> (Maruyama *et al.*, 1994).**

The maximum fuel temperature at the hot spots was approximately 1653° C. From this deduction, it was concluded that the integrity of the core was still maintained even though some coolant channels were blocked (Maruyama *et al.*, 1994).

Cioni *et al.* (2006) conducted a 3-D CFD analysis using TRIO\_U on a modular block-type HTR core. A 3-D fuel/graphite conduction problem was coupled with a simplified 1-D thermal hydraulic model in the coolant (helium) channels. The main aim was to investigate an emergency situation by blocking a few coolant channels in the core.

Two scenarios were created. The first scenario consisted of one fuel assembly surrounded by six half fuel assemblies. The second scenario comprised of one fuel assembly surrounded by five half fuel assemblies and one half reflector block. These two scenarios are illustrated in **Figure 2-14** and **Figure 2-15**.

The flow area was partially isolated by a fragment for both scenarios. The fragment was placed on the central fuel assembly and as a result approximately 23 % (24 channels) of coolant channels were blocked.

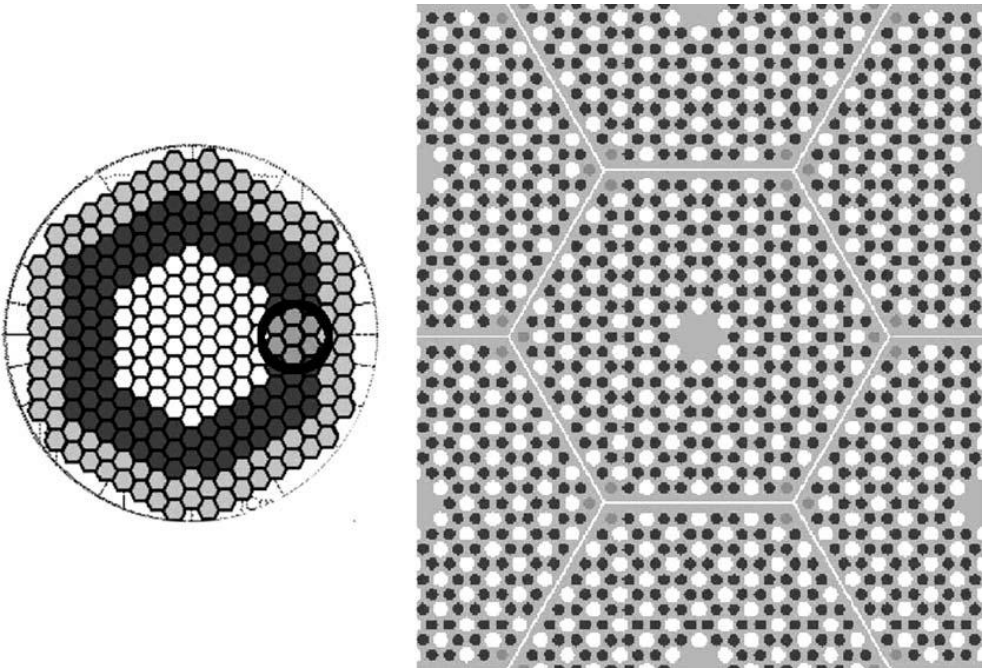


Figure 2-14: One fuel assembly surrounded by six half fuel assemblies (Cioni *et al.*, 2006).

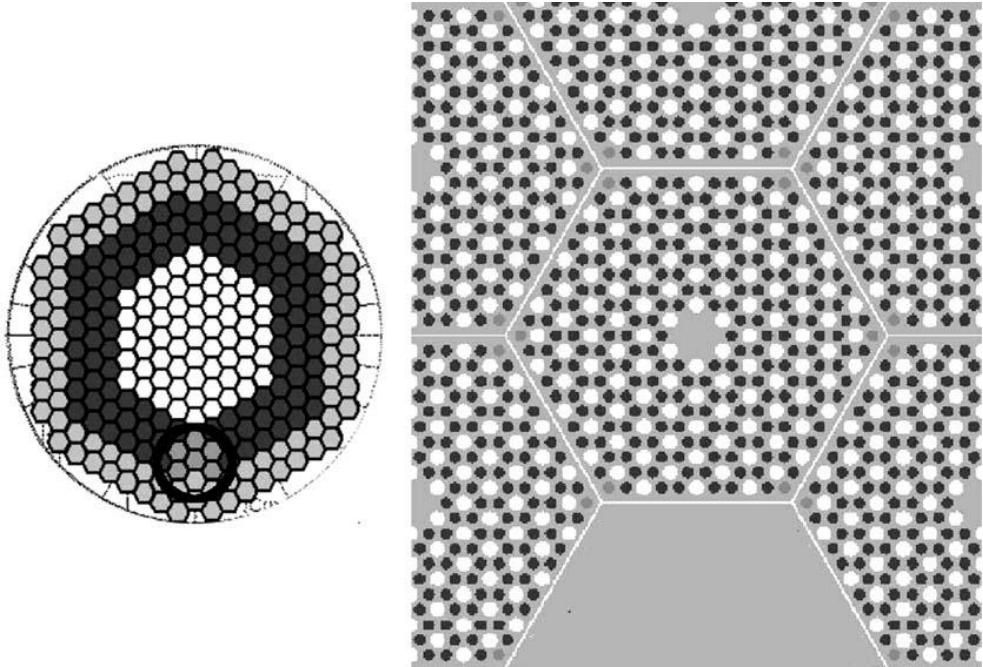


Figure 2-15: One fuel assembly surrounded by five half fuel assemblies and one half reflector block (Cioni *et al.*, 2006).

The graphite and the fuel compacts which made up the solid component were treated like a 3-D conduction problem. The boundary conditions were adiabatic walls with an exception of the coupling between the fluid and the solid. The solid component i.e. the graphite and fuel were modelled using the graphite physical properties. At the same time, the fuel compacts were modelled explicitly. The heat source distribution followed a cosine profile in the streamwise  $x$ -direction. The helium flow in the channels as well as in the bypass gaps were modelled using a 1-D thermal hydraulic approach i.e. the continuity equation as well as the energy balance equations were implemented. The Nusselt number correlation was used for the coupling between the 3-D solid model and 1-D fluid model (Cioni *et al.*, 2006).

Cioni *et al.* (2006) concluded that the maximum temperature criterion of the reactor (with 23 % of the coolant channels blocked) was not respected since the maximum fuel temperature obtained from this study was above 1600 °C. However, Cioni *et al.* (2006) observed that at power level of 80 % the nominal power, the fuel temperatures did not exceed 1600 °C.

Lee *et al.* (2014) also investigated the effects of blocking coolant channels in a prismatic gas cooled reactor. They investigated the effect firstly by blocking a single channel and extended the study to multi-channel blockage. This study was conducted on a standard fuel block using CORONA. Three blockage locations were first identified in a standard block and CORONA calculations were conducted one location at a time. Two types of fuel elements and two blockage locations were selected for the multi-channel blockage analysis (Lee *et al.*, 2014). The number of blocked coolant channels was based on the coolant channel rings or rows depending on the location (Lee *et al.*, 2014).

The maximum temperatures obtained using the single-coolant channel blocking did not exceed 1600 °C and therefore within the safety limit. A temperature rise for a single-channel blockage was obtained at the local region around the blocked channel. Lee *et al.* (2014) concluded that it was not necessary to shut down the reactor if there happened to be single-channel blockage since the fuel temperatures were within the design limit. However, for the multi-channel blockage, fuel temperatures rose significantly. Overall, a blockage of more than ten coolant channels compromises the integrity of the fuel since the temperatures would rise above the safety limit (Lee *et al.*, 2014).

### **2.7.3 Modelling of flow and heat transfer**

Rousseau and Greyvenstein (2002) described a thermal network and a flow discretization path that was used to simulate the fluid passages and solid structures of the HTTR. The difference between the PMR200 or PMR600 (studied by Tak *et al.* (2008 & 2011)) and the HTTR is the flow path of the coolant. The coolant flow in the PMR200 and PMR600 reactors has no direct

contact with the fuel. Heat is transferred from the fuel via the graphite moderator to the coolant. In the HTTR, the coolant flows between fuel rods and the fuel assembly blocks. This is illustrated in **Figure 2-16** and **Figure 2-17**.

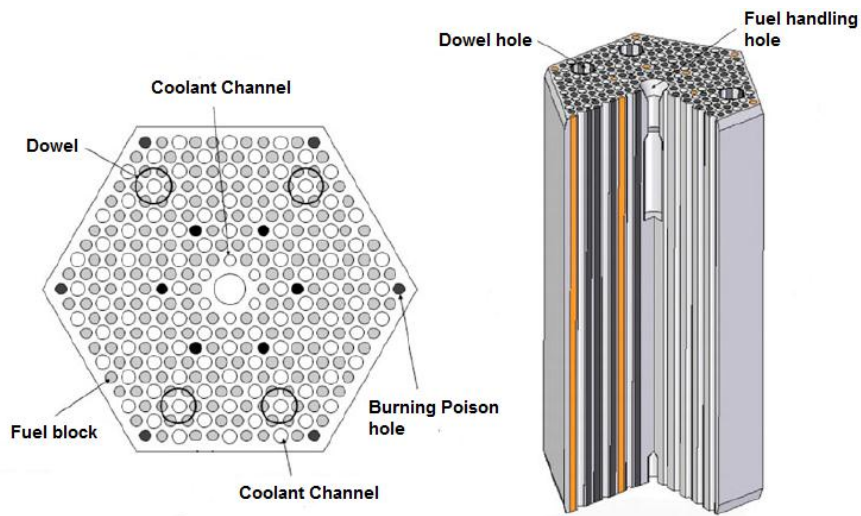


**Figure 2-16: Coolant flow path in the fuel block of the PMR200 (Tak *et al.*, 2012).**

The reactor core of the HTTR is made up of layers of fuel assembly blocks and reflector blocks. Rousseau and Greyvenstein (2002) reduced the HTTR core to a simplified axi-symmetric 2-D geometry. This is illustrated in **Figure 2-18(a)**. The outer ring represented the permanent reflector blocks while the ring adjacent to it represented the replaceable reflector blocks. The rings labelled 3, 2 and 1 represented the fuel assemblies at different positions within the core. In order to improve accuracy, each ring was discretized into a number of control volumes in the axial direction. A uniform temperature distribution was assumed for each control volume at any time step. As a result, each control volume was represented by a single thermal mass node connected by a thermal resistance to the adjacent thermal mass nodes at the top, bottom, inside and outside.

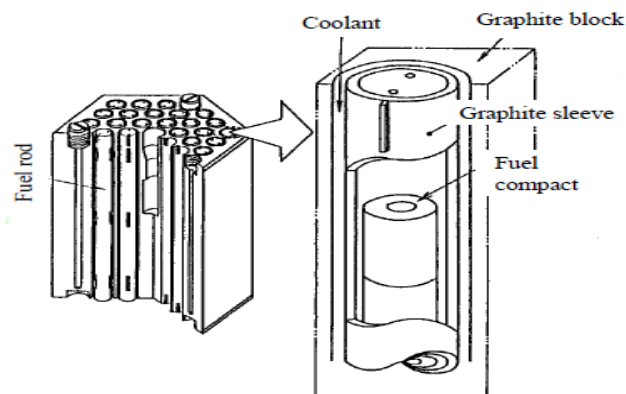


**Figure 2-17: Coolant flow path in the fuel block of the HTTR (Takamatsu *et al.*, 2006).**

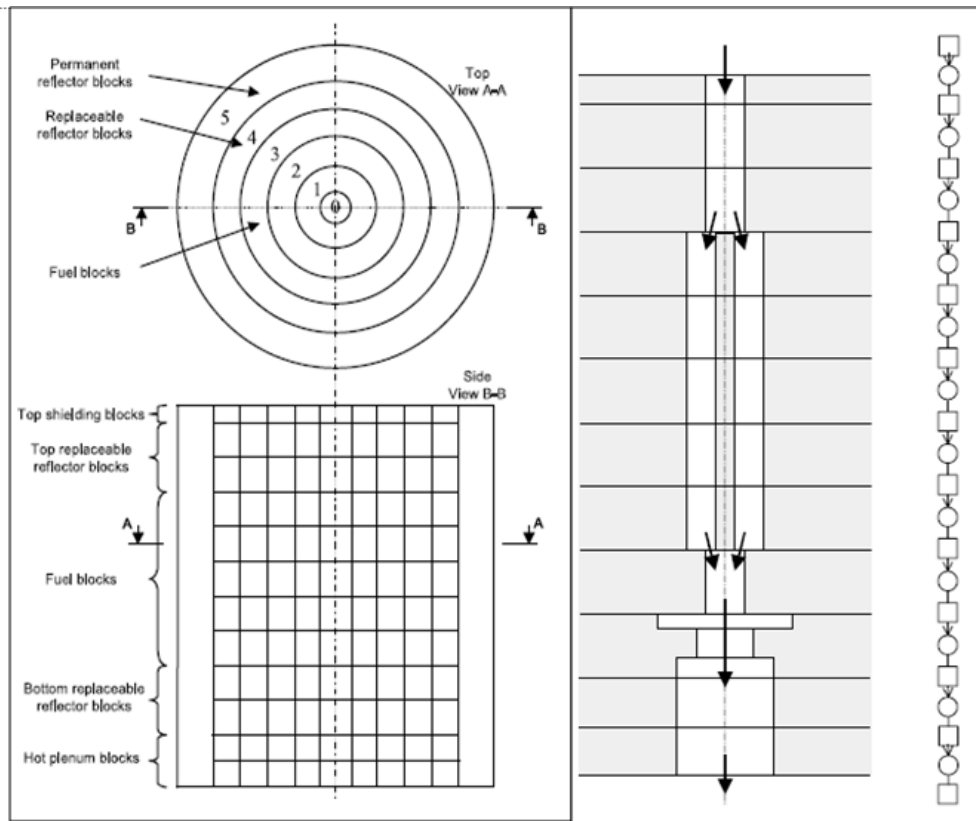


**Figure 2-18: (a) Schematic layout of the core (b) Schematic layout of the coolant flow path (Rousseau & Greyvenstein, 2002)**

Each node that represented a fuel assembly block also represented the surface temperature of the flow passages inside the fuel assembly block. The surface temperature was connected by a forced convection heat transfer resistance to the gas flow flowing through the gas passages (Rousseau & Greyvenstein, 2002). The gas flow was connected to the outside surface of the graphite shield (part of the fuel rod) by a forced convection heat transfer resistance. The graphite shield and fuel compact were discretized into a number of layers and these were represented by a single thermal mass node. This single thermal mass node was connected to the neighbouring nodes by conduction heat transfer resistances. The inner most surface of the fuel compact was assumed to be adiabatic due to the negligible heat capacity of the gas within the inner cylinder. **Figure 2-19** illustrates the thermal network for the heat transfer for a single fuel assembly block control volume.

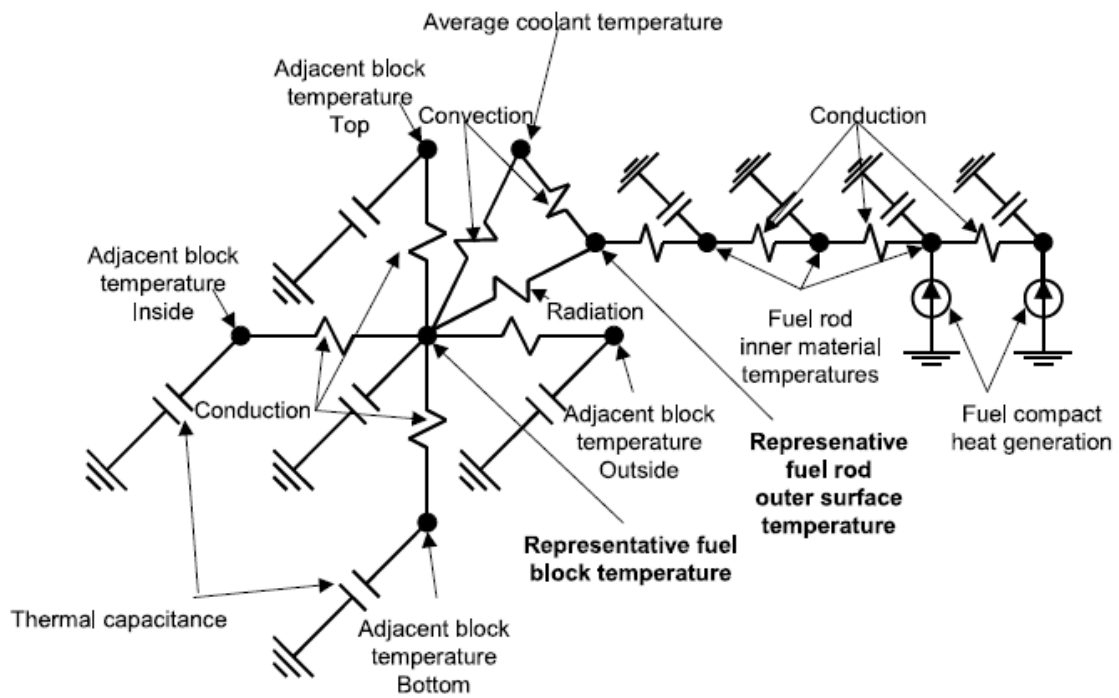


**Figure 2-19: Thermal network schematic for the heat transfer for a single fuel assembly block control volume (Rousseau & Greyvenstein, 2002).**

The flow path of the coolant was discretised by the node – element – node configuration as illustrated in **Figure 2-18(b)**. The complete flow element and solid thermal mass node network is presented in **Figure 2-20**. Each ring in the axi-symmetric core was only presented by a single Control Volume (CV).

A 1-D approach for flow and conduction in solids was implemented. The blocks in a zone were represented by a single representative node and thus averaged single temperatures were obtained. Therefore a representative network for fuel rod(s) and coolant channels in a zone was implemented.

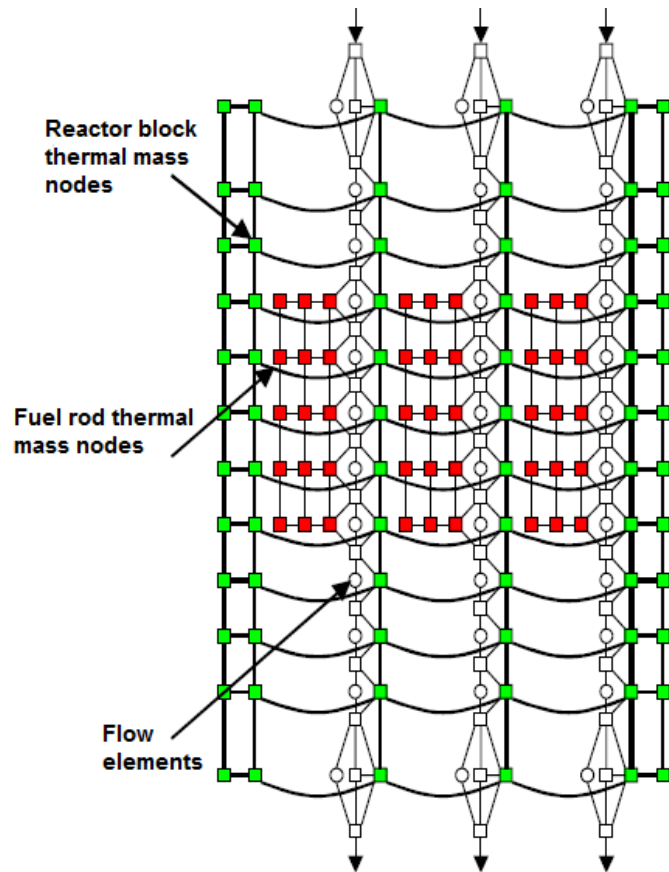


**Figure 2-20: Completed flow element and solid thermal mass node network (Rousseau & Greyvenstein, 2002).**

Du Toit and Rousseau (2012) also gave a brief overview on how to apply the system CFD approach on a packed bed reactor. They modelled the flow and heat transfer for a pebble bed HTGR using a systems-CFD approach. A lumped up model with discretized sub-networks of 1-D models represented the reactor (Du Toit & Rosseau, 2012). The 1-D models accounted for the pressure drop through the reactor, the convective heat transport by the coolant and also between the coolant and the solids, radiation and convection heat transfer between the pebbles and the heat conduction in the pebbles and the core structure materials. **Figure 2-21** displays a simplified network of the solids in the pebble bed core structures.

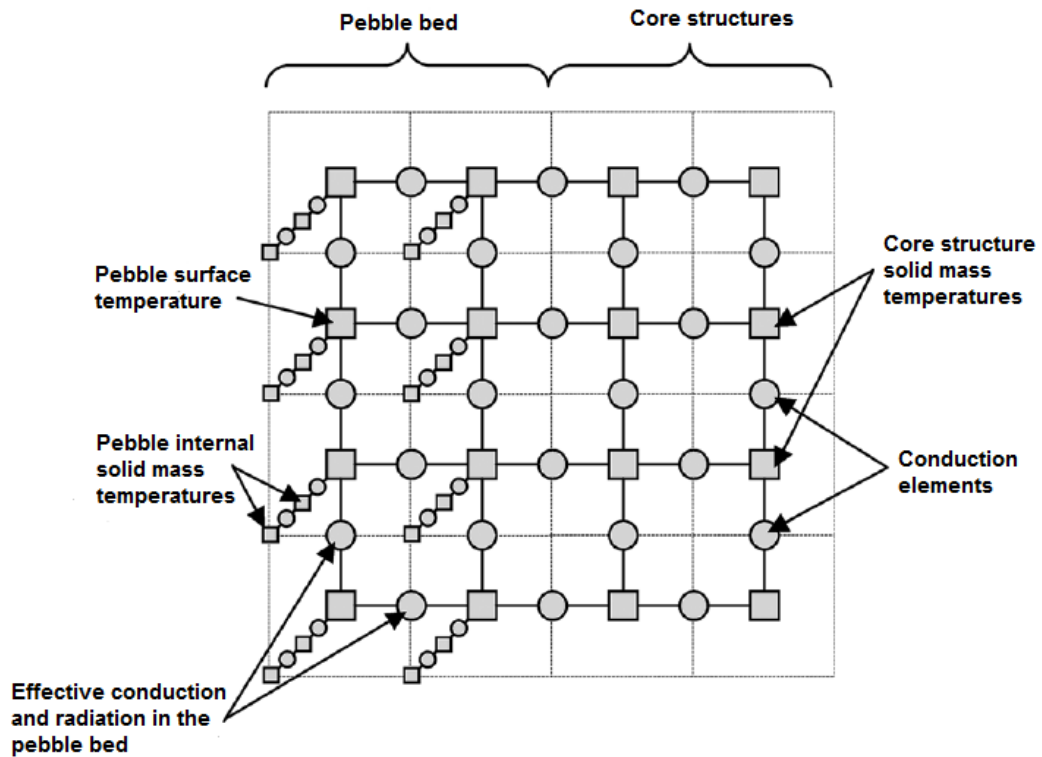


**Figure 2-21: Schematic for a simplified network of the solids in the pebble bed core structures (Du Toit & Rosseau, 2012).**

Tak et al. (2014) developed a code, CORONA (Core Reliable Optimization and thermo-Network Analysis) for the core thermo-fluid analysis of a prismatic gas cooled reactor. The CORONA was developed for the whole core thermo-fluid analysis of a prismatic gas cooled reactor with fast and reasonable accuracy (Tak *et al.*, 2014). The development of the CORONA code was primarily focused on efficient numerical methods, efficient grid generation and parallel computation. The fundamental aspect for the efficient numerical method of CORONA was to solve a 3-D solid heat conduction equation together with 1-D fluid flow network equations. The likely problems in generating computational grids for the whole core were defeated by using a basic unit cell concept. **Figure 2-22** shows the modelling procedure from basic unit cell to the whole prismatic core.

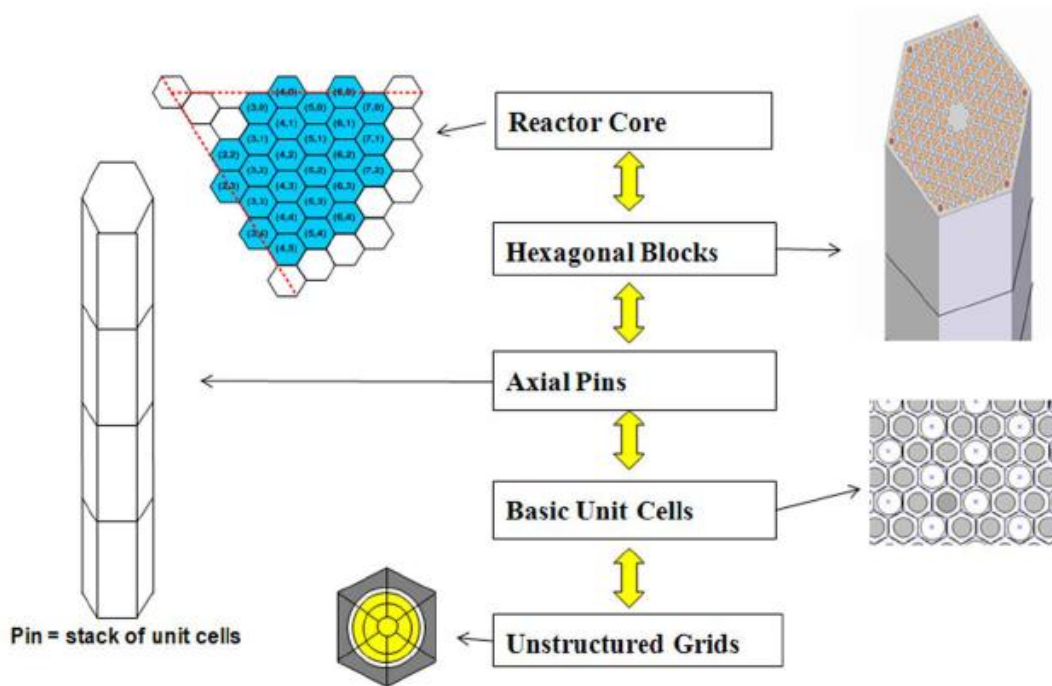


**Figure 2-22: Modelling procedure from basic unit cell to whole prismatic core (Tak et al., 2014).**

Similarly to Cioni et al. (2006), a numerical model for the solid and the fluid flow were developed and coupled using the Nusselt number correlation. A 3-D heat conduction equation was solved using the finite volume method for the solid model. The fluid flow model was modelled using a 1-D conservation equation for a fluid flow. The fluid flow network in CORONA was executed based on the pressure correction method.

**Figure 2-23** displays the results obtained for a one sixth core of a PMR600 using CORONA.

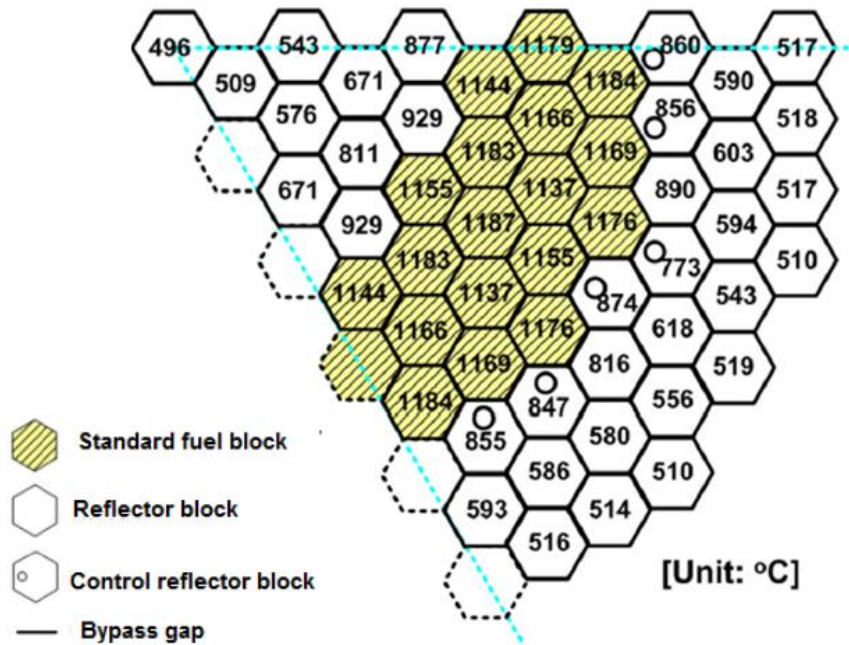


**Figure 2-23: Maximum predicted temperatures for a one sixth core of PMR600 (Tak *et al.*, 2014).**

## 2.8 Summary

This chapter dealt with the fundamentals of thermal-fluid networks. The simulation of thermal systems through different elements and the network analogy was described. The advantages and disadvantages of applying a network approach have been clearly outlined. The differences between the CFD and systems-CFD approaches have been indicated.

An overview on the numerical solution algorithms mainly with reference to the explicit and implicit numerical methods was also surveyed. The explicit and implicit numerical methods were compared in terms of stability and accuracy.

The methods which are used to solve for a 2-D steady state conduction have been discussed. The discretisation schemes particularly the FV method has been discussed. The collocated and the staggered grids have also been discussed.

Most approaches use a 1-D formulation to simulate the flow and a 2-D/3-D approach to simulate the heat transfer/conduction through the solids/blocks. They also only model a part of the core (even for a full core analysis) and do not integrate the reactor model with the simulation of the rest of the system (thermal-fluid cycle).

The current Flownex model for the HTTR has only one representative solid node and one representative fluid element for the blocks in a zone. As in the case of the advanced PBR model in Flownex (Du Toit & Rosseau, 2012) there is a need for an advanced prismatic HTR model in

Flownex which can be used in the context of a system CFD approach. The first step in the development of such a model would be to extend the representative one node model for a zone of blocks to a heat network for each block. The single representative coolant channel element for each block zone should also be extended to a representative multi-channel model for each block

## 3. IMPLICIT METHOD FOR THE SOLUTION OF THE THERMAL-FLUID NETWORK

---

### 3.1 Introduction

In this chapter the governing equations used by Flownex will be presented. The discretization schemes as well as discretization of partial differential equations used in thermal-fluid networks will be discussed. This will give a basic understanding of when the governing equations are applied to unstructured networks in the Implicit Pressure Correction Method (IPCM). The conduction shape factor particularly on the HTR block will also be discussed, as this will aid in solving for a 2-D conduction phenomena. The heat transfer parameters, the Biot and Fourier numbers will also be used as these will assist in determining a suitable time step for transient analysis. The chapter is concluded by the IPCM solution algorithm discussion which is utilised in Flownex.

### 3.2 Governing equations

The analysis of thermal-fluid networks is based on the numerical solution of the governing equations of fluid dynamics and heat transfer (M-Tech, 2013). The governing equations are mass, momentum and energy conservation, together with the equation of state. These four equations are discussed in the next sections.

#### 3.2.1 Conservation of mass

Using a 1-D coordinate system, the conservation of mass can be represented in the following form:

$$\frac{\partial \rho}{\partial t} + \frac{\partial(\rho VA)}{\partial x} = 0 \quad (3-1)$$

Where

$x$  = distance along the pipe in the direction of the flow,

$\rho$  = density,

$V$  = volume,

$A$  = area and

$t$  = time.

#### 3.2.2 Conservation of momentum

The momentum equation for a 1-D flow may be written in a non-conservation form as:

$$\rho \frac{\partial V}{\partial t} + \rho V \frac{\partial V}{\partial x} = -\frac{\partial p}{\partial x} - \rho g \frac{\partial z}{\partial x} - \frac{f\rho|V|V}{2D_H} \quad (3-2)$$

Where

$D_H$  = hydraulic diameter of pipe,

$f$  = friction factor,

$g$  = acceleration due to gravity,

$p$  = static pressure and

$z$  = elevation.

In the solution of equation (3-2) a distinction is made between compressible and incompressible flow (Shames, 1992). The following sections will differentiate the two flows.

### 3.2.2.1 Incompressible flow

For an incompressible flow, equation (3-2) is manipulated by writing the convective term of equation (3-2) in terms of kinetic energy. The pressure gradient and gravitational force terms are grouped into a total pressure (stagnation pressure) term to yield equation (3-3):

$$\rho \frac{\partial V}{\partial t} + \frac{\partial p_o}{\partial x} + \rho g \frac{\partial z}{\partial x} + \frac{f\rho|V|V}{2D_H} = 0 \quad (3-3)$$

### 3.2.2.2 Compressible flow

For a compressible flow, equation (3-2) is expressed in terms of the total pressure and temperature i.e.  $p_o$  and  $T_o$  respectively:

$$\rho \frac{\partial V}{\partial t} + \frac{p}{p_o} \frac{\partial p_o}{\partial x} + \rho g \frac{\partial z}{\partial x} + \frac{\partial T_o}{\partial x} + \frac{f\rho|V|V}{2D_H} = 0 \quad (3-4)$$

### 3.2.3 Conservation of energy

The conservation of energy principle (a.k.a. the first law of thermodynamics) simply states that during an interaction, energy can change from one form to another. However, the total amount of energy remains constant (Cengel & Turner, 2005). The one-dimensional flow energy equation is expressed as:

$$\frac{\partial(\rho(h_o + gz) - p)}{\partial t} + \frac{\partial(\rho V(h_o + gz))}{\partial x} = Q - W \quad (3-5)$$

Where  $h_o$  = the specific total enthalpy,

$Q$  = net heat added to the system and

$W$  = net work done by the system.

Extracting the continuity equation and simplifying equation (3-5) in terms of the total temperature yields:

$$\frac{\partial(\rho c_p T_o)}{\partial t} - \frac{\partial p}{\partial t} + \frac{\partial(\rho V c_p T_o)}{\partial x} + \rho g V \frac{\partial z}{\partial x} = Q - W \quad (3-6)$$

### 3.2.4 Equation of state

In compressible flows, an equation of state that expresses the pressure in terms of the density and temperature is utilised (Greyvenstein, 2002). This equation of state is:

$$p = s \rho R T \quad (3-7)$$

Where

$R$  = gas constant,

$T$  = temperature and

$s$  = compressibility factor.

Most gases such as helium, oxygen and air behave very closely to an ideal gas, and as a result can be represented by equation (3-7) with  $s = 1$  (Shames, 1992).

Equations (3-1), (3-4) and (3-6) govern gas flows, while equations (3-1), (3-3) and (3-6) govern liquid flows. Even though the equations exhibited in this section are valid for both gas and liquid flows, only the gas flow variant method will be discussed in the next sections. These conservation equations together with the equation of state are applied to each component (element) in the thermal-fluid network and as a result form a set of equations that can be solved using implicit or explicit solution algorithms. In order to obtain the set of equations, the conservation equations must first be discretised.

### 3.3 Discretization of partial differential equations

The key step in the finite volume method is to divide the domain into discrete control volumes. This section will show how the pipe flow and heat equations are discretised.

### 3.3.1 Pipe flow

A pipe is divided into finite control volumes, at whose centres the flow properties e.g. pressure, temperature and density are defined. This is illustrated in **Figure 3-1** below:

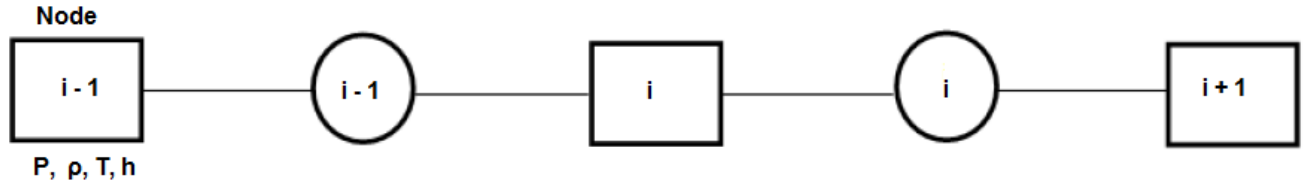


**Figure 3-1: Discretisation of a pipe section.**

Discretising the pipe flow incorporates discretising the three conservation law equations.

Spatial discretisation of the continuity equation **(3-1)** yields:

$$\frac{dp_i}{dt} = -\frac{(\rho_e V_i - \rho_w V_{i-1})}{\Delta x} \quad (3-8)$$

With

$$\begin{aligned} \rho_w &= 0.5(\rho_{i-1} + \rho_i) \\ \rho_e &= 0.5(\rho_i + \rho_{i+1}) \end{aligned} \quad (3-9)$$

Where  $\rho_e$  =density of the eastern elements and  
 $\rho_w$ =density of the western elements.

Spatial discretisation of the compressible flow equation **(3-4)** yields:

$$\frac{dV_i}{dt} = \frac{1}{\rho_i} \left[ \frac{p_i}{p_{0i}} + \frac{(p_{0i} - p_{0i-1})}{\Delta x} \right] + \frac{fV_i |V_i|}{2D} \quad (3-10)$$

Spatial discretisation of the energy equation **(3-6)** yields:

$$\frac{d(\rho u_0)}{dt} = -\frac{(\rho_e h_{0e} V_i - \rho_w h_{0w} V_{i-1})}{\Delta x} + Q \quad (3-11)$$

With

$$\begin{aligned} h_{0w} &= 0.5(h_{0i-1} + h_{0i}) \\ h_{0e} &= 0.5(h_{0i} + h_{0i+1}) \end{aligned} \quad (3-12)$$

Where

$h_{0e}$  = total enthalpy of the eastern element and

$h_{0w}$  = total enthalpy of the western element.

### 3.3.2 Equations for heat transfer

The first law of thermodynamics at an instant time  $t$ , states that the rate of increase of stored energy in a control volume must equal the rate at which thermal and mechanical energy enters the control volume, minus the rate at which thermal and mechanical energy exits the control volume, plus the rate at which thermal energy is generated within the control volume (Incropera *et al.*, 2007). This statement can be written in an equation form as:

$$\dot{E}_{st} \equiv \frac{dE_{st}}{dt} = \dot{E}_{in} - \dot{E}_{out} + \dot{E}_g \quad (3-13)$$

Where

$\dot{E}_{st}$  =stored mechanical and thermal energy,

$\dot{E}_g$  =thermal energy generation,

$\dot{E}_{in}$ =inflow of thermal and mechanical energy across the control surface and

$\dot{E}_{out}$ =outflow of thermal and mechanical energy across the control surface.

The inflow or outflow of heat transfer from a control volume can take place through three different processes that is conduction, convection and radiation. These three modes of heat transfer are discussed in the following sections.

#### 3.3.2.1 Conductive heat transfer

Conduction is the transfer of energy from the more energetic particles of a substance to the neighbouring less energetic ones as a result of interactions between the particles (Cengel & Turner, 2005). In rectangular coordinates, the heat conduction equation vector can be expressed in terms of its components as:

$$Q_n = Q_x i + Q_y j + Q_z k \quad (3-14)$$

Equation (3-14) can be determined from Fourier's law as:

$$Q_x = -kA_x \frac{\partial T}{\partial x}$$

$$Q_y = -kA_y \frac{\partial T}{\partial y} \quad (3-15)$$

$$Q_z = -kA_z \frac{\partial T}{\partial z}$$

Applying equation (3-15) to a control volume about the interior node  $i, j$  of **Figure 3-2** yields:

$$Q_{\text{cond}} = -\frac{(T_{i,j} - T_{i-1,j})}{\frac{\Delta x}{kA}} - \frac{(T_{i,j} - T_{i+1,j})}{\frac{\Delta x}{kA}} - \frac{(T_{i,j} - T_{i,j+1})}{\frac{\Delta y}{kA}} - \frac{(T_{i,j} - T_{i,j-1})}{\frac{\Delta y}{kA}} \quad (3-16)$$

Where

$A$  is the heat transfer area,

$\Delta x$  is the distance between the nodes in the  $x$ -direction and

$\Delta y$  is the distance between the nodes in the  $y$ -direction.

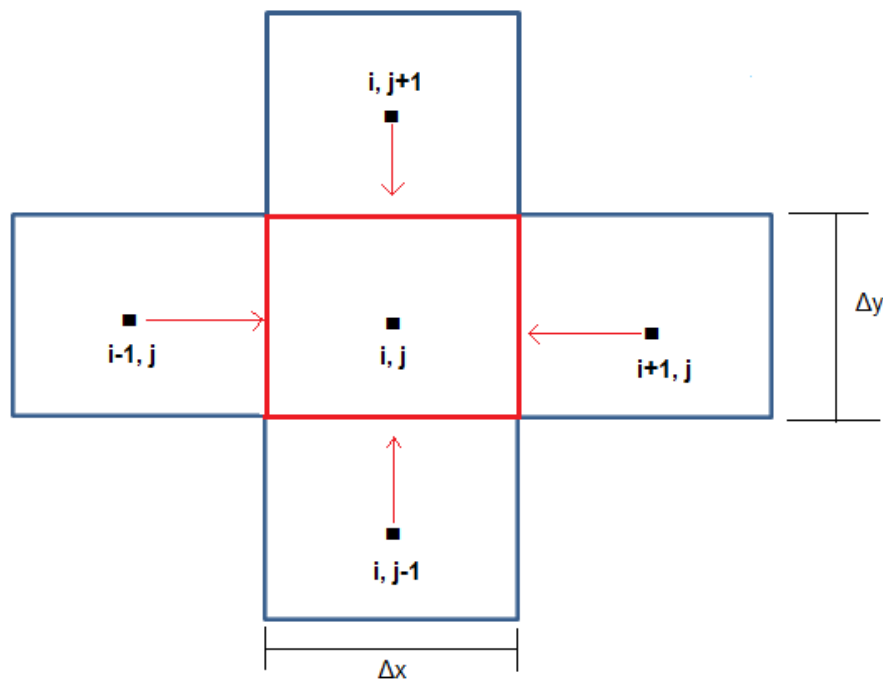


**Figure 3-2: Conduction to an interior node from its adjacent nodes (Incropera *et al.*, 2007).**

The conduction phenomenon is represented by a conductive heat transfer element and a cross conductive element in Flownex. These elements will be further described in section **4.3.2** and **4.3.3**.

### **3.3.2.2 Convective heat transfer**

Convection is the mode of heat transfer between a solid surface and the neighbouring fluid that is in motion. Convection embodies the collective effects of conduction and fluid motion (Cengel & Turner, 2005). Convection can either be natural (free) or forced. Natural convection is when the fluid motion is caused by buoyancy forces that are prompted by density differences due to the variation of temperature in the fluid. Forced convection is when the fluid is forced to flow over the surface by external aids such as pumps or the wind (Cengel & Turner, 2005).

The rate of convection heat transfer is conveniently expressed by Newton's law of cooling:

$$Q_{\text{conv}} = hA_s(T_s - T_\infty) \quad (3-17)$$

Where

$A_s$  = surface area through which convection heat transfer takes place,

$h$  = convection heat transfer coefficient,

$Q_{\text{conv}}$  = rate of convection heat transfer,

$T_s$  = surface temperature and

$T_\infty$  = temperature of the fluid sufficiently far from the surface.

**Figure 3-3** below shows the convection heat transfer to a fluid node, surrounded by three solid nodes at a plane surface with convection.

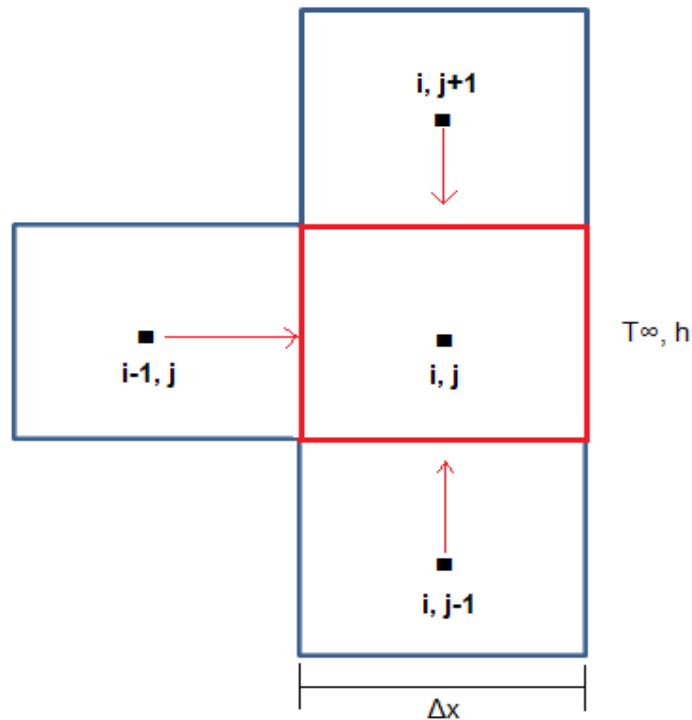


**Figure 3-3: Node at plane surface with convection (Incropera *et al.*, 2007).**

The convection phenomenon is represented by a convective heat transfer element in Flownex. This element will be further described in section 4.3.4.

### 3.3.2.3 Radiative transfer

Radiation is the energy emitted by matter in the form of electromagnetic waves or photons as a result of the changes in the electronic configurations of the atoms or molecules (Cengel & Turner, 2005). The net rate of radiation heat transfer between 2 surfaces is given by:

$$Q_{\text{rad}} = \varepsilon \sigma A_s (T_s^4 - T_{\text{surr}}^4) \quad (3-18)$$

Where

$A_s$  = surface area through which radiation takes place,

$T_{\text{surr}}$  = surface absolute temperature of a larger (black) surface,

$Q_{\text{rad}}$  = rate of radiation heat transfer,

$\varepsilon$  = surface emissivity and

$\sigma$  = Stefan-Boltzmann constant.

In Flownex, the radiation heat transfer between 2 surfaces is calculated using equation (3-19) below:

$$Q = \frac{\sigma(T_{s1}^4 - T_{s2}^4)}{\frac{1 - \varepsilon_1}{\varepsilon_1 A_1} + \frac{1}{A_1 F_{12}} + \frac{1 - \varepsilon_2}{\varepsilon_2 A_2}} \quad (3-19)$$

Where

$F_{12}$  = geometric view factor,

$\varepsilon_1$  = upstream surface emissivity and

$\varepsilon_2$  = downstream surface emissivity.

Even though radiation heat transfer occurs in a prismatic high temperature reactor, in this study radiation is not accounted for.

### 3.4 The conduction shape factor

The conduction shape factor is a function of only the geometry of a system. Shape factors for numerous 2-D and 3-D systems have been obtained analytically. Shape factors may also be derived for 1-D geometries. Considering conduction through a plane wall, the shape factor may be derived as follows:

Thermal resistance for a plane wall is given by equation (3-20):

$$R_{t,cond} = \frac{L}{kA} \quad (3-20)$$

Equating equation (2-3) and (3-20), and rearranging yields equation (3-21):

$$S = \frac{A_s}{L_c} \quad (3-21)$$

Where

$A_s$  = surface area of the object and

$L_c$  = conduction length.

In this section the conduction shape factor used in modelling a one sixth block of a standard VHTR fuel block in Flownex will be deduced. More details on the construction of the heat transfer network for a one sixth standard fuel block are given in chapter 5.

#### 3.4.1 Conduction between fuel rods and coolant channels in a prismatic fuel block

**Figure 3-4** shows a schematic layout of a one sixth section of a prismatic VHTR fuel block. The fuel rods are represented by the red circles and the coolant channels are represented by the open blue circles. Super-imposed on that are the solid nodes of a conduction network (see chapter 5). The CVs associated with the solid nodes are indicated by the dashed green lines

surrounding each solid node. Each CV (except for those at the apex) contains one or more (or parts of) fuel rods and coolant channels. The fuel rods contained in a CV are represented by a single node at which the appropriate heat input is specified. This is illustrated in **Figure 3-4**; and as an example partial fuel rods F2 and F4 are contained in a CV represented by a single node N2. The coolant channels contained in a CV are represented by a single pipe element with the appropriate area, wetted perimeter and mass flow rate. This section gives a full description of the conduction path/network between the fuel rods node, graphite node and the pipe element (coolant channels).

**Figure 3-5** zooms in on a typical coolant channel (C7) surrounded by six fuel rods (F7, F8, F10, F11, F13 and F14). There are three possible unit cells (marked *a*, *b* and *c*) that can be considered for the analysis of the heat transfer between the fuel rods and the coolant channels (see **Figure 3-5**).

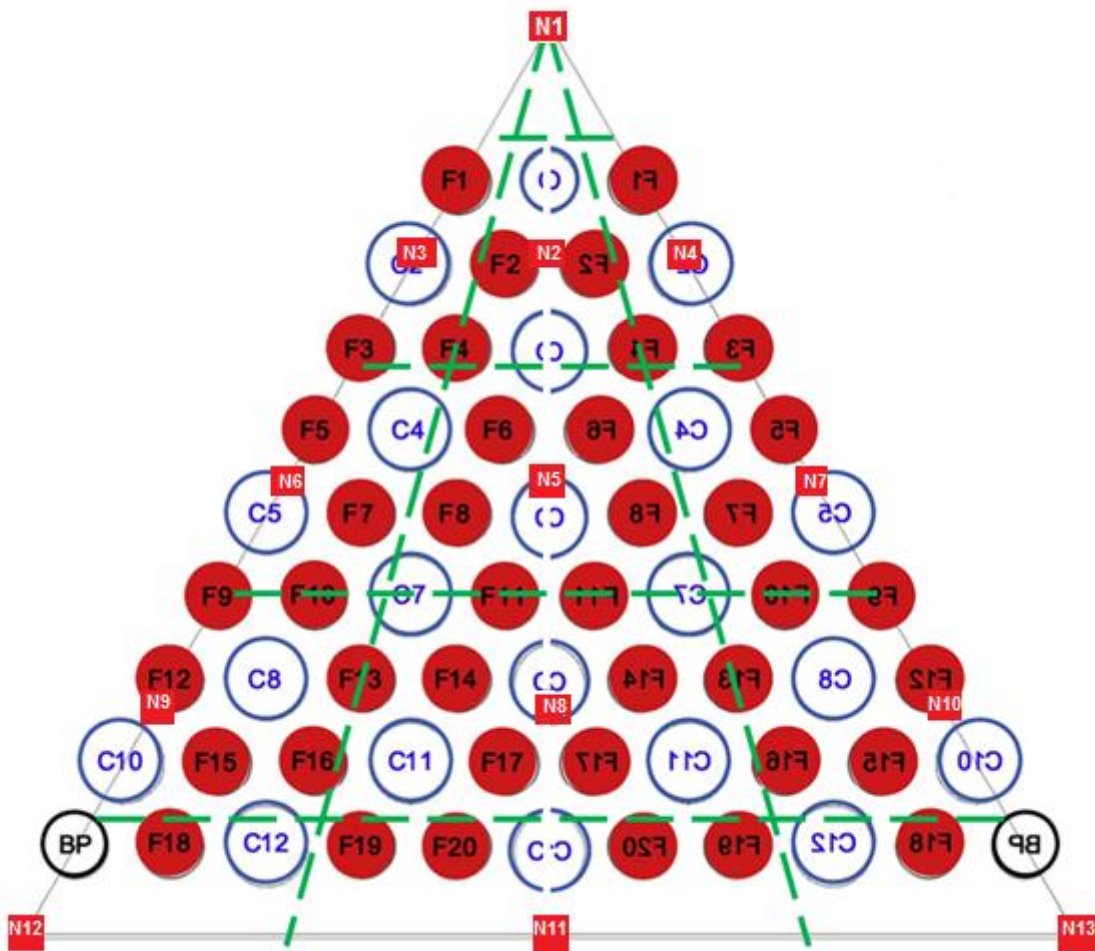


**Figure 3-4: Schematic layout of fuel rods, coolant channels, Flownex solid nodal points and the associated Flownex CVs.**

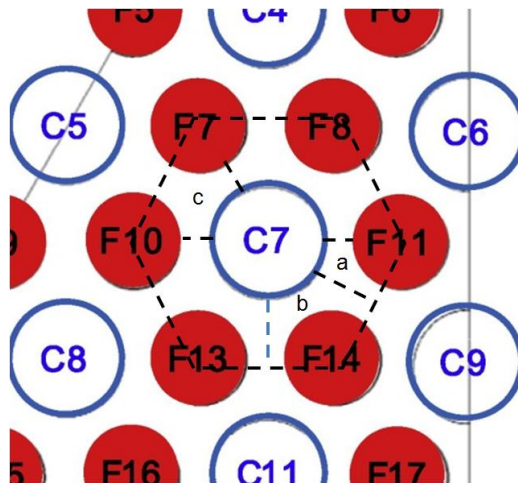


**Figure 3-5: Coolant channel surrounded by fuel rods.**

The most elementary unit cell is *a*. However the most appropriate unit cell to analyse the heat transfer between a fuel rod and a coolant channel is *b*. An alternative that could also be considered is unit cell *c*. Unit cell *c* can possibly be represented by a trapezium shaped unit cell. Unit cell *b* will be used as basis for the heat transfer between a fuel rod and a coolant channel. The unit cell is shown in **Figure 3-6** and is formed by the indicated symmetry planes, fuel rod surface and coolant channel surface.

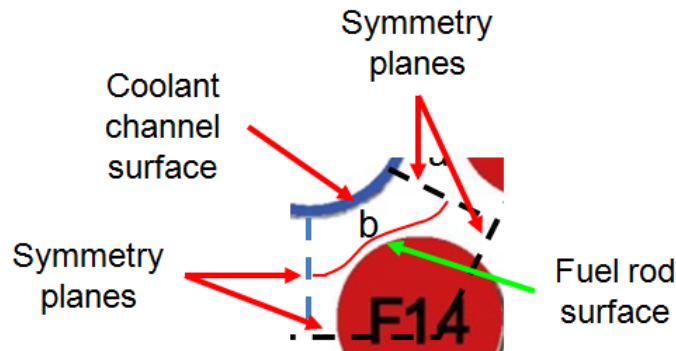


**Figure 3-6: Unit cell for conduction between fuel rod and coolant channel.**

A CFD (STAR-CCM+) simulation was conducted on the unit cell *b* (see Appendix **A-2**) to determine the mass averaged graphite block temperature  $T_s$  indicated by the red line in **Figure 3-6**. The graphite block node will then be placed at the intersection of the contour and the line connecting the centre of the fuel rod with the centre of the coolant channel.

The conduction shape factor for the heat transfer from the fuel rod surface to the graphite block node was determined from equation (3-22) after acquiring the mass averaged graphite block temperature from STAR-CCM+.

$$Q = S_{fs}k(T_f - T_s) \quad (3-22)$$

Where

$S_{fs}$  = conduction shape factor for the heat transfer from the fuel rod to the graphite node,

$T_f$  = temperature of the fuel rod surface and

$T_s$  = temperature of the mass averaged graphite block.

Similarly the conduction shape factor for the heat transfer from the graphite block to the coolant channel wall was determined from equation (3-23):

$$Q = S_{sw}k(T_s - T_w) \quad (3-23)$$

Where

$S_{sw}$  = conduction shape factor for the heat transfer from the graphite block node to the coolant channel and

$T_w$  = temperature of the coolant channel wall.

The conduction shape factor can also be implemented to determine the equivalent areas as indicated in equations (3-24) and (3-25):

$$S_{fs} = \frac{A_{fs}}{L_{fs}} \quad (3-24)$$

$$S_{sw} = \frac{A_{sw}}{L_{sw}} \quad (3-25)$$

Where

$A_{fs}$  = Equivalent surface area of the fuel rods,

$A_{sw}$  = Equivalent surface area of the coolant channels,

$L_{fs}$  = radial distance from the fuel rod surface to the graphite block node and

$L_{sw}$  = radial distance from the graphite block node to the coolant channel wall.

### 3.5 Heat transfer dimensionless parameters

#### 3.5.1 Biot number

The lumped capacitance method is the simplest and most convenient method used for solving transient heating and cooling problems. Considering a plane wall with surface convection, the steady state temperature distribution is attained by reducing the surface energy balance:

$$\dot{E}_{in} - \dot{E}_{out} = 0 \quad (3-26)$$

Equation (3-26) is reduced to:

$$\frac{kA}{L}(T_{s,1} - T_{s,2}) = hA(T_{s,2} - T_{\infty}) \quad (3-27)$$

Equation (3-27) is rearranged to:

$$\frac{T_{s,1} - T_{s,2}}{T_{s,2} - T_{\infty}} = \frac{(L/kA)}{(1/hA)} = \frac{R_{\text{cond}}}{R_{\text{conv}}} = \frac{hL}{k} = \text{Bi} \quad (3-28)$$

Where

L = characteristic length and

Bi = Biot number.

The Biot number as calculated in equation (3-28) is a dimensionless quantity and indicates a measure of the temperature drop in the solid relative to the temperature difference between the surface and the fluid (Incropera *et al.*, 2007).

A small value of the Biot number implies that the inner resistance of the body to heat conduction is small relative to the resistance to heat convection between the surface and the fluid (Cengel & Turner, 2005). If the  $\text{Bi} \ll 1$ , then the resistance to conduction within the solid is much less than the resistance to convection across the fluid boundary layer. However if  $\text{Bi} \gg 1$ , then the temperature difference across the solid is much larger than that between the surface and the fluid (Incropera *et al.*, 2007).

### 3.5.2 Fourier number

The Fourier number is a measure of heat conducted through a body relative to heat stored (Cengel & Turner, 2005). This number shows the propagation of heat through a body before and after a time step and is used for solids in transient heat transfer. The Fourier number is expressed as:

$$F_o = \frac{\alpha \Delta t}{\Delta x^2} = \frac{kL^2(1/L)\Delta T}{\rho C_p L^3 / T} \Delta T = \frac{\text{Heat conduction rate}}{\text{Heat storage rate}} \quad (3-29)$$

Where  $\alpha = \frac{k}{\rho C_p}$  = thermal diffusivity,

$\Delta t$  = time step size,

$\Delta x$  = thickness of conduction layer and

$F_o$  = Fourier number.

According to Pupeikis et al. (2012), the most acceptable value of the Fourier number is 0.5. A higher value of the Fourier number may give rise to significant errors in the calculation of temperature (Pupeikis et al., 2012).

The accuracy of the finite difference approach is enhanced by decreasing the  $\Delta x$  and  $\Delta t$  values. This is because the number of interior nodal points that must be considered increases with decreasing  $\Delta x$ , and the number of time intervals needed to take the solution to a recommended final time increases with decreasing  $\Delta t$  (Incropera et al., 2007) resulting in a better spatial and time resolution. Therefore the computation time increases with decreasing values of both  $\Delta t$  and  $\Delta x$ .

The choice of  $\Delta x$  is mostly based on a compromise between accuracy and computational requirements. However, the  $\Delta t$  value may not be chosen independently, it is determined by stability requirements.

Depending on the nature of the transient, the solution of the nodal temperatures should progressively approach steady state values with increasing time. One of the drawbacks of an explicit method is that the solution may be characterised by numerically induced oscillations, which are non-physical. The oscillations may turn out to be unstable, generating a solution which is divergent from the actual steady-state conditions. To avoid such errors, the prescribed  $\Delta t$  value must be maintained below a certain limit, which is dependent on  $\Delta x$  and other parameters of the system (Incropera et al., 2007).

**Table 3-1** below lists 4 configurations and their stability criteria.

**Table 3-1: Transient, 2D finite difference equations (Incropera et al., 2007).**

Configuration	Stability Criterion
Interior node	$Fo \leq \frac{1}{4}$
Node at interior corner with convection	$Fo(3 + Bi) \leq \frac{3}{4}$
Node at plane surface with convection	$Fo(2 + Bi) \leq \frac{1}{2}$
Node at exterior corner with convection	$Fo(1 + Bi) \leq \frac{1}{4}$

### 3.6 The Implicit Pressure Correction Method (IPCM)

Some numerical methods for steady state calculations can be treated as solving transient problems up until a steady state is reached. The main difference is that, when solving transient problems, the time step is selected in such a way that an accurate history is obtained and yet when a steady state solution is sought, large time steps are used to reach the steady state quickly (Ferziger & Peric, 2013). The IPCM is used in Flownex to solve the discretised equations for any unstructured thermal-fluid network. The computational grid and the procedure of the IPCM to attain a solution for the discretised equations will be outlined in this section.

#### 3.6.1 Computational grid

The IPCM uses a staggered grid discretisation scheme. The staggered grid uses nodes and elements to represent a network. The nodes are the centre points in a control volume for mass continuity of fluid and energy conservation, while the elements are the control volumes for momentum conservation. Pressures, temperatures and densities are defined at the nodes while velocities and volumetric flow rates are defined at the elements.

#### 3.6.2 Discretisation of governing equations for the IPCM

The key step of the finite volume method is the integration of partial differential equations to yield discretised equations (Greyvenstein, 2002).

Integration of the conservation of mass equation (3-1) over a control volume  $i$  lead to:

$$v_i \frac{\rho_i - \rho_i^o}{\Delta t} + \alpha(\rho_e Q_i - \rho_w Q_{i-1}) + (1 - \alpha)(\rho_e Q_i - \rho_w Q_{i-1})^o = 0 \quad (3-30)$$

Where

$v_i$  = volume of the CV,

subscripts  $e$  and  $w$  refer to the values on the right and left hand sides of the CV boundaries as indicated in **Figure 3-7**

$Q$  = volumetric flow rate and

$\alpha$  = weighting factor between the previous and the present time steps.

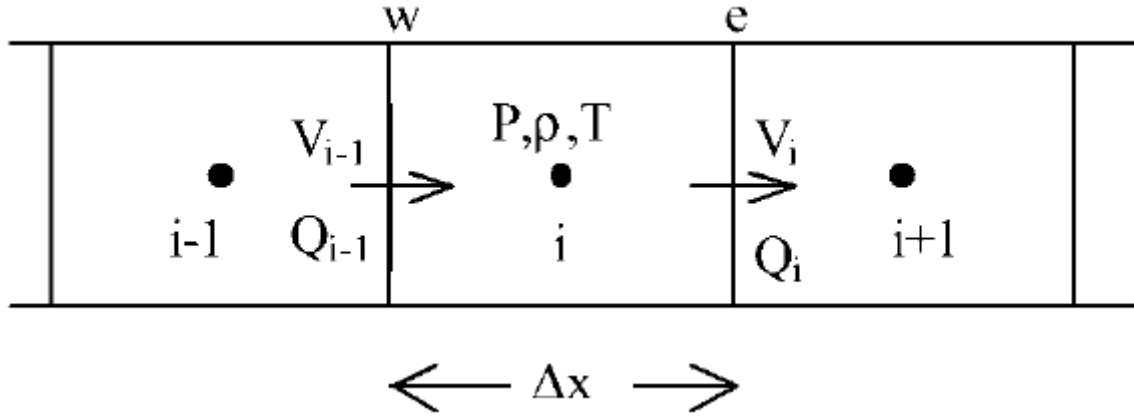


**Figure 3-7: Finite volume discretisation scheme (Greyvenstein, 2002).**

The superscript 0 refers to the previous time level,  $t$ , while terms without any subscripts are taken at the new time level ( $t+\Delta t$ ). The weighting factor can vary between 0 and 1 depending on the type of scheme used. When  $\alpha = 0$  the scheme becomes fully explicit and when  $\alpha = 1$  the scheme becomes fully implicit. If  $\alpha = 0.5$ , the time integration is equivalent to that of the Crank-Nicholson method (Greyvenstein, 2002).

Integration of the momentum equation (3-4) over a control volume centred at interface  $e$  leads to:

$$\begin{aligned} \frac{\rho_e \Delta x (Q_i - Q_i^0)}{A_e \Delta t} + \alpha \left( \frac{p_e}{p_{0e}} (p_{0_{i+1}} - p_{0_i}) + \frac{f \Delta x p_e Q_i |Q_i|}{2 D A_e^2} \right) \\ + (1 - \alpha) \left( \frac{p_e}{p_{0e}} (p_{0_{i+1}} - p_{0_i}) + \frac{f \Delta x p_e Q_i |Q_i|}{2 D_H A_e^2} \right)^0 = 0 \end{aligned} \quad (3-31)$$

Where  $A_e$  is the cross-sectional area at the control volume face,  $e$ .

Integration of the energy equation (3-6) over a control volume  $i$  lead to:

$$\begin{aligned} v_i \left( \frac{\rho_i h_{0_i} - \rho_i^0 h_{0_i}^0}{\Delta t} \right) - v_i \left( \frac{p_i - p_i^0}{\Delta t} \right) + \alpha (\rho_e Q_i h_{0_e} - \rho_w Q_{i-1} h_{0_w}) \\ + (1 - \alpha) (\rho_e Q_i h_{0_e} - \rho_w Q_{i-1} h_{0_w})^0 = v_i Q \end{aligned} \quad (3-32)$$

Equations (3-7), (3-30), (3-31) and (3-32) will be solved simultaneously for all unknowns i.e.  $p_{0_i}$ ,  $Q_i$ ,  $h_{0_i}$  and  $p_i$  at the new time level given their values at the previous time level at the boundaries (Greyvenstein, 2002). These discretised equations are solved using IPCM. The procedure is described in the next section.

### 3.6.3 Solution procedure

Flownex employs the IPCM solution algorithm that results in fast and accurate simulations (M-Tech, 2013). Below is a list of consecutive steps of the IPCM:

- I. Guess initial node pressures
- II. Calculate mass flows using  $\Delta p$ -Q relationships.
- III. Test for continuity at all nodes.
- IV. Adjust pressures to ensure continuity at all nodes.
- V. Update mass flows using new updated pressures.
- VI. Repeat steps **1** to **5** until convergence.
- VII. Solve the energy equation.
- VIII. Repeat steps **1** to **7** until convergence.
- IX. Move to next time step and repeat steps **1** to **8** (Only for transient simulations).

### 3.7 Summary

This chapter dealt with the governing equations involved in fluid dynamics and heat transfer. The discretisation of pipe flow has been dealt with in more detail as well as the modes of heat transfer. The Biot and Fourier numbers which are important heat transfer parameters have been presented. The conduction shape factor with particular emphasis on the HTR block has also been dealt with. The conduction length as well as the conduction areas have been calculated as indicated in Appendix **A-3**. The IPCM solution algorithm which is implemented in Flownex has been discussed together with the procedure on how Flownex employs it.

## **4. SEPARATE EFFECTS MODELLING AND VERIFICATION**

---

### **4.1 Introduction**

In this chapter, different Flownex elements which are relevant to this study will be described. Five different cubical block and three triangular block cases will be modelled in both Flownex and STAR-CCM+ to illustrate the capabilities of Flownex (and possible deficiencies) and at the same time verifying Flownex by comparing the results obtained with the corresponding results obtained from STAR-CCM+ simulations. STAR-CCM+ is the code that is used to verify the Flownex results because it was mainly designed to be accurate and efficient while solving for problems involving flow, heat transfer and stress. In this study, heat transfer is the main objective, STAR-CCM+ analyses heat transfer in 3-D and therefore simulates what really occurs in real life situations.

### **4.2 Thermal fluid network code – Flownex**

Flownex is a thermal-fluid systems simulation and design software. Similar to CFD codes, Flownex provides the ability to simulate, design and optimize complete integrated thermal-fluid systems based on fundamental principles. Results in Flownex can be obtained within short computer processing times, even for transient event simulations, unlike the CFD codes which typically need much longer computational times to generate the corresponding results. The solution procedure implemented in Flownex has been briefly discussed in the previous chapter.

### **4.3 Different elements in Flownex**

Flownex uses nodes and elements to represent a thermal-fluid network graphically. Elements are components such as pipes, pumps, valves, compressors or heat exchangers, while nodes are the end points of elements. Elements can be connected in any random way at common nodes to form a network (M-Tech, 2013). In these next sections, the elements applicable to this study, mostly the heat transfer elements, will be discussed in more detail.

#### **4.3.1 The pipe element**

There are five different components found in the piping functionality group namely: basic pipe, bend, insulated pipe, mine ventilation duct and pipe component. The pipe element is chosen for this study due to a number of factors. The pipe element is used to model flow in pipes and ducting with non-constant, arbitrary cross sectional area. It takes into account the frictional and secondary losses. In dynamic simulations, pressure waves due to sudden changes in boundary conditions can be modelled.

In Flownex, ducts can be modelled using either the Darcy-Weisbach or the Hazen-Williams pressure drop model. The Hazen-Williams model is mostly used in civil engineering and is therefore not discussed further. Pipes with a constant cross sectional area as well as different inlet and outlet cross sectional areas can be modelled as well. Both compressible and incompressible flows can be simulated in Flownex. However in this section emphasis will be placed on compressible flow.

The total pressure drop for a transient compressible flow is given by:

$$p_{0i} - p_{0e} = \left( \frac{fL}{D} + \sum K_S + \frac{\Delta T_0}{T_0} \right) \frac{p_0 \gamma M^2}{2} + \Delta p_{0r} \quad (4-1)$$

$$+ \frac{p_0}{\rho} \left( \rho g \Delta z + K_i \frac{1}{2} \rho |v_i| v_i + K_e \frac{1}{2} \rho |v_e| v_e \right) + \frac{p_0 \rho L}{p} \frac{dv}{dt}$$

Where

$\Delta p_{0r}$  = total pressure drop over an orifice in the pipe,

$L$  = length of the pipe,

$D$  = inside diameter of the pipe,

$\Delta T_0 = T_{0e} - T_{0i}$  = total temperature difference,

$\sum K_S$  = sum of the secondary loss components like bends, valves and junctions,

$v_i$  and  $v_e$  = the velocity at the pipe inlet and outlet respectively,

$K_i$  and  $K_e$  = the inlet and outlet loss coefficient respectively and

$\Delta z = z_e - z_i$  = the height difference between the inlet and outlet.

In the case of steady state compressible flow, equation (4-1) is still valid but the temporal term is not present.

The mean total temperature and pressure are calculated using equations (4-2) and (4-3) respectively:

$$T_0 = \frac{T_{01} + T_{02}}{2} \quad (4-2)$$

$$p_0 = \frac{p_{01} + p_{02}}{2} \quad (4-3)$$

Where the subscripts 1 and 2 refer to the up and downstream nodes respectively.

The mean Mach number is calculated using:

$$M = \frac{v}{\sqrt{\gamma RT}} \quad (4-4)$$

Where  $v$  is the mean velocity based on pipe diameter.

The friction factor may be calculated for a laminar and turbulent flow (Lindeburg, 2013):

$$f = \frac{64}{Re} \quad \text{if } Re < 2300 \quad (4-5)$$

$$f = \frac{0.25}{\left(\log\left(\frac{\varepsilon}{3.7D_H} + \frac{5.74}{Re^{0.9}}\right)\right)^2} \quad \text{if } Re > 5000 \quad (4-6)$$

Where

$Re$  = the Reynolds's number,

$Re < 2300$  designates laminar flow,

$Re > 5000$  designates turbulent flow and

$\varepsilon$  = the mean inside wall roughness.

However, for the transitional region that exists in the region  $2300 \leq Re \leq 5000$ , a linear interpolation between equation (4-6) and (4-7) is used to calculate the friction factor (Rousseau, 2013).

In Flownex, the required input data for pipes in parallel includes: fluid data reference, length, inlet circumference and area, roughness and number of discretisation increments.

### 4.3.2 The conductive heat transfer element

Flownex has two purely Conductive Heat Transfer elements (CHT). One is used for linear, one-dimensional heat transfer i.e. in one direction. The other one is a cross Conductive Heat Transfer element and will be discussed in section 4.3.3.

The CHT is used for 1-D heat transfer, therefore it can only be connected either in the horizontal or vertical directions. The CHT element can only be connected between two solid nodes (Figure 4-1).

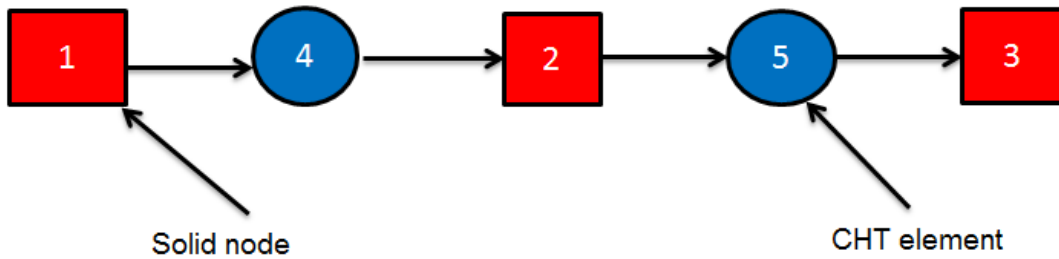


**Figure 4-1: Node and element representation for two connected CHT elements.**

The required input data in Flownex includes: the material data, length and height for conduction, inlet and outlet areas as well as inlet and outlet solid fractions.

#### 4.3.3 The cross conductive heat transfer element

The cross CHT elements are used in conjunction with ordinary CHT elements to model heat transfer in 2-D domain. Unlike the ordinary CHT elements, cross CHT elements are used to connect adjacent ordinary CHT elements to create a 2-D domain (M-Tech, 2013). The cross CHT element can be connected directly to a flow node, or a un-incremented flow element. They represent 1-D heat transfer. **Figure 4-2** below shows the node and element representation for two connected cross CHT elements.

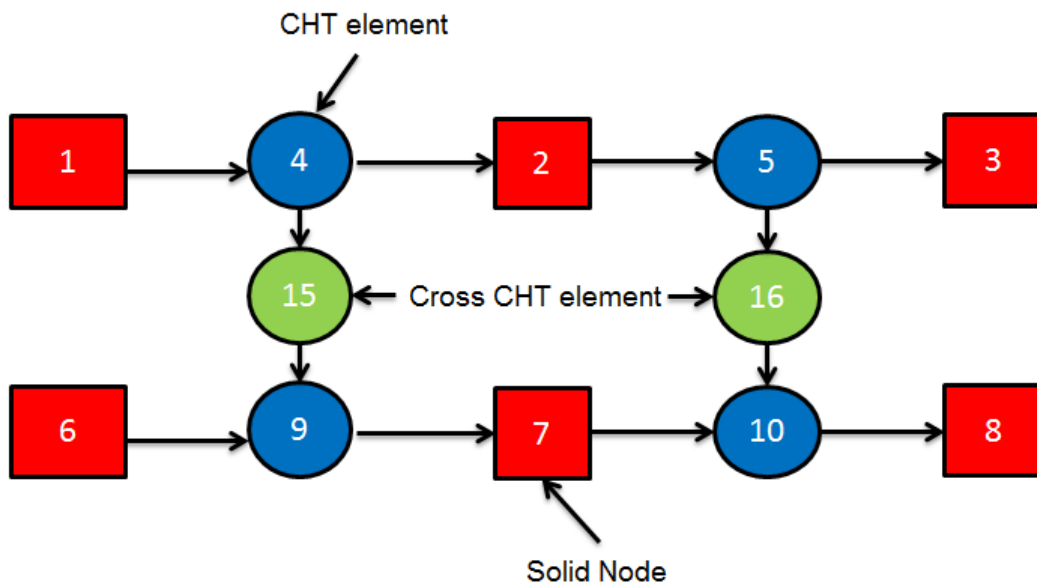


**Figure 4-2: Node and element representation for two cross CHT elements.**

The required input data in Flownex includes the flow direction as well as the connection orientation.

**4.3.4 The convective heat transfer element**

Convection elements represent the heat exchange link between a fluid and a solid surface (M-Tech, 2013). A convection element can be connected to either an incremented flow element or a flow node. One end of the convection element will always be a solid node. A convection element cannot be connected between two flow elements or two flow nodes or a combination of a flow node and a flow element. **Figure 4-3** below indicates a node and element representation for a convection element.

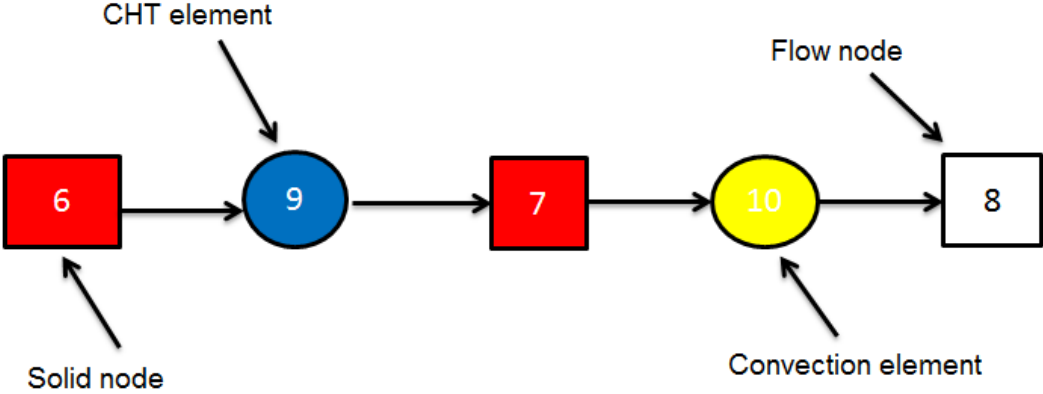


**Figure 4-3: Node and element representation for a convection element.**

The required input data in Flownex includes heat transfer area, and either the Dittus-Boelter relationship or a local heat transfer coefficient.

**4.3.4.1 Dittus-Boelter type correlation**

Calculating the Nusselt number (Nu) is the first step in calculating the convection heat transfer coefficient:

$$Nu = Nu_{lam} \quad \text{if } Re < 2300 \quad (4-7)$$

$$Nu = CRe^mPr^n \quad \text{if } Re \geq 5000 \quad (4-8)$$

Where

- Nu<sub>lam</sub> = specified laminar Nusselt number,
- C and m = constants specified by the user,
- Pr = Prandtl number and
- n = value of n<sub>h</sub> or n<sub>c</sub> depending on whether the fluid is heated or cooled.

The Nusselt number for the transitional region between the laminar and turbulent regions is calculated by interpolating as illustrated in equation **(4-9)**:

$$Nu = [(C5000^m Pr^n) - Nu_{lam}] \frac{Re - 2300}{5000 - 2300} + Nu_{lam} \quad (4-9)$$

The heat transfer coefficient (h) is now calculated from the Nusselt number (Cengel & Turner, 2005):

$$h = \frac{Nu k}{D_H} \quad (4-10)$$

The right hand side values of equation **(4-10)** can be either be at a flow node or flow element depending on what is connected to the convection element (M-Tech, 2013).

#### **4.3.4.2 Heat transfer coefficient**

Newton's law of cooling calculates the convective heat transfer from the fluid to the solid. This was illustrated in equation **(3-17)** with h being the heat transfer coefficient.

#### **4.3.5 Nodes and boundary conditions**

In Flownex, nodes can be classified either into solid or flow nodes. Flow nodes are the end points of flow elements and the solid nodes are the end points of conduction or convection elements. In conduction elements, heat transfer occurs through a solid material and therefore solid nodes represent a fixed mass of solid material.

The boundary condition component in Flownex is used to specify the boundary conditions of a network (M-Tech, 2013). The boundary condition component is only connected to a node component and thus the boundary condition specified in the boundary condition component is only applied to the node it is linked to. Some possible input combinations that can be specified on the boundary condition component are:

- I. Pressure and temperature.
- II. Pressure and quality.
- III. Temperature and quality.
- IV. Temperature and a mass source.
- V. A mass source only.
- VI. Pressure only.
- VII. Pressure and enthalpy.
- VIII. Enthalpy and a mass source.

The quality specification is only valid when a two-phase fluid is used (M-Tech, 2013). In the next section, five different test cases will be modelled and simulated in Flownex. The results of the simulations will be compared with the corresponding results obtained from the CFD code, STAR-CCM+ of the same model to verify Flownex. These five simple cases are basic scenarios that can occur in an HTR.

**4.4 Cubical block test cases**

A graphite block which measures 0.5 m × 0.5 m × 0.5 m was considered. The graphite block has the following properties:

- k : 88.4 [W/m.K]
- ρ : 1760 [kg/m<sup>3</sup>]
- C<sub>p</sub> : 0.966 [kJ/kg.K]

The block geometry and properties were used in all the five test cases. These five test cases consider 1-D (axial) conduction. In Flownex, the block was discretised into a total of seven CVs in the axial direction whereby the first and last CVs were half length and five full length CVs, whilst in the case of STAR-CCM+ it was discretised into 6 × 6 × 6 CVs with the CVs next to faces having a length normal to the face of half of a Flownex CV. The nodes from the Flownex model corresponded to the CV centres of the STAR-CCM+ model as well as the surfaces. **Figure 4-4** shows a schematic layout of the heat transfer network model for the cubical block. Each CV is assumed to have a constant temperature.

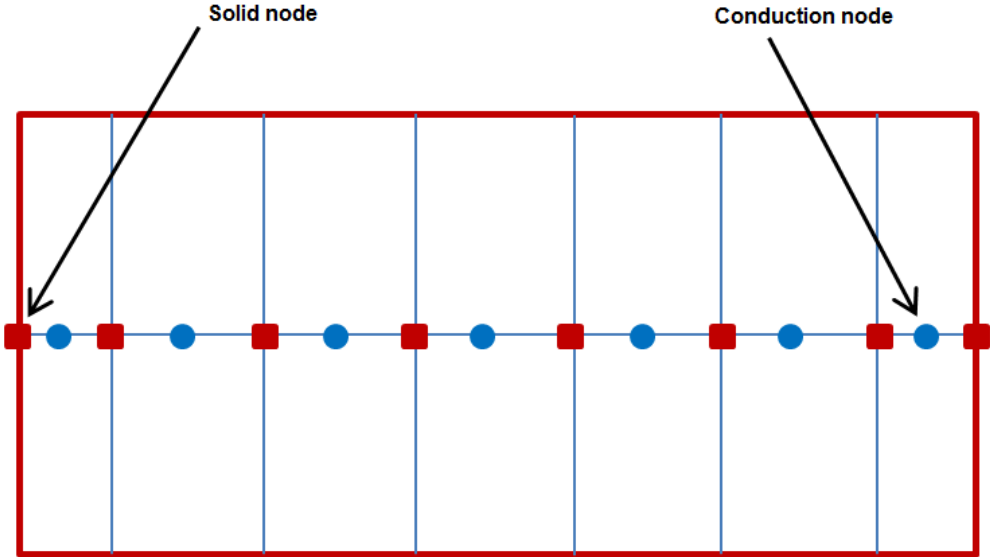


**Figure 4-4: Schematic layout of heat transfer in a cubical block in Flownex.**

4.4.1 Case 1

4.4.1.1 Steady state

In the first case, two boundary temperatures are specified. The left boundary condition is specified to be 300 K and the right boundary condition is specified to be 600 K. The other two boundaries were considered to be adiabatic. This is illustrated below in **Figure 4-5**.

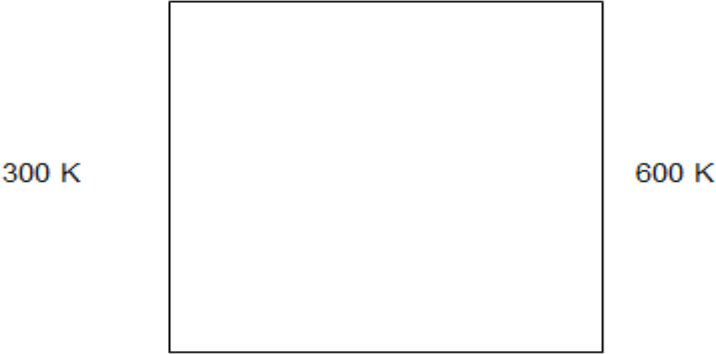


**Figure 4-5: Schematic representation of the block and the boundary conditions for the first case.**

This block was modelled and simulated in Flownex and STAR-CCM+ and a steady state temperature distribution was attained using both codes. **Figure 4-6** below compares the results obtained with the two codes with each other. **Figure 4-6** shows that there is a good comparison between the two codes.

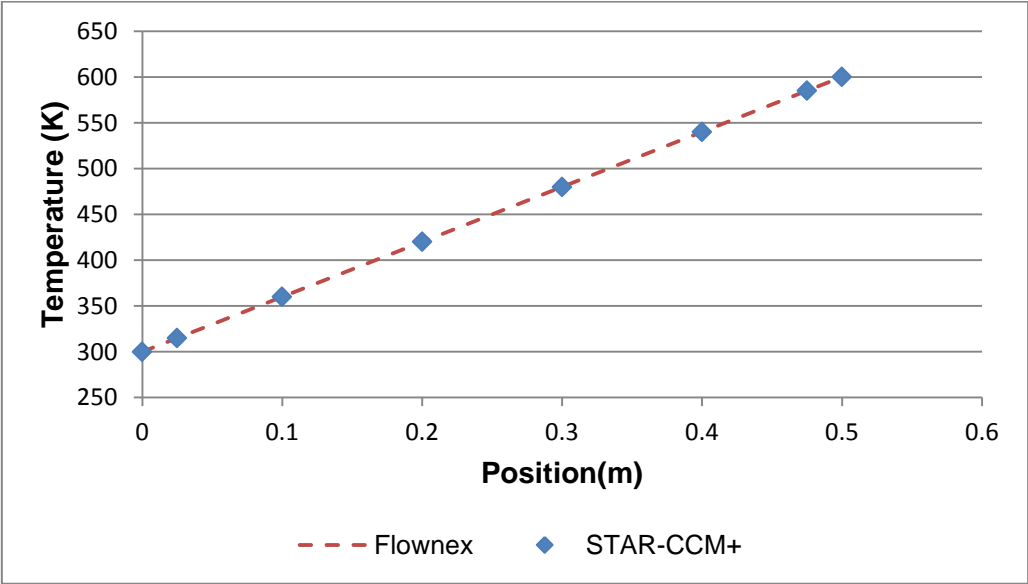


**Figure 4-6: Steady state temperature results from Flownex and STAR-CCM+ for the first case.**

#### 4.4.1.2 Transient

For the transient analysis, the whole block was initially maintained at a constant temperature of 300 K. A step change from 300 K to 350 K was implemented on the left hand boundary at 0 seconds. The Fourier number as explained in section 3.5.2 is an indication of the propagation of heat transfer through a body before and after a step change is instigated. A maximum time step size of 6 seconds was obtained using the Fourier number relation. This calculation is indicated in Appendix B-2.

In order to get a time step size which portrays accurate transient results, four different time step sizes (6, 4, 2 and 1 second) were investigated. The second node along the length of the block was isolated and analysed for all the different time step sizes. The second node is also used in the next four test cases. The simulations were run for 200 seconds. Appendix B-5 displays the results of these four time step sizes. The four different time step sizes show very good comparison.

Even though there is little difference between the results for the various time step sizes, the time step of 1 second was chosen as the basis of the other test cases. This is because using a shorter time step size requires shorter spatial increments, and thus more interior nodes which leads to a better spatial resolution. This also leads to an increase in computational time. However, using a time step size of 1 second it was found that the computational time was still reasonable.

**Figure 4-7** below shows the transient results with a 1 second time step size. The comparison between the two codes is very good.

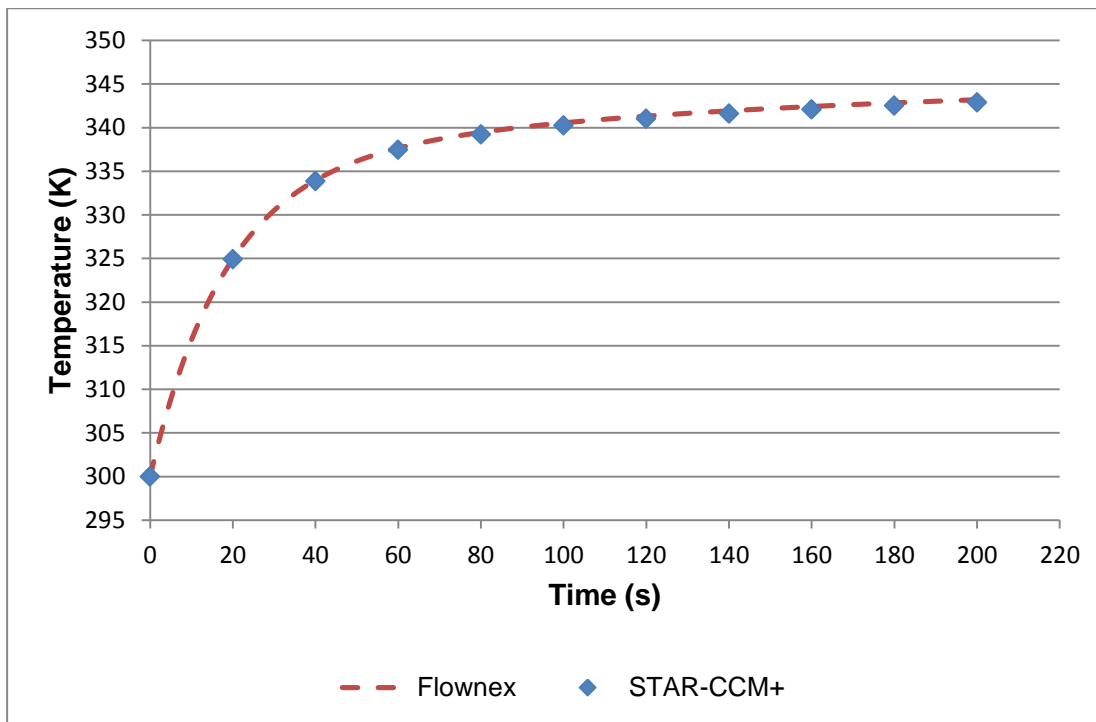


**Figure 4-7: Transient temperature results from Flownex and STAR-CCM+ for the first case.**

#### 4.4.2 Case 2

##### 4.4.2.1 Steady state

In the second case, a heat flux and temperature were specified. The left hand boundary condition was specified to be 5000 W and the right hand boundary condition was specified to be 600 K. In STAR-CCM+ a heat flux of 20000W/m<sup>2</sup> was specified at the left boundary. The other two boundaries were considered to be adiabatic. This is illustrated below in **Figure 4-8**.



**Figure 4-8: Schematic representation of the block and the boundary conditions for the second case.**

The block was modelled and simulated in STAR-CCM+ and Flownex and a steady state temperature distribution was obtained using both codes. In Flownex, the heat flux was specified at the first node. **Figure 4-9** below shows the results comparison between the results obtained with the two codes. There is a linear decline in temperature along the block and the comparison between the two codes is good.

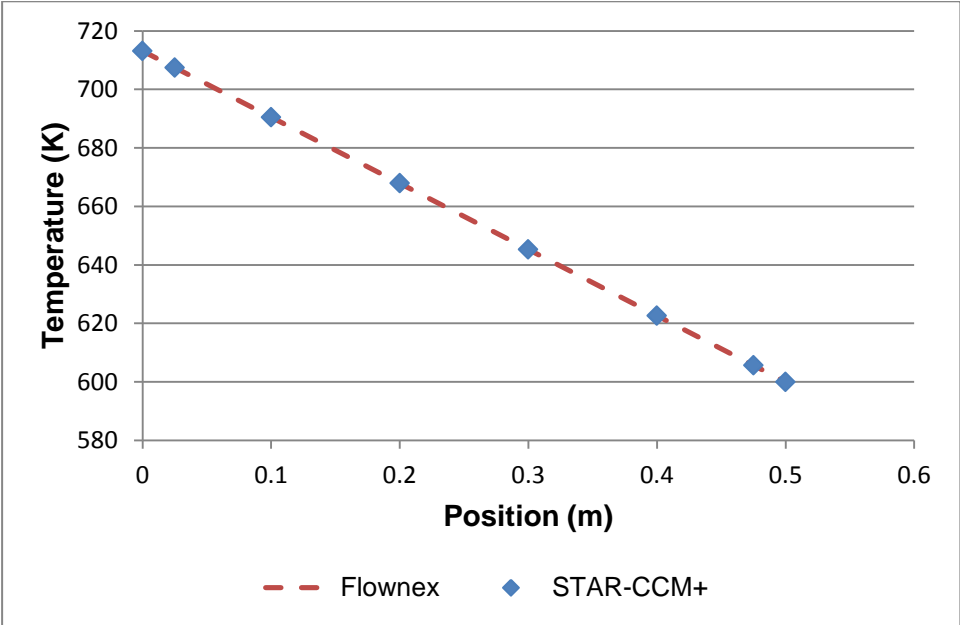


**Figure 4-9: Steady state temperature results from Flownex and STAR-CCM+ for the second case.**

#### 4.4.2.2 Transient

For the transient analysis, the whole block was initially maintained at a constant temperature of 600 K. A step change of the heat flux from 0 W to 5000 W was implemented on the left hand boundary at 0 seconds. The propagation of the heat transfer was observed by isolating the second node along the length of the block. The maximum physical time for both codes was 8000 seconds. **Figure 4-10** displays the comparison between the transient results obtained with the two codes using a time step size of 1 second. An increase in temperature was observed for both codes from 600 K up until the system reached steady state at 706 K. The results comparison between the two codes is good.

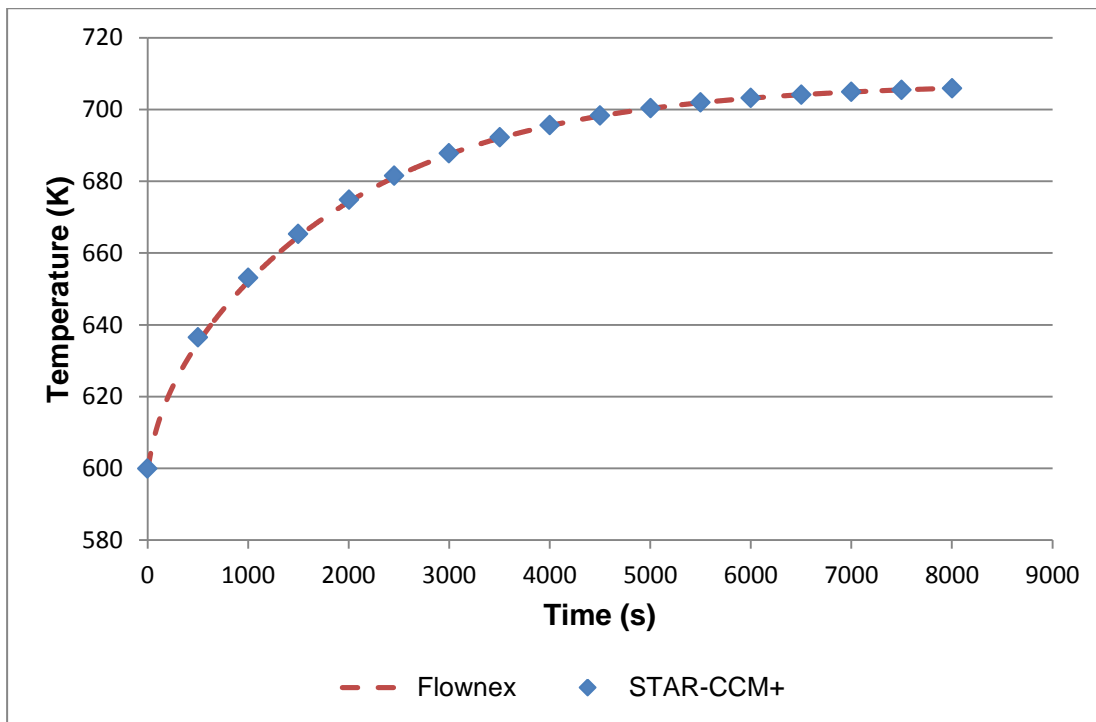


**Figure 4-10: Transient temperature results from Flownex and STAR-CCM+ for the second case.**

### 4.4.3 Case 3

#### 4.4.3.1 Steady state

In the third case, a distributed heat source and a temperature are specified. The distributed heat source was specified to be 5000 W and the right hand boundary condition was specified to be 600 K. The heat source was evenly distributed within the nodes in Flownex, but in STAR-CCM+ a volumetric heat source of 40000 W/m<sup>3</sup> was specified. The two unspecified surfaces were assumed to be adiabatic. This is illustrated below in **Figure 4-11**:

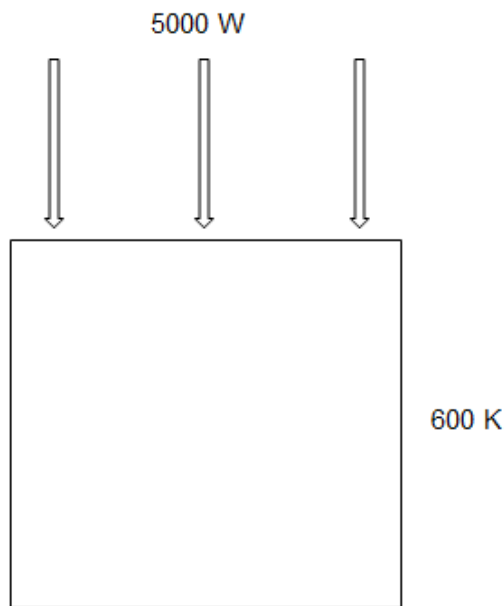


**Figure 4-11: Schematic representation of the block and the boundary conditions for the third case.**

The block was modelled and simulated in STAR-CCM+ and FlowNex and a steady state temperature distribution was obtained using both codes. **Figure 4-12** below displays the comparison between the results obtained with the two codes. The decrease in temperature resembles a parabolic function. The comparison between the two codes is good.

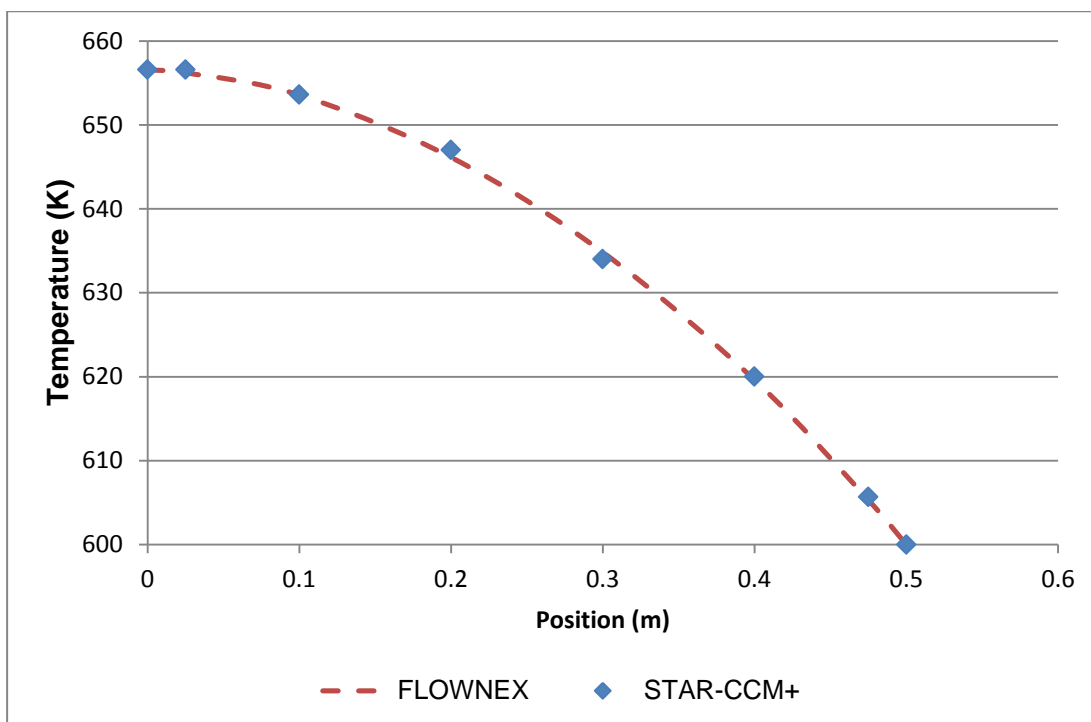


**Figure 4-12: Steady state temperature results from FlowNex and STAR-CCM+ for the third case.**

#### 4.4.3.2 Transient

Similar to the second case, the whole block was also initially maintained at a constant temperature of 600 K. A step change of the distributed heat source was implemented from 0 W to 5000 W. The maximum physical time for both codes was 8000 seconds. **Figure 4-13** displays the comparison between the results obtained with the two codes using a time step size of 1 second. From **Figure 4-13**, there is an increase in temperature from 600 K to 655 K before steady state is reached. Both codes display good comparison with each other.

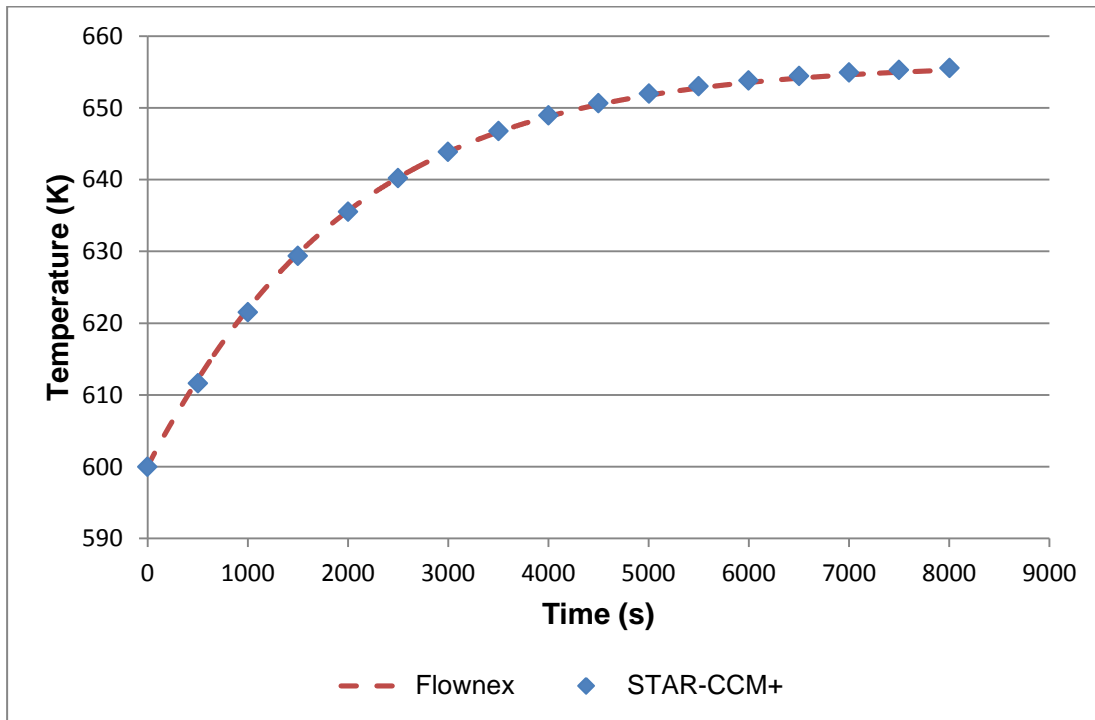


**Figure 4-13: Transient temperature results from Flownex and STAR-CCM+ for the third case.**

#### 4.4.4 Case 4

##### 4.4.4.1 Steady state

In the fourth case, a distributed heat source, heat flux and temperature were specified. The left hand boundary condition was specified to be 5000 W and the right hand boundary condition was specified to be 600 K. A distributed heat source was also specified to be 5000 W. In STAR-CCM+ a heat flux of 20000W/m<sup>2</sup> and a volumetric heat source of 40000 W/m<sup>3</sup> were specified. This is illustrated below in **Figure 4-14**:

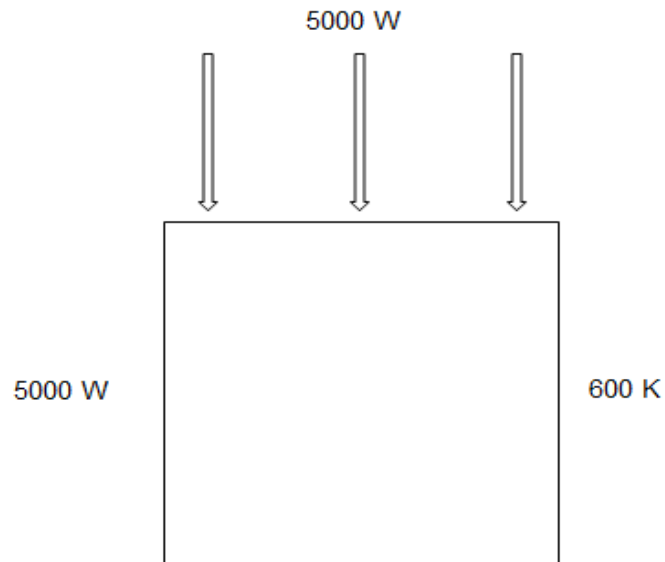


**Figure 4-14: Schematic representation of the block and the boundary conditions for the fourth case.**

The block was modelled and simulated in STAR-CCM+ and Flownex and a steady state temperature distribution was obtained using both codes. **Figure 4-15** below shows the comparison between the results comparison between the two codes. There is a decline in temperature from 770 K to 600 K along the block. The results from the two codes are very comparable.

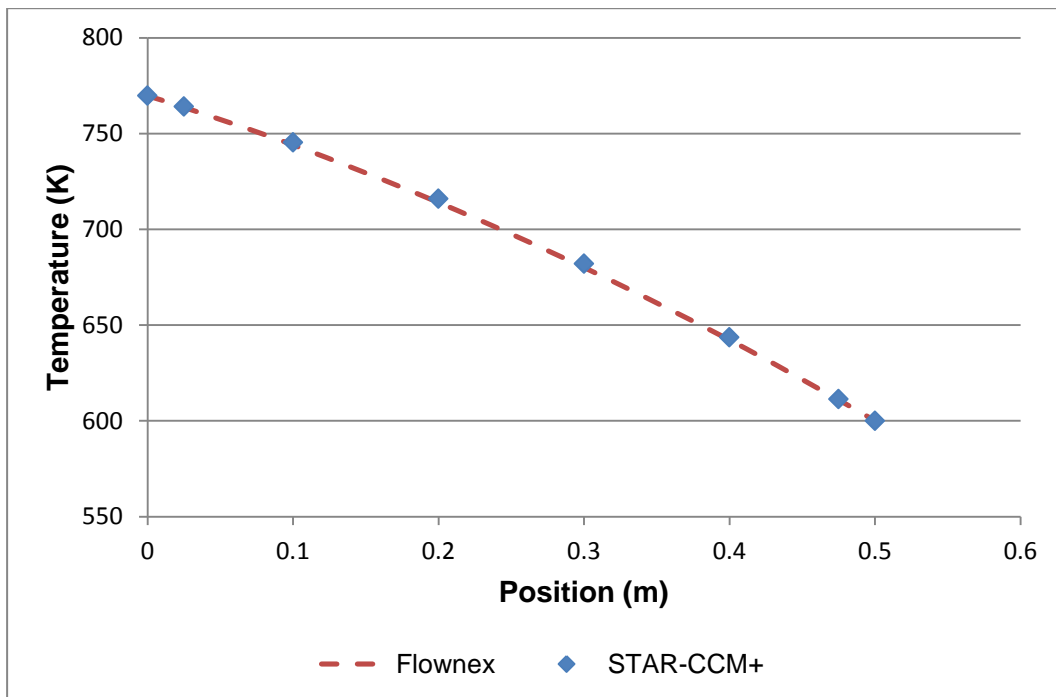


**Figure 4-15: Steady state temperature results from Flownex and STAR-CCM+ for the fourth case.**

4.4.4.2 Transient

Similar to the second and third cases, the whole block was also initially maintained at a constant temperature of 600 K. A step change of the distributed heat source was implemented from 0 W to 5000 W and also a step change of the heat flux was implemented from 0 W to 5000 W. The maximum physical time for both codes was 8000 seconds. **Figure 4-16** displays the comparison between the results obtained with the two codes. There is an increase in temperature from 600 K to 761.5 K before the system reaches steady state. The results from the two codes are very comparable.

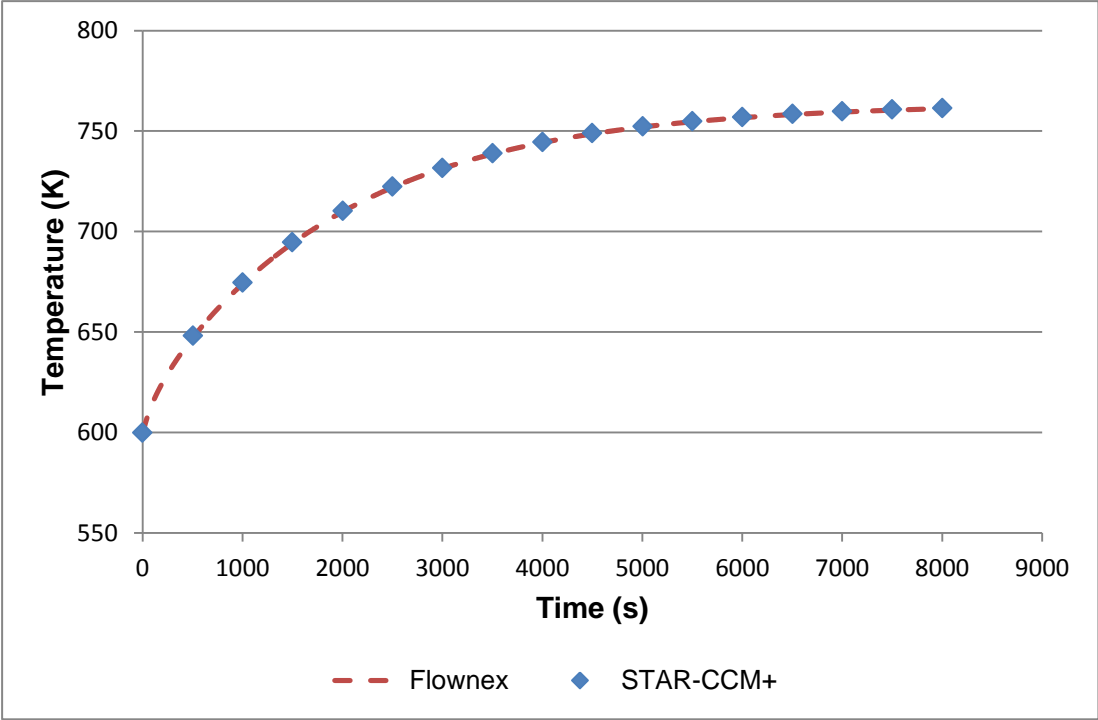
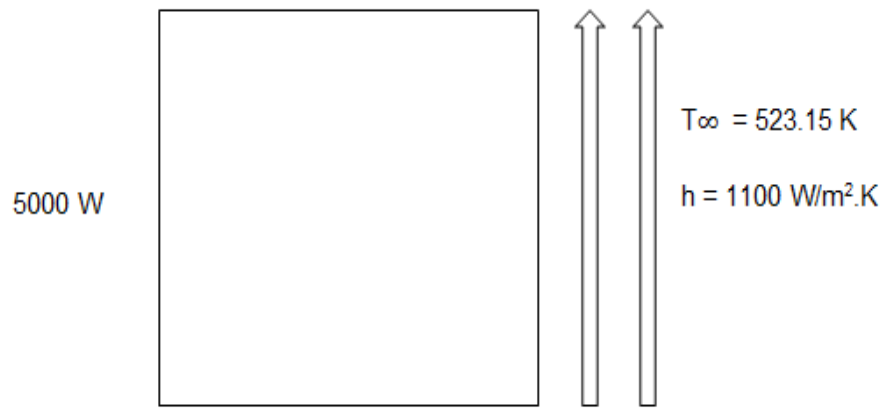


Figure 4-16: Transient temperature results from Flownex and STAR-CCM+ for the fourth case.

4.4.5 Case 5

4.4.5.1 Steady state

In the fifth case, three initial boundary conditions were specified. A heat flux was specified to be 5000 W on the left hand boundary, a fluid temperature of 523.15 K and a convective heat transfer coefficient of 1100 W/m<sup>2</sup>.K were specified on the right hand boundary. This is illustrated below in **Figure 4-17**:



**Figure 4-17: Schematic representation of the block and the boundary conditions for the fifth case.**

This block was modelled and simulated in Flownex and STAR-CCM+ and a steady state temperature distribution was obtained using both codes. **Figure 4-18** below displays the comparison between the results obtained with the two codes. The decline in temperature resembles a linear relationship from 654 K to 541 K along the length of the block. The results from the two codes are in agreement.

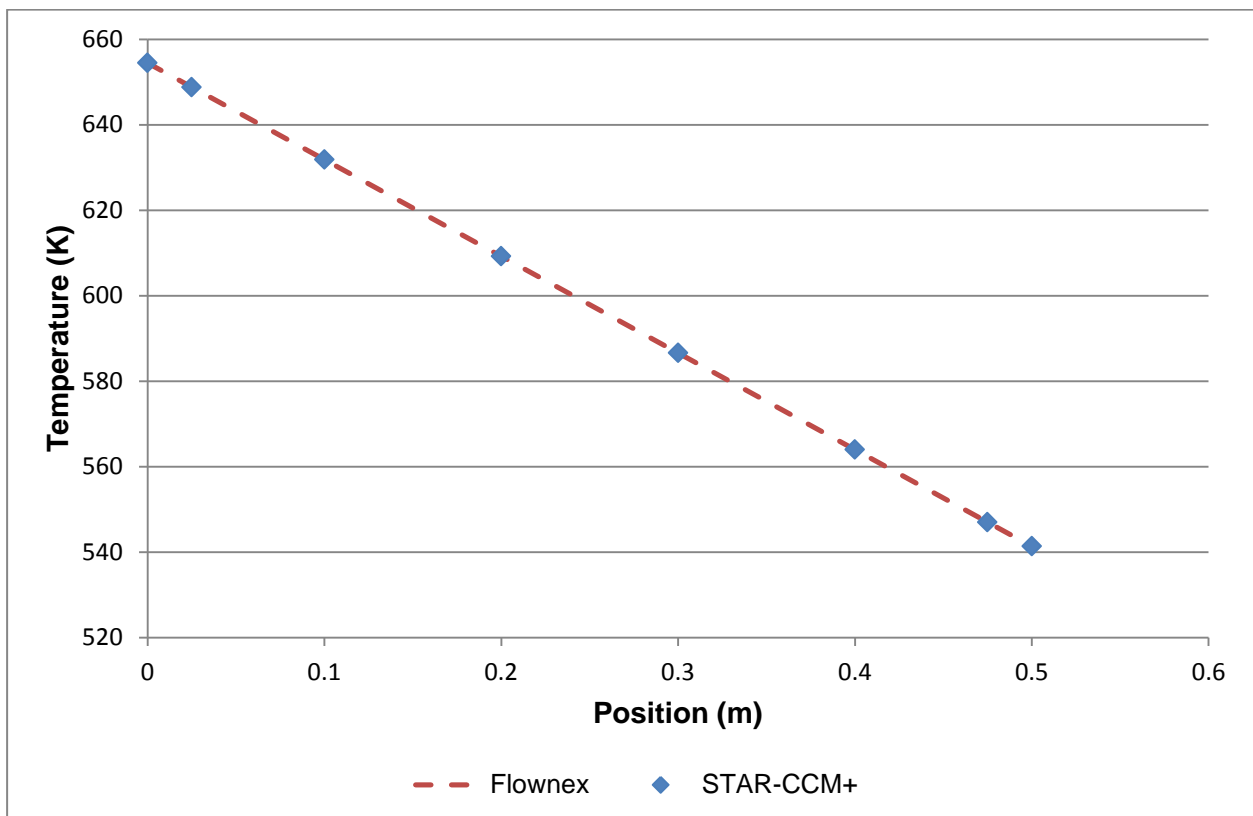


**Figure 4-18: Steady state temperature results from Flownex and STAR-CCM+ for the fifth case.**

4.4.5.2 Transient

A constant temperature of 523.15 K for the block was initially maintained before a step change was implemented. A step change of the heat flux from 0 W to 5000 W was implemented on the left hand boundary of the block. Similar to the second, third and fourth cases, the maximum physical time for both codes was 8000 seconds.

The Biot number as explained in section 3.5.1 is a measure of the temperature drop in the solid relative to the temperature difference between the surface and the fluid (Incropera *et al.*, 2007). This test case involves both conduction and convection and as a result both the Fourier and Biot numbers are involved in calculating the most stable time step size. This calculation is shown in Appendix B-3.

The maximum time step size was calculated to be 4 seconds (refer to Appendix B-3). However since using a smaller time step size gives more accurate results, this test case also adopted a 1 second time step size similar to the previous four test cases.

Figure 4-19 shows the transient results for the fifth case using a time step of 1 second. There was an increase in temperature from 524.2 K to 644 K before the system reached steady state. The results obtained from both codes are very comparable.

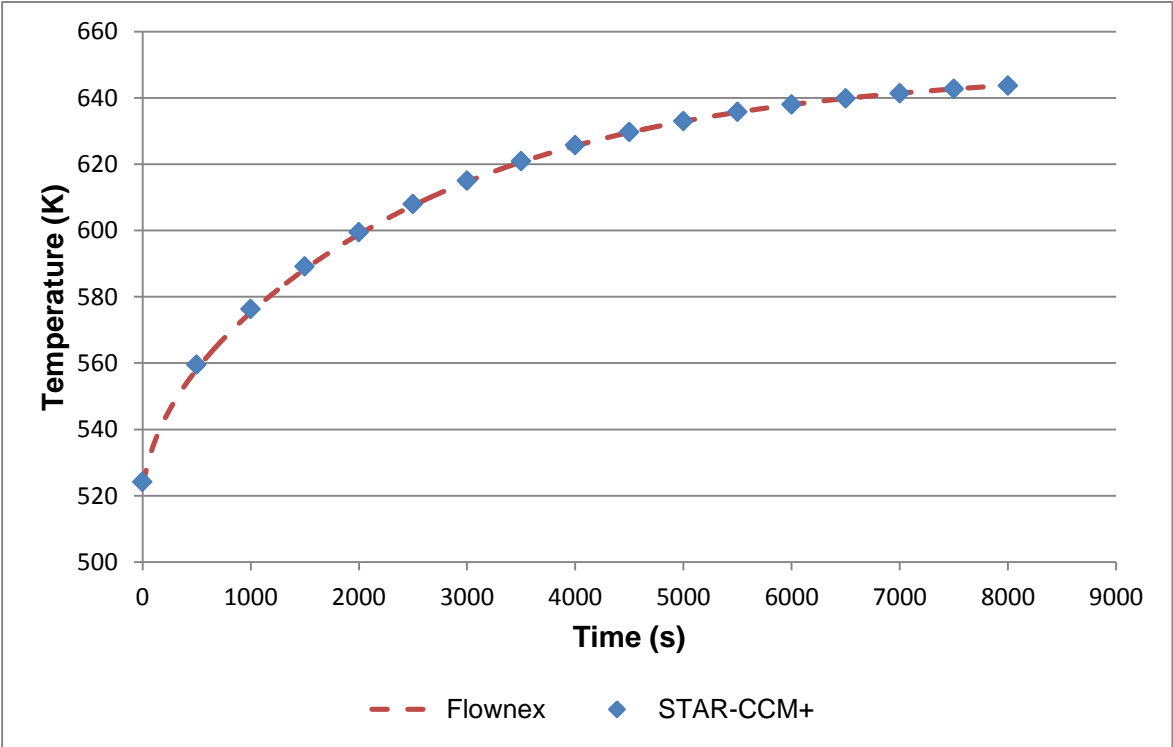


Figure 4-19: Transient temperature results from Flownex and STAR-CCM+ for the fifth case.

## 4.5 Triangular block test cases

Section 4.4 dealt with verification studies on a cubical block and a good comparison for both steady state and transient cases with different conditions was achieved between the results obtained with the codes, STAR-CCM+ and Flownex. In this section, more verification studies were conducted and discussed on a triangular block. A triangular block was chosen because it is similar to the section of the reactor to be studied, also conducting verification studies on a triangular block verified if Flownex was able to solve for non-orthogonal geometries. The dimensions and properties of the prismatic block were also applied to the triangular block verification case studies.

### 4.5.1 Effect of grid size in Flownex

2-D models (radial and tangential) were simulated with different discretisation levels in Flownex. **Figure 4-20** illustrates the discretisation in two directions, radial and tangential directions for the triangular block.

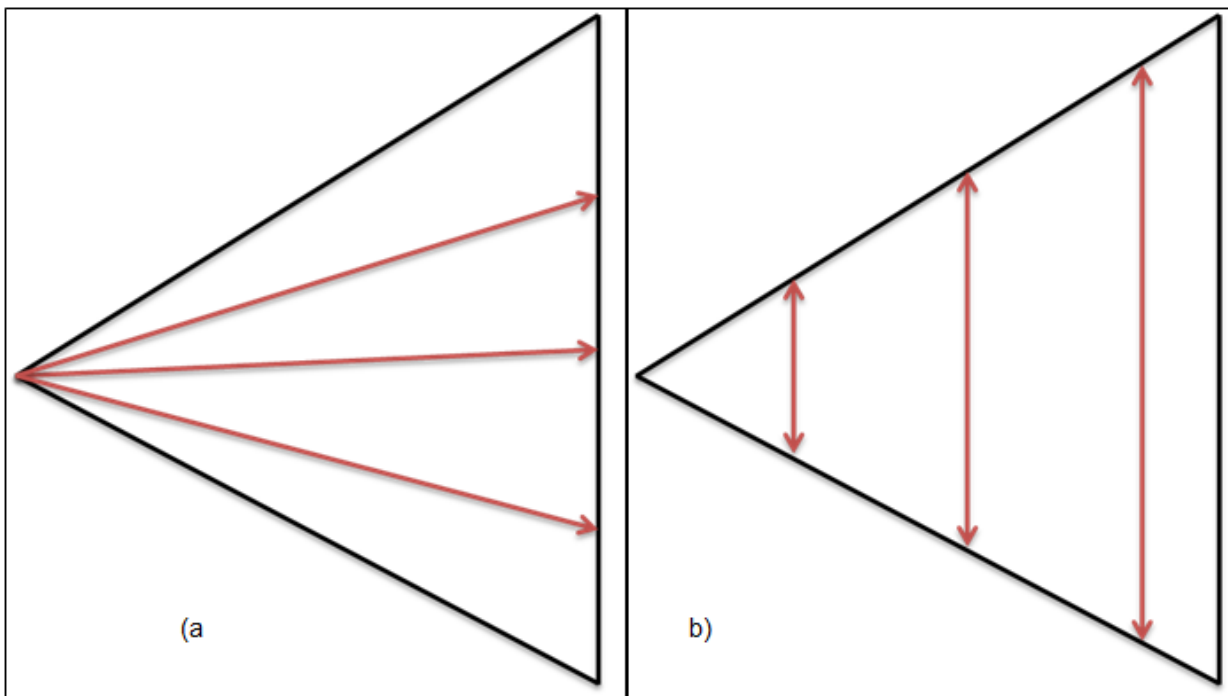


**Figure 4-20: Discretisation of the block in the (a) radial and (b) tangential directions.**

The material properties used in the triangular block verification studies are the same as the graphite properties used for the prismatic block. These material properties are indicated in **Table 5-1**.

3, 5, 9, 11 and 13 2-D node models were set up. These node models consisted of a specific number of nodes for instance  $n$  nodes along the centre-line in the radial direction and three

equally spaced nodes in the tangential direction. These models were termed to be  $n \times 3$  node models. As an example, the five node model is a  $5 \times 3$  node model whereby the centreline along the radial direction has 5 nodes and the tangential direction has 3 nodes. The dimensions of the block on which the models were set up are the same as the dimensions of the one sixth segment of a VHTR (see chapter 5 ) apart from the height which is now fixed at 0.099 m.

A steady state pure conduction case is set on the models. Firstly, the models have fixed boundary temperatures conditions as illustrated in **Figure 4-21**:

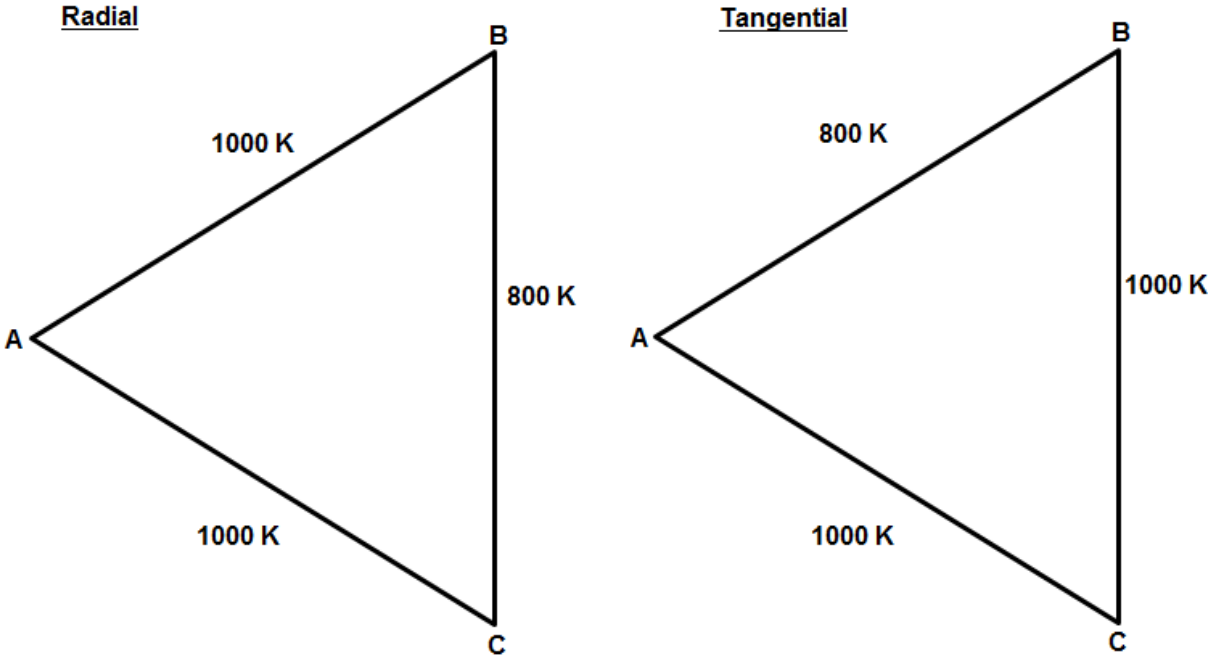


**Figure 4-21: Boundary temperature conditions for Flownex models.**

**4.5.1.1 Radial direction**

**Figure 4-21** (a) illustrates heat conduction which is dominant in the radial direction. The Flownex models were simulated with the above temperature boundary conditions. **Figure 4-22** illustrates a layout for the simple 3 node model heat transfer network; the other 4 models were simulated in a similar manner.

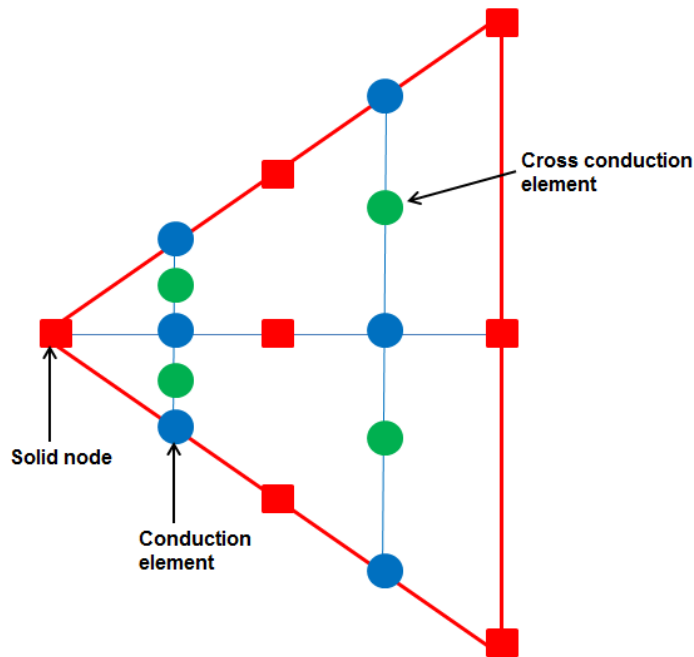


**Figure 4-22: Schematic layout for the simple 3 × 3 node model heat transfer network.**

The temperatures obtained at the centreline solid nodes for all the models are displayed **Table 4-1**. The red coloured temperatures indicate the centre solid node temperatures for the model.

**Table 4-1: Centreline temperatures for the different node models of heat conduction dominantly in the radial direction.**

Node Number	3 - Node Temperature (K)	5 - Node Temperature (K)	9 - Node Temperature (K)	11 - Node Temperature (K)	13 - Node Temperature (K)
0	1000	1000	1000	1000	1000
1	958.229435	998.4705144	999.9071754	999.9608255	999.9793434
2	800	980.4491345	998.8134558	999.4992461	999.7499693
3		911.623773	994.6364372	997.7364305	998.8809063
4		800	984.2605711	993.3575327	996.7273537
5			963.6443289	984.6569176	992.4527886
6			927.8826259	969.5645058	985.0419055
7			871.2515334	945.6646438	973.3098812
8			800	910.2106776	955.9095288
9				860.1367424	931.3370823
10				800	897.9370284
11					853.9062358
12					800

Considering the centre nodes, the 11 node model has been chosen to be the master model. This is because the temperatures are no longer changing significantly. This is graphically illustrated in **Figure 4-23**. The 13 node model indicates that further discretisation will result in very small changes on the centre node. The 11 node model was therefore used as a comparison with the STAR-CCM+ models.

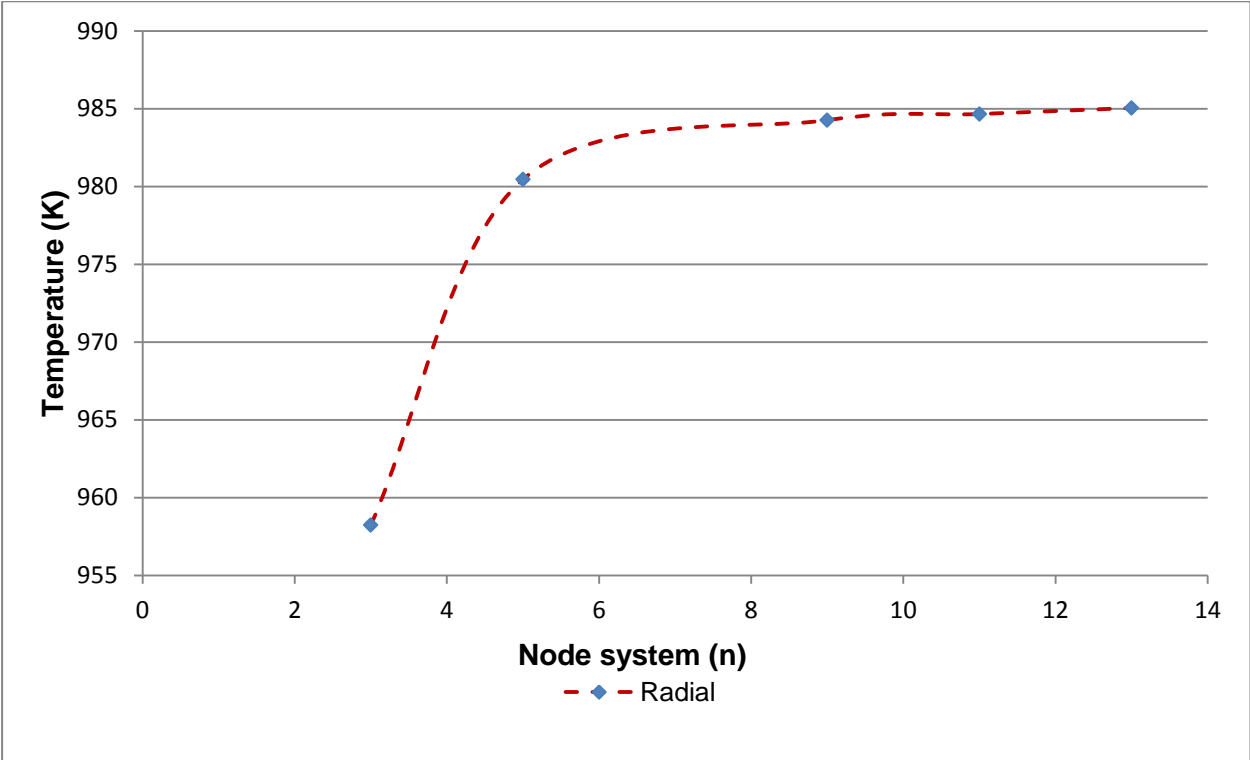


**Figure 4-23: Comparison of n node systems in the radial direction.**

**4.5.1.2 Tangential direction**

**Figure 4-21(b)** illustrates heat conduction which is dominant in the tangential direction. The Flownex models were simulated with the stated temperature boundary conditions. **Table 4-2** indicates the centreline temperatures for all the node models.

**Table 4-2: Centreline temperatures for the different node models of heat conduction dominantly in the tangential direction.**

Node Number	3 - Node Temperature (K)	5 - Node Temperature (K)	9 - Node Temperature (K)	11 - Node Temperature (K)	13 - Node Temperature(K)
0	900	900	900	900	900
1	920.8852825	900.7647428	900.0464123	900.0195873	871.8762777
2	1000	909.7754328	900.5932721	900.250377	897.2344315
3		944.1881135	902.6817814	901.1317847	900.1723297
4		1000	907.8697145	903.3212336	901.6501484
5			918.1778355	907.6715412	903.8324737
6			936.0586871	915.2177471	907.4895163
7			964.3742333	927.1676781	913.2618691
8			1000	944.8946612	921.8275326
9				969.9316288	933.9313626
10				1000	950.3902675
11					972.0932057
12					1000

Also considering the centre nodes, the 11 node model was chosen to be the master model. The same reasoning for the radial discretisation is still valid for the tangential discretisation. **Figure 4-24** illustrates the small change between the 11 node and 13 node models, which justifies the selection of the 11 node model.

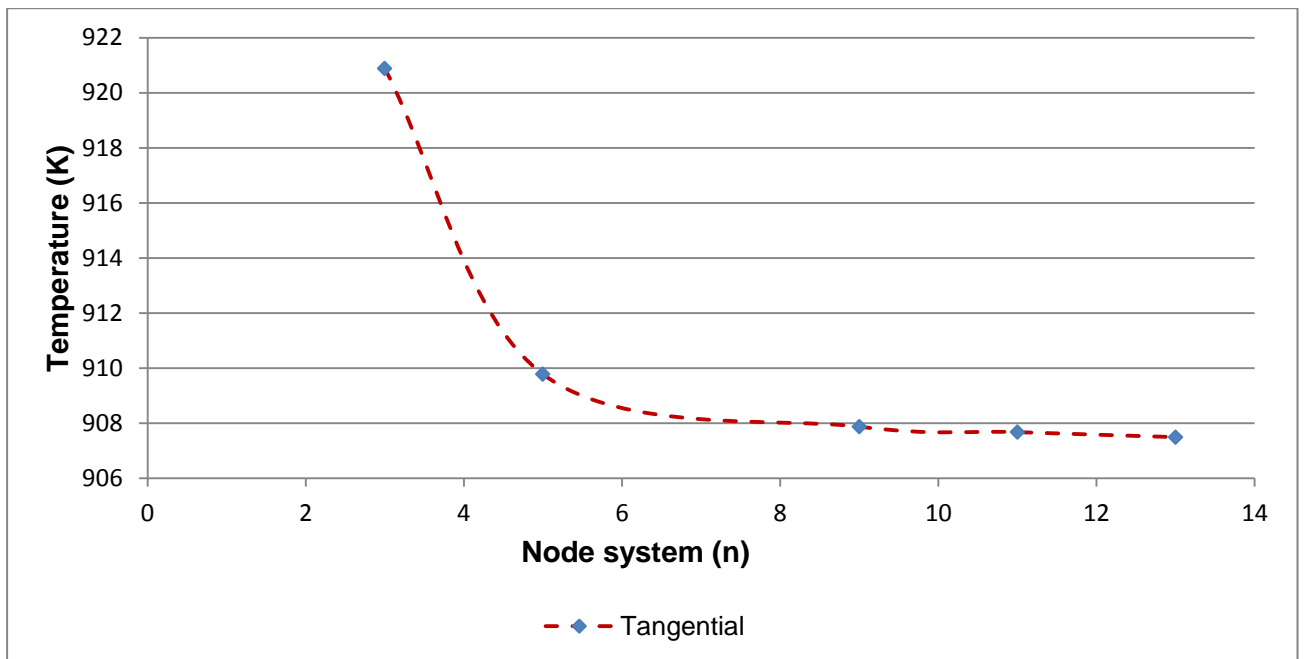


**Figure 4-24: Comparison of n node systems in the tangential direction.**

#### 4.5.2 Case 1

In the first case, three boundary temperature conditions are specified as indicated in **Figure 4-21**. Pure heat conduction is investigated in two dimensions i.e. radial and tangential directions.

The results from the two chosen models in Flownex from section **4.5.1.1** and **4.5.1.2** will be compared with the results from STAR-CCM+.

In STAR-CCM+, the same block with the same dimensions and material properties was simulated. The polyhedral mesher and surface remesher were the chosen grid models. A 2 mm base size of the grid was implemented. A line probe which was placed at the centreline (from vertex A to the midpoint of BC) is used to measure the temperatures along the centreline. **Figure 4-25** shows the modelled block in STAR-CCM+ and the meshed cells.

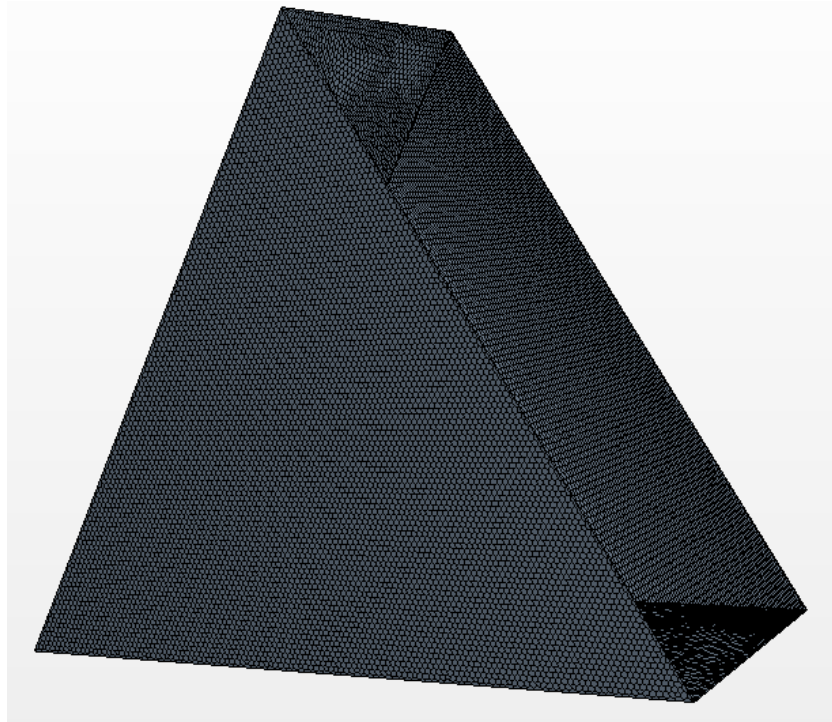


**Figure 4-25: STAR-CCM+ triangular block model and the meshed cells.**

#### **4.5.2.1 Results and discussion**

##### **4.5.2.1.1 Comparison between the $11 \times 5$ , $11 \times 3$ and STAR-CCM+ models in the radial and tangential directions**

An  $11 \times 5$  Flownex model was also chosen to be compared against the  $11 \times 3$  Flownex model. The  $11 \times 5$  model is an  $11 \times 3$  version which has been further discretised in the tangential direction. These two models are compared against the STAR-CCM+ model. **Figure 4-26** shows the results obtained in the radial direction.

From **Figure 4-26**, the  $11 \times 5$  Flownex model is in better agreement with the STAR-CCM+ model compared to the  $11 \times 3$  model. Therefore in the radial direction, the  $11 \times 5$  model will be utilised.

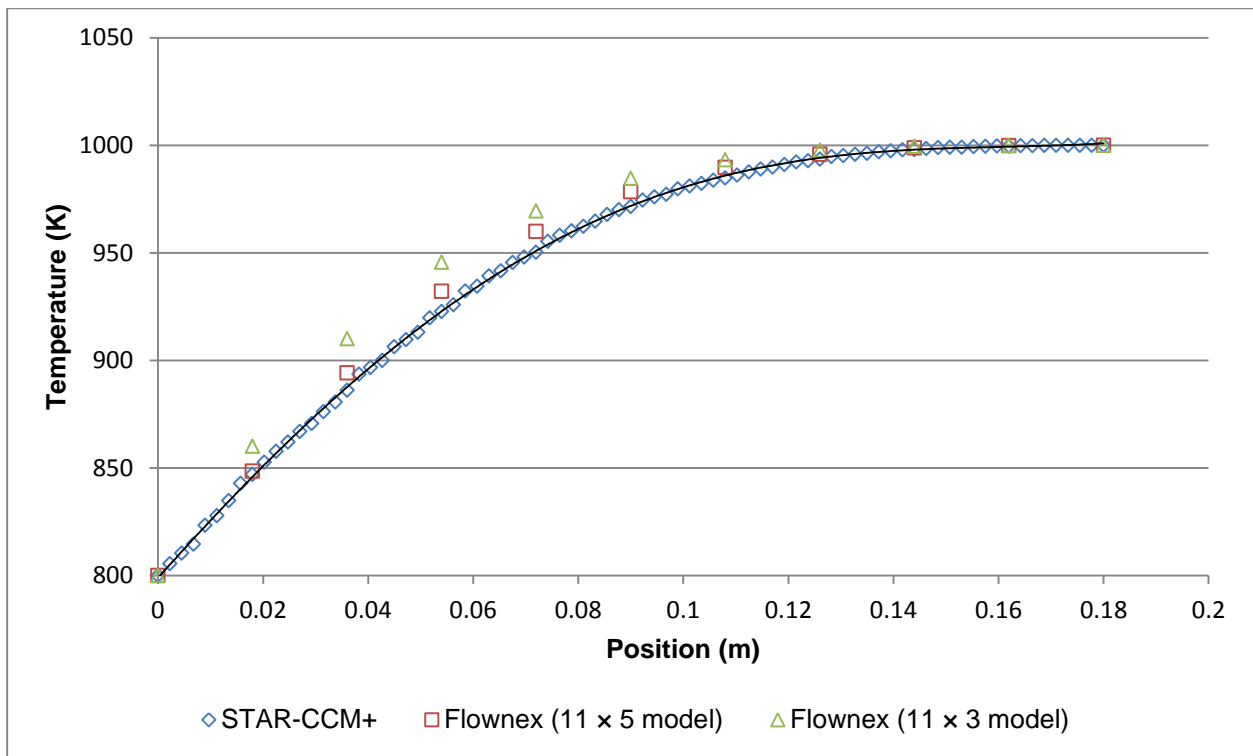


**Figure 4-26: Comparison between the 11 x 3, 11 x 5 and STAR-CCM+ models in the radial direction.**

**Figure 4-27** indicates the comparison between the three models in the tangential direction. The 11 x 5 model is also in better agreement with the STAR-CCM+ model in the tangential direction. Therefore the 11 x 5 model will also be utilised in the tangential direction.

The STAR-CCM+ model have some scattered points towards the 0.18 m position. This is because there is a steep temperature gradient near the vertex A and STAR-CCM+ does not interpolate along the line probe but rather extracts the constant temperature values associated with the cells in which the line probe points falls.

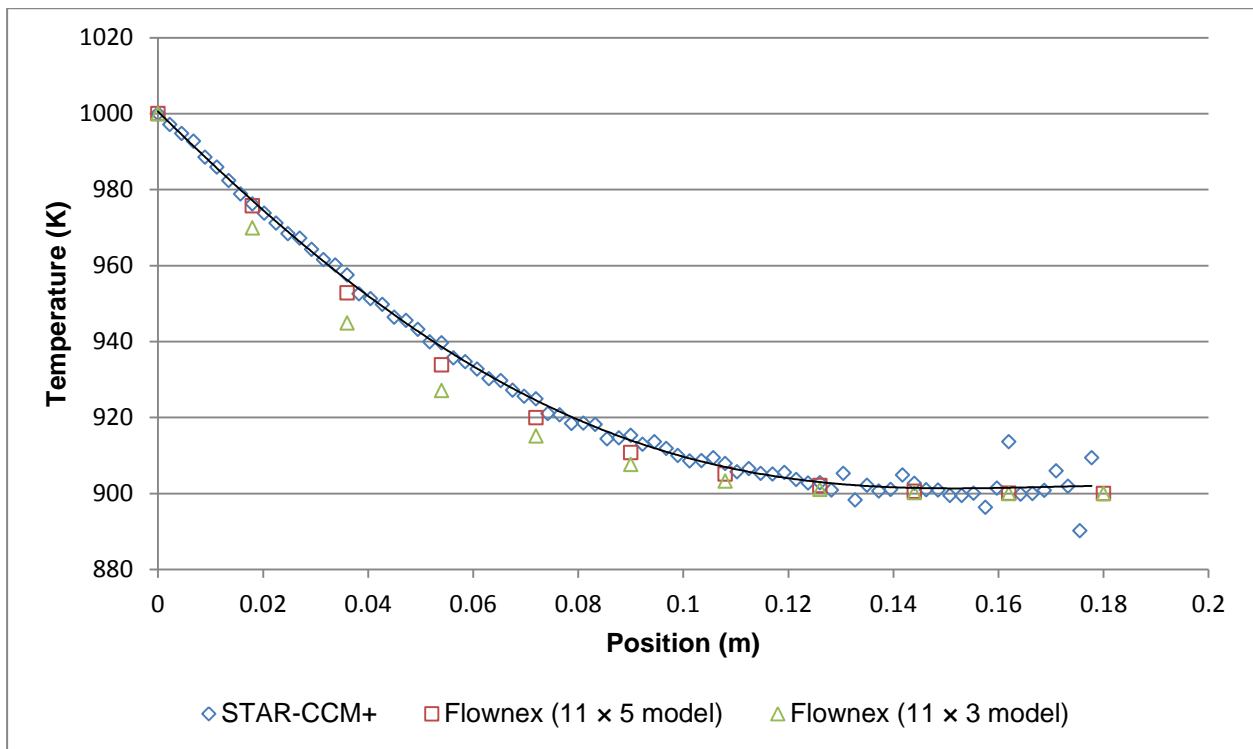


**Figure 4-27: Comparison between the 11 x 5, 11 x 3 and STAR-CCM+ models in the tangential direction.**

#### 4.5.2.1.2 Comparison between the 11 x 5 and STAR-CCM+ models in the radial and tangential directions with 800 K and 900 K vertex temperatures

It should be noted that in Flownex, two vertex nodes are shared nodes. Zooming into **Figure 4-21 (a)**, vertices B and C are given the average values of the two boundary planes where they intersect. As a result vertices B and C are given the values of 900 K each. The same phenomenon is observed in **Figure 4-21 (b)**. The effect of the boundary values specified at the vertex nodes in Flownex will be investigated as well. A comparison of specifying 800 K boundary values at the vertex nodes versus specifying averaged (900 K) boundary values at the vertex nodes was conducted against the STAR-CCM+ model. In STAR-CCM+, this problem is not encountered since the boundary values for the boundaries are specified on the surfaces of the boundary cells unlike in Flownex where the boundary values are specified on the nodes. This comparison was conducted for both the radial and tangential directions.

Since the 11 x 5 model is now the master model in Flownex, it will be compared against the STAR-CCM+ model in both directions of dominant heat conduction. **Figure 4-28** and **Figure 4-29** show the comparisons in Flownex with the 800 K vertex corners against the STAR-CCM+ model in the radial and tangential directions respectively.

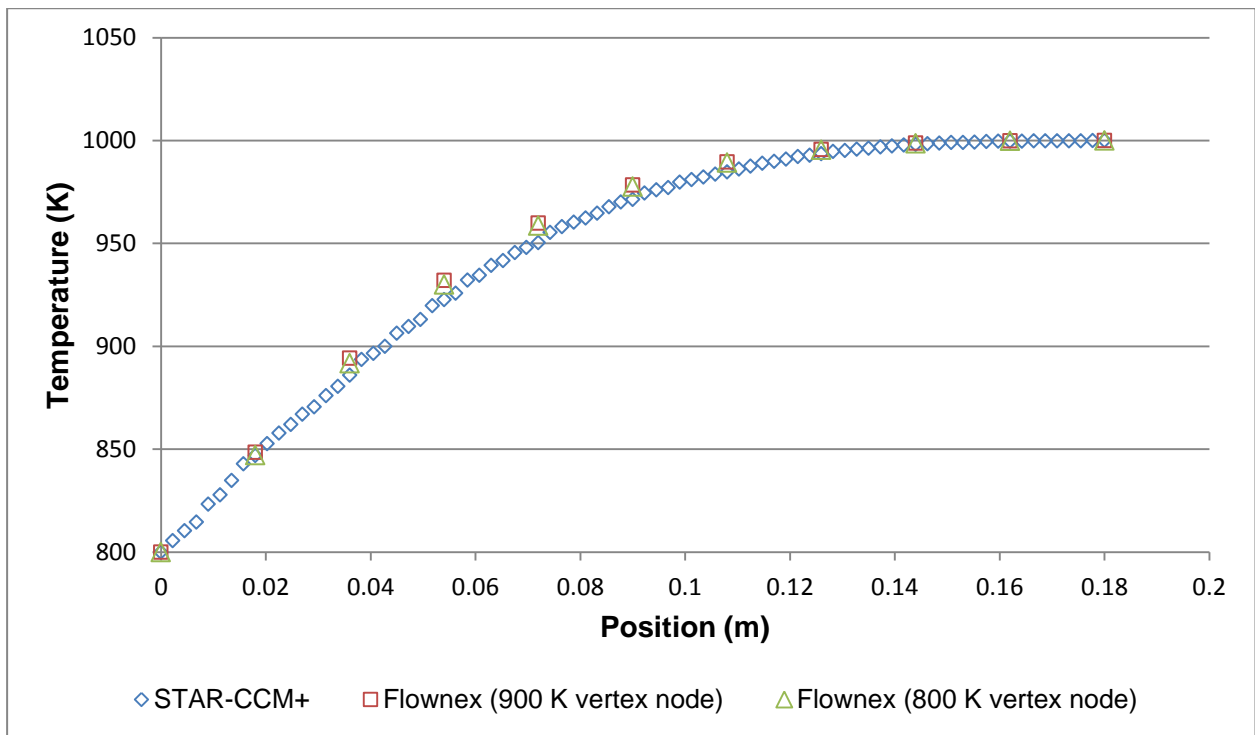


**Figure 4-28: Comparison between the 800 K and 900 K vertex Flownex models with the STAR-CCM+ model in the radial direction.**

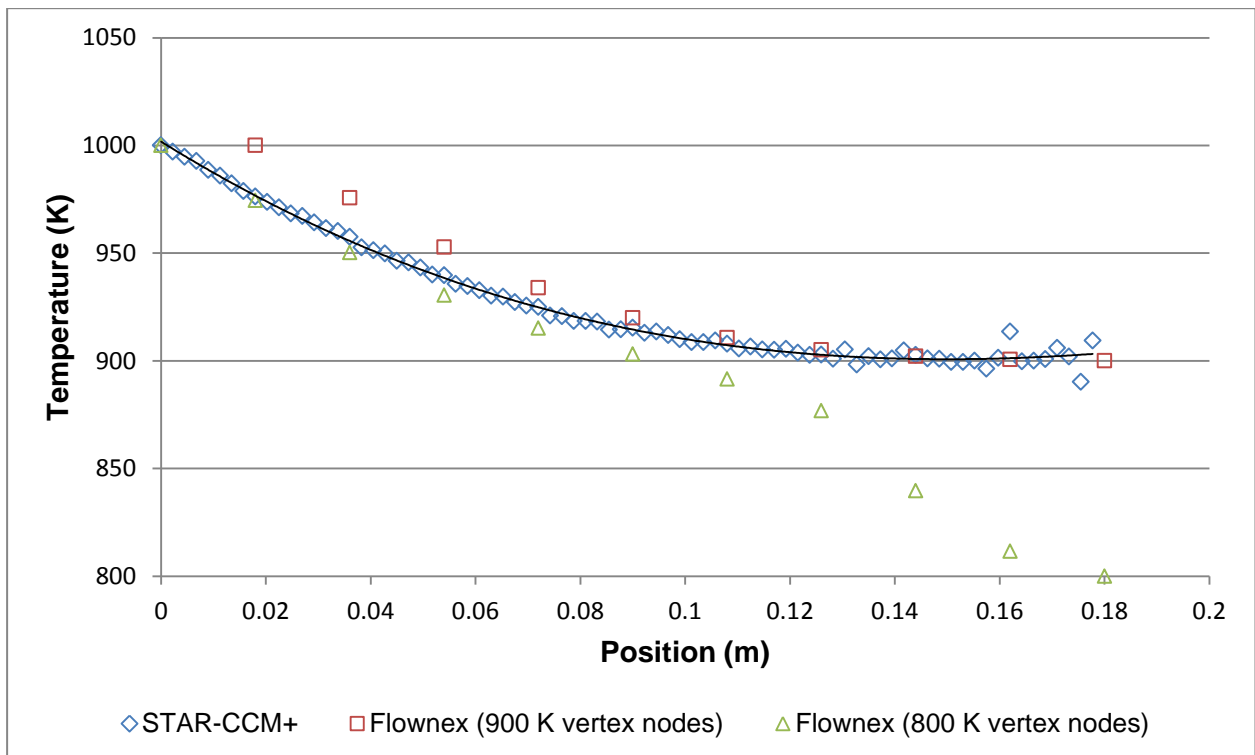


**Figure 4-29: Comparison between the 800 K and 900 K vertex Flownex models with the STAR-CCM+ model in the tangential direction.**

From **Figure 4-28** there is no difference between using 800 K or 900 K vertex node temperatures. However in the tangential direction (**Figure 4-29**), there is a huge difference, the 800 K vertex node is out of range from the 0.1 m position to 0.18 m. This is because the node point at A in the tangential case is a singular node with respect to the boundary conditions. Specifying a boundary value of 900 K is more in accordance with the value of 900 K that will be obtained by STAR-CCM+ at the centre of the cell in the corner at A.

Therefore the 900 K vertex temperatures were utilised for both the radial and tangential directions.

### 4.5.3 Case 2

In the second case, a transient analysis was conducted on the conditions stated in case 1. The block was first maintained at a uniform temperature of 1000 K i.e. all sides having boundary temperatures of 1000 K. In **Figure 4-21** (a) the temperature of the boundary BC was dropped to 800 K at  $t = 0$  seconds. In **Figure 4-21** (b) the temperature of the boundary AB was also dropped to 800 K at  $t = 0$  seconds. The Fourier number as explained in section 3.5.2 is an indication of the propagation of heat transfer through a body before and after a step change is instigated. A maximum time step size of 4 seconds was obtained using the Fourier number relation. This calculation is indicated in Appendix B-4.

Even though a time step of 4 seconds will still give a stable and accurate enough solution, in this study a time step of 1 second was chosen. This is because as the time step decreases, the resolution time dependant phenomena becomes better and therefore the solution can become more accurate.

The transient analysis was monitored at the central node within the block. The central position in the block will be located at the point (0.104, 0.06, 0.05) m. However in Flownex this position lies between the third and fourth node from the boundary BC. Therefore in-order to get round this obstacle one has to either interpolate the values in Flownex or use the nearest node readings. In this study the nearest node readings were implemented, and in Flownex the fourth node from the boundary BC along the centreline was monitored. The coordinates of this node is (0.104, 0.054, 0.05) m. This point was also monitored in STAR-CCM+.

#### 4.5.3.1 Results and discussion

**Figure 4-30** displays the variation with time in the temperature at the selected node as a result of dropping the temperature of boundary BC from 1000 K to 800 K.

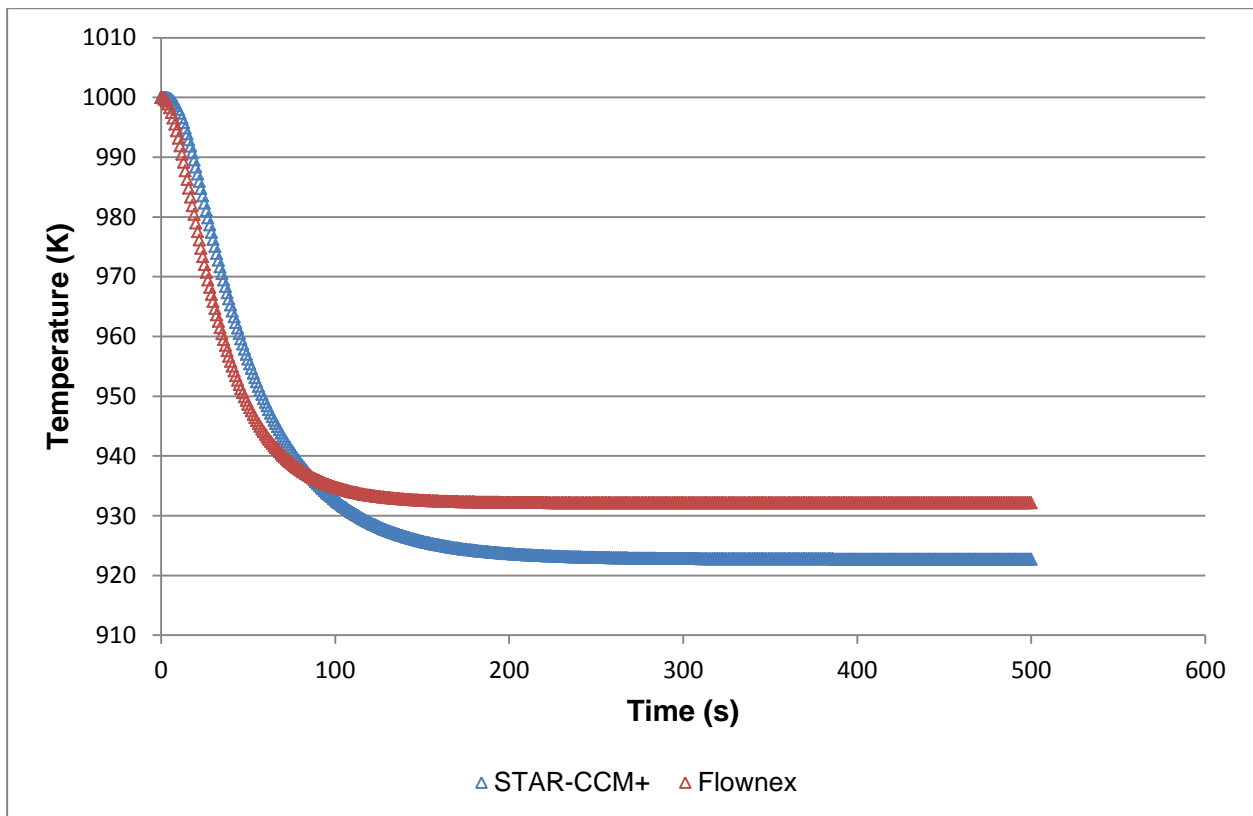


**Figure 4-30: Case 2 comparison between STAR-CCM+ and FLOWNEX at the centroid after dropping the temperature at the boundary BC.**

The average percentage difference between the two codes is 0.84 %. Therefore the agreement between the two transient temperature profiles is good and the final values are in agreement with the corresponding steady state values at the same positions in **Figure 4-28**

In a similar manner, **Figure 4-31** displays the results obtained after dropping the temperature at boundary surface AB from 1000 K to 800 K. The average percentage difference between the two codes is 0.89 % and therefore the comparison good.

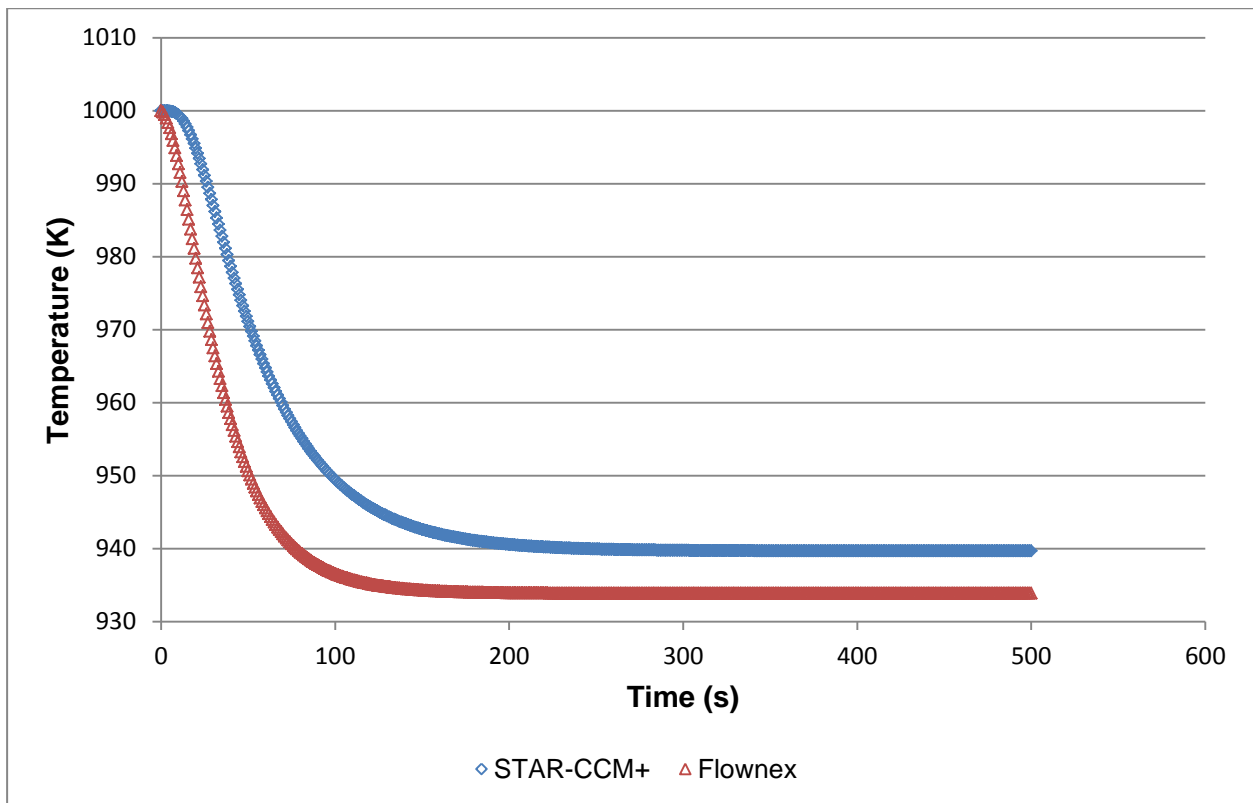


**Figure 4-31: Case 2 comparison between STAR-CCM+ and Flownex at the centroid after dropping the temperature at the boundary AB.**

#### 4.5.4 Case 3

Case 3 consists of a steady state and a transient analysis. In the steady state, the whole triangular block was maintained at a temperature of 1000 K and a uniform volumetric heat source was also added. A heat source of 10 kW was uniformly distributed over the triangular prism. For the steady state case, the temperatures along the centreline (from vertex A to BC) were analysed and for the transient analysis the centroid with the coordinates stated in case 2 was utilised.

In Flownex, the heat source was uniformly distributed in the nodes and in STAR-CCM+, a uniform volumetric heat source of  $5.4 \text{ MW/m}^3$  was used.

##### 4.5.4.1 Steady state results and discussion

**Figure 4-32** shows the results for the steady state simulation.

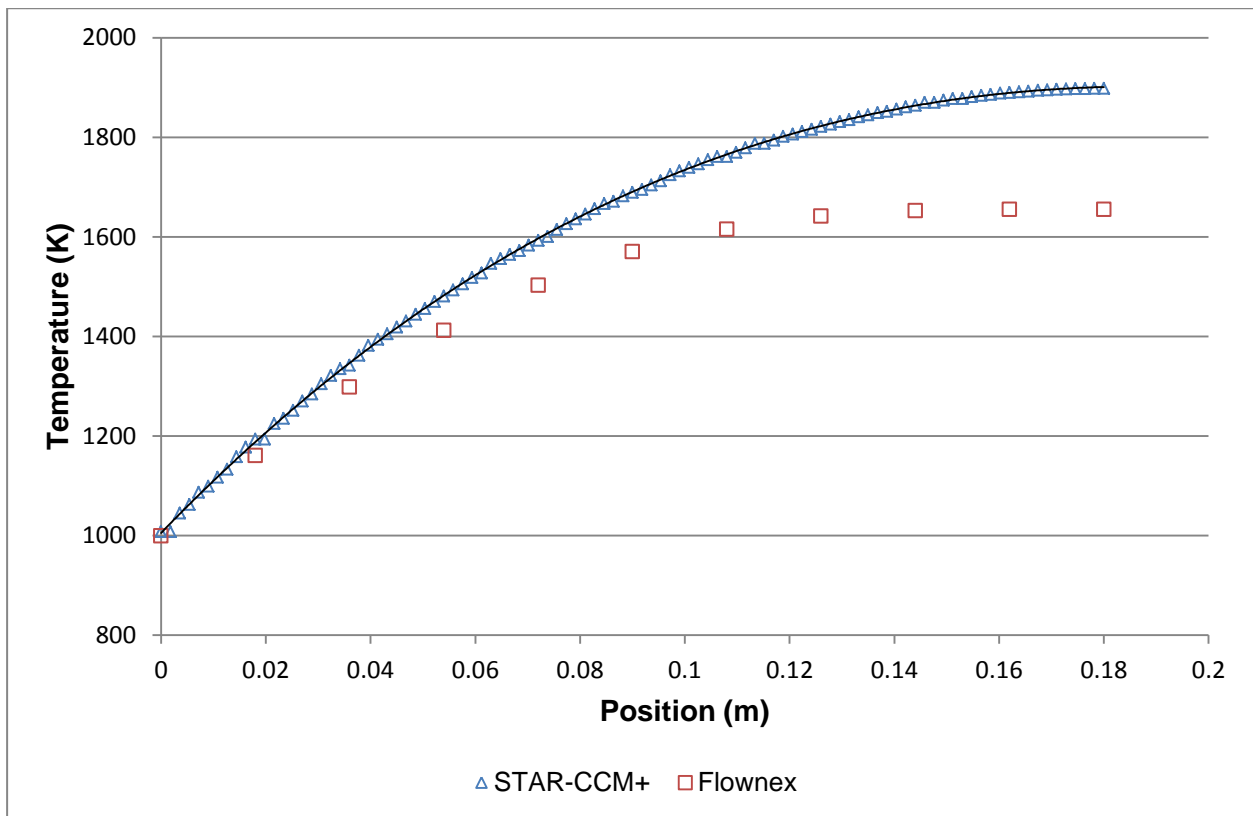


**Figure 4-32: Case 3 comparison between STAR-CCM+ and Flownex for a steady state.**

The comparison between the two codes is good from 0 m up until 0.06 m. From 0.06 m to 0.18 m, the Flownex results appear to reach an asymptotic value sooner. The average percentage difference between the two codes is 3.83 %.

This incorrect result in Flownex may be attributed by the non-orthogonality of the network. Flownex assumes the conduction network to be orthogonal and therefore does not make provision for non-orthogonal correction terms (see **Figure 4-2** and **Figure 4-22**). This needs to be studied in detail.

#### 4.5.4.2 Transient results and discussion

For the transient analysis, the block was first maintained at a constant temperature of 1000 K. At time  $t = 0$  seconds the uniform heat source was increased from 0 kW to 10 kW. The temperatures at the centroid were monitored and indicated in **Figure 4-33**.

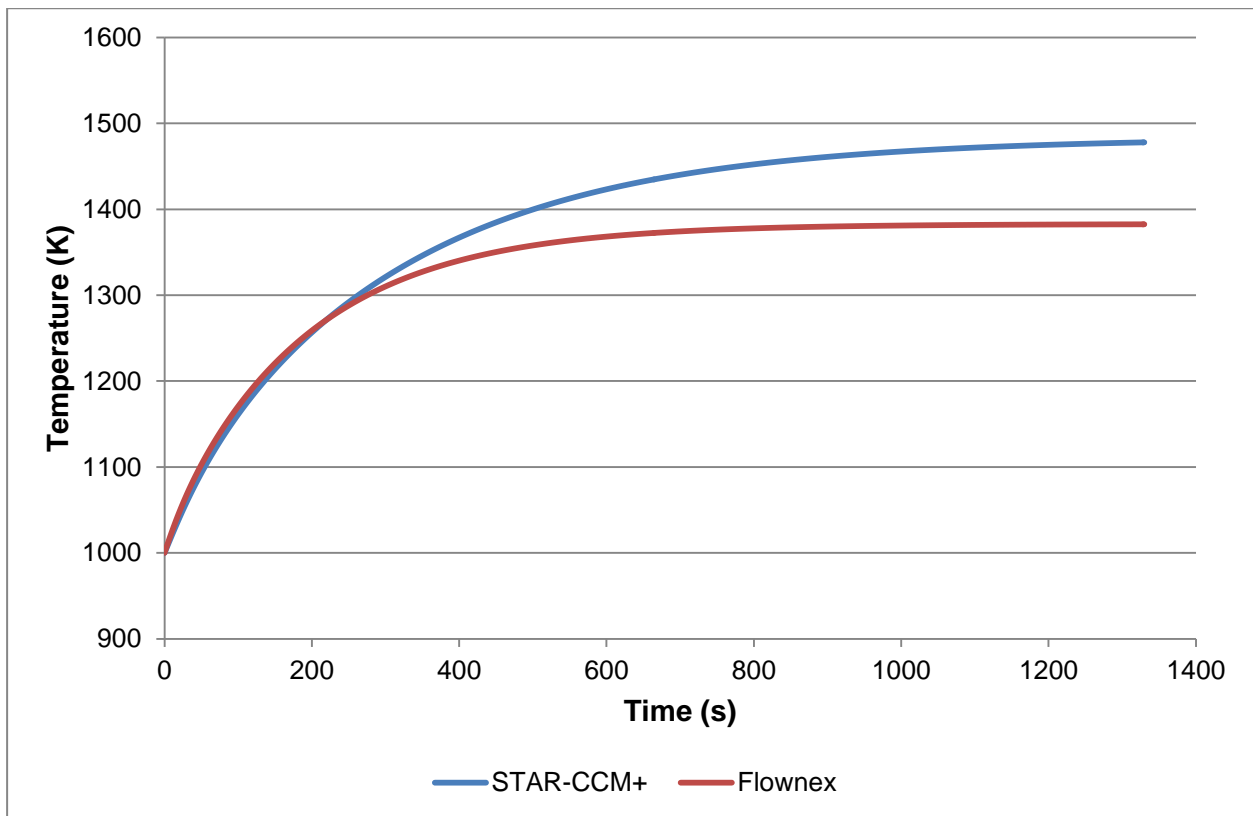


**Figure 4-33: Case 3 comparison between STAR-CCM+ and Flownex at the centroid after increasing the heat source.**

**Figure 4-33** also shows that the Flownex values after initially following the STAR-CCM+ values tends to reach the steady state condition quicker compared to STAR-CCM+.

#### 4.5.5 Conclusion

From the above first two detailed cases, it can be concluded that Flownex can be used to develop an integrated network model of a prismatic fuel block despite the discrepancies in the third case because a volumetric heat source is present in the actual prismatic block. A study will have to be conducted on how to address the problem encountered in case 3.

#### 4.6 Summary

Chapter four dealt with the capabilities of Flownex particularly in comparison to the CFD code, STAR-CCM+. The different elements in Flownex that are relevant in this study were presented. Five simple test cases were modelled and simulated in Flownex and STAR-CCM+. The purpose of these five simple test cases was not to check for grid dependence. Time step dependence study was conducted and dealt with the validity of the effect of the Fourier and Biot numbers on change in time. These simple cases resemble events that can occur in an HTR.

Steady state results and transient results obtained using the two codes for each case were compared. From the steady state and transient results for each case, it is clear that the two codes are in good agreement and therefore it is concluded that Flownex gives accurate results for spatial discretisation in the axial direction. Flownex was used to model the heat transfer in a prismatic block of an HTR by applying the methodology outlined in the next chapter.

## 5. PRISMATIC BLOCK MODELLING METHODOLOGY AND RESULTS

### 5.1 Introduction

In this chapter the VHTR will be described with particular emphasis on the PMR200 reactor. The core components particularly the fuel assemblies and the flow paths in the PMR200 reactor will be discussed. The modelling approach towards building a thermal-fluid network of a standard fuel block will be reviewed. Since this project mainly focuses on building a thermal-fluid network model using Flownex, emphasis will also be placed on the components in Flownex used to build this network. A comparison of results obtained with Flownex and STAR-CCM+ for a one sixth block will be conducted.

### 5.2 Description of prismatic HTR core design

A VHTR is a graphite moderated reactor and helium gas is used as the coolant. A PMR200 reactor core was selected in this study as a representative of a prismatic design. **Figure 5-1** below illustrates the core internals structure together with the nominal flow in a PMR200.

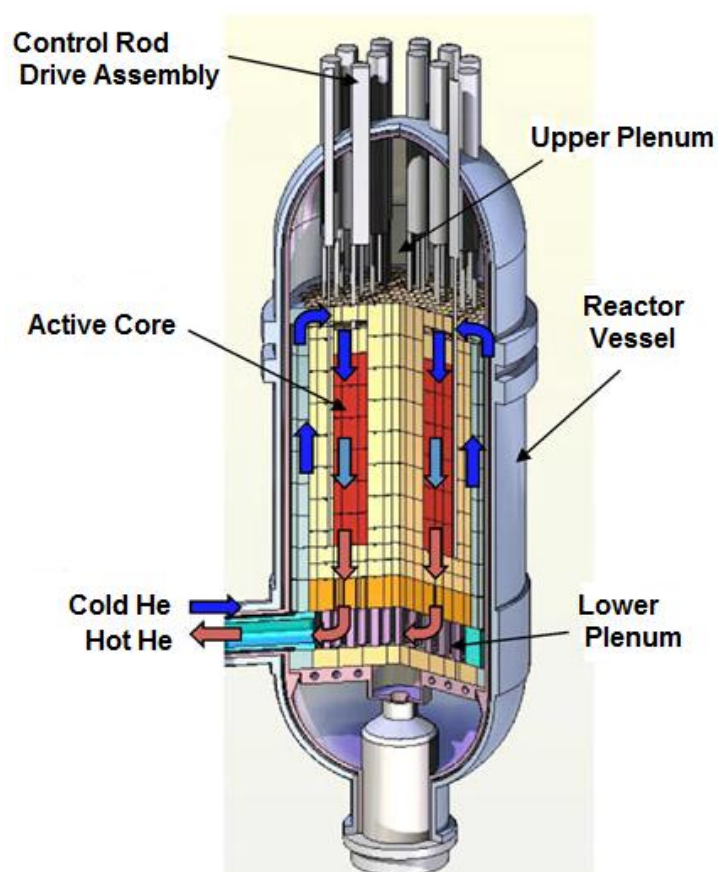
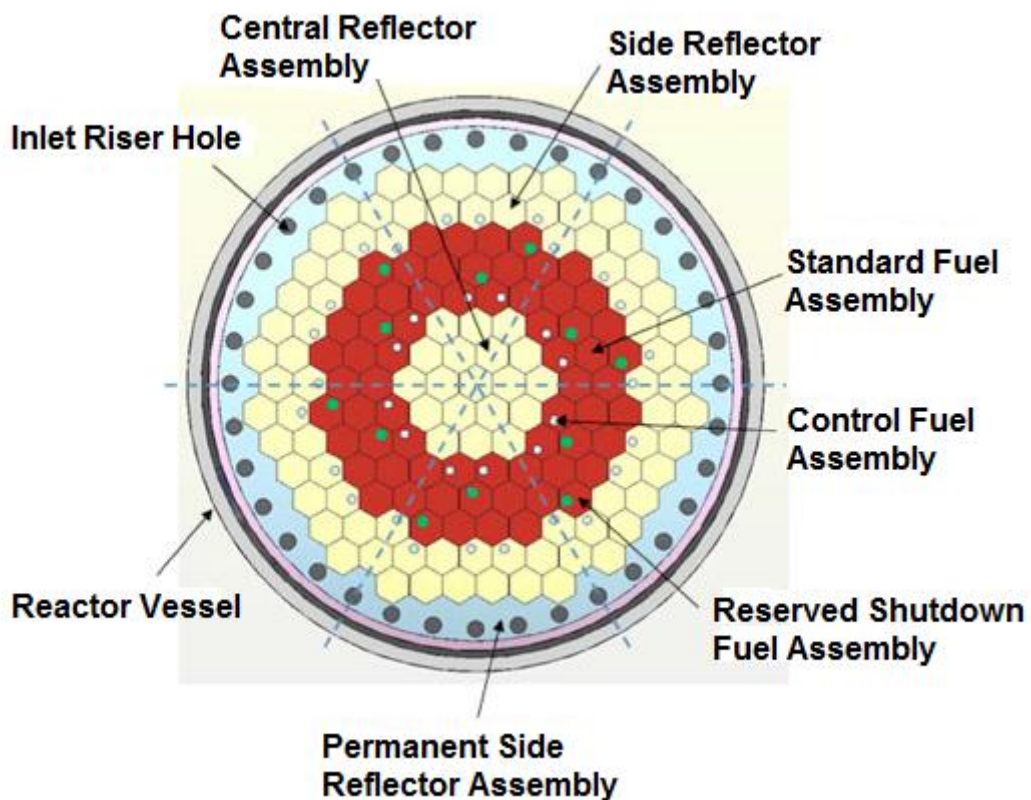


Figure 5-1: PMR200 core internal structure and nominal flow (Tak *et al.*, 2012).

Cold helium at a nominal temperature of 490 °C enters the reactor pressure vessel through the outer side of the cross duct, flows upward through the inlet riser holes which are positioned between the reactor pressure vessel and the core barrel, and reverses its direction at the upper plenum. The helium now flows downward in the fuel assemblies, cooling the fuel blocks from the top to the bottom. It joins at the lower plenum at a nominal temperature of 950 °C, and exits the reactor pressure vessel through the inner side of the cross duct (Sato *et al.*, 2010).

The active core comprises of a cluster of prismatic graphite fuel blocks. **Figure 5-2** below shows the core radial layout of the PMR200.



**Figure 5-2: Core radial layout (Tak *et al.*, 2012).**

The ring-shaped active core is composed of sixty-six fuel assemblies enclosed by the central and side reflector assemblies. The active part of the fuel assembly of the PMR200 comprises of ten fuel blocks vertically stacked on top of each other (Tak *et al.*, 2012).

### 5.2.1 Fuel elements

There are three types of fuel elements: standard fuel blocks, reserved shutdown fuel blocks and control fuel blocks (Tak *et al.*, 2012). The fuel elements are identical to the Fort St. Vrain HTGR elements in shape and size i.e. right hexagonal prisms. The fuel holes and the coolant channels are equidistant from each other throughout the fuel element (Ortensi *et al.*, 2013).

The standard fuel element has 210 blind fissures for the fuel compacts and 108 channels for the flow of the helium coolant. Six burnable poison rods manufactured from boron carbide ( $B_4C$ ) are positioned at the corners of the hexagonal fuel element and six more are located on the interior of the fuel element (Tak *et al.*, 2012). The fuel holes and coolant channels are arranged in a systematic triangular cluster whereby each coolant channel is surrounded by six fuel holes (Ortensi *et al.*, 2013). The hexagonal fuel elements are dowelled together to maintain alignment of the coolant channels between the vertically stacked fuel elements. A fuel handling hole located at the centre of the fuel element has a diameter of 3.5 cm and extends to a third down the height of the fuel element (Ortensi *et al.*, 2013).

The structure and the geometry of the standard fuel element of a PMR200 is summarised below in **Figure 5-3**:

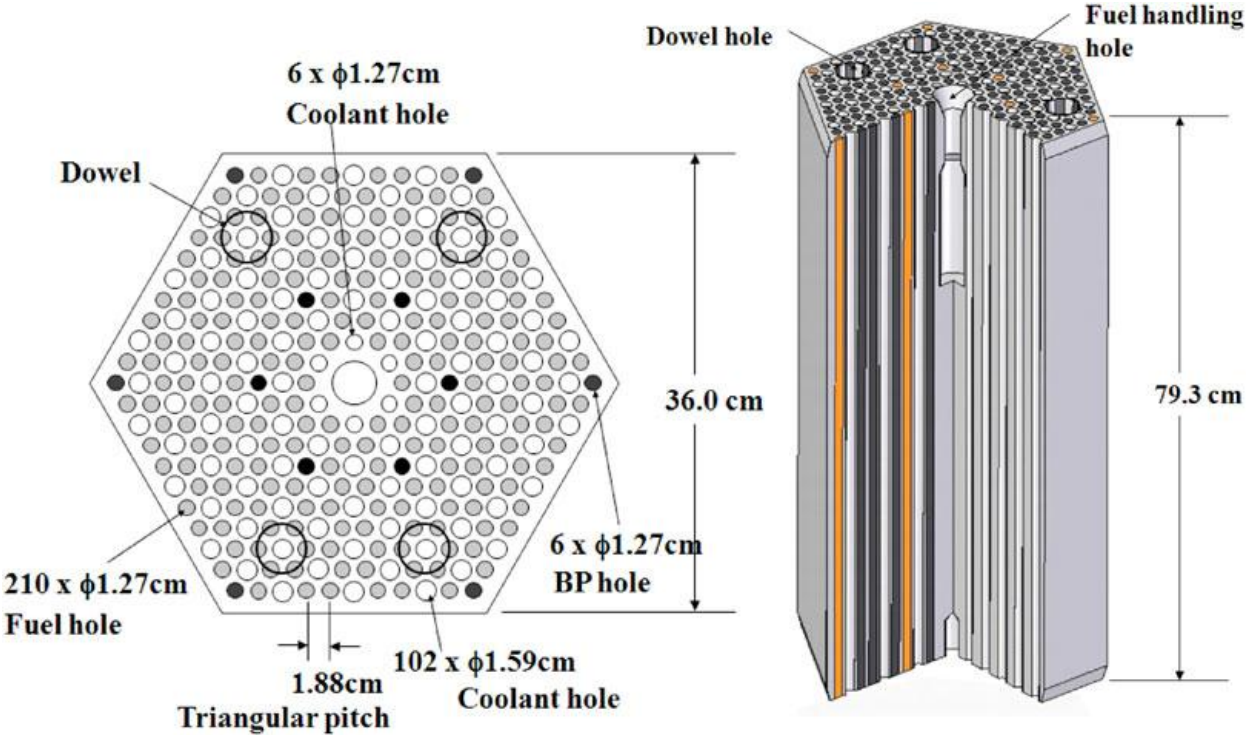


**Figure 5-3: Standard fuel element of PMR200 (Tak *et al.*, 2012).**

The reserved and shutdown fuel elements are similar to the standard fuel elements with an exception of the hole which will be occupied by the reserved shutdown rod or control rod (Ortensi *et al.*, 2013).

The structure and the geometry of the control or reserved shutdown fuel element is summarised below in **Figure 5-4**:

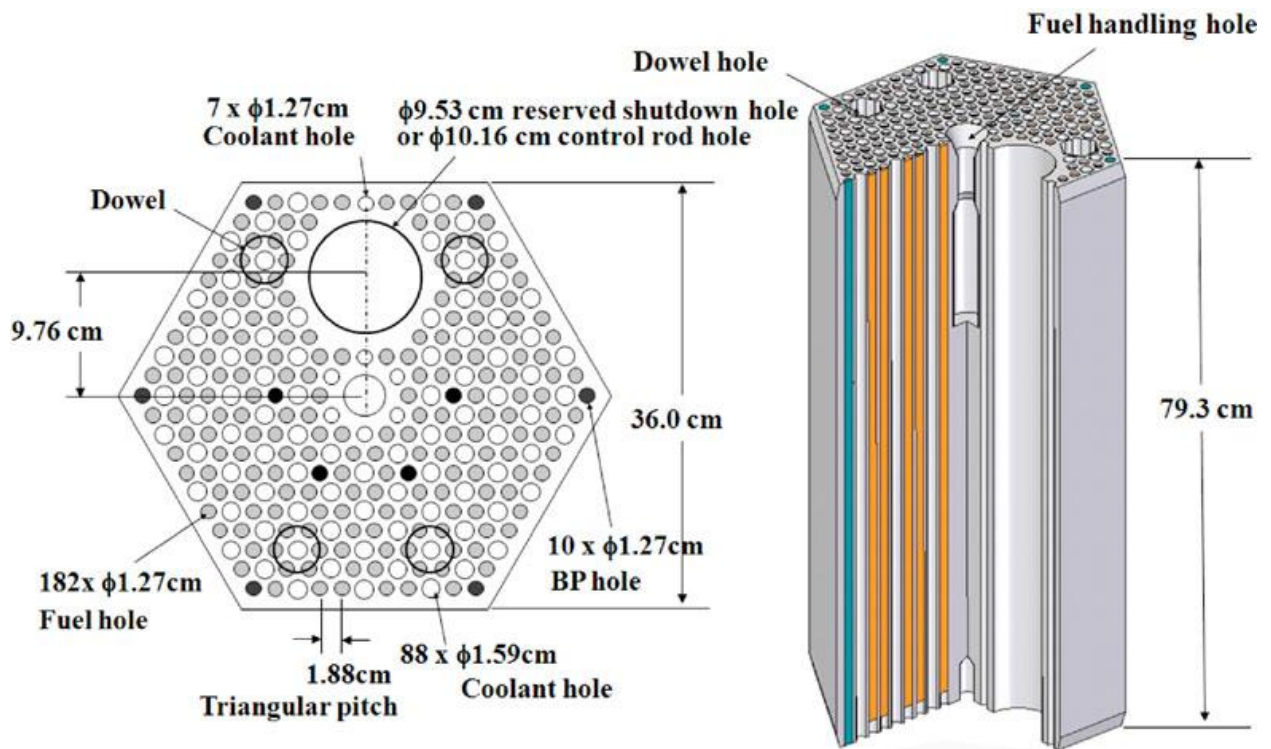


Figure 5-4: Control or reserved shutdown fuel element of PMR200 (Tak *et al.*, 2012).

### 5.3 Flow paths in an HTR

Since the graphite core internals are made up of stacks of hexagonal graphite blocks, several gaps are formed between neighbouring columns of fuel block elements, reflector blocks and permanent side reflector blocks or margins of coolant channels in permanent side reflector stacks (Nakano *et al.*, 2008). A great portion of the coolant flows in the coolant channels within the fuel element blocks and a small portion flows into these gaps without directly cooling the fuel element blocks. The latter flow is classified as the core bypass flow. Furthermore, the coolant also flows through interfacial gaps between two stacked blocks. This flow is demarcated to be the cross flow (Yoon *et al.*, 2012).

The cross gap has an impact on the coolant channel and the bypass gap; as a result it prompts a complex flow distribution in the core. The bypass gap fluctuates in accordance to the fuel cycle. This is due to the irradiation shrinkage and thermal expansion of the graphite block elements (Yoon *et al.*, 2012). **Figure 5-5** below demonstrates the flows paths in a prismatic HTR core.

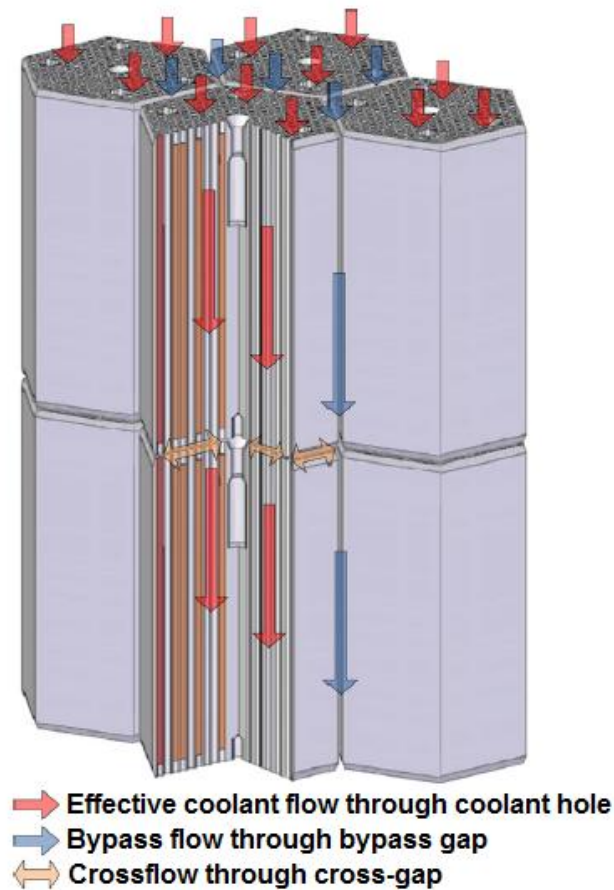


Figure 5-5: Flow paths in the prismatic HTR core (Yoon *et al.*, 2012).

## 5.4 Modelling Approach

In this section the modelling approaches used in Flownex and STAR-CCM+ will be discussed.

### 5.4.1 Flownex and the inputs

Flownex has already been described as a simulation software environment that models mass, momentum and heat transfer in thermal-fluid systems. The geometry as well and the direction of discretisation are very important when modelling in Flownex. These important aspects are discussed below in reference to a standard prismatic fuel element.

#### 5.4.1.1 Geometry and discretisation

In a prismatic fuel block, the solid geometry is very complex while the fluid channel geometry is simple. An approach to simplifying the geometry is to adopt a simple x y z cartesian coordinate system. Firstly a one sixth segment of a standard fuel block is isolated and analysed. This is indicated below:

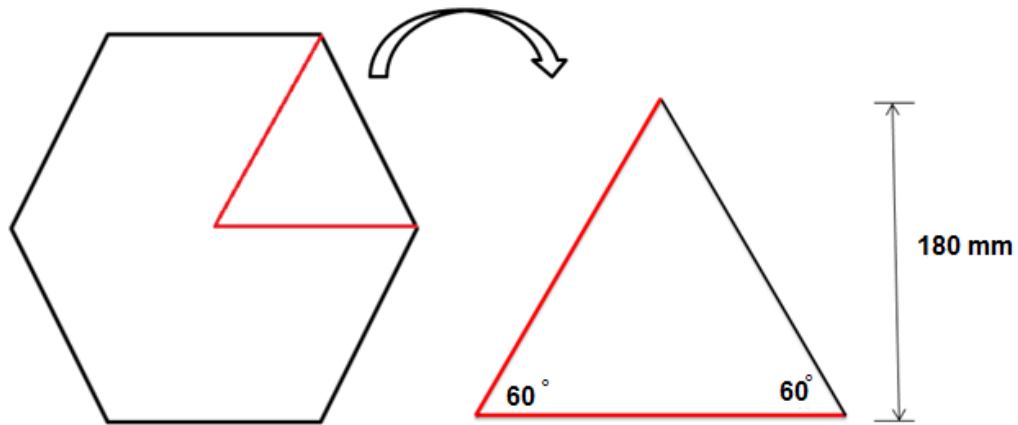


**Figure 5-6: Isolated one sixth segment of a prismatic block and its dimensions.**

Discretisation as discussed in chapter 3 is a process of dividing a continuum into small control volumes on a computational grid and solving on them. The one sixth segment is discretised in two directions, the radial and tangential directions as indicated in **Figure 4-20**.

#### **5.4.1.2 Network structure**

Solid cubical block and triangular blocks have been modelled in both Flownex and STAR-CCM+. A triangular block with perforations (coolant channels), which resembled a VHTR block is modelled in this chapter. The input data used in Flownex for all the elements is shown in Appendix **C4**. For the purposes of illustration, an illustrative simple  $3 \times 3$  node network structure with all the different elements built in Flownex is indicated in **Figure 5-8**. The heat transfer network for the transfer of heat from the fuel rod to the coolant channel is indicated in **Figure 5-7**. In **Figure 5-7**, the two yellow triangles represent the fuel and coolant channel wall nodes. The left yellow triangle represents the adjacent fuel node and the right yellow triangle represents the coolant channel wall node. The dotted line indicates where the solid (graphite) nodes are. The yellow circle, blue circle and the blue squares which are connected to the coolant wall channel node are the convection element, flow element and the flow nodes respectively. These are also indicated in **Figure 5-8** at the bypass gap.

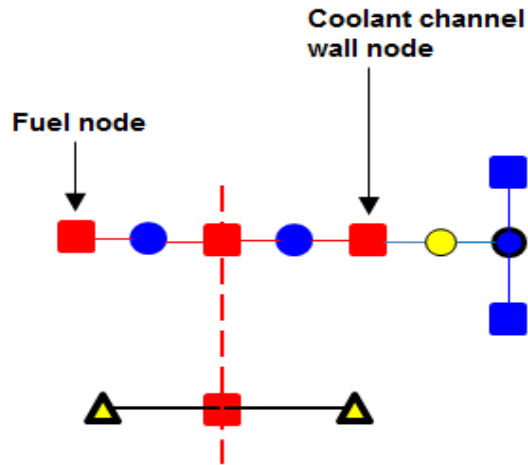


**Figure 5-7: Flownex network for heat transfer from the fuel rod surface to the coolant channel.**

Conduction of heat in the block in the radial direction is represented by the CHT elements while conduction of heat in the tangential direction is represented by the Cross CHT elements. A uniform volume heat source is applied at the fuel nodes. The heat transfer to the coolant channels takes place through convection and therefore was represented by the Convection elements. The convection elements are connected to a flow element in this case a pipe. The pipe is a representative of the coolant channels. The pipe element is connected to two flow nodes (inlet and outlet). Pressure, temperature and a mass source are specified at the two flow nodes. At the bypass gap, convection also takes place between the solid surface and the fluid.

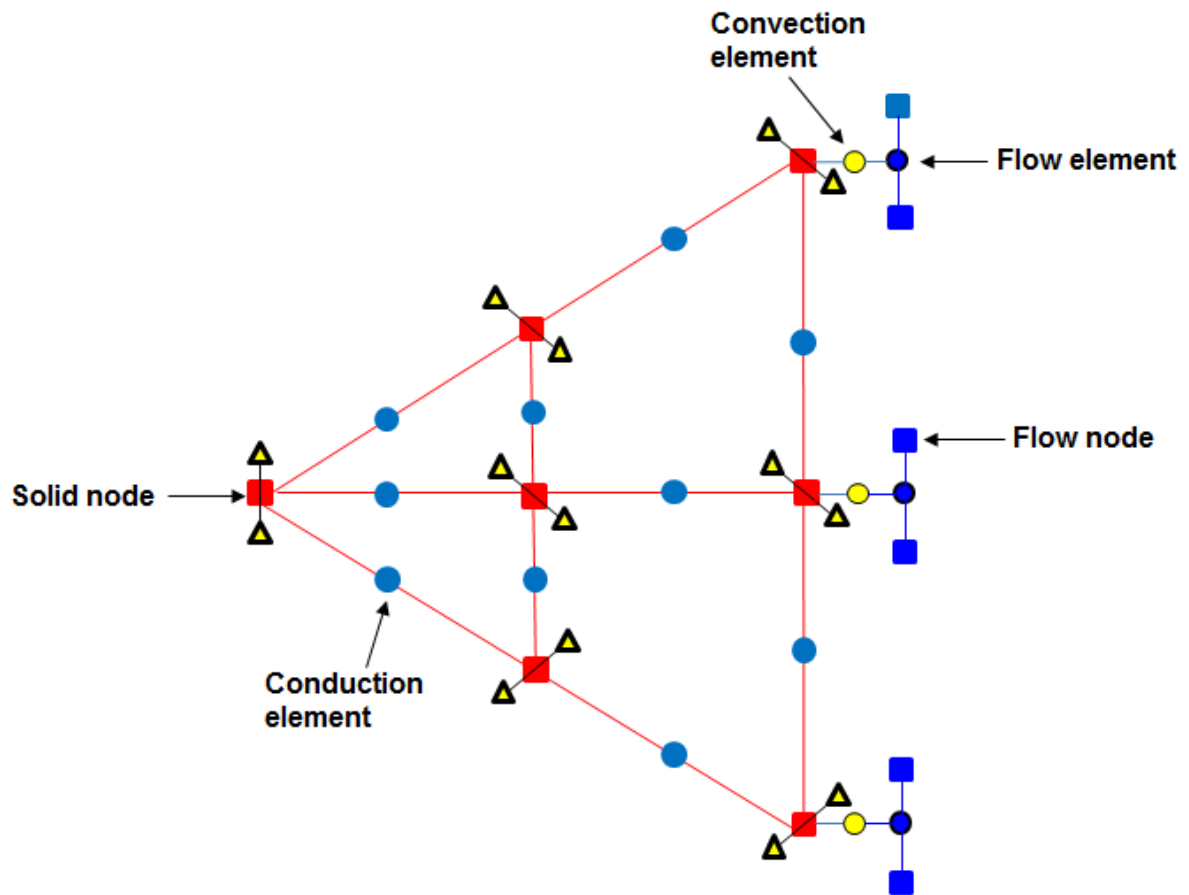


**Figure 5-8: An illustration layout of a heat transfer and flow network for a 3 × 3 node model.**

Therefore in brief, the solid temperatures are associated with the solid nodes, whilst the fluid enthalpies, densities and pressures are associated with the fluid nodes. The mass flow rates are associated with the flow elements.

#### **5.4.1.3 Material properties**

The moderator material used for the standard fuel block is IG-110 graphite (Boyce & El-Genk, 2013). The coolant as already mentioned in section 5.2 is helium. The graphite properties used in this study are indicated in **Table 5-1**:

**Table 5-1: Graphite properties used in Flownex.**

Material property	Value
Density (kg/m <sup>3</sup> )	1740
Axial conductivity (W/m.K)	52.7
Radial conductivity (W/m.K)	52.7
Specific heat (kJ/kg.K)	1.5

In order to simplify the problem, constant helium properties were calculated using the correlations given by Sage (2003). From the inlet and outlet temperatures of the coolant (refer to section 5.2), the average temperature is calculated (993.15 K) and incorporated in the correlations. The correlations are indicated in **Table 5-2**:

**Table 5-2 : Helium material property correlations.**

Material property	Value or correlation
Density (kg/m <sup>3</sup> )	$\frac{p}{R_g T}$
Specific heat (J/kg.K)	5197.6
Thermal conductivity (W/m.K)	$2.682 * 10^{-3} T^{0.71(1-2*10^{-9}p)}(1 + 1.123 * 10^{-8}p)$
Dynamic viscosity (Pa.s)	$3.674 * 10^{-7} \cdot T^{0.7}$

Where p for the thermal conductivity is the pressure in bars and p for the density is the pressure in Pascals.

In Flownex, additional properties have to be incorporated. **Table 5-3** shows all the helium constant input properties.

**Table 5-3: Helium properties used in Flownex.**

Material property	Value
Density (kg/m <sup>3</sup> )	3.3931
Specific heat (J/kg.K)	5197.6
Thermal conductivity (W/m.K)	0.36
Dynamic viscosity (Pa.s)	4.6 × 10 <sup>-5</sup>

The effective thermal conductivity is a phenomenological parameter that seeks to express the combined conductive properties of the various materials comprising the prismatic block, accounting also for the volume fractions as well as radiative effects.

In an HTR core under accident conditions such as loss of coolant and loss of cooling, heat transfer occur mainly by conduction and radiation (Yoon *et al.*, 2013). Despite the fact that the HTR has its own inherent safety features such as natural convective cooling of the core, an assumption that the natural convective cooling of the core is lost can be made. This leaves solid conduction within the graphite matrix, gas conduction and radiation in the coolant channels and bypass gap to be the main heat transfer mechanisms in the core (Yoon *et al.*, 2013). In a study conducted by Yoon *et al.* (2013); the heat conduction of the TRISO particle and fuel compact are solved by a 1-D equation while the heat conduction of the fuel block is solved by a 3-D equation. The complex structure of the fuel block was simplified by grouping all the coolant channels and fuel compacts separately, i.e. all coolant channels were grouped into one channel and the fuel compacts were modelled in the same way. In an accident scenario, the main heat transfer mechanism is conduction since the coolant will be stagnant.

The core effective thermal conductivity of the fuel block in the radial direction is given by equation (5-1):

$$\frac{k_{\text{eff,rad(1)}}}{k_s} = \frac{1 - \frac{\alpha_c(k_s - k_c)}{(k_s + k_c)} - \alpha_f \frac{(k_s - k_f)}{(k_s + k_f)}}{1 + \frac{\alpha_c(k_s - k_c)}{(k_s + k_c)} + \alpha_f \frac{(k_s - k_f)}{(k_s + k_f)}} \quad (5-1)$$

Where

$k_s$  = thermal conductivity of the graphite block,

$k_{\text{eff,rad}(1)}$  = effective thermal conductivity of the fuel block in the radial direction,

$\alpha_C$  = volume fraction of the coolant channels,

$\alpha_f$  = volume fraction of the fuel compacts,

$k_C$  = thermal conductivity of the coolant channel and

$k_f$  = thermal conductivity of the fuel compact

The axial conductivity which is parallel conduction is given by equation **(5-2)**:

$$k_{\text{eff,axial}(1)} = k_S + \alpha_C(k_C - k_S) + \alpha_f(k_f - k_S) \quad \text{(5-2)}$$

Where  $k_{\text{eff,axial}(1)}$  is the effective thermal conductivity of the fuel block in the axial direction.

The thermal conductivity of the coolant channel includes the radiation heat transfer as indicated in equation **(5-3)**:

$$k_C = k_{\text{gas}} + 0.5D_h^{\text{CH}}4F\sigma T^3 \quad \text{(5-3)}$$

Where

$D_h^{\text{CH}}$  = hydraulic diameter of the coolant channel,

$k_{\text{gas}}$  = thermal conductivity of helium and

$F$  = geometric view factor.

The geometric view factor calculation is shown in Appendix **C-3**.

#### **5.4.1.4 Conduction elements**

In the CHT element, the mass related to half the heat transfer length is lumped at the upstream or downstream node depending on the position of the mass in the CHT element. This is shown in **Figure 5-9**.

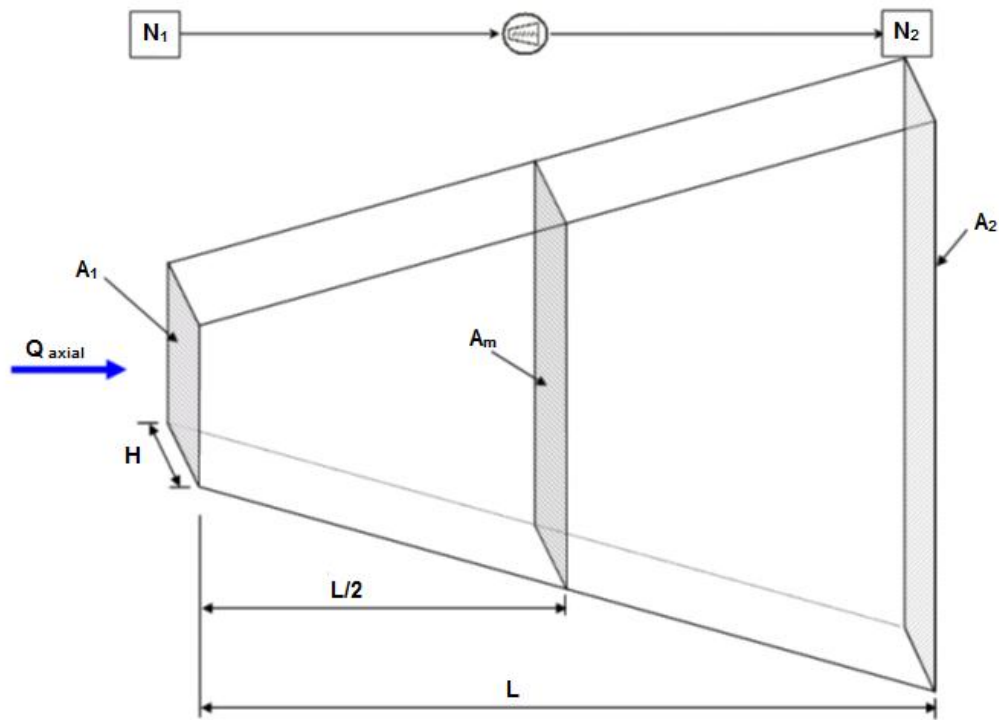


**Figure 5-9: CHT element layout (M-Tech, 2013).**

Where

$A_1$  and  $A_2$  =up- and downstream cross sectional areas,

$A_m$  =average area between  $A_1$  and  $A_2$ ,

$N_1$  and  $N_2$  = corresponding nodes and

$L$  = the length of heat transfer path.

An example for an input data page for a CHT is indicated in **Figure 5-10**. Focusing mainly on the material, geometry and mass calculation entities, the following are required for the CHT element:

- **Material:** The material on which conduction takes place. The material can be selected from the Flownex data reference library. However in this study, the conduction material has been custom defined using the properties in **Table 5-1**
- **Length:** Length of the CHT as indicated in **Figure 5-9**.
- **Height:** This is the height of the CHT element as indicated in **Figure 5-9**.
- **Inlet and outlet area:** Total frontal and posterior areas of the CHT element as indicated in **Figure 5-9**.

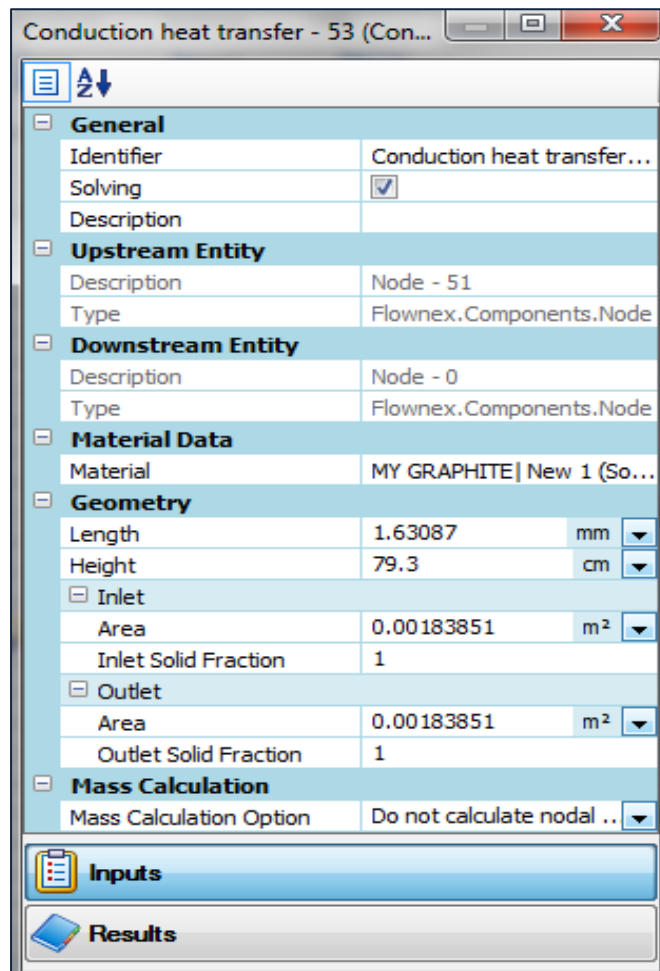


**Figure 5-10: CHT element property window.**

- **Inlet and outlet solid fractions:** Solid fraction in a material. The solid fractions are mainly used to specify porous materials.
- **Mass calculation option:** This option allows the user to calculate the nodal masses i.e. the mass of the CHT element is calculated and summed up to the up- and downstream nodes. In the cases of transients, the transient thermal inertia should be accounted for and therefore the nodal masses should be calculated.

The results obtained from the CHT include: total heat transfer, conductivity, average temperature and upstream and downstream results which both include specific heat, temperature, area volume and density.

#### 5.4.1.5 Cross conduction elements

Cross CHT elements are used in junction with CHT elements to simulate a 2-D heat transfer. Since the cross CHT elements are positioned between two contiguous CHT elements, the only inputs required are the heat transfer configuration and the connection orientation. Figure 2-11 indicates an example on how a Cross CHT is used.

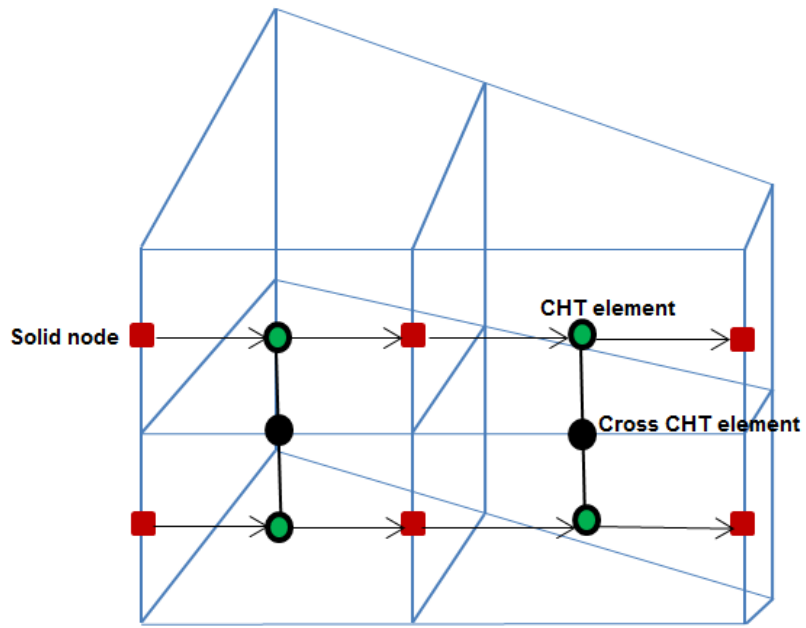


**Figure 5-11: Example of a 2D plate represented by CHT cross CHT elements.**

The connection orientation is either in the width or height direction.

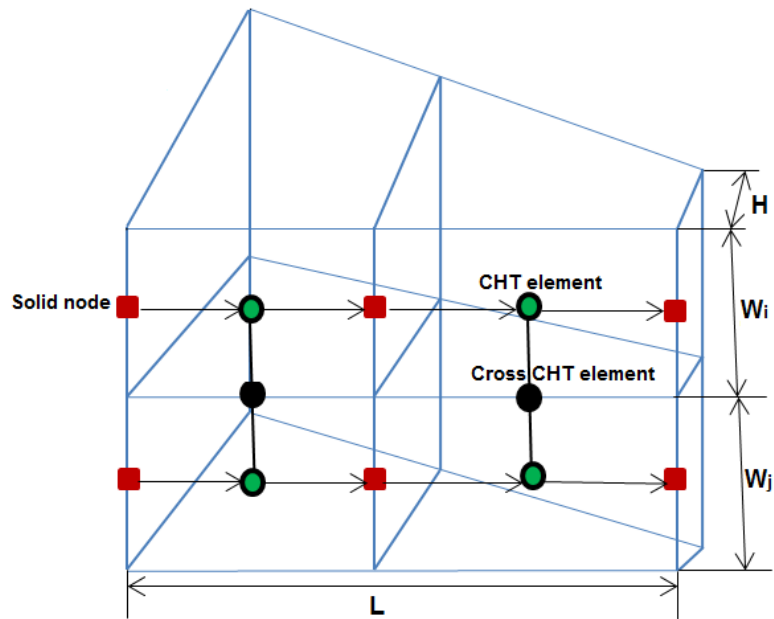


**Figure 5-12: Cross CHT connection in the width direction.**

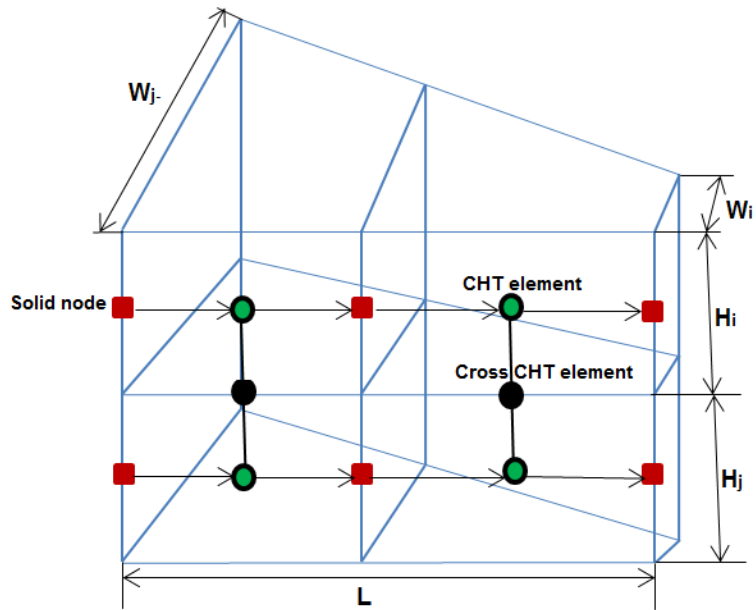


**Figure 5-13: Cross CHT connection in the height direction.**

In this study the width connection orientation is implemented. An input data page for the Cross CHT element is indicated below:

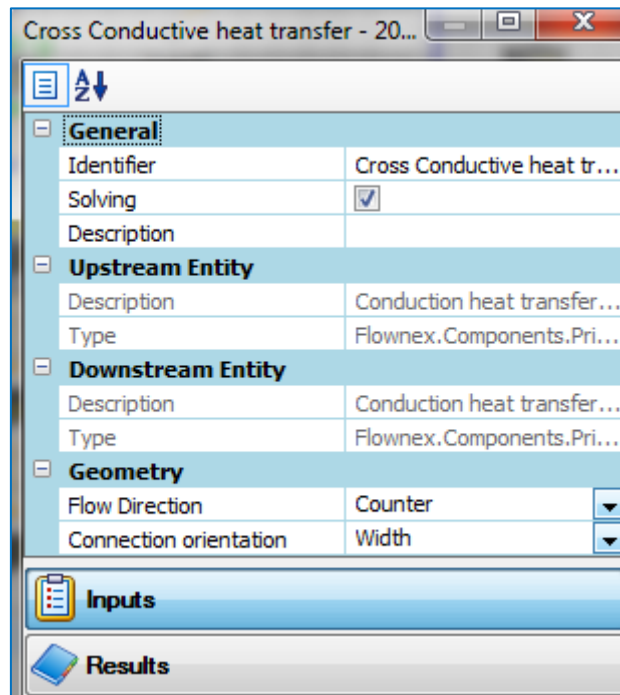


**Figure 5-14: Cross CHT element property window.**

On the geometry section, the flow configuration and connection orientation are the inputs.

- The **Flow direction** is either parallel or counter flow. In this study, counter flow is utilised.
- The **connection orientation** is considered either in the width or height directions.

The total heat transfer is the only result obtained from the cross CHT.

#### 5.4.1.6 Convection elements

Convection elements simulate the heat transfer between a fluid and a single incremented solid surface. **Figure 5-15** displays heat transfer through convection from a solid node.

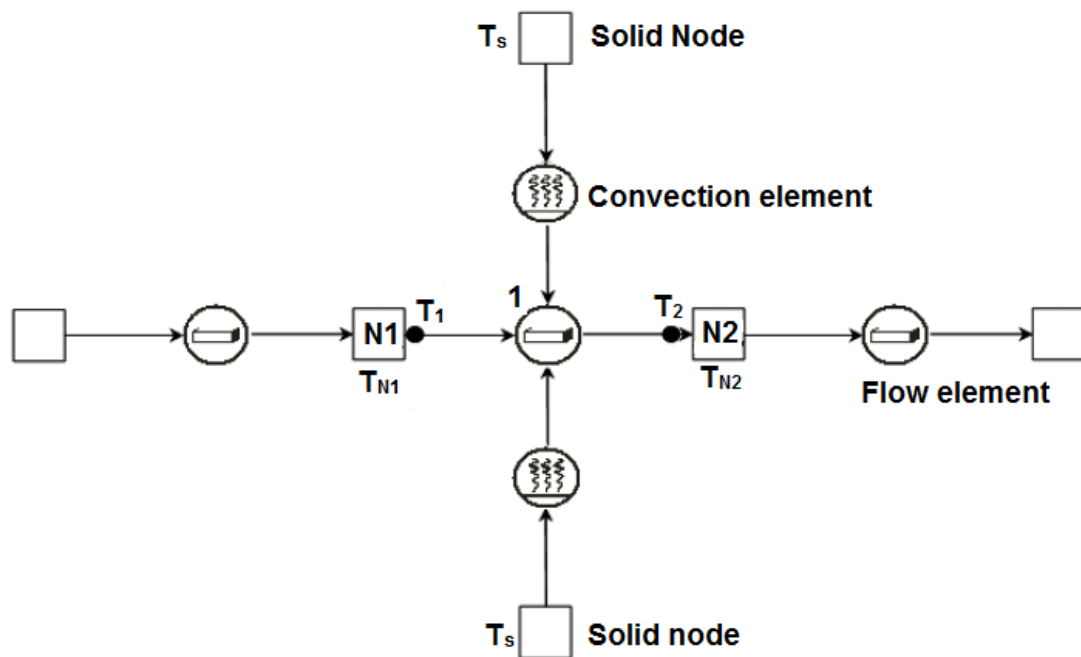


**Figure 5-15: Convection from a solid node (M-Tech, 2013).**

However convection can also take place from a solid element, between a solid node and a flow node, between a solid node and a flow non-incremented element as well as between a heat element and a flow element. However in this study, convection is only restricted to convection from a solid node.

The convection element input data page is indicated in **Figure 5-16**. Focusing on the geometry and convection entities, the following are required for the convection element:

- **Flow direction:** The flow direction of the convection element becomes significant if there is convection heat transfer between a flow element and conduction element. Therefore in this study the flow direction is insignificant.

- **Heat transfer area:** This is the flow area that the convection heat transfer coefficient associated with the hydraulic diameter is based on.
- **Convection coefficient option:** The options for the convection coefficient include the Dittus-Boelter correlation or a constant heat transfer coefficient.
- **Laminar Nusselt number:** This is the Nusselt number for laminar flow.
- **Turbulent Nusselt number:** The constants for the Dittus-Boelter correlation for turbulent flow  $Nu_{turb} = C \cdot Re^m \cdot Pr^n$  for forced convection are specified where C is taken to be 0.023, m is 0.8 and n is 0.4.
- **Constant convection coefficient:** If a constant convection coefficient is selected then the h value has to be specified.

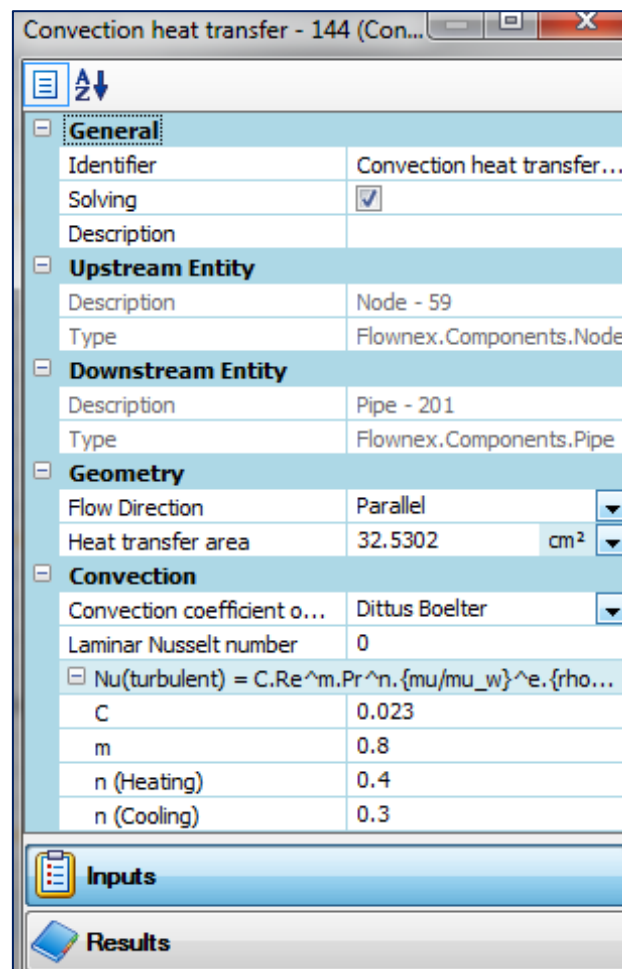


**Figure 5-16: Convection element property window.**

The results obtained from the convection element include: total heat transfer, convection coefficient, Nusselt number as well as the upstream and downstream temperatures.

In this study, the Dittus-Boelter correlation is used for convection both for the standard cooling within the block and the bypass.

### 5.4.1.7 Nodes and boundaries

A boundary condition element is used to specify the boundary condition of a network. Boundary condition elements can only be linked to a node component and therefore the boundary condition can only be specified on the applied node. Different combinations consisting of pressure, temperature, quality, enthalpy and a mass source may be specified on a node.

**Figure 5-17** shows the input data page for a boundary condition element.

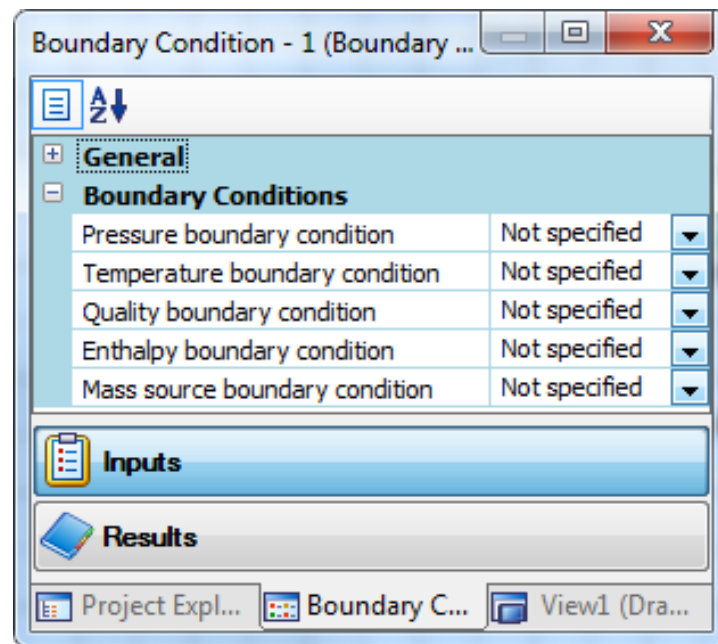


**Figure 5-17: Boundary condition input property page layout.**

The pressure, temperature, quality, enthalpy and/or mass source at a node can be selected in each respective boundary condition drop down list box. A positive value of the mass source indicates an inflow into the node and a negative mass source values denotes an outflow the node.

A heat source can specified at a node as indicated in the property window of a node. This is particularly very important in a nuclear reactor as heat is generated with different power profiles. Heat can be distributed in the nodes evenly or follow a specified power profile. In this study a uniform heat source is utilised.

The results obtained from a boundary condition element include: pressure, temperature, quality, mass flow rate and enthalpy of the assigned fluid. The node results includes: total mass, conductivity viscosity, specific heat Prandtl number, solid and liquid density and a solid temperature.

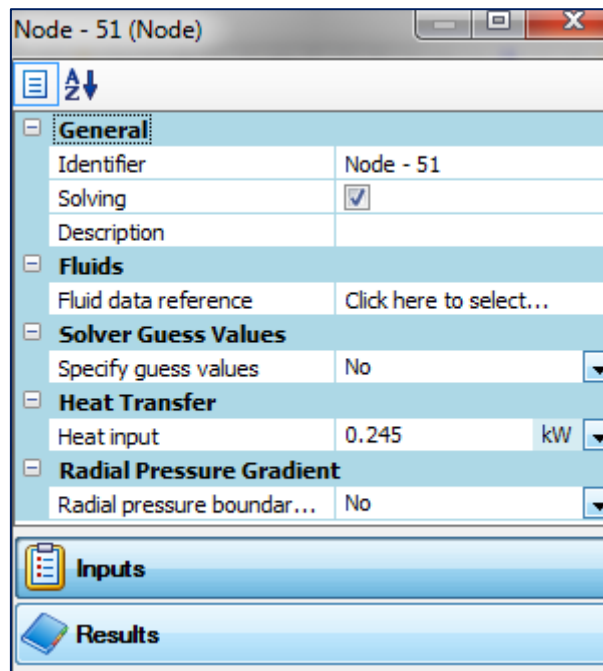
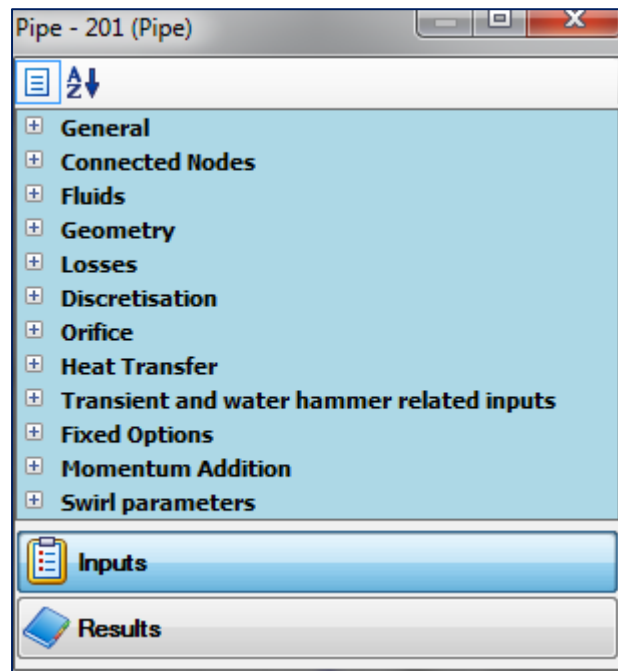


Figure 5-18: Node property window.

#### 5.4.1.8 Pipes

The pipes represent the standard cooling channels in the block as well as the bypass gap. The input data for the pipe is indicated in **Figure 5-19**. A one sixth segment of a prismatic block has a total of 17 standard coolant channels and 1 small coolant channel. In this study a homogeneous system is assumed and therefore the small coolant channel takes the dimensions of a standard coolant channel summing the number of standard coolant channels to 18.

On the geometry tab, the length, inlet circumference and area are required. These represent the length, combined circumference and area of the coolant channels in a specific control volume. The coolant channels are not smooth and a surface roughness of 20  $\mu\text{m}$  (Tung *et al.*, 2012) is implemented.



**Figure 5-19: Pipe property window.**

The results from the pipe element comprises of generic energy and heat transfer variables, fluid variables, non-dimensional variables, convergence, second law properties, forces, upstream and downstream as well as water Hammer parameters.

## **5.4.2 STAR-CCM+**

A few key aspects of the development for a one twelfth standard prismatic HTR block is described using the CFD code STAR-CCM+. The methodology for developing a heat transfer model for the fuel element is demonstrated by addressing three specific key aspects of such a model. These aspects include geometry and mesh generation, cooling channel flow modelling and the integrated fuel element model or combined fluid-solid model. Each of these key aspects will be discussed.

### **5.4.2.1 Geometry and mesh generation**

The geometry and dimensions of the hexagonal fuel element are shown in **Figure 5-3** in section **5.2.1**. The focus is on the fuel rods, graphite, cooling channels and bypass gaps. Modifications to the fuel element such as for fuel handling are therefore ignored in particular the dowel and fuel handling holes. A further assumption is that heat transfer symmetry exists in the cross-section of the fuel element and this allows then for only 1/12th of the fuel element to be modelled. The 1/12th section is indicated as the red triangle in **Figure 5-20**.

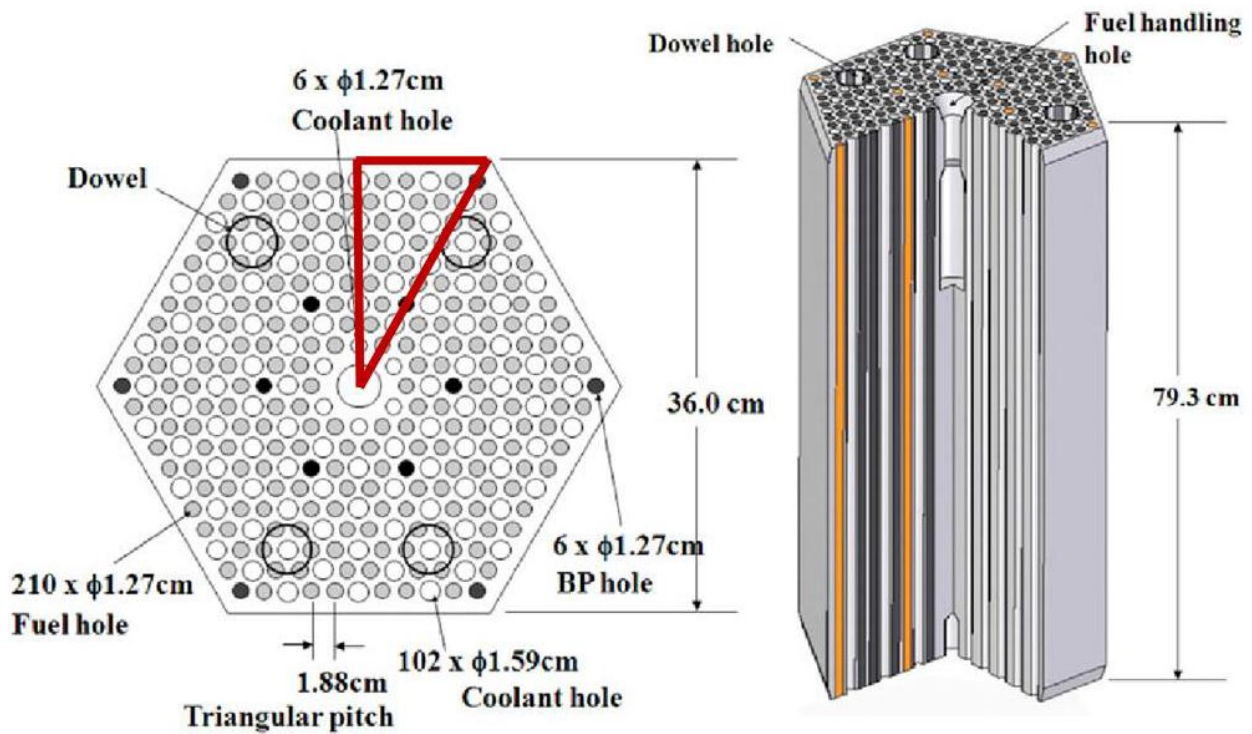


**Figure 5-20: A one twelfth fuel element block showing the fuel compacts, cooling channels and graphite structure (Tak *et al.*, 2012).**

A very important consideration regarding mesh generation for the fuel element configuration needs attention. The cross section of the fuel element has a detailed geometry and high temperature gradients are expected between the fuel rods and the helium cooling channels. This requires a very fine mesh for accurate temperature predictions. In the length direction of the fuel element the geometry is however regular and relative small temperature gradients are expected. Therefore a much coarser mesh is proposed along the length of the fuel element, which will be important from a computer memory and speed requirement point of view. A typical mesh point distribution appropriate for the fuel element modelling is shown in **Figure 5-21**. A fine mesh point distribution can be seen in the cross section while a coarser mesh is used along the length.

STAR-CCM+ has a very powerful automatic mesh generator capable of handling the detailed geometry of the fuel element. By applying the mesh generator to the fuel element the resulting mesh will however be equally fine in both the cross section as in the length direction. This will result in a mesh that is too fine for practical solution.

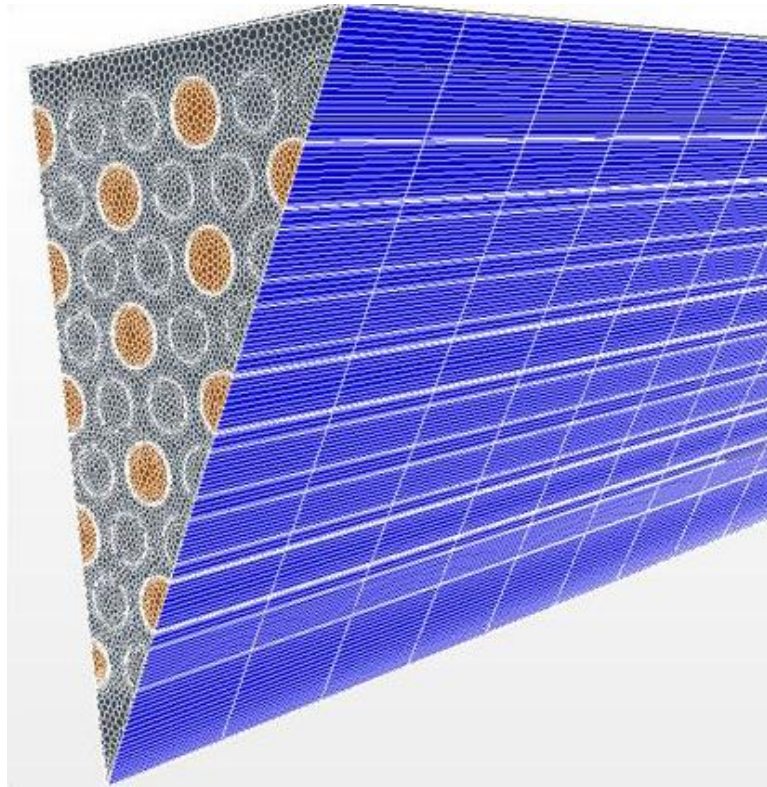


**Figure 5-21: Fine and coarse mesh point distribution.**

A special strategy needs to be followed in order to generate a mesh similar to that in **Figure 5-21**. In short one needs to generate a detailed mesh that will be suitable for the cross section and then use mesh extrusion to generate the mesh in the length direction using coarse mesh point increments. The mesh generation strategy will now be discussed in more detail.

#### 5.4.2.1.1 CAD model

A computer aided design (CAD) model of a thin section of the fuel element was generated using SolidWorks 2013 and consists of the individual parts representing the fuel rods, the graphite structure, the cooling channels and the by-pass gap. Different views of the CAD geometry are shown in **Figure 5-22**.

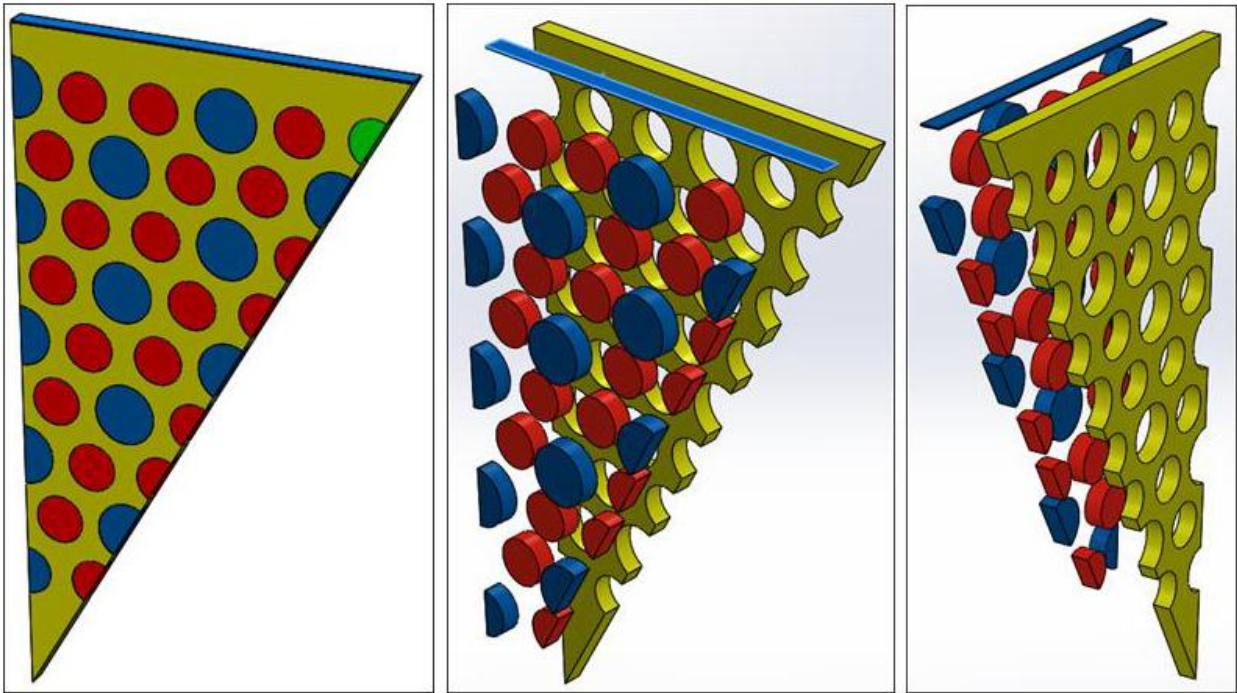


**Figure 5-22: Expanded CAD model showing graphite, fuel rods, cooling channels and bypass gap.**

#### 5.4.2.1.2 Mesh generation

A mesh was generated using the automatic polyhedral mesh generator of STAR-CCM+ within the thin CAD section shown in **Figure 5-22** above. STAR-CCM+ has a special feature for extruding a mesh normal to a boundary. Once the polyhedral mesh was generated inside the thin section the extrusion process was activated to generate the mesh in the length direction. The resulting mesh is shown in **Figure 5-23** below.

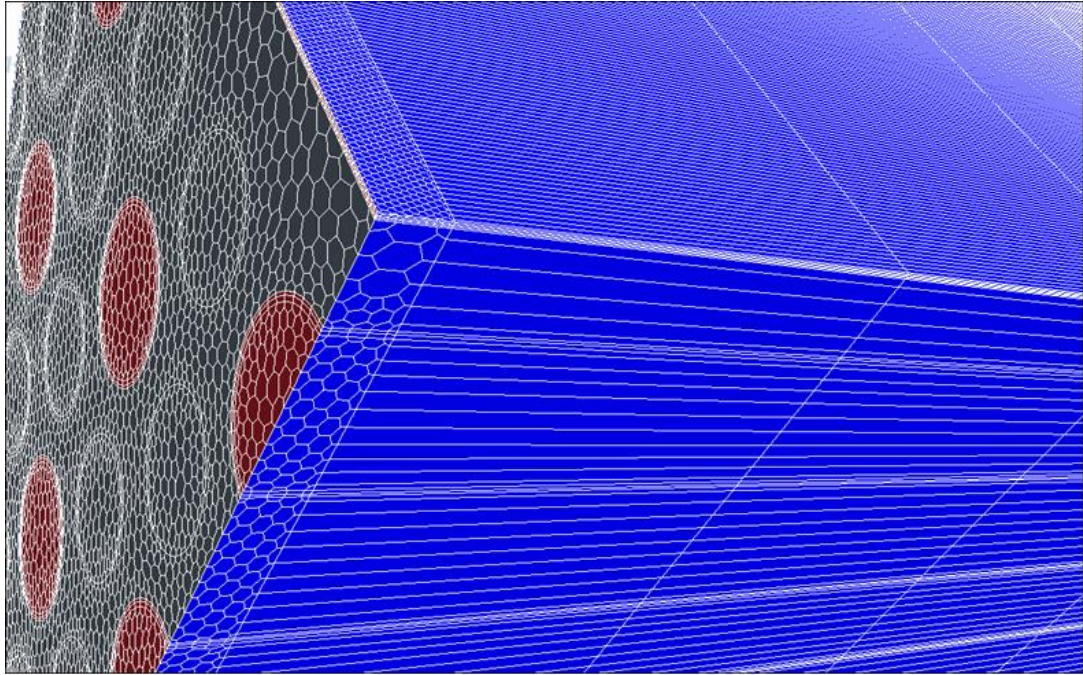


**Figure 5-23: Initial fine mesh and extrude coarse mesh representing the fuel element.**

Finally the thin mesh section needs to be deleted leaving only the extruded mesh. For helium flow in the cooling channels a special flat cell boundary layer mesh was used adjacent to solid materials. This allows accurate resolution of the turbulent boundary layer by using appropriate wall functions. The flat boundary layer cells used for the flow of helium are shown in **Figure 5-24**. The red circle represents a helium cooling channel and the orange section represents helium in the by- pass gap. An ordinary integral mesh line mapping can be seen between the fuel rod and graphite (all grey). There exists a small gap between the fuel rods and the graphite but that is not physically modelled. Instead a heat transfer resistance of the gas gap between the fuel rods and the graphite can be represented by a special heat transfer interface resistance, which is a feature of STAR-CCM+.

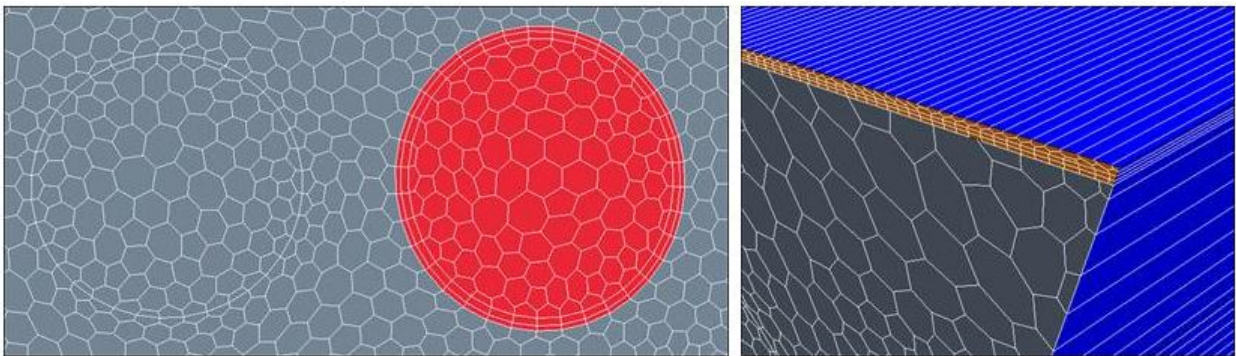


**Figure 5-24: Flat boundary layer cells for fluid adjacent to solid walls.**

A step-by-step procedure for generating the mesh for the fuel element is given in Appendix D. Detail of dimensions of the geometry and mesh is given in **Table 5-4**.

**Table 5-4: Geometrical dimensions.**

<b>Parameter</b>	<b>Value</b>
Fuel compact diameter (mm)	12.7
Coolant channel diameter (mm)	15.9
By-pass gap size (mm)	0.5
Fuel element height (mm)	793
Fuel element side to side (mm)	360

#### **5.4.2.2 Modelling flow in the coolant channels**

Modelling turbulent flow of helium inside the cooling channels require special attention to both the inlet boundary conditions and boundary layer flow. At the inlet of an intermediate fuel element cooling channel a fully developed turbulent boundary layer is expected (Reynolds's number is 40687.6). Regarding the boundary layer, the CFD solution of the boundary layer at the walls should be accurate for the heat transfer from the graphite to the helium depends on the existence and nature of the turbulent boundary layer.

A separate model of a single cooling channel is considered in order to fine tune the inlet flow conditions and the mesh quality to ensure that the cooling channels are accurately presented inside the global CFD model.

##### **5.4.2.2.1 Inlet boundary conditions**

The helium flow through the cooling channels is designed to be turbulent for this condition provides the best heat transfer. The inlet velocity is assumed to be a fully developed turbulent profile. An empirical power-law velocity profile is applied to the inlet boundary as shown in **Figure 5-25**.

The temperature at the inlet is 490 °C. The mass flow rate through the standard cooling channel is assumed to be 0.02017 kg/s.

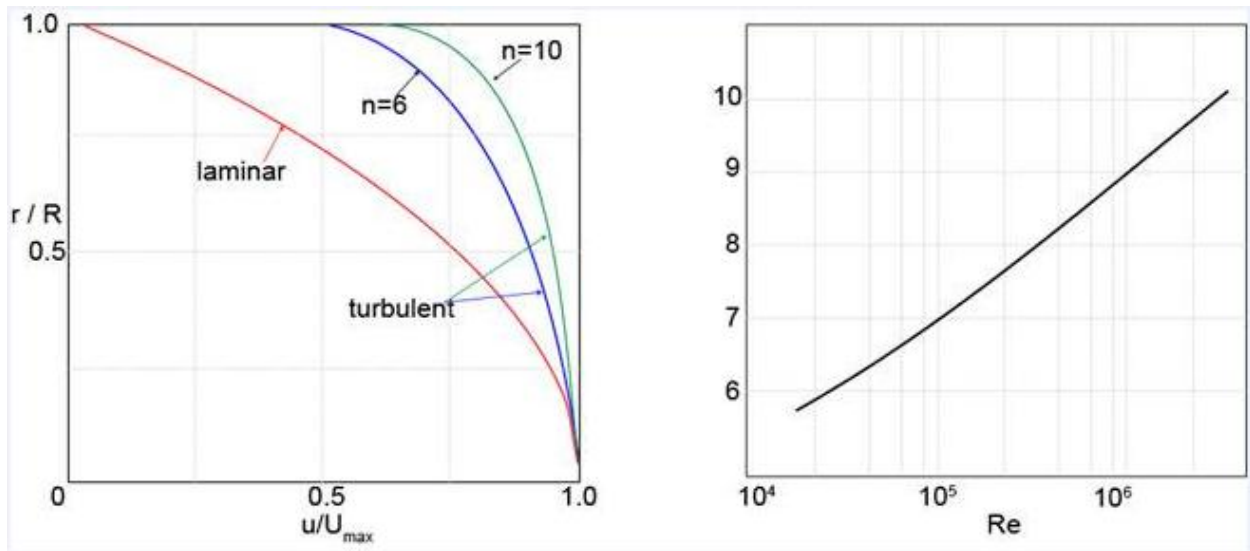


**Figure 5-25: (a) Turbulent and laminar velocity power-law empirical velocity profile (b) exponent  $n$  as a function of the Reynolds number (Morrison, 2013).**

#### 5.4.2.2.2 Wall boundary conditions

The existence of a turbulent boundary layer inside the cooling channels is very important for this condition provides for good heat transfer. The turbulent boundary layer inside the cooling channel is however very thin (in the order of 1% of the diameter). Full resolution of the boundary layer will however be very expensive in terms of computer resources due to the large number of mesh points required resulting in long solution times. The use of a wall function is therefore suggested. A wall function is an empirical relationship between Reynolds number, distance from the wall and boundary layer velocity. The use of a wall function requires only 1 cell adjacent to the wall to represent the full turbulent boundary layer and is therefore a very economical option. A requirement for the use of a wall function is that the normalized distance from the wall, represented by  $y^+$  be in the order of 12 to 30. In STAR-CCM+ the  $y^+$  value can be plotted on the wall surface of the channel. The thickness requirement of the boundary layer cells can therefore be checked once an initial simulation is done.

A special mesh is used inside the cooling channels that contain thin flat cells adjacent to the walls. Using uniform flat cells adjacent to the wall provide the best accuracy in numerical solution of boundary layer flows inside pipes since it introduces very little numerical diffusion. The special boundary layer mesh and a plot of the  $y^+$  values on the walls are shown **Figure 5-26**. The mesh size was adjusted so that the required  $y^+$  values were obtained. The specific mesh structure and inlet velocity profile is used in the full assembly of the fuel element.

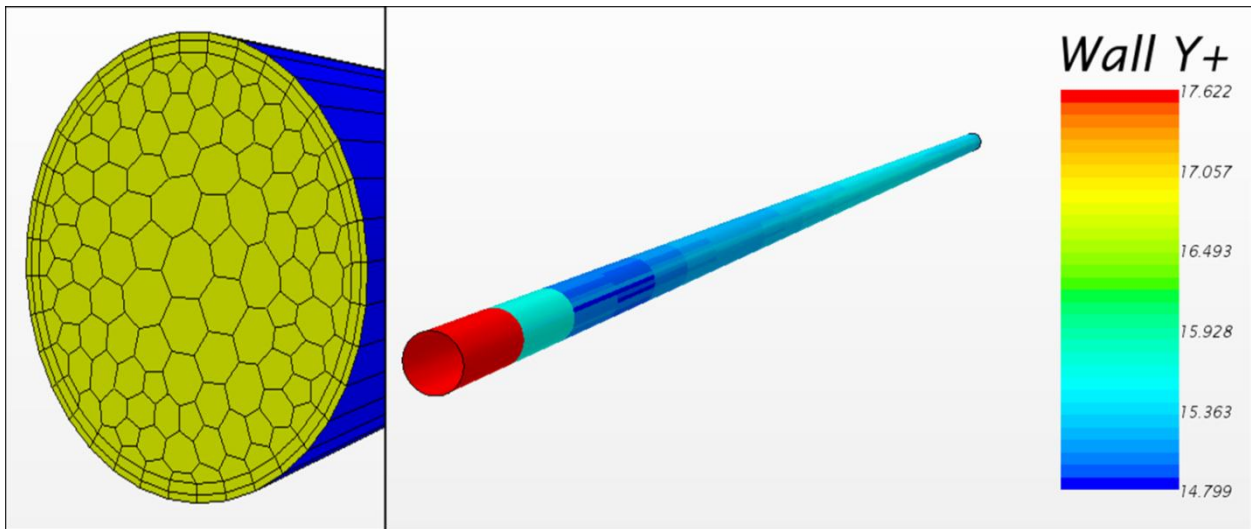


**Figure 5-26: (a) Flat boundary layer cells (b)  $y^+$  values plotted on the walls of the cooling channel.**

### 5.4.2.3 Integrated fuel element model

The integrated fuel element model consists of the graphite moderator structure with channels for fuel rods, lumped burning poison (LBP) rods and cooling flow. By-pass flow between adjacent fuel blocks is also considered. In this section the boundary conditions for the integrated model is considered as well as mesh density considerations and time step size selection for unsteady calculations.

#### 5.4.2.3.1 Boundary and initial conditions

The boundary conditions for the fuel element are shown in **Figure 5-27**. Details for the different materials follow;

##### (a) Graphite and LBP

The graphite connects to the cooling channel flow, the by-pass flow, the fuel rods and LBP rods. In all these cases the interface boundary conditions are handled implicitly in the code. Symmetry conditions are applied in the cross-section where the cuts are made localizing the 1/12th section. At the inlet and outlet sides of the fuel element adiabatic conditions are assumed. The same condition applies for the LBP rods.

##### (b) Fuel

Adiabatic conditions are applied to the fuel rods at the inlet and outlet sides of the fuel element. Conduction to graphite is handled implicitly. An interface resistance can be applied on the

interface between the fuel rods and the graphite. Currently a zero resistance is assumed. A constant volumetric heat flux of  $27.8 \text{ MW/m}^3$  is applied inside the fuel rods.

(c) Cooling channels

At the inlet side of the cooling channels a velocity profile is applied as described in section 5.4.2.2.1. The magnitude of the velocity profile is adjusted until a mass flow of  $0.02 \text{ kg/s}$  is observed in the standard cooling channels. A mass flow of  $0.012 \text{ kg/s}$  is assumed in the smaller cooling channel. The fully developed turbulent pipe flow profiles can be seen in **Figure 5-28** at the entrances of the cooling channels. An inlet temperature of  $490 \text{ }^\circ\text{C}$  is applied. At the outlet a constant pressure of  $7 \text{ MPa}$  is assumed.

(d) By-pass gap

A constant velocity is applied at the inlet to the by-pass gap and adjusted to give a mass flow of  $0.002 \text{ kg/s}$ . As for the cooling channels a temperature of  $490 \text{ }^\circ\text{C}$  is applied. At the outlet a constant pressure of  $7 \text{ MPa}$  is applied.

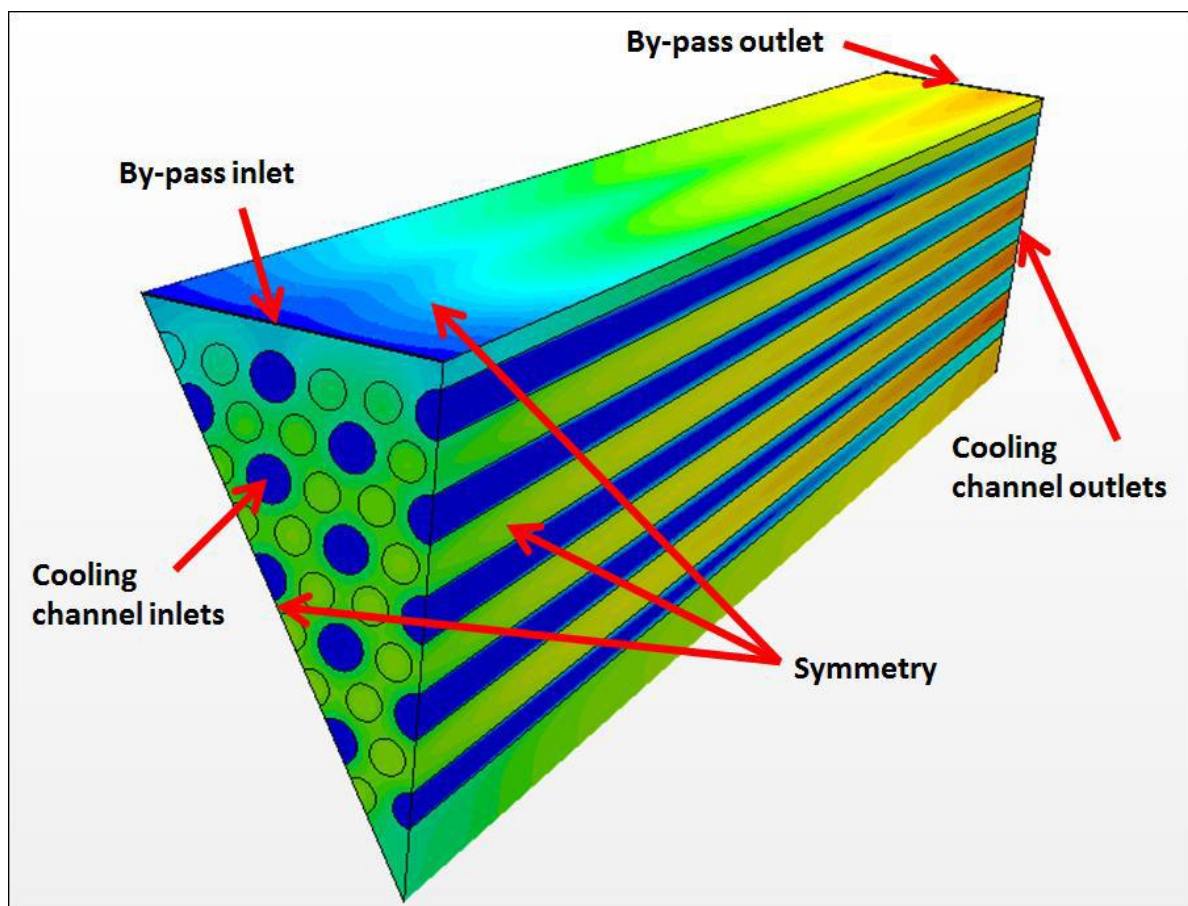


**Figure 5-27: Boundary conditions for the fuel element.**

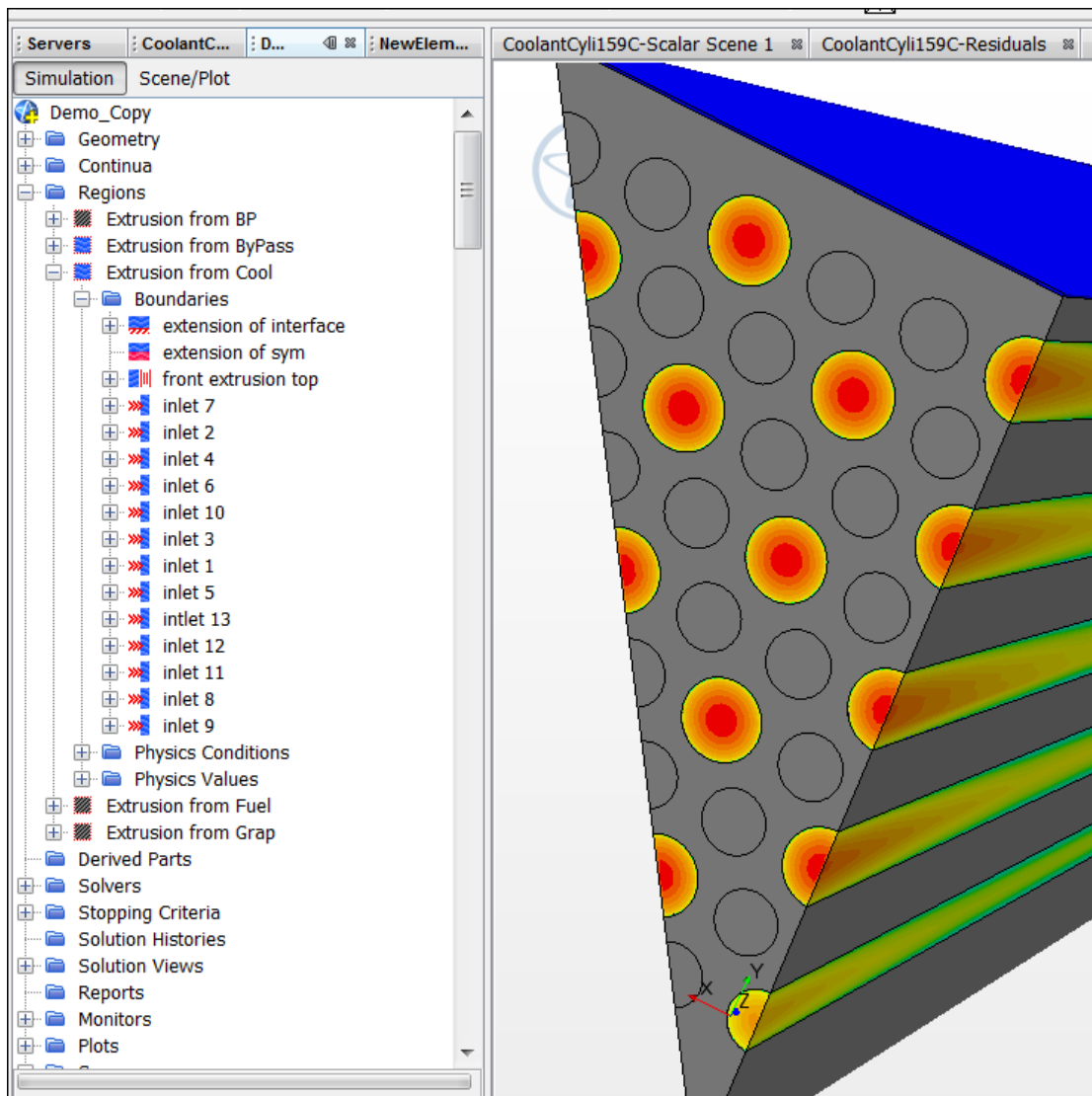


**Figure 5-28: Fully developed turbulent velocity profiles at the cooling channel inlets.**

#### 5.4.2.3.2 Material properties

In this study the results from STAR-CCM+ and Flownex will be compared. In order to compare the same models, these two codes will use the same material properties. The graphite, LBP and fuel will have the same material properties specified in **Table 5-1** and helium will also have the same properties specified in **Table 5-3**.

#### 5.4.2.3.3 Mesh density

It is important to evaluate the sensitivity of the CFD solution to variation in mesh density to ensure accurate results. As a first step the sensitivity of the temperature solution on the variation of mesh density in the cross sectional direction was investigated.

## Temperature variation in the cross sectional direction

In order to study the effect of mesh density in the cross sectional direction on the solution it is necessary to consider the fluid and solid regions separately. The reason for this is due to the wall-function being used in the cooling channel. The wall-function calculates the wall shear stress from empirical data and therefore requires a certain cell thickness near the boundary. If the cell size should go out of a prescribed range due to mesh refinement a loss of accuracy can be expected.

### **-Mesh density in the solid region**

In the absence of the cooling channels a fixed temperature boundary condition of 490 °C is used on the solid-fluid interface. A volumetric heat source is applied in the fuel channels. A typical temperature profile for a coarse mesh is shown in **Figure 5-29** below. The highest solid temperatures appear in the fuel rods as can be expected. A fixed point on the centre of a fuel rod at the flow outlet face is chosen to monitor the temperature for the purpose of the mesh density study.

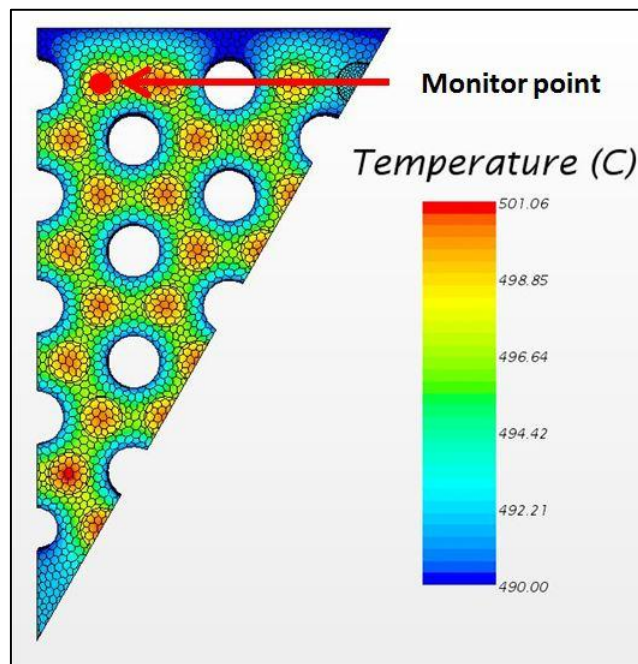


**Figure 5-29: Solid temperature profiles for a coarse mesh.**

A graph showing the variation in temperature versus cell size for the monitored point is displayed in **Figure 5-30**. As the cell size is decreased the solution becomes less sensitive to the change in cell size

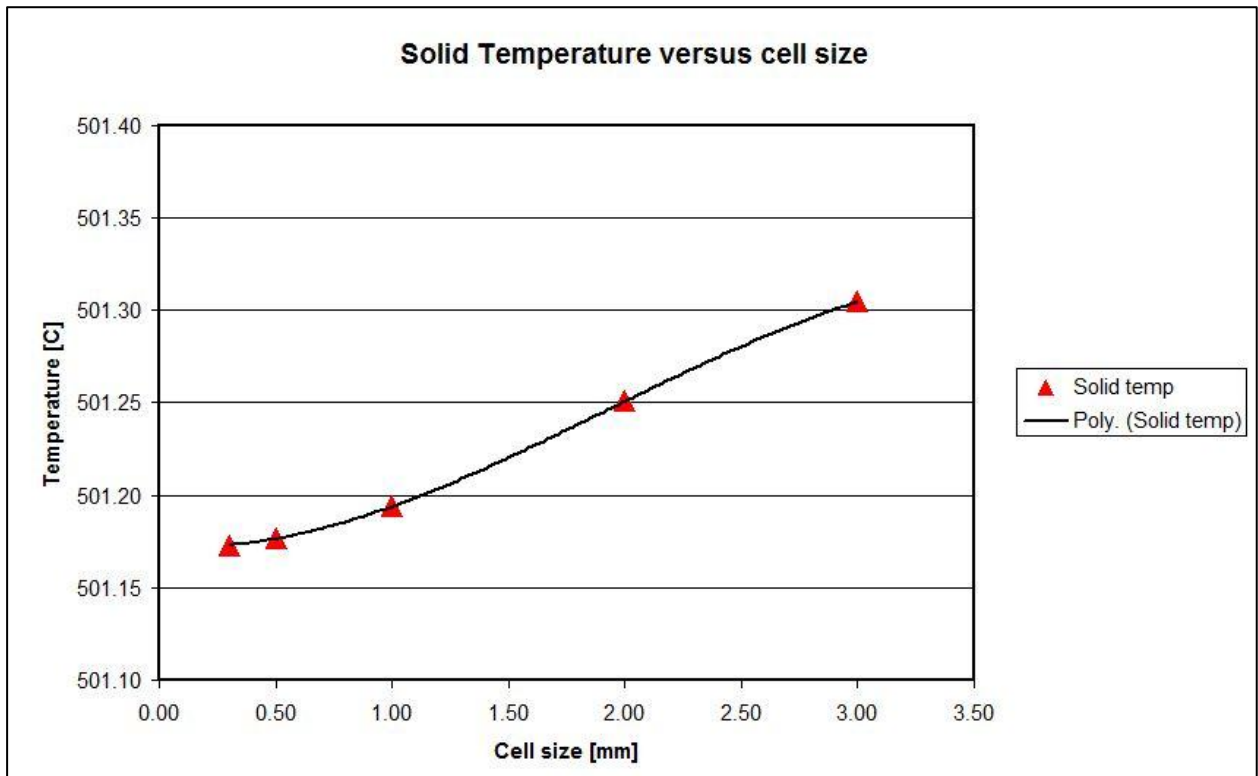


**Figure 5-30: Sensitivity of solid temperature to mesh density.**

**- Mesh density in the fluid region**

In order to test the solution sensitivity to mesh density in the fluid region the cooling channel mesh is divided into a core region and a boundary layer region as displayed in **Figure 5-31**. A typical cell size of 3 mm is chosen for the core region while the boundary region is taken as 7 mm. Further refinement of the core region has little effect on the solution but the refinement of the boundary layer region is significant. A cooling channel with a refined boundary layer is shown on the right side of **Figure 5-31**.

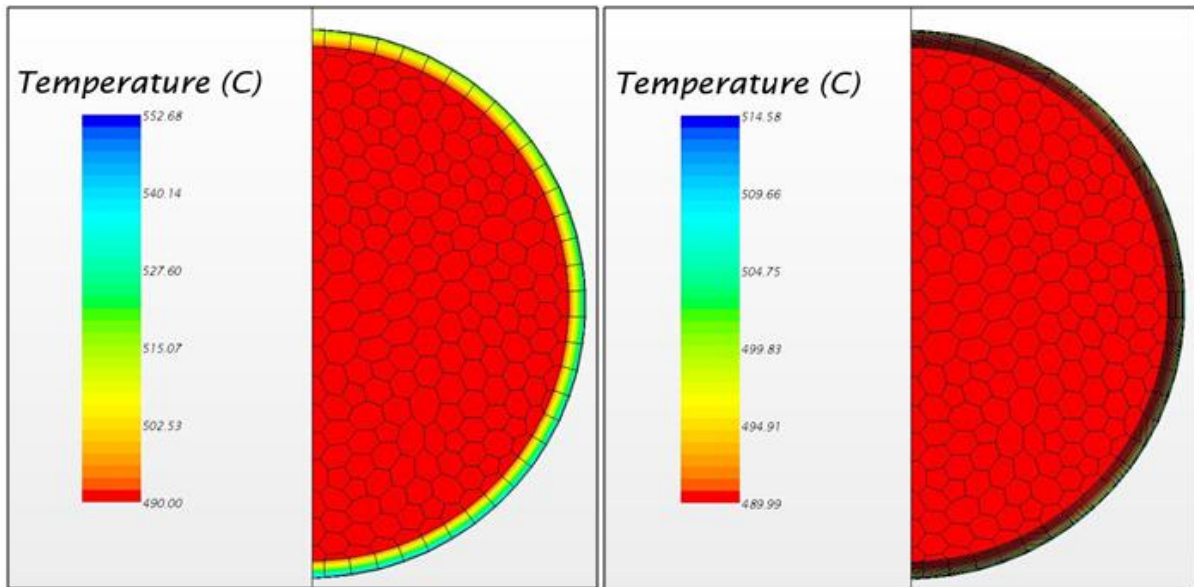


**Figure 5-31: Boundary layer refinement for the cooling channel.**

The gas flow in the cooling channels is solved using the high Reynolds number version of the k-eps turbulence model. The wall function for this particular implementation requires that the centre of the first cell adjacent to the boundary lies in the turbulent region of the boundary layer. This corresponds to a  $y^+$  value greater than 11. The boundary region of the cooling channel is accordingly refined and the solid temperature at the monitor point (see **Figure 5-29**) is plotted versus  $y^+$  value in **Figure 5-32**. The form of the graph indicates that the convection heat transfer stabilizes at a  $y^+$  value of about 25. This corresponds to 3 increments of the boundary layer.

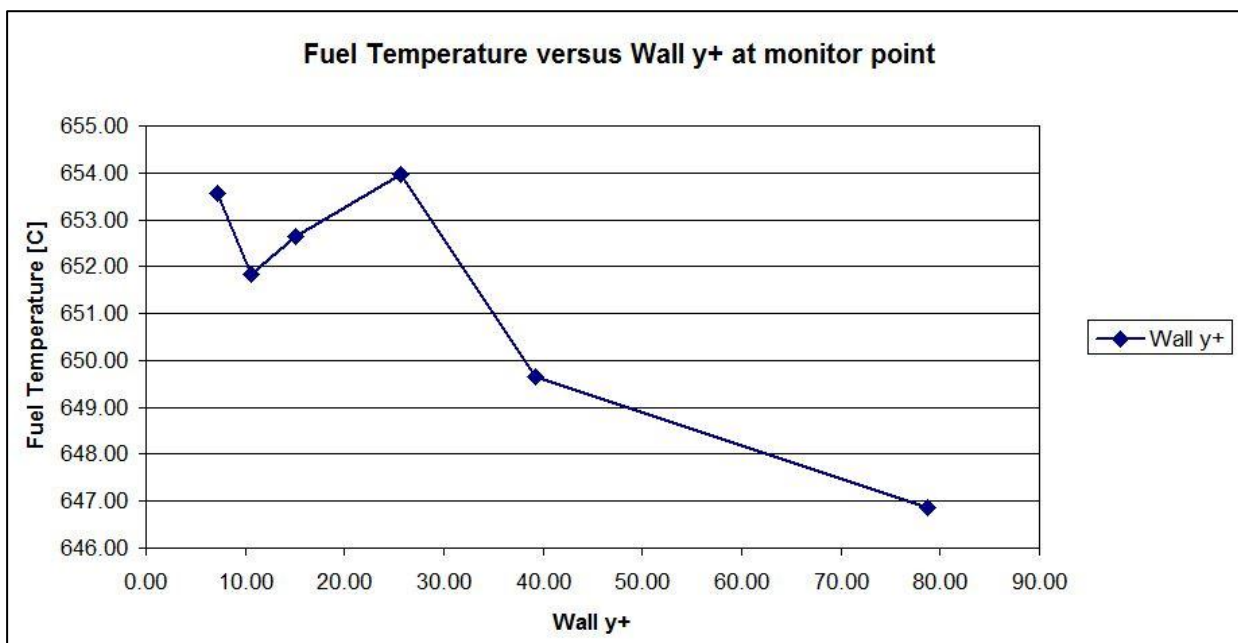


**Figure 5-32: Sensitivity of solid temperature to  $y^+$  value.**

The number of increments in the boundary layer region that corresponds to the different  $y^+$  values is given in **Table 5-5** below.

**Table 5-5: Boundary layer increment relation to  $y^+$  value.**

Increments	$Y^+$
1	78.7
2	39.2
3	25.6
5	15.1
7	10.6
10	7.18

The final mesh sizes to be used in the cross-section of the fuel element was selected from the mesh sensitivity study as 3 mm in both the solid and fluid core regions with 3 increments in the boundary layer.

#### Temperature variation along the length of the fuel element

In contrast to the cross-sectional direction, the sensitivity of the temperature solution to a variation of the number of cells in the length direction is not significant. The left image in **Figure 5-33** shows the case of 10 increments in the length direction and the right image shows the case of 80 increments

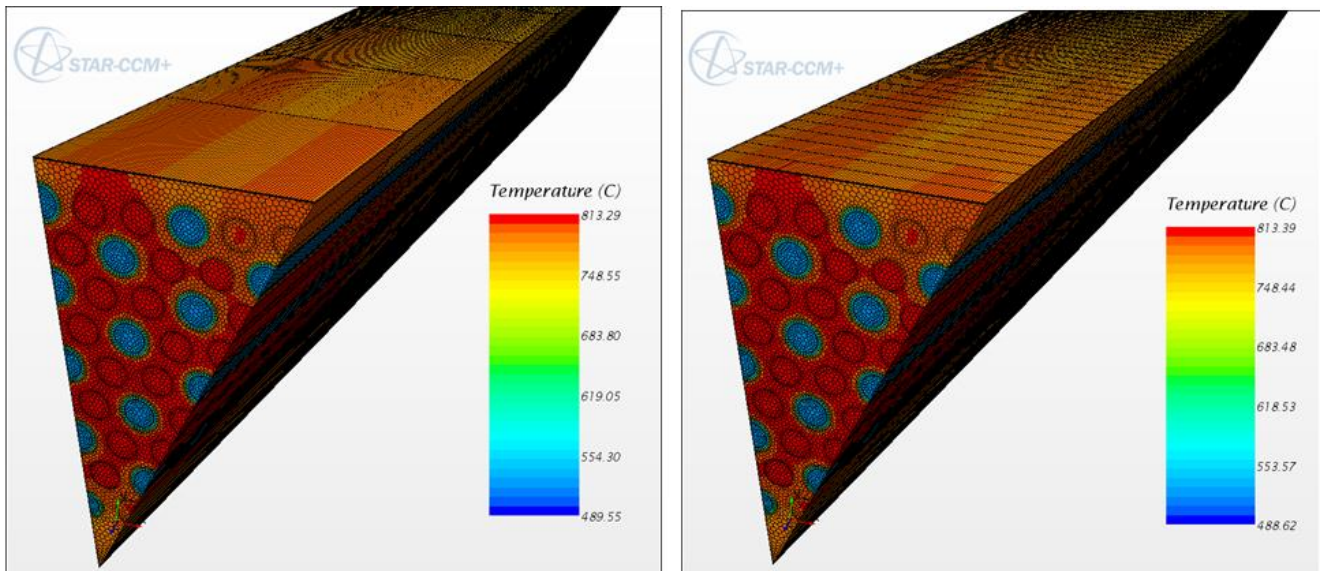


**Figure 5-33: Variation in maximum temperature versus cell size in the length direction.**

The variation of the maximum fuel temperature on the front end surfaces of the fuel rods are monitored to evaluate the sensitivity of the solution to a variation in cell size in the length direction. It is found that for a case in which the length of the fuel element is divided into 10 equal sections the maximum temperature on the front ends of the fuel rods is 813.20 °C. The maximum temperature for 80 increments is 813.39 °C.

#### 5.4.2.3.4 Steady state calculations

A steady state calculation for the integrated fuel element model was performed. The residual history is shown in **Figure 5-34**. The graphs show strong convergence behaviour. A temperature solution of the final integrated fuel element model is shown in **Figure 5-35**. Under relaxation factors for the temperature solution in the fluid is set to 0.995 while under relaxation of 0.999 is used for the solids.

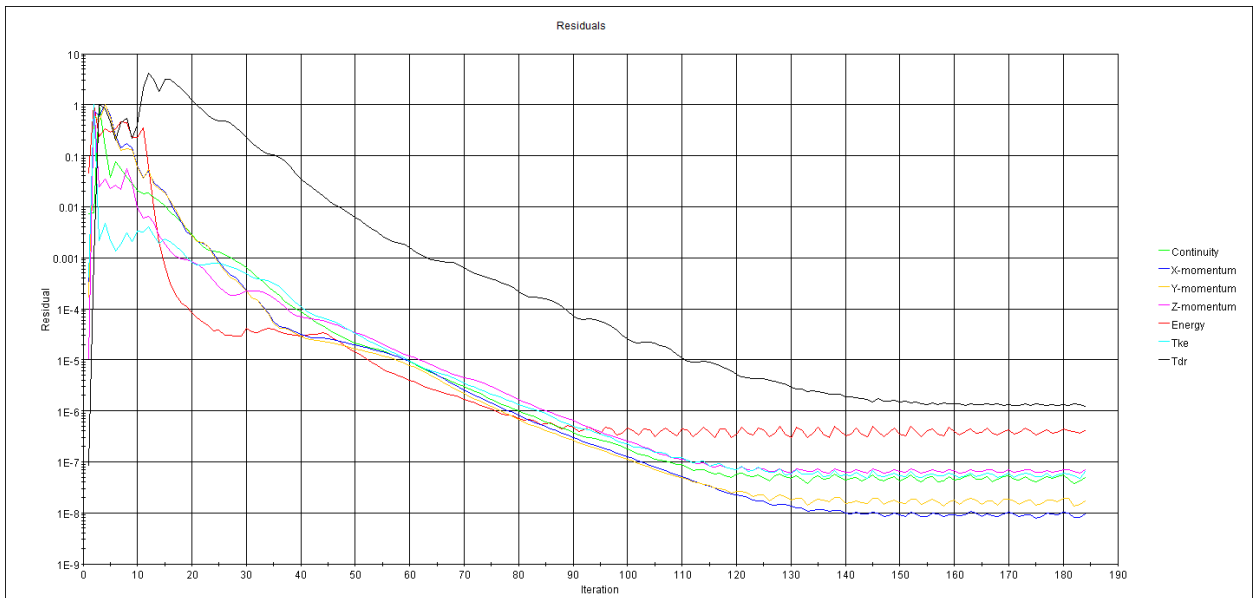


**Figure 5-34: Convergence behaviour for a steady state solution of the fuel element.**

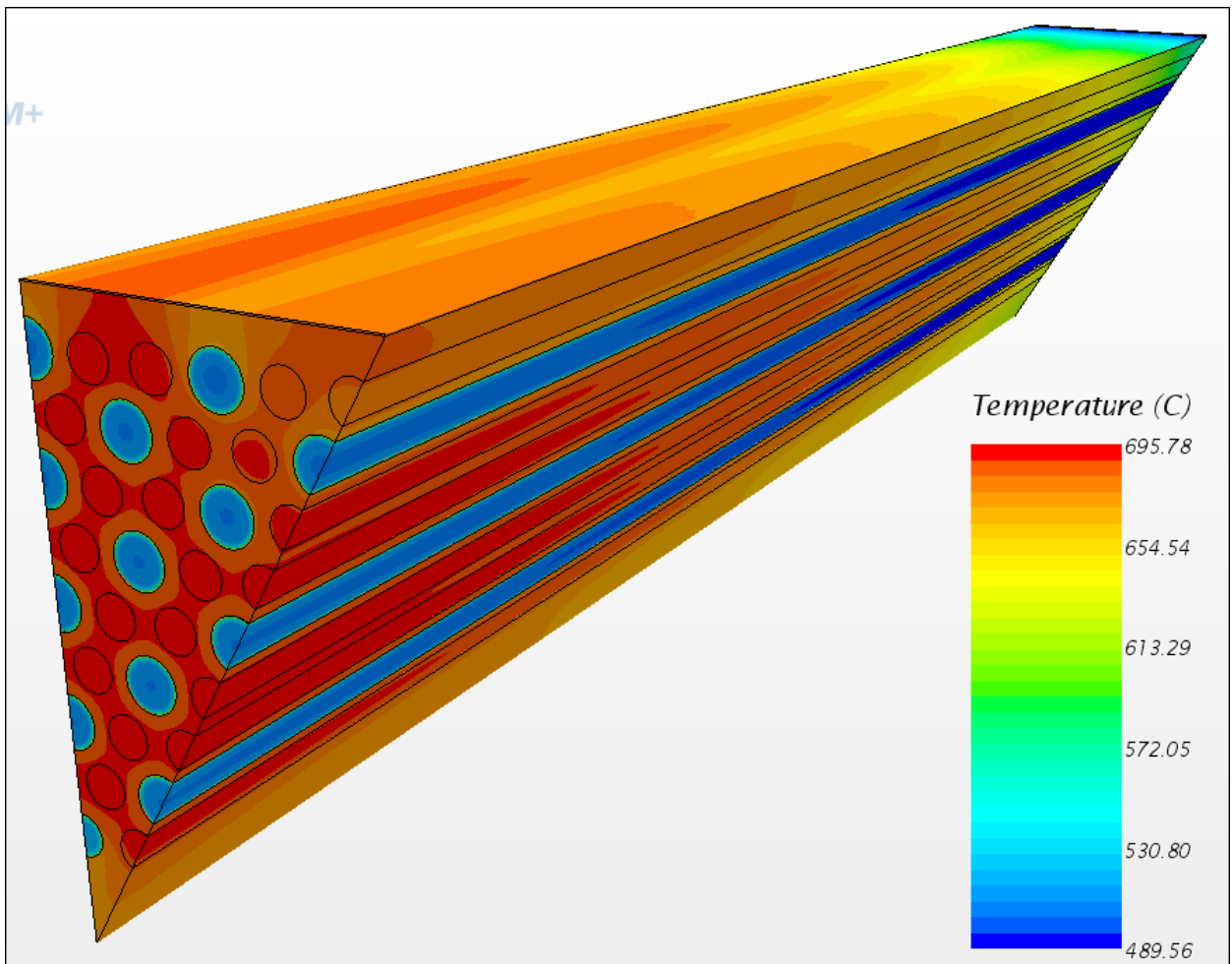


**Figure 5-35: Temperature contours for a steady state solution of the fuel element for the bottom/outlet side of the block.**

## 5.5 Integrated prismatic block

Flownex has been verified that it can be used in 2-D analysis (radial and tangential). Flownex and STAR-CCM+ will now be used to simulate an integrated analysis of a standard PMR200 block.

In Flownex, a one sixth section of a standard PMR200 fuel block is used. **Table 5-6** displays some the parameters used in Flownex to simulate the block.

**Table 5-6: Parameters used to simulate the one sixth block in Flownex.**

Number of standard coolant channels	18
Diameter of coolant channels (cm)	1.59
Area of coolant channel (cm <sup>2</sup> )	1.99
Area of 1/6 <sup>th</sup> segment (cm <sup>2</sup> )	187.1
Height of block (cm)	79.3
Total heat input (kW)	98
Bypass gap width (cm)	0.5

The LBP and fuel compacts are not modelled in Flownex. The heat generated from the fuel is uniformly distributed in the nodes. The total coolant mass flow rate into the block is 0.358 kg/s. A surface roughness of 20  $\mu\text{m}$  (Tung *et al.*, 2012) is assumed for the coolant channels and the bypass gap. The geometry of the PMR200 also includes a small coolant channel positioned near the fuel handling hole. In Flownex this coolant channel assumes the dimensions of a standard coolant channel, and that increases the number of coolant channels. A pressure of 7 MPa is prescribed at the inlet of the coolant channels and bypass gap. The inlet coolant temperature is also prescribed to 490 °C. The properties of the graphite are indicated in **Table 5-1**.

In STAR-CCM+, the same conditions as in Flownex are applied. However, in STAR-CCM+, the BP and fuel rods are modelled and these have the same material properties as the graphite. A one twelfth block is modelled in STAR-CCM+ because a one twelfth segment is the smallest region that has symmetry boundaries on all edges. **Table 5-7** lists some of the important parameters in STAR-CCM+.

**Table 5-7: Parameters used to simulate the one sixth block in STAR-CCM+.**

Number of standard coolant channels	8.5
Number of small coolant channels	0.5
Number of BP	0.5
Height of the block (cm)	79.3
Volumetric heat source (MW/m <sup>3</sup> )	27.8

A turbulent flow profile was prescribed at the inlet of the coolant channels and was adjusted until a mass flow rate of 0.02 kg/s for the standard coolant channels and a mass flow rate of 0.012 kg/s for the smaller coolant channel was reached. The constant velocity for the by-pass gap was adjusted to give a mass flow rate of 0.012 kg/s.

The helium coolant was assumed to be an incompressible fluid in both codes. **Table 5-3** displays the helium properties used in both codes.

### 5.5.1 Results and discussion

**Figure 5-36** shows a schematic of the centreline and outer margin where steady-state results were read from in both codes. In STAR-CCM+, a line probe was inserted at the middle of the block, in the height direction and also three quarter way down the height of the block.

**Figure 5-37** shows the steady state results obtained from both codes at the centreline of the prismatic block. The STAR-CCM+ results were obtained by using a middle line probe and therefore measured the graphite and coolant temperatures simultaneously. The Flownex results indicate the fuel surface, graphite and coolant temperatures which were obtained from the fuel nodes, graphite nodes and the pipe elements respectively. The STAR-CCM+ results gives a 3-D distribution of the temperature while Flownex only gives the representative temperatures in the middle of the block due to the fact that the Flownex model consists of one layer of CVs.

In the STAR-CCM+ results, it can be observed how the temperature of the solids and the helium varies along the block. Referring back to **Figure 5-35**, which displays the final STAR-CCM+ model with the temperature contours along the block, values were read off from the adjacent side of the bypass gap which is not the hypotenuse side. From that side four half standard coolant channels and one half small coolant channel are present. At the apex of the block, lower temperatures are presented in the STAR-CCM+ model; this is due to the absence

of fuel rods at the apex, only graphite is present there. Therefore there is no heat source at the apex only heat that is conducted from the first fuel rod which is situated on the hypotenuse side of the block. In the Flownex model the result is different. This is because the heat source has been uniformly distributed throughout the block which includes the node at the apex. The average percentage difference between the STAR-CCM+ and Flownex models for the graphite at the apex is 1.6 % and near the bypass gap is 0.09 %.

The high peaks in temperature in the STAR-CCM+ model are due to the graphite which is in close proximity to the fuel rods, and the low peaks in temperature are because the values are read off from the coolant channels. The Flownex model coolant temperatures are very comparable to the STAR-CCM+ results. The black dots in **Figure 5-37** represent the average STAR-CCM+ coolant temperatures and even though they don't portray a certain trend, the values are very close to the Flownex model results.

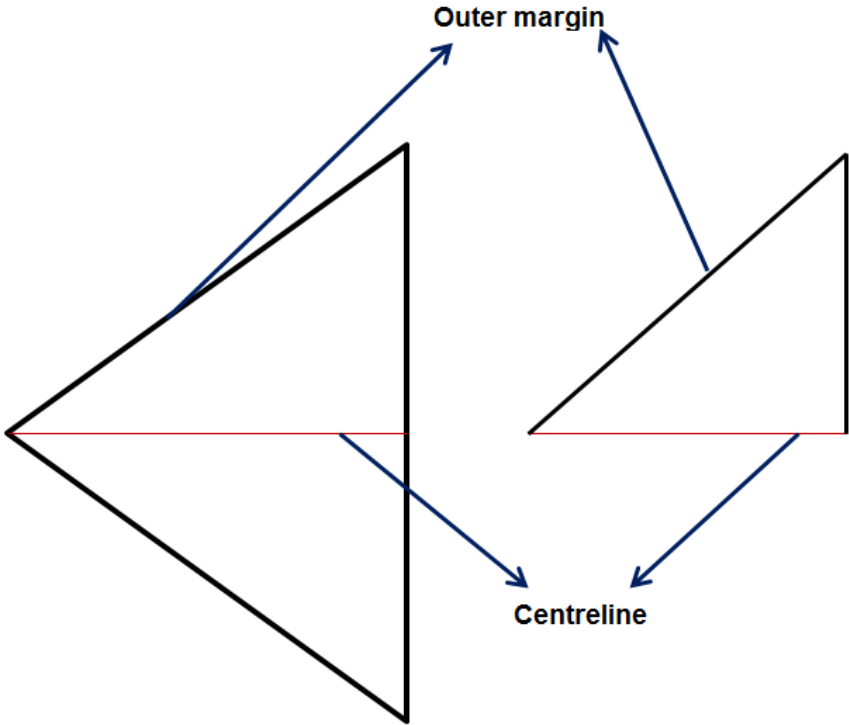


**Figure 5-36: Schematic indicating the centreline and the outer edge in the Flownex and STAR-CCM+ models.**

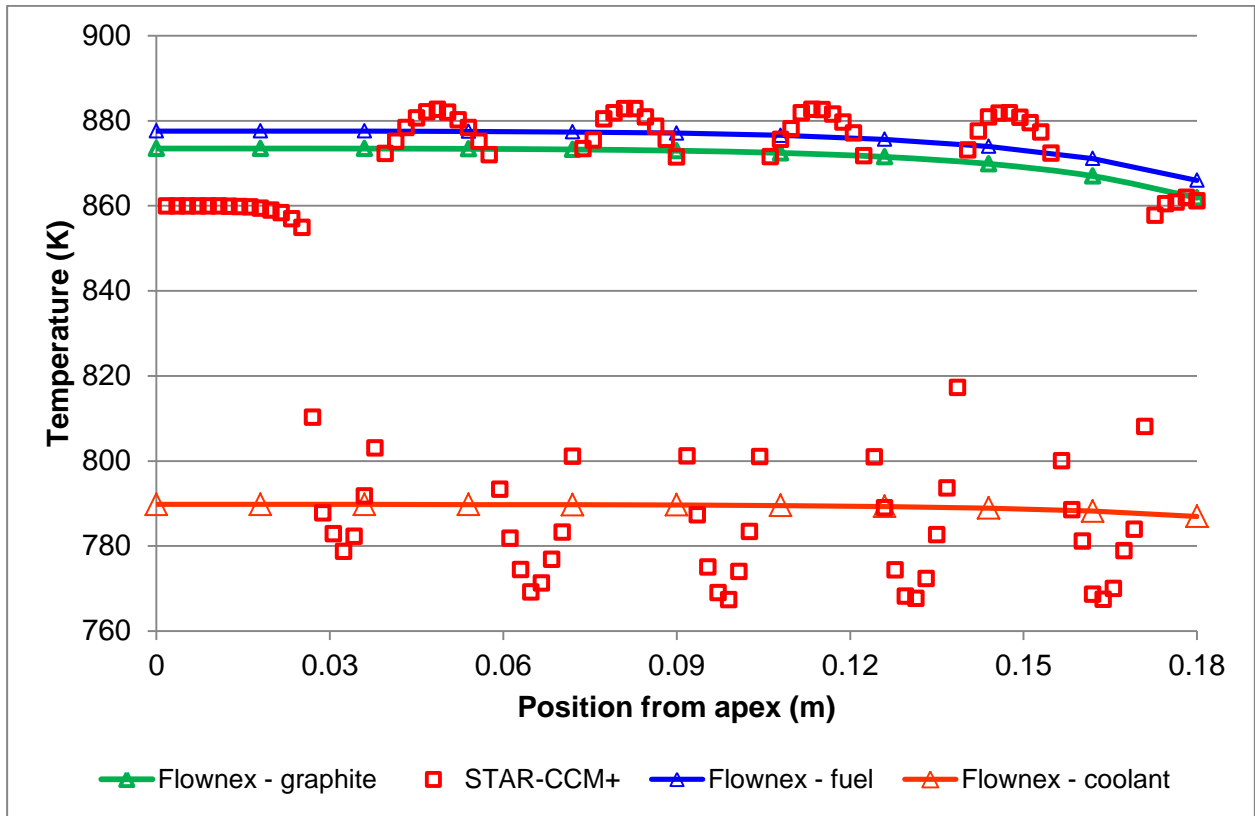


**Figure 5-37: Temperature distributions along the centreline for both STAR-CCM+ and Flownex for the integrated block.**

**Figure 5-38** shows the steady state results obtained from both codes at the outer margin of the prismatic block.

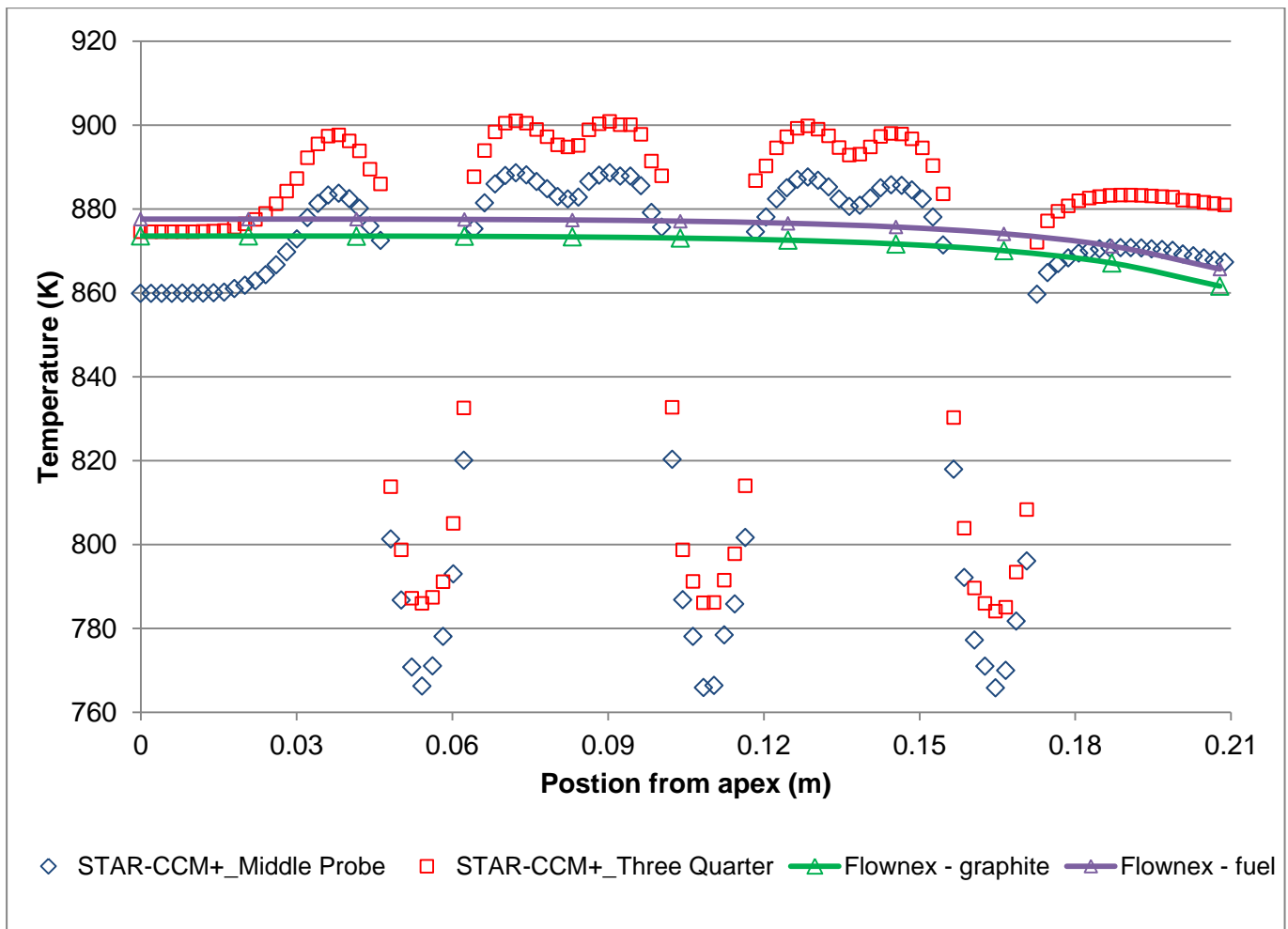


**Figure 5-38: Temperature distributions along the outer margin for both STAR-CCM+ and Flownex for the integrated block.**

In a similar manner to the centreline analysis, the outer margin analysis was also conducted by comparing the Flownex temperature profile to the middle probe STAR-CCM+ temperature profile and additionally a three quarter probe. The three quarter probe was placed in order to see the variation between the three quarter and the middle probes. As expected, the three quarter probe has higher temperatures compared to the middle probe even though the same trend is still achieved; this is because the three quarter probe is near the outlet of the block and the progression of heat transfer has far advanced compared to the middle probe.

Referring to **Figure 5-35** as well, the results are taken from the hypotenuse side of the prismatic block. The hypotenuse side contains three half standard coolant channels, five half fuel rods and one half LBP (which in this study takes the properties of the graphite). This can be observed in **Figure 5-38**, whereby the five high temperature peaks represent the fuel, and the three low temperature peaks represent the coolant channels in STAR-CCM+. A low temperature at the apex is still observed due to the absence of a fuel rod.

The average temperature difference between the respective fuel temperatures (STAR-CCM+ middle probe and Flownex) near the apex (at the zero position) is 2.03 % and next to the bypass gap is 0.19 %.

One must note that the distance from the apex to the bypass gap has increased (0.18 m to 0.2 m); this is because the analysis is conducted on the hypotenuse side of the triangle in both Flownex and STAR-CCM+ as indicated in **Figure 5-36**.

The mass averaged helium inlet and outlet temperatures are indicated in **Table 5-8**.

**Table 5-8: Inlet and outlet coolant temperatures.**

Code	Inlet temperature (°C)	Outlet temperature (°C)
STAR-CCM+	490	542.94
Flownex	490	542.98

The rise in temperature is in accordance with energy conservation. According to Tak et al. (2011), the inlet and outlet temperature of the coolant is 490 °C and 950 °C respectively for a full assembly which comprises of 10 fuel blocks vertically stacked on top of each other. This implies that for each block there is an increase in temperature by 46 °C. In this study the maximum increase in temperature of the coolant is 52.98 °C. The average percent difference is 14.1 %. This difference could be attributed by the constant properties that were assumed in both models.

### 5.5.2 Conclusion

The Flownex model also provided details for the fuel, graphite and coolant temperatures but separately as compared to the STAR-CCM+ which combined all the details into one graph. The Flownex results might also have been affected by the problem that was observed in case 3 in section 4.5.4. However, the presence of the effect of the coolant channels probably also alleviated the problem to some extent. It can nevertheless be concluded that the Flownex results and the STAR-CCM+ results exhibit the same trend and that the agreement is satisfactory. It can thus be concluded that Flownex could form the basis of representative integrated network to model a prismatic block reactor.

### 5.6 Summary

In this chapter, the prismatic HTR core with reference to the PMR200 was described. The components that make up the prismatic core especially the standard fuel blocks were also described. The cooling of the block via standard coolant channels, bypass gaps and cross flows

was also explained. The modelling of the block was conducted in two codes, STAR-CCM+ and Flownex. The network structure in Flownex was given and for each component the inputs and outputs were described. In STAR-CCM+, the procedure describing the development of a basic fluid and heat transfer model for a fuel element was given. Details of the model include a CAD model of the geometry, mesh generation, coolant channel modelling and integration of the different materials into a combined fuel element model. A one sixth model was simulated in Flownex and in STAR-CCM+ a one twelfth model was simulated due to symmetry.

The integrated block steady state results showed a very good trend between the two codes and therefore it can be concluded that Flownex can be used to build a representative integrated network model of a prismatic block reactor.

## 6. CONCLUSION AND RECOMMENDATIONS

---

### 6.1 Introduction

In this study, a system CFD (Flownex) model that simulates the heat transfer and fluid flow in a prismatic block in a representative manner and which can be extended to model the entire reactor and the associated thermal-flow systems was discussed. The model consists of a collection of one-dimensional solid conduction heat transfer, convection heat transfer and pipe elements that are arranged in such a manner to represent the heat transfer and fluid flow in the prismatic block using a network approach. This model represents one sixth of a hexagonal prismatic block. The validity of the model was investigated by comparing the heat transfer and temperature distribution in the block for various scenarios with the corresponding values obtained using a detailed CFD model of one twelfth of a prismatic block.

This chapter presents the conclusions made from the simulation results for both the verification studies and the prismatic block, as well as recommendations for future work on this study.

### 6.2 Conclusions

The following conclusions were deduced from this study:

- Time dependence which dealt with the validity of the effect of the Fourier and Biot numbers was conducted on a rectangular block. The grid dependence in this instance was not checked. A very good comparison between the Flownex and STAR-CCM+ results was achieved. This indicated that Flownex gives correct results for pure radial conduction.
- The effect of the grid size was tested in Flownex by conducting a pure conduction case using a triangular block. Five different levels of discretisation were conducted, and an 11 node model was selected. The centre node was used to compare the temperatures of each model. There was an increase in temperature from the 3 node model to the 9 node model; however the centre node temperatures for the 11 and 13 node models were now constant indicating that the systems had reached convergence. As a result the 11 node model was chosen to be the model that other models were built on. These models were based on heat transfer in the radial direction. At the same time discretisation in the tangential direction was tested on a triangular block. Models with 3 and 5 nodes in the tangential directions were tested against a STAR-CCM+ model and results for a model with 11 nodes in the radial direction and 5 nodes in the

tangential direction (11 × 5 model) was very close to the STAR-CCM+ results. Therefore an 11 × 5 model was chosen.

- The Flownex results from a triangular block verification cases were very comparable with the STAR-CCM+ results except the case where a temperature and a uniform heat source were specified. The results were comparable in the first four equidistant points but after that Flownex reached an asymptotic value sooner than STAR-CCM+. It was concluded that this incorrect result was due to the non-orthogonal grid employed and Flownex not being able to make a provision for non-orthogonal correction terms.
- The results from the integrated block simulated in Flownex showed a good comparison with the STAR-CCM+ results. The outlet helium temperatures from Flownex and STAR-CCM+ were 542.98 ° C and 542.94 ° C respectively. In the STAR-CCM+ results, the temperatures of the solids and helium were observed how they increased along the block with a difference in the temperature between the two levels of approximately 15 K. The Flownex model provided three sets of temperatures for the fuel, graphite and coolant. The agreement between the STAR-CCM+ and Flownex models is satisfactory to good. It was thus concluded that Flownex could be used to build more advanced integrated network model of a prismatic block reactor.

### 6.3 Recommendations

The following recommendations for future work are drawn following the current study:

- Conducting a thorough study on the effect of the non-orthogonal grid in Flownex and possible way to address the issue.
- Discretising the block in the height direction in Flownex, thereby forming a 3-D model which can also account for the variation in temperature in the axial direction.
- Joining six one sixth blocks together forming a full prismatic block and investigating the effect on parameters such as helium outlet temperatures etc.
- After forming a full block from the one sixth blocks, ten blocks can then be stacked vertically on top of each other thereby forming a fuel assembly. The fuel assembly results can also be compared with other results from literature, for instance Tak et al. (2008) who investigated a numerical analysis of heat transfer within a prismatic fuel assembly of a VHTR.

## Bibliography

- Becker, S. & Laurien, E. 2003. Three-dimensional numerical simulation of flow and heat transport in high-temperature nuclear reactors. *Nuclear Engineering and Design*, 222(1):189-201.
- Bejan, Adrian. 1993. Heat Transfer. 1st ed. New York: John Wiley & Sons, Inc.
- Boyce, W. Travis. & El-Genk, Mohamed. S. 2013. Thermal-hydraulics analyses for 1/6 prismatic VHTR core and fuel element with and without bypass flow. *Energy conversion and management*, 67(1):325 - 341.
- Cengel, Yunus. A. & Turner, Robert. H. 2005. Fundamentals of thermal-fluid sciences. 2nd ed. New York: McGraw-Hill Science.
- Chapin, Doug., Scott Kiffer & Jim Nestell. 2004. The Very High Temperature Reactor: A Technical Summary. <http://www.mpr.com/uploads/news/very-high-temperature-reactor.pdf>  
Date of access: 27 August. 2014.
- Chung, T. J. 2002. Computational Fluid Dynamics. Cambridge: Cambridge University Press.
- Cioni, O., M Marchand, G Geffraye & F Ducros. 2006. 3D thermal-hydraulic calculations of a modular block-type HTR core. *Nuclear Engineering and Design*, 236(1):565-573.
- Cruz, Luis. Miguel de la. & Monsivais, Daniel. 2014. Parallel numerical simulation of two-phase flow model in porous media using distributed and shared memory architectures. *Geofísica Internacional*, 53(1):59-75.
- Du Toit, C. G. & Rosseau, P. G. 2012. Modelling the flow and heat transfer in a Packed Bed High Temperature Gas-Cooled Reactor in the context of a systems CFD Approach. *Journal Of Heat Transfer*, 134:1 - 12.
- Ferziger, J.H. & Peric, M. 2013. Computational Methods for Fluid Dynamics. 3rd ed. New York: Springer Berlin Heidelberg.
- Flow3D. 2014. Flow 3D CFD Software. <http://www.flow3d.com> Date of access: 29 October. 2014.
- Forum, U.S. DOE Nuclear Energy Advisory Committee and the Generation IV international. 2002. A Technology Roadmap for Generation IV Nuclear Energy Systems.

- Greyvenstein, GP. 2002. An implicit method for the analysis of transient flows in pipe networks. *International Journal for Numerical Methods in Engineering*, 53(2):1127 - 1143.
- Greyvenstein, G. P., van Ravenswaay, J. P. & Rousseau, P. G. 2002. Dynamic modelling of heat, mass and momentum transfer in the pebble bed modular reactor. (*In 1st International Conference on Heat Transfer, Fluid Mechanics, and Thermodynamics. Kruger Park.* )
- Harlow, H. Francis. & Welch, J. Eddie. 1965. Numerical calculation of time-dependent viscous incompressible flow of fluid with free surface. *Physics of fluids*, 8(12):1958 - 1988.
- IAEA. 2003. Evaluation of high temperature gas cooled reactor performance: Benchmark analysis related to initial testing of the HTTR and HTR-10. Vienna: Nuclear Power Technology Development Section.: IAEA-TECDOC-1382.
- IEO. 2013. International Energy Outlook. <http://www.eia.gov/forecasts/ieo/world.cfm> Date of access: 29 August. 2014.
- Incropera, Frank. P., Dewitt, David. P., Theodore, Bergman. L. & Lavine, Adrienne. S. 2007. Fundamentals of Heat and Mass Transfer. 6th ed. Hoboken: John Wiley & Sons.
- Intergraph. 2014. PBMR (Pty) Ltd., South Africa.  
<http://www.intergraph.com/customerstories/PBMR.aspx> Date of access: 04 September. 2014.
- Jayanthi, T., S. Rajeswari, K.R.S. Narayanan, H.Seetha, S. Anathanarayanan, S. Athinarayanan & P. Swaminathan. 2007. Process Simulation of Nuclear power plant using latest techniques. (*In Proceedings of the 51st Annual Meeting of the ISSS. Tokyo. p. 1-12.*)
- Kim, Min. Hwan., Tak, Nam-il. & Noh, Man. Jae. 2010. CFD Analysis of Hot Spot Fuel Temperature in the Control Fuel Block Assembly of a VHTR core. (*In Transactions of the Korean Nuclear Society Autumn Meeting. Jeju: Korea Atomic Energy Research Institute. p. 73 - 74.*)
- Kiryushin, A.I., N.G. Kodochigov , N.G. Kouzavkov , N.N. Ponomarev-Stepnoi , E.S. Gloushkov & V.N. Grebennik. 1997. Project of the GT-MHR high-temperature helium reactor with gas turbine. *Nuclear Engineering and Design*, 173(1):119-129.
- Kugeler, Kurt. & Schulten, Rodolf. 1989. HTR Technology Handbook. Illustrated ed. Berlin: Springer Berlin Heidelberg.

Lee, Sung. Nam., Tak, Nam-il., Kim, Min. Hwan. & Noh, Man. Jae. 2014. Thermal analysis of prismatic gas-cooled reactor core under coolant channel blockage accidents. *Annals of Nuclear Energy*, 71(1):11 - 22.

Lindeburg, Michael. R. 2013. Mechanical Engineering Reference Manual (for the PE Exam). 13th ed. California: Professional Publications Inc.

Lior, Noam. 2008. Energy resources and use: The present situation and possible paths to the future. *Energy*, 33(2):842 - 857.

Maruyama, So., Fujimoto, Nozomu., Sudo, Yukio., Kiso, Yoshihiro. & Hayakawa, Hitoshi. 1994. Fuel temperature analysis method for channel-blockage accident in HTTR. *Nuclear Engineering and Design*, 150(1):69 - 80.

Milman, Mark. & Petrick, Walt. 2000. A note on the solution to a common thermal network problem encountered in heat-transfer analysis of spacecraft. *Applied Mathematical Modelling*, 24(1):861 - 879.

Morrison, Faith. A. 2013. An introduction to fluid mechanics. 1st ed. New York: Cambridge University Press.

M-Tech. 2013. Flownex Library manual.

M-Tech. 2013. Flownex Library Theory Manual.

Nakano, Masaaki., Nobumasa Tsuji & Yujiro Tazawa. 2008. Conceptual Reactor Design Study of Very High Temperature Reactor (VHTR) with Prismatic - Type core. *Journal of power and Energy Systems*, 2(2):768-774.

NASA. 2000. Thermal Network Modelling Handbook. Westminster: K & K Associates.

Ortensi, Javier., Gerhard Strydom, R. Sonat Sen, Michael A. Pope, Avery Bingham, Hans Gougar, Volkan Seker, Ben Collins, Thomas Downar, Chris Ellis, Alan Baxter, Karen Vierow, Ivor D. Clifford & Kostadin Ivanov. 2013. Prismatic coupled neutronics/thermal fluids transient benchmark of the MHTGR-350 MW core design. (Benchmark Definition).

Pupeikis, Darius., Seduikyte, Lina. & Bruzgevicious, Patrikas. 2012. The Impact of the Fourier Number on Calculation Accuracy of Transient Heat Transfer in Homogeneous Enclosures. *Materials Science*, 18(3):280 - 283.

Rohde, U., S. Baier, S. Duerigen, E. Fridman, S. Kliem & B. Merk. 2012. Development and verification of the coupled 3D neutron kinetics/thermal-hydraulics code DYN3D-HTR for the

simulation of transients in block-type HTGR. *Nuclear Engineering and Design*, 251(1):412 - 422.

Rousseau, P. G. 2013. Thermal-fluid systems modelling 1 course notes. Potchefstroom: Unpublished.

Rousseau, P. G. & Greyvenstein, G. P. 2002. Modelling of the HTTR in FLOWNET. (*In Proceedings of the high temperature reactor conference. Petten.* )

Sage, Martin. 2003. PBMR Thermophysical properties. (PP100-003392-4003).

Sato, Hiruyuki., Johnson, Richard. & Schultz, Richard. 2010. Computational fluid dynamic analysis of core bypass flow phenomena in a prismatic VHTR. *Annals of Nuclear Energy*, 37(1):1172-1185.

Schallhorn, Paul. & Popok, Daniel. 1999. Interfacing a general purpose fluid network flow program with the SINDA/G thermal analysis program. Huntsville: Sverdrup Technology, Inc. (Preprint).

Shames, Irving. H. 1992. *Mechanics of Fluids*. 3rd ed. New York: McGraw-Hill.

Siemens. 2013. Flownet Library. SIMIT-HB-V7FLOWNET-2013-01-en (Reference manual).

Takamatsu, Kuniyoshi., Nakagawa, Shigeaki. & Takeda, Tetsuaki. 2006. Development of core dynamics analysis of coolant flow reduction tests of HTTR. (*In HTR2006. Johannesburg: Japan Atomic Energy Agency.* )

Tak, Nam-il., Kim, Min. Hwan. & Lee, Won. Jae. 2008. Numerical investigation of a heat transfer within the prismatic fuel assembly of a very high temperature reactor. *Annals of Nuclear Energy*, 35(1):1892-1899.

Tak, Nam-il., Kim, Min. Hwan., Lim, Hong. Sik. & Noh, Jae. Man. 2012. A practical method for whole core thermal analysis of a prismatic gas cooled reactor. *Nuclear Technology*, 177(1):352-364.

Tak, Nam-il., Kim, Min. Hwan., Lim, Hong. Sik. & Noh, Jae. Man. 2012. A practical method for whole core thermal analysis of a prismatic gas-cooled reactor. *Nuclear Technology*, 177(1):352-365.

Tak, Nam-il., Lee, Nam. Sung., Kim, Min-Hwan., Lim, Hong. Sik. & Noh, Jae. Man. 2014. Development of a core thermo-fluid analysis code for prismatic gas cooled reactors. *Nuclear Engineering and Technology*, 46(1):614 - 654.

- Tsinghua, University. 2010. Institute of Nuclear and New Energy Technology.  
<http://www.inet.tsinghua.edu.cn/publish/ineten/5696/index.html> Date of access: 02 September. 2014.
- Tung, Yu-Hsin., Johnson, Richard. W. & Sato, Hiroyuki. 2012. Effects of graphite surface roughness on bypass flow computations for an HTGR. *Nuclear Engineering and Design*, 252(1):78-87.
- Van Der Merwe, J. J. 2003. Simulation of heat and momentum transfer the High Temperature Test Reactor. Potchefstroom: North West University. (Thesis - M.Eng).
- Versteeg, H. K. & Malalasekera, W. 2007. An Introduction to Computational Fluid Dynamics: The Finite Volume Method. 2nd ed. England: Pearson Education Limited.
- WNA. 2014. Nuclear Power in South Africa. <http://www.world-nuclear.org/info/country-profiles/countries-o-s/south-africa/> Date of access: 04 September. 2014.
- Yangping, Zhou., Zhou, Kefeng., Ma, Yuanle. & Sui, Zhe. 2013. Thermal hydraulic simulation of reactor of HTR-PM based on thermal-fluid network and SIMPLE algorithm. *Progress in Nuclear Energy*, 62(1):83-93.
- Yoon, Su-Jong., Dong-Ho Shin, Hong-Sik Lim, Goon-Cherl Park & Taewan Kim. 2013. Improvement of core effective thermal conductivity model of GAMMA+ code based on CFD analysis. *Annals of Nuclear Energy*, 59(1):157-168.
- Yoon, Su. Jong., Jeong Hun Lee, Min Hwan Kim & Goon Cherl Park. 2012. The effects of crossflow gap axial bypass gap distribution on the flow characteristics in prismatic VHTR core. *Nuclear Engineering and Design*, 250(1):465-479.
- Zvizdić, Davor. & Ružinski, Nikola. 2000. Design of Heat Transfer Network Analogy Model for Complex Thermal Systems. (*In Proceedings of the 6th international design conference. Cavtat-Dubrovnik. p. 721-726.*)

## Appendix A

### A.1 Introduction

This section exhibits the determination of the mass averaged graphite block temperature ( $T_S$ ) from STAR-CCM+ using the unit cell *b* as indicated in section 3.4.1. The determination of  $T_S$  enabled the calculation of the interpolated distances from the fuel rod surface wall to the graphite and from the graphite to the coolant channel wall. The fuel surface temperature, coolant surface temperature, mass averaged graphite block temperature as well as the interpolated distances enabled the calculations of the conduction shape factors as well as the equivalent areas.

### A-2 STAR-CCM+ simulation for the unit cell *b*

**Figure A2-1** below shows the dimensions for the unit cell *b*. All measurements are in millimetres. Blocked 1 represents the coolant channel and blocked 2 represent the fuel rod. A fuel rod surface temperature of 1000 K and coolant surface temperature of 800 K was assumed. A heat transfer of 16404.6 W was obtained for the 0.793 m block.

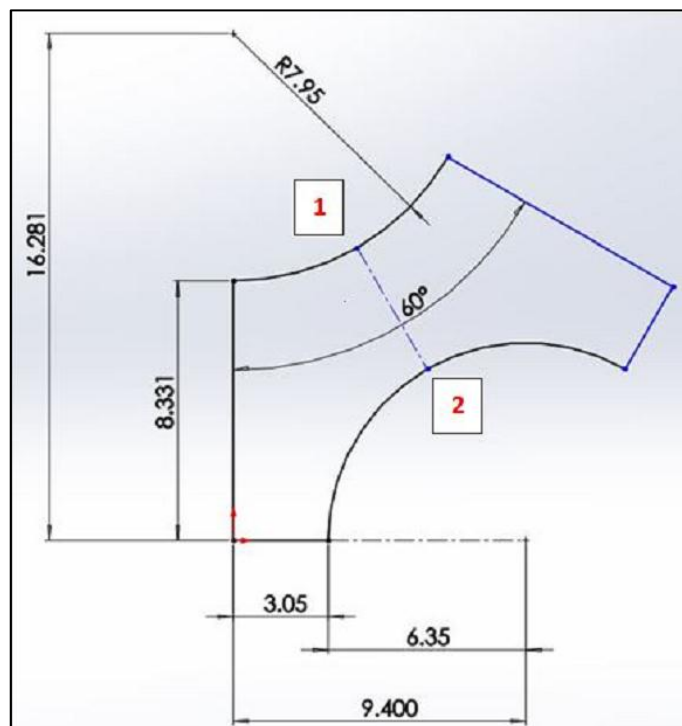


**Figure A2-1: Dimensions for the unit cell *b*.**

An average graphite block temperature of 927.5 K was obtained from STAR-CCM+ as indicated in **Figure A2-2**.

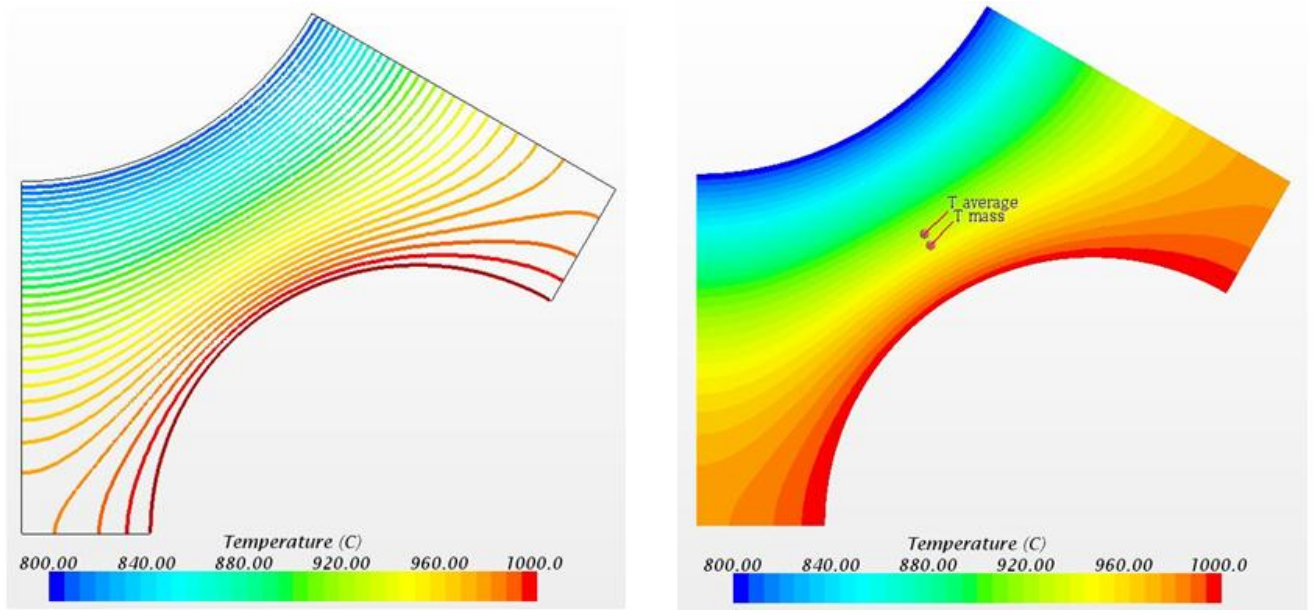


**Figure A2-2: STAR-CCM+ temperature contour lines for the unit cell *b*.**

**A-3 Calculation of interpolated distances, conduction shape factors and equivalent areas.**

The distance between the two surfaces i.e. between the fuel rod surface and coolant channel surface was first calculated. The distance between the two surfaces is indicated in **Figure A2-1** (distance between surface 1 and surface 2). Firstly two reference points were selected using the normal Cartesian plane ( $x, y$ ). The two reference points are calculated as follows:

*Point 1*

$$X_1 = 7.95 \times \sin 30^\circ \quad (\text{A3-1})$$

$$\underline{X_1 = 3.975 \text{ mm}}$$

$$Y_1 = \sin 60^\circ \times (18.8 - 7.95) \quad (\text{A3-2})$$

$$\underline{Y_1 = 9.396 \text{ mm}}$$

*Point 2*

$$X_2 = \sin 30^\circ \times (18.8 - 6.35) \quad (\text{A3-3})$$

$$\underline{X_2 = 6.225 \text{ mm}}$$

$$Y_2 = \sin 60^\circ \times 6.35 \quad (\text{A3-4})$$

$$\underline{Y_2 = 5.499 \text{ mm}}$$

Therefore the distance between the two surfaces is calculated using:

$$L_{12} = \sqrt{((X_2 - X_1)^2 + (Y_2 - Y_1)^2)} = \underline{4.5 \text{ mm}} \quad (\text{A3-5})$$

The linear temperature ratio variation was also calculated using:

$$\text{Del}_{\text{ratio}} = \frac{T_f - T_S}{T_S - T_W} = \left( \frac{1000 - 927.52}{1000 - 800} \right) \text{K} = 0.362 \quad (\text{A3-6})$$

The distance from the fuel rod surface to the graphite is calculated using:

$$L_{f(\text{average})} = \text{Del}_{\text{ratio}} \times L_{12} \quad (\text{A3-7})$$

$$L_{f(\text{average})} = 0.362 \times 4.5$$

$$L_{f(\text{average})} = 1.631 \text{ mm}$$

The distance from the graphite to coolant surface wall is calculated using:

$$L_{W(\text{average})} = (1 - 0.362) \times 4.5 = 2.869 \text{ mm} \quad (\text{A3-8})$$

It has already been established that the conduction shape factor can be calculated as indicated equation (2-2). The conduction shape factor for the heat transfer from the fuel rod to the graphite is calculated as follows:

$$S_{fs} = \frac{Q}{52.7 \times (T_f - T_S)} \quad (\text{A3-9})$$

$$S_{fs} = \frac{16404.59}{52.7 \times (1000 - 927.52)} = 4.295 \text{ m}$$

Where 52.7 is the thermal conductivity (W/m.K) and is indicated in **Appendix C-2**.

The conduction shape factor for the heat transfer from the graphite to the coolant channel wall is calculated as follows:

$$S_{sw} = \frac{Q}{52.7 \times (T_s - T_w)}$$

**(A3-10)**

$$S_{sw} = \frac{16404.59}{52.7 \times (927.52 - 800)} = 2.441 \text{ m}$$

The equivalent area for conduction is also calculated as indicated in equation **(3-24)** and equation **(3-25)**. The equivalent area for the fuel rod surface to the graphite was calculated as indicated below:

$$A_{fs} = S_{fs} \times \frac{L_{f \text{ average}}}{1000}$$

**(A3-11)**

$$A_{fs} = 4.295 \times \frac{1.631}{1000} = 0.007 \text{ m}^2$$

The equivalent area for the graphite to the coolant channel wall was also calculated as indicated below:

$$A_{sw} = S_{sw} \times \frac{L_{w \text{ average}}}{1000}$$

**(A3-12)**

$$A_{sw} = 2.441 \times \frac{2.869}{1000} = 0.007 \text{ m}^2$$

## Appendix B

### B-1 Introduction

In this section the Fourier and Biot numbers are calculated for sections 4.4.1.2 and 4.4.5.2. The corresponding time step sizes are deduced for case 1 and case 5 in the case of cubical blocks. The four different time steps discussed in section 4.4.1.2 are displayed in figures B5-1 to B5-4.

### B-2 Fourier number calculation and time step size calculation for case 1 of the cubical block (section 4.4.1.2).

A graphite block which measured 0.5 m × 0.5 m × 0.5 m was considered. The graphite block had material properties indicated in section 4.4.

The Fourier number was calculated using equation (3-29). The thermal diffusivity of the block was calculated using the graphite properties indicated in section 4.4. After converting the Watt and joule to basic units the thermal diffusivity was calculated as:

$$\alpha = \frac{k}{\rho C_p} \tag{B2-1}$$
$$\alpha = \frac{88.4}{1760 \times 0.966} = 5.2 \times 10^{-5} \text{m}^2/\text{s}$$

Incorporating the stability criterion for a 1-D interior node, where  $F_0 \leq \frac{1}{2}$  into the Fourier number equation (3-29), then  $\Delta t$  is calculated as follows:

$$\Delta t = \frac{F_0 \times \Delta x^2}{\alpha} \tag{B2-2}$$
$$\Delta t = \frac{0.5 \times 0.025^2}{5.1995 \times 10^{-5}} \approx 6 \text{ seconds}$$

Where 0.025 m is the distance between nodes.

### B-3 Biot and Fourier number collaboration for case 5 of the cubical block (section 4.4.5.2).

The graphite block discussed in B-2 now uses the Fourier and Biot numbers because there is convection. The most restrictive stability criterion (Table 3-1) for a node at the exterior corner with convection is given by:

$$Fo(1 + Bi) \leq \frac{1}{4} \quad (\text{B3-1})$$

where the Biot number (Bi) is calculated using equation (3-28).

Since the convective heat coefficient is already given for case 5, the Biot number is calculated as follows:

$$Bi = \frac{h \times L}{k} \quad (\text{B3-2})$$

$$Bi = \frac{1100 \times 0.025}{88.4} = 0.311$$

The Fourier number is now calculated using the relation in equation Error! Reference source not found. and  $F_o \leq 0.191$ . Using equation (3-29)  $\Delta t$  is calculated as:

$$\Delta t = \frac{F_o \times \Delta x^2}{\alpha} \quad (\text{B3-3})$$

$$\Delta t = \frac{0.191 \times 0.025^2}{5.1995 \times 10^{-5}} = 2.29 \text{ seconds}$$

#### **B-4 Fourier number calculation and time step size calculations for case 2 of the triangular block (section 4.5.3).**

An equilateral triangular graphite block was considered. The block material properties are given in **Table 5-1**. The thermal diffusivity of the block after converting the Watt and Joule to basic units was calculated as indicated below:

$$\alpha = \frac{k}{\rho C_p} \quad (\text{B4-1})$$

$$\alpha = \frac{52.7}{1740 \times 1.5 \times 1000} = 2.019 \times 10^{-5} \text{ m}^2/\text{s}$$

The stability criterion for a 2-D is given by:

$$F_o \leq \frac{1}{4} \quad (\text{B4-2})$$

Using equation (3-29) and (B4-2)  $\Delta t$  is calculated to be:

$$\Delta t = \frac{F_o \times \Delta x^2}{\alpha}$$

(B4- 3)

$$\Delta t = \frac{0.25 \times 0.018^2}{2.019 \times 10^{-5}} = 4 \text{ seconds}$$

Where 0.018 m is the distance between nodes.

## B-5 Results of the four different time step sizes for section 4.4.1.2.

### B-5.1 Six seconds time step size

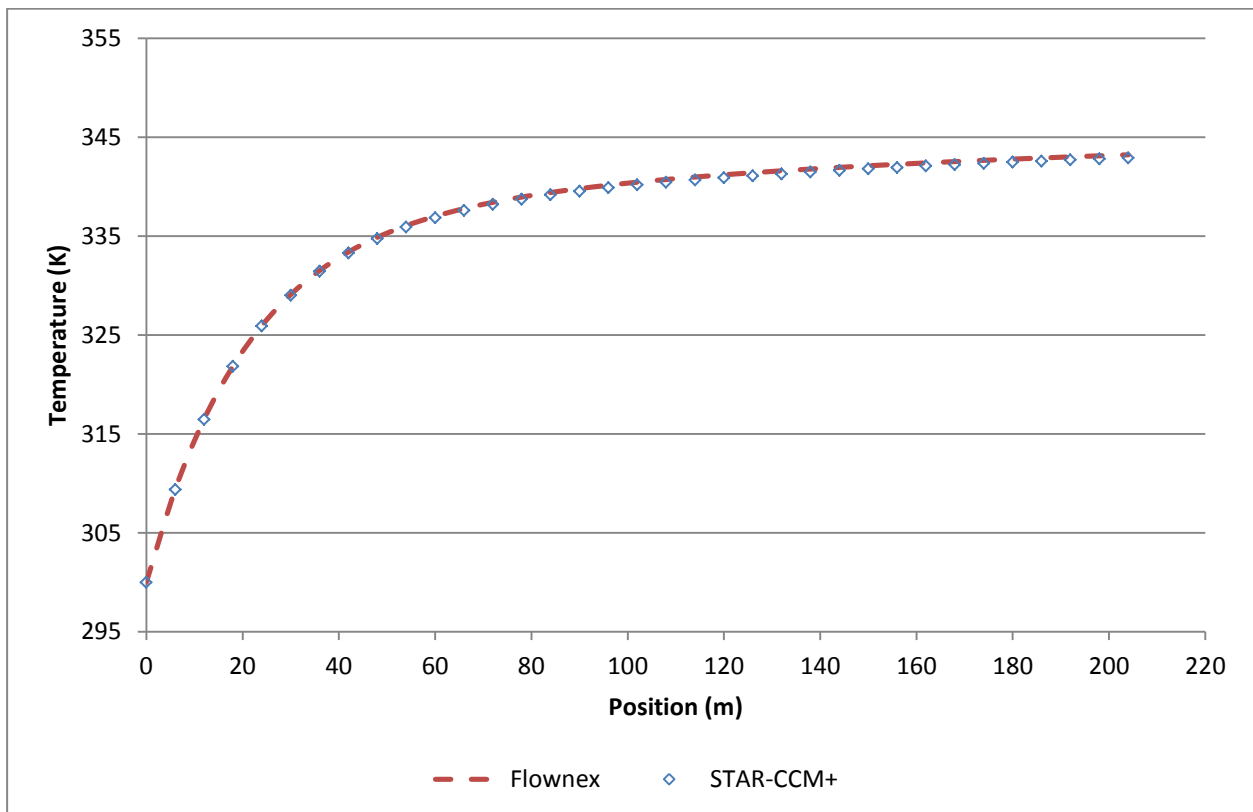


Figure B5-1: Six seconds time step size for case 1.

### B-5.2 Four seconds time step size

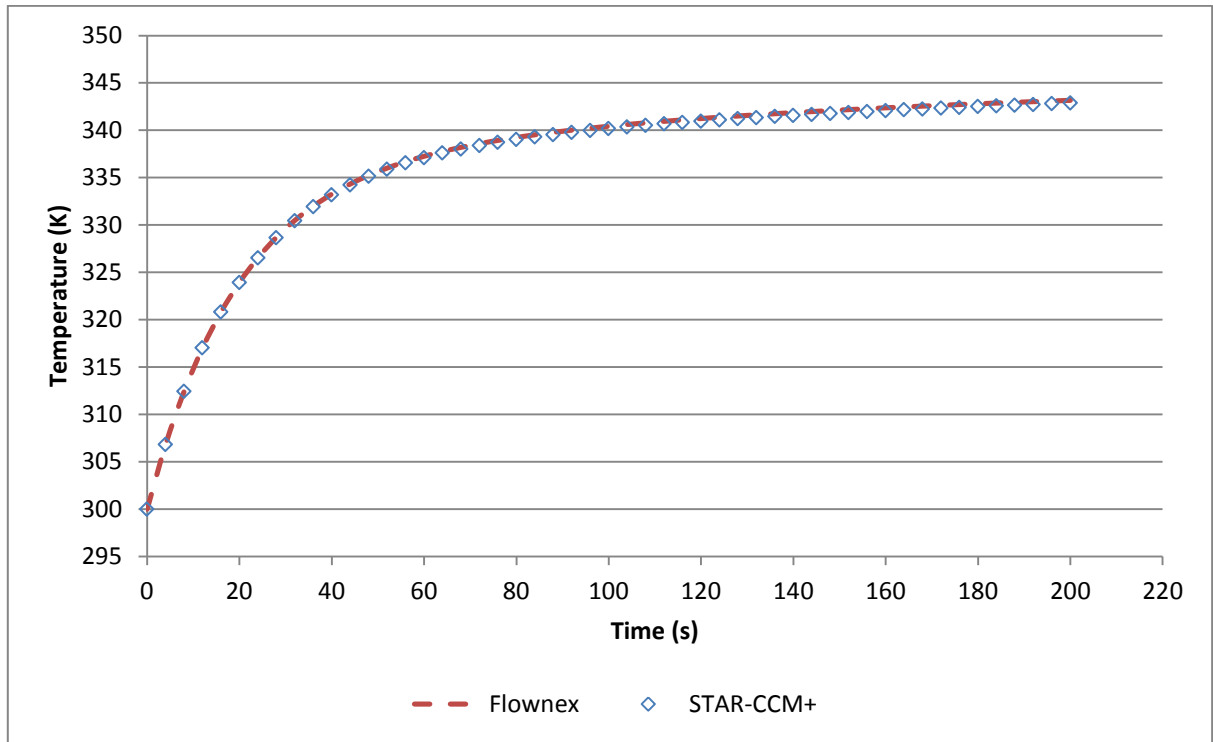


Figure B5-2: Four seconds time step size for case 1.

### B-5.3 Two seconds time step size

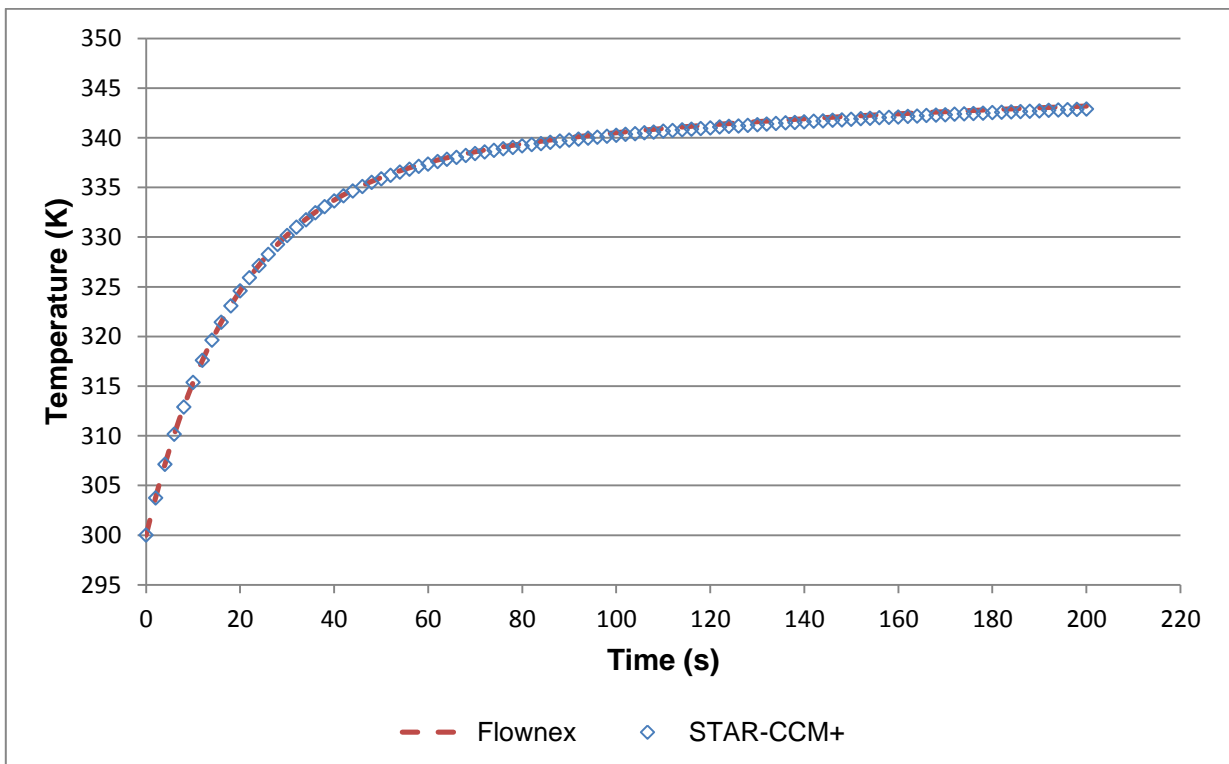
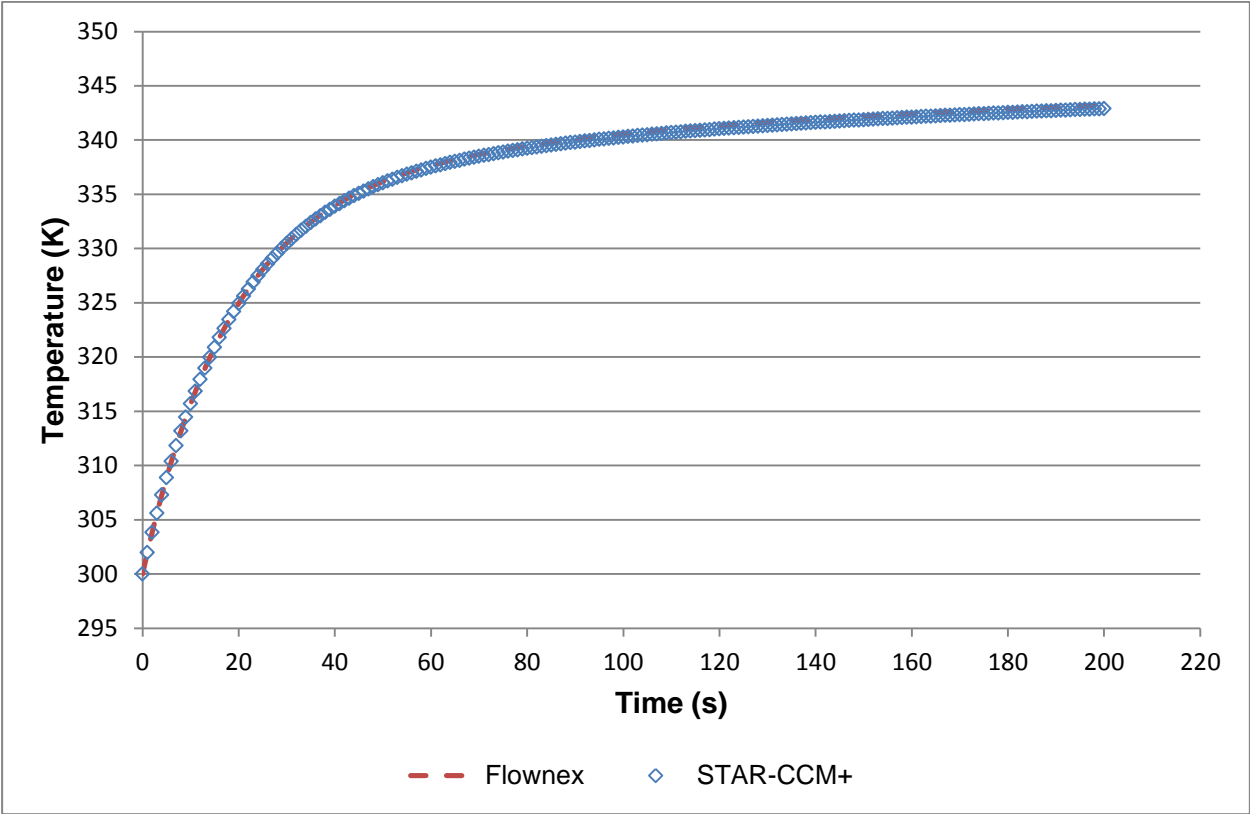


Figure B5-3: Two seconds time step size for case 1.

**B-5.4 One second time step size**



**Figure B5-4: One second time step size for case 1.**

## Appendix C

### C-1 Introduction

In this section the calculation of the effective thermal conductivity of the core as well as the geometric view factor will be exhibited. The calculations conducted for the different elements in Flownex will also be displayed. These elements include: the CHT element, convection element, the pipe element as well as the nodes and boundary elements. The final 11 × 5 node model will be displayed as well.

### C-2 Calculation of the effective thermal conductivity of the fuel block.

As already mentioned the effective thermal conductivity of the fuel block is a phenomenological parameter that seeks to express the combined conductive properties of the various materials comprising the prismatic block, accounting also for the volume fractions as well as radiative effects.

The radial thermal conductivity of the block is calculated from equation (5-1):

$$\frac{k_{\text{eff,rad}(1)}}{k_S} = \frac{1 - \frac{\alpha_C(k_S - k_C)}{(k_S + k_C)} - \alpha_f \frac{(k_S - k_f)}{(k_S + k_f)}}{1 + \frac{\alpha_C(k_S - k_C)}{(k_S + k_C)} + \alpha_f \frac{(k_S - k_f)}{(k_S + k_f)}} \quad (\text{C2-1})$$

According to Yoon et al. (2013), the thermal conductivity of the graphite ( $k_S$ ) is 116 W/m.K and that of the fuel compact ( $k_f$ ) is 12 W/m.K.

The thermal conductivity of the coolant channel includes the radiation heat transfer as indicated in equation (C2-2):

$$k_c = k_{\text{gas}} + 0.5D_h^{\text{CH}}4F\sigma T^3 \quad (\text{C2-2})$$

The geometric view factor calculation will be shown in Appendix C-3. The thermal conductivity of helium ( $k_{\text{gas}}$ ) is 0.1513 W/m.K (Yoon *et al.*, 2013). The average graphite temperature within the core is estimated to be 1039.5 K. Therefore the thermal conductivity of the coolant channel is calculated to be:

$$k_c = 0.1513 + 0.5 \times 0.0159 \times 4 \times 0.636619772 \times 5.67 \times 10^{-8} \times 1039.5^3 \quad (\text{C2-3})$$

$$k_c = 1.441$$

The volume fraction of the coolant channels ( $\alpha_C$ ) is calculated by dividing the total volume covered by the coolant channels by the total volume of the block. This is indicated below:

$$\text{Volume fraction } (\alpha_c) = \frac{\text{Total volume covered by coolant channels}}{\text{Total volume of prismatic block}} \quad (\text{C2-4})$$

$$\text{Volume of 1 coolant channel} = \pi \times r^2 \times H \quad (\text{C2-5})$$

$$\text{Volume of 1 coolant channel} = \pi \times 0.795^2 \times 79.3$$

$$\text{Volume of 1 coolant channel} = 157.46 \text{ cm}^3$$

Total volume of coolant channels

$$= \text{Volume of 1 coolant channel}$$

$$\times \text{total number of coolant channels in a block} \quad (\text{C2-6})$$

$$\text{Total volume of coolant channels} = 157.46 \times 18$$

$$\text{Total volume of coolant channels} = 2834.2 \text{ cm}^3$$

$$\text{Total volume of prismatic block} = \frac{1}{2} \times \text{length} \times \text{width} \times \text{height}$$

$$\text{Total volume of prismatic block} = \frac{1}{2} \times 20.7846 \times 18 \times 79.3 \quad (\text{C2-7})$$

$$\text{Total volume of prismatic block} = 14833.98 \text{ cm}^3$$

Therefore:

$$\alpha_c = \frac{2835.336381}{14833.97594} = 0.191 \quad (\text{C2-8})$$

In a similar manner, the volume fraction of the fuel compacts was calculated in a similar manner i.e. the total volume covered by the fuel rods was divided by the total volume of the prismatic block.

$$\text{Volume fraction } (\alpha_f) = \frac{\text{Total volume covered by fuel rods}}{\text{Total volume of the prismatic block}} \quad (\text{C2-9})$$

$$\text{Volume of 1 fuel rod} = \pi \times r^2 \times H$$

$$\text{Volume of 1 fuel rod} = \pi \times 0.635^2 \times 79.3 \quad (\text{C2-10})$$

$$\text{Volume of 1 coolant channel} = 100.455 \text{ cm}^3$$

$$\begin{aligned}
& \text{Total volume of fuel rods} \\
& = \text{Volume of 1 fuel rod} \qquad \qquad \qquad \text{(C2-11)} \\
& \quad \times \text{total number of fuel rods in a block} \\
& \text{Total volume of fuel rods} = 100.455 \times 35 \\
& \text{Total volume of fuel rods} = 3515.917 \text{ cm}^3
\end{aligned}$$

Therefore:

$$\alpha_f = \frac{3515.917}{14833.97594} = 0.237 \qquad \qquad \qquad \text{(C2-12)}$$

The radial thermal conductivity of the graphite was then calculated using equation (C2-1) after substituting  $\alpha_f, \alpha_c, k_c, k_s$  and  $k_f$ . The radial thermal conductivity was calculated to be 52.225 W/m.K. In order to make sure all material properties are the same the axial thermal conductivity assumed the value of the radial thermal conductivity.

**C-3 Radiation geometric view factor calculation**

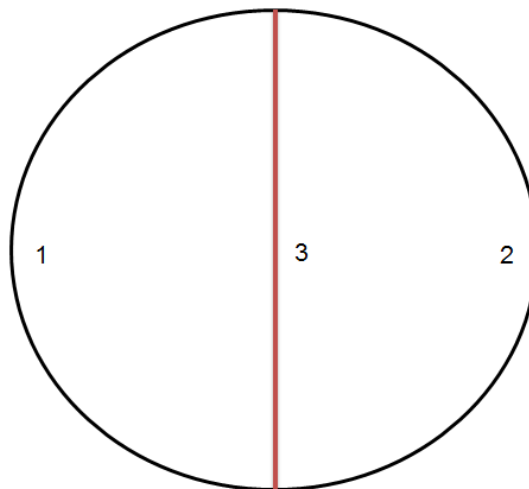


**Figure C3-1: Radiation view factor between two enclosed surfaces.**

Since all radiation leaving the inner surface must reach the outer surface, it follows that  $F_{31} = 1$  and  $F_{32} = 1$ . Using

$$A_i F_{ij} = A_j F_{ji} \quad (\text{C3-1})$$

$$A_3 F_{31} = A_1 F_{13}$$

Since  $F_{31} = 1$ , which leaves:

$$A_3 = A_1 F_{13}$$

$$F_{13} = \frac{A_3}{A_1}$$

(C3-2)

$$F_{13} = \frac{D \times H}{\frac{1}{2} \times \pi \times D \times H}$$

Therefore:

$$F_{13} = \frac{2}{\pi} \approx 0.6366 \quad (\text{C3-3})$$

#### C-4 Flownex Parameters

In this section the calculations conducted for the Flownex model are given. An 11 × 5 node model is used in this study, but however a 3 × 3 node model is described in this section. This is because the calculations for both models were conducted in a similar manner, and as a manner of simplifying all calculations, calculations for a 3 × 3 node model will be given.

**Figure 5-7** and **Figure 5-8** shows the heat transfer and flow network for a simple 3 × 3 node model. **Table C4-1** below shows some parameters used for the Flownex model.

**Table C4-1: Flownex parameters used in modelling a 1/6<sup>th</sup> segment.**

Number of fuel rods	35
Number of coolant channels	18
Height of block (cm)	79.3
Diameter of the coolant channel (cm)	1.59
Width of each segment (cm)	4.5
Total Heat Input (kW)	98

The area of the coolant channels is calculated as indicated in equation **(C4-1)**.

$$\text{Area of coolant channel} = \pi \times \frac{D^2}{4}$$

$$\text{Area of coolant channel} = \pi \times \frac{1.59^2}{4} \quad \text{(C4-1)}$$

$$\text{Area of coolant channel} = 1.99 \text{ cm}^2$$

The area of the 1/6<sup>th</sup> segment is calculated as indicated in equation **(C4-2)**.

$$\text{Area of } \frac{1}{6} \text{th segment} = \frac{1}{2} \times b \times h$$

$$\text{Area of } \frac{1}{6} \text{th segment} = \frac{1}{2} \times 20.78 \times 18 \quad \text{(C4-2)}$$

$$\text{Area of } \frac{1}{6} \text{th segment} = 187.02 \text{ cm}^2$$

The 1/6<sup>th</sup> segment was divided into sixteen CVs as indicated in **Figure C4-1**. The following calculations indicate how the 16 CVs were calculated. Each CV is indicated in **Figure C4-1**.

$$\begin{aligned} \text{Area of CV 1} = & \left( \text{Width of each segment} \times \tan 30^\circ \times \text{Width of segment} \right. \\ & \left. \times \frac{1}{2} \right) - \left( \text{Width of each segment} \times \tan 15^\circ \right. \\ & \left. \times \text{Width of each segment} \times \frac{1}{2} \right) \quad \text{(C4-3)} \end{aligned}$$

$$\text{Area of CV 1} = \left( 4.5 \times \tan 30^\circ \times 4.5 \times \frac{1}{2} \right) - \left( 4.5 \times \tan 15^\circ \times 4.5 \times \frac{1}{2} \right)$$

$$\underline{\text{Area of CV 1} = 3.13 \text{ cm}^2}$$

$$\text{Area of CV 2} = \text{Width of segment} \times \tan 15^\circ \times \text{Width of segment} \times \frac{1}{2}$$

$$\text{Area of CV 2} = 4.5 \times \tan 15^\circ \times 4.5 \times \frac{1}{2} \quad \text{(C4-4)}$$

$$\underline{\text{Area of CV 2} = 2.71 \text{ cm}^2}$$

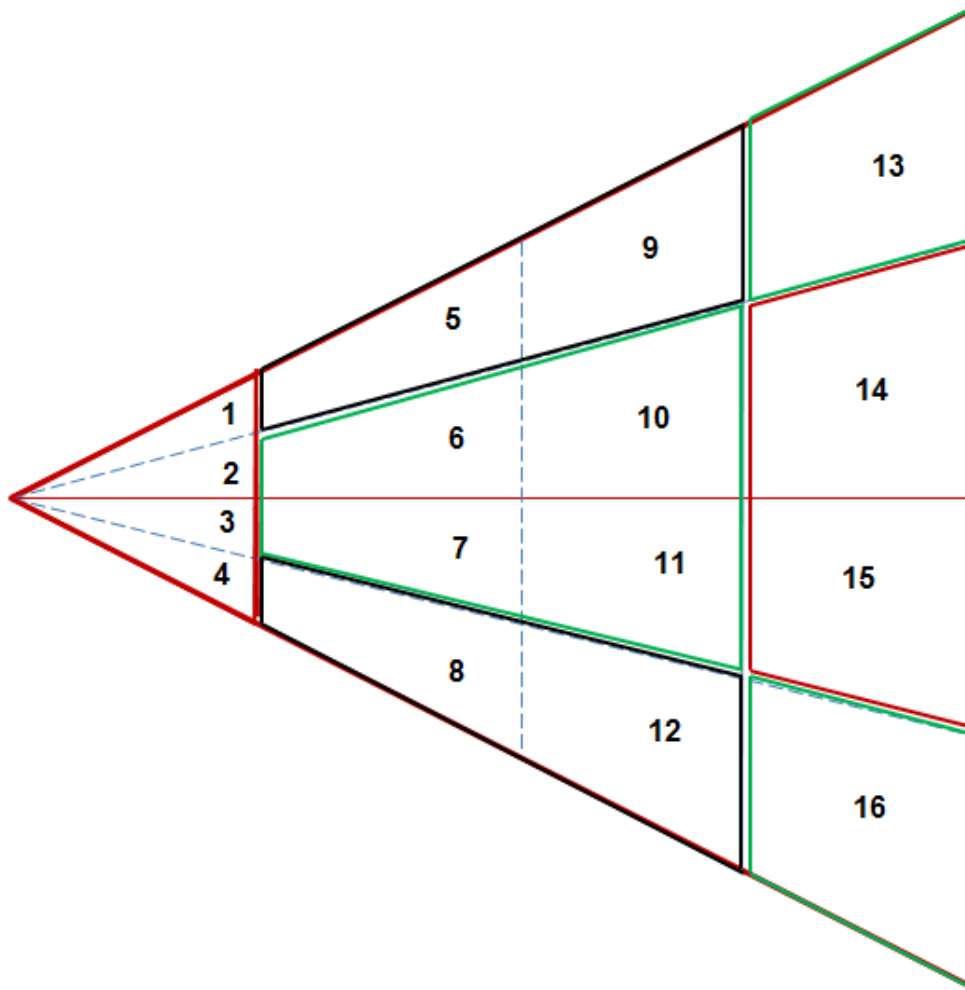


**Figure C4-1: Control volumes for a 3 × 3 node model.**

$$\underline{\text{Area of CV 3} = \text{Area of CV 2} = 2.71 \text{ cm}^2} \quad \text{(C4-5)}$$

$$\underline{\text{Area of CV 4} = \text{Area of CV 1} = 3.13 \text{ cm}^2} \quad \text{(C4-6)}$$

$$\begin{aligned} \text{Area of CV 5} = & ((2 \times \text{Width of segment} \\ & \times \tan 30^\circ \times 2 \times \text{width of segment} \times \frac{1}{2}) - (2 \\ & \times \text{Width of segment} \\ & \times \tan 15^\circ \times 2 \times \text{Width of segment} \times \frac{1}{2}) - \text{Area of CV 1} \end{aligned} \quad \text{(C4-7)}$$

$$\begin{aligned} \text{Area of CV 5} &= (2 \times 4.5 \\ &\quad \times \tan 30^\circ \times 2 \times 4.5 \times \frac{1}{2}) - (2 \times 4.5 \\ &\quad \times \tan 15^\circ \times 2 \times 4.5 \times \frac{1}{2}) - 3.13 \end{aligned}$$

$$\underline{\text{Area of CV 5} = 9.40 \text{ cm}^2}$$

$$\begin{aligned} \text{Area of CV 6} &= (2 \times \text{Width of segment} \\ &\quad \times \tan 15^\circ \times 2 \times \text{Width of segment} \times \frac{1}{2}) - \text{Area of CV 2} \end{aligned} \quad \text{(C4-8)}$$

$$\text{Area of CV 6} = (2 \times 4.5 \times \tan 15^\circ \times 2 \times 4.5 \times \frac{1}{2}) - 2.71$$

$$\underline{\text{Area of CV 6} = 8.14 \text{ cm}^2}$$

$$\underline{\text{Area of CV 7} = \text{Area of CV 6} = 8.14 \text{ cm}^2} \quad \text{(C4-9)}$$

$$\underline{\text{Area of CV 8} = \text{Area of CV 5} = 9.40 \text{ cm}^2} \quad \text{(C4-10)}$$

$$\begin{aligned} \text{Area of CV 10} &= ((3 \times \text{Width of segment} \\ &\quad \times \tan 15^\circ \times 3 \times \text{Width of segment} \times \frac{1}{2}) - (\text{Area of CV 6} \\ &\quad + \text{Area of CV 2})) \end{aligned} \quad \text{(C4-11)}$$

$$\text{Area of CV 10} = ((3 \times 4.5 \times \tan 15^\circ \times 3 \times 4.5 \times \frac{1}{2}) - (8.14 + 2.17))$$

$$\underline{\text{Area of CV 10} = 13.56 \text{ cm}^2}$$

$$\begin{aligned}
 \text{Area of CV 9} = & ((3 \times \text{Width of segment} \\
 & \times \tan 30^\circ \times 3 \times \text{Width of segment} \times \frac{1}{2}) \\
 & - (\text{Area of CV 1} + \text{Area of CV 2} \\
 & + \text{Area of CV 5} + \text{Area of CV 6} \\
 & + \text{Area of CV 10}))
 \end{aligned} \tag{C4-12}$$

$$\begin{aligned}
 \text{Area of CV 9} = & ((3 \times 4.5 \\
 & \times \tan 30^\circ \times 3 \times 4.5 \times \frac{1}{2}) - (3.13 + 2.17 \\
 & + 9.40 + 8.14 + 13.56))
 \end{aligned}$$

$$\underline{\text{Area of CV 9} = 15.66 \text{ cm}^2}$$

$$\underline{\text{Area of CV 11} = \text{Area of CV 10} = 13.56 \text{ cm}^2} \tag{C4-13}$$

$$\underline{\text{Area of CV 12} = \text{Area of CV 9} = 15.66 \text{ cm}^2} \tag{C4-14}$$

$$\begin{aligned}
 \text{Area of CV 14} = & ((4 \times \text{Width of segment} \\
 & \times \tan 15^\circ \times 4 \times \text{Width of segment} \times \frac{1}{2}) - (\text{Area of CV 10} \\
 & + \text{Area of CV 6} + \text{Area of CV 2}))
 \end{aligned} \tag{C4-15}$$

$$\begin{aligned}
 \text{Area of CV 14} = & ((4 \times 4.5 \times \tan 15^\circ \times 4 \times 4.5 \times \frac{1}{2}) - (13.56 + 8.14 \\
 & + 2.17))
 \end{aligned}$$

$$\underline{\text{Area of CV 14} = 18.99 \text{ cm}^2}$$

$$\begin{aligned}
\text{Area of CV 13} = & ((4 \times \text{Width of segment} \\
& \times \tan 30^\circ \times 4 \times \text{Width of segment} \times \frac{1}{2}) \\
& - (\text{Area of CV 14} + \text{Area of CV 10} + \text{Area of CV 9} \\
& + \text{Area of CV 6} + \text{Area of CV 5} + \text{Area of CV 2} \\
& + \text{Area of CV 1}))
\end{aligned}
\tag{C4-16}$$

$$\begin{aligned}
\text{Area of CV 13} = & ((4 \times 4.5 \\
& \times \tan 30^\circ \times 4 \times 4.5 \times \frac{1}{2}) - (18.99 + 13.56 + 15.66 + 8.14 \\
& + 9.40 + 2.71 + 3.13))
\end{aligned}$$

$$\text{Area of CV 13} = \underline{21.93 \text{ cm}^2}$$

$$\text{Area of CV 15} = \text{Area of CV 14} = \underline{18.99 \text{ cm}^2}
\tag{C4-17}$$

$$\text{Area of CV 16} = \text{Area of CV 13} = \underline{21.93 \text{ cm}^2}
\tag{C4-18}$$

The areas can be combined to form 7 CVs. This is indicated in **Figure C4-2**. Below are the calculations for combined segments.

$$\begin{aligned}
\text{Area of combined CV 1} & \tag{C4-19} \\
& = \text{Area of CV 1} + \text{Area of CV 2} \\
& + \text{Area of CV 3} + \text{Area of CV 4}
\end{aligned}$$

$$\text{Area of combined CV 1} = 3.13 + 2.71 + 2.71 + 3.13$$

$$\text{Area of combined CV 1} = \underline{11.69 \text{ cm}^2}$$

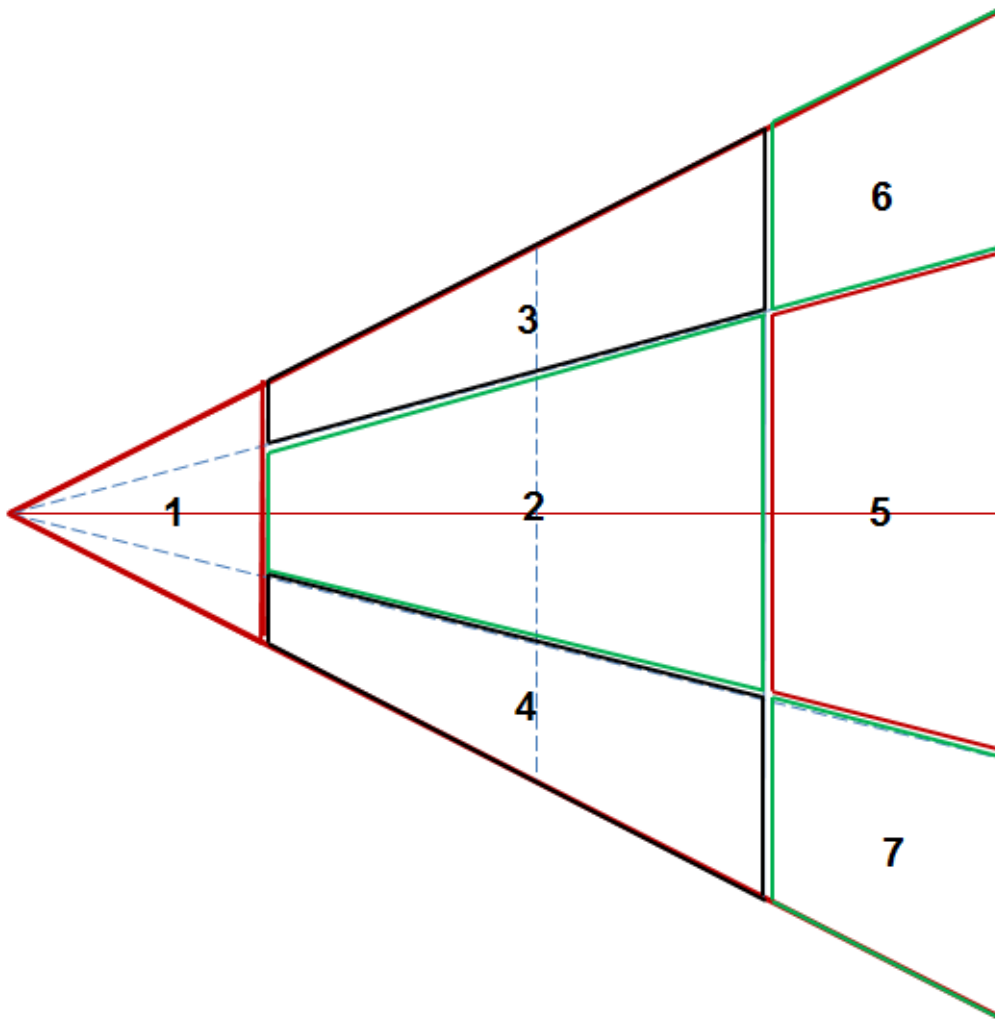


**Figure C4-2: Combined CV schematic.**

$$\begin{aligned}
 \text{Area of combined CV 2} \\
 &= \text{Area CV 6} + \text{Area of CV 7} + \text{Area of CV 10} \\
 &\quad + \text{Area of CV 11}
 \end{aligned}
 \tag{C4-20}$$

$$\text{Area of combined CV 2} = 8.14 + 8.14 + 13.56 + 13.56$$

$$\underline{\text{Area of combined CV 2} = 43.41 \text{ cm}^2}$$

$$\text{Area of combined CV 3} = \text{Area of CV 5} + \text{Area of CV 9}$$

$$\text{Area of combined CV 3} = 9.40 + 15.66
 \tag{C4-21}$$

$$\underline{\text{Area of combined CV 3} = 25.06 \text{ cm}^2}$$

$$\text{Area of combined CV 4} = \text{Area of CV 8} + \text{Area of CV 12}$$

$$\text{Area of combined CV 4} = 9.40 + 15.66 \quad \text{(C4-22)}$$

$$\underline{\text{Area of combined CV 4} = 25.06 \text{ cm}^2}$$

$$\text{Area of combined CV 5} = \text{Area of CV 14} + \text{Area of CV 15}$$

$$\text{Area of combined CV 5} = 18.99 + 18.99 \quad \text{(C4-23)}$$

$$\underline{\text{Area of combined CV 5} = 37.98 \text{ cm}^2}$$

$$\text{Area of combined CV 6} = \text{Area of CV 13}$$

$$\underline{\text{Area of CV 6} = 21.93 \text{ cm}^2} \quad \text{(C4-24)}$$

$$\text{Area of combined CV 7} = \text{Area of CV 16} \quad \text{(C4-25)}$$

$$\underline{\text{Area of combined CV 7} = 21.93 \text{ cm}^2}$$

The number of coolant channels for each CV is calculated as indicated below.

Number of coolant channels for the  $\frac{1}{6}$ th segment

$$= \frac{\text{Total number of coolant channels in a standard fuel block}}{6 \text{ Segments}}$$

**(C4-26)**

$$\text{Number of coolant channels for the } \frac{1}{6} \text{th segment} = \frac{108}{6} = 18$$

number of coolant channels in all CVs

$$= \frac{\text{Area of CV}}{\text{Area of } \frac{1}{6} \text{th segment}} \times \text{Total number of coolant channels}$$

**(C4-27)**

$$\text{Number of coolant channels in CV 1} = \frac{3.13}{187.02} \times 18 = 0.30 \quad \text{(C4-28)}$$

$$\text{Number of coolant channels in CV 2} = \frac{2.71}{187.02} \times 18 = 0.26 \quad \text{(C4-29)}$$

$$\text{Number of coolant channels in CV 3} = \frac{2.71}{187.02} \times 18 = 0.26 \quad \text{(C4-30)}$$

$$\text{Number of coolant channels in CV 4} = \frac{3.13}{187.02} \times 18 = 0.30 \quad \text{(C4-31)}$$

$$\text{Number of coolant channels in CV 5} = \frac{9.40}{187.02} \times 18 = 0.90 \quad \text{(C4-32)}$$

$$\text{Number of coolant channels in CV 6} = \frac{8.14}{187.02} \times 18 = 0.78 \quad \text{(C4-33)}$$

$$\text{Number of coolant channels in CV 7} = \frac{8.14}{187.02} \times 18 = 0.78 \quad \text{(C4-34)}$$

$$\text{Number of coolant channels in CV 8} = \frac{9.40}{187.02} \times 18 = 0.90 \quad \text{(C4-35)}$$

$$\text{Number of coolant channels in CV 9} = \frac{15.66}{187.02} \times 18 = 1.51 \quad \text{(C4-36)}$$

$$\text{Number of coolant channels in CV 10} = \frac{13.56}{187.02} \times 18 = 1.31 \quad \text{(C4-37)}$$

$$\text{Number of coolant channels in CV 11} = \frac{13.56}{187.02} \times 18 = 1.31 \quad \text{(C4-38)}$$

$$\text{Number of coolant channels in CV 12} = \frac{15.66}{187.02} \times 18 = 1.51 \quad \text{(C4-39)}$$

$$\text{Number of coolant channels in CV 13} = \frac{21.93}{187.02} \times 18 = 2.11 \quad \text{(C4-40)}$$

$$\text{Number of coolant channels in CV 14} = \frac{18.99}{187.02} \times 18 = 1.83 \quad \text{(C4-41)}$$

$$\text{Number of coolant channels in CV 15} = \frac{18.99}{187.02} \times 18 = 1.83 \quad \text{(C4-42)}$$

$$\text{Number of coolant channels in CV 16} = \frac{21.93}{187.02} \times 18 = 2.11 \quad \text{(C4-43)}$$

The number of coolant channels can also be combined to form total coolant channels in the seven combined CVs. The calculations are indicated below:

$$\begin{aligned} &\text{Total number of coolant channels in combined CV 1} \\ &= \text{Number of coolant channels in CV 1} \\ &+ \text{Number of coolant channels in CV 2} \\ &+ \text{Number of coolant channels in CV 3} \\ &+ \text{Number of coolant channels in CV4} \end{aligned} \quad \text{(C4-44)}$$

$$\begin{aligned} &\text{Total number of coolant channels in combined CV1} \\ &= 0.30 + 0.26 + 0.26 + 0.30 \end{aligned}$$

Total number of coolant channels in combined CV 1 = 1.13

$$\begin{aligned} & \text{Total number of coolant channels in combined CV 2} \\ & = \text{number of coolant channels in CV 6} \\ & + \text{number of coolant channels in CV 7} \\ & + \text{number of coolant channels in CV 10} \\ & + \text{number of coolant channels in CV 11} \end{aligned} \tag{C4-45}$$

$$\begin{aligned} & \text{Total number of coolant channels in combined CV 2} \\ & = 0.78 + 0.78 + 1.31 + 1.31 \end{aligned}$$

Total number of coolant channels in combined CV 2 = 4.18

$$\begin{aligned} & \text{Total number of coolant channels in combined CV 3} \\ & = \text{number of coolant channels in CV 5} \\ & + \text{number of coolant channels in CV 9} \end{aligned} \tag{C4-46}$$

$$\text{Total number of coolant channels in combined CV 3} = 0.90 + 1.51$$

Total number of coolant channels in combined CV 3 = 2.41

$$\begin{aligned} & \text{Total number of coolant channels in combined CV 4} \\ & = \text{number of coolant channels in CV 8} \\ & + \text{number of coolant channels in CV 12} \end{aligned} \tag{C4-47}$$

$$\text{Total number of coolant channels in combined CV 4} = 0.90 + 1.51$$

Total number of coolant channels in combined CV 4 = 2.41

$$\begin{aligned}
 &\text{Total number of coolant channels in combined CV 5} \\
 &= \text{number of coolant channels in CV 14} \\
 &+ \text{number of coolant channels in CV 15}
 \end{aligned}
 \tag{C4-48}$$

$$\text{Total number of coolant channels in combined CV 5} = 1.83 + 1.83$$

$$\underline{\text{Total number of coolant channels in combined CV 5} = 3.66}$$

$$\begin{aligned}
 &\text{Total number of coolant channels in combined CV 6} \\
 &= \text{number of coolant channels in CV 13}
 \end{aligned}
 \tag{C4-49}$$

$$\underline{\text{Total number of coolant channels in combined CV 6} = 2.11}$$

$$\begin{aligned}
 &\text{Total number of coolant channels in combined CV 7} \\
 &= \text{number of coolant channels in CV 16}
 \end{aligned}
 \tag{C4-50}$$

$$\underline{\text{Total number of coolant channels in combined CV 7} = 2.11}$$

### **Graphite to Graphite Conduction elements**

The conduction elements require the solid fraction of the material. In the HTR modelling this takes into account the fraction of the perforations which are the coolant channels. The calculations of the solid fraction of the conduction elements from the graphite to the graphite (see **Figure 5-8**) are calculated as indicated below.

The total area covered by coolant channels in combined CVs is first calculated and then subtracted from the total area covered by solids. The solid fractions are calculated by dividing the total area covered by solids by the total area of the 1/6<sup>th</sup> block.

$$\begin{aligned}
 &\text{Total area covered by coolant channels in combined CV} \\
 &= \text{Area of a coolant channel} \times \text{number of coolant channels}
 \end{aligned}
 \tag{C4-51}$$

$$\text{Total area covered by coolant channels in combined CV 1} = 1.99 \times 1.13 \tag{C4-52}$$

$$\underline{\text{Total area covered by coolant channels in combined CV 1} = 2.24 \text{ cm}^2}$$

Total area covered by coolant channels in combined CV 2 =  $1.99 \times 4.18$  **(C4-53)**

Total area covered by coolant channels in combined CV 2 =  $8.32 \text{ cm}^2$

Total area covered by coolant channels in combined CV 3 =  $1.99 \times 2.41$  **(C4-54)**

Total area covered by coolant channels in combined CV 3 =  $4.80 \text{ cm}^2$

Total area covered by coolant channels in combined CV 4 =  $1.99 \times 2.41$  **(C4-55)**

Total area covered by coolant channels in combined CV 4 =  $4.80 \text{ cm}^2$

Total area covered by coolant channels in combined CV 5 =  $1.99 \times 3.66$  **(C4-56)**

Total area covered by coolant channels in combined CV 5 =  $7.28 \text{ cm}^2$

Total area covered by coolant channels in combined CV 6 =  $1.99 \times 2.11$  **(C4-57)**

Total area covered by coolant channels in combined CV 6 =  $4.20 \text{ cm}^2$

Total area covered by coolant channels in combined CV 7 =  $1.99 \times 2.11$  **(C4-58)**

Total area covered by coolant channels in combined CV 7 =  $4.20 \text{ cm}^2$

The total area covered by solid material is calculated as follows:

Total area covered by solids in combined CVs **(C4-59)**  
= Total area of combined CVs  
– Total area covered by coolant channels in combined CVs

$$\underline{\text{Total area covered by solids in combined CV 1} = 11.69 - 2.24 = 9.45 \text{ cm}^2} \quad \text{(C4-60)}$$

$$\underline{\text{Total area covered by solids in combined CV 2} = 43.41 - 8.32 = 35.09 \text{ cm}^2} \quad \text{(C4-61)}$$

$$\underline{\text{Total area covered by solids in combined CV 3} = 25.06 - 4.80 = 20.26 \text{ cm}^2} \quad \text{(C4-62)}$$

$$\underline{\text{Total area covered by solids in combined CV 4} = 25.06 - 4.80 = 20.26 \text{ cm}^2} \quad \text{(C4-63)}$$

$$\underline{\text{Total area covered by solids in combined CV 5} = 37.98 - 7.28 = 30.7 \text{ cm}^2} \quad \text{(C4-64)}$$

$$\underline{\text{Total area covered by solids in combined CV 6} = 21.93 - 4.20 = 17.73 \text{ cm}^2} \quad \text{(C4-65)}$$

$$\underline{\text{Total area covered by solids in combined CV 7} = 21.93 - 4.20 = 17.73 \text{ cm}^2} \quad \text{(C4-66)}$$

Therefore the solid fraction for each conduction element calculated using:

$$\text{Solid fraction} = \frac{\text{Total area covered by solids in combined CVs}}{\text{Total area of combined CVs}} \quad \text{(C4-67)}$$

$$\text{Solid fraction for combined CV 1} = \frac{9.45}{11.69} \quad \text{(C4-68)}$$

$$\underline{\text{Solid fraction for combined CV 1} = 0.808}$$

$$\text{Solid fraction for combined CV 2} = \frac{35.09}{43.41} \quad \text{(C4-69)}$$

$$\underline{\text{Solid fraction for combined CV 2} = 0.808}$$

$$\text{Solid fraction for combined CV 3} = \frac{20.26}{25.06} \quad \text{(C4-70)}$$

$$\underline{\text{Solid fraction for combined CV 3} = 0.808}$$

$$\text{Solid fraction for combined CV 4} = \frac{20.26}{25.06} \quad \text{(C4-71)}$$

$$\underline{\text{Solid fraction for combined CV 4} = 0.808}$$

$$\text{Solid fraction for combined CV 5} = \frac{30.7}{37.98} \quad \text{(C4-72)}$$

$$\underline{\text{Solid fraction for combined CV 5} = 0.808}$$

$$\text{Solid fraction for combined CV 6} = \frac{17.73}{21.93} \quad \text{(C4-73)}$$

$$\underline{\text{Solid fraction for combined CV 6} = 0.808}$$

$$\text{Solid fraction for combined CV 7} = \frac{17.73}{21.93} \quad \text{(C4-74)}$$

$$\underline{\text{Solid fraction for combined CV 7} = 0.808}$$

The inlet and outlet nodal areas for the conduction elements are calculated as indicated in equations

$$\begin{aligned} \text{Inlet area} &= \text{Inlet width of the CV associated with the conduction element} \\ &\times \text{height of the CV (height of the block)} \end{aligned} \quad \text{(C4-75)}$$

$$\text{Outlet area} = \text{Outlet width of the CV associated with the conduction element} \times \text{height of the CV (height of the block)} \quad (\text{C4-76})$$

Note that the inlet areas for conduction elements 1, 2 and 3 are 0 cm<sup>2</sup> because these inlet areas are situated at the apex of the block (see **Figure C4-3**)

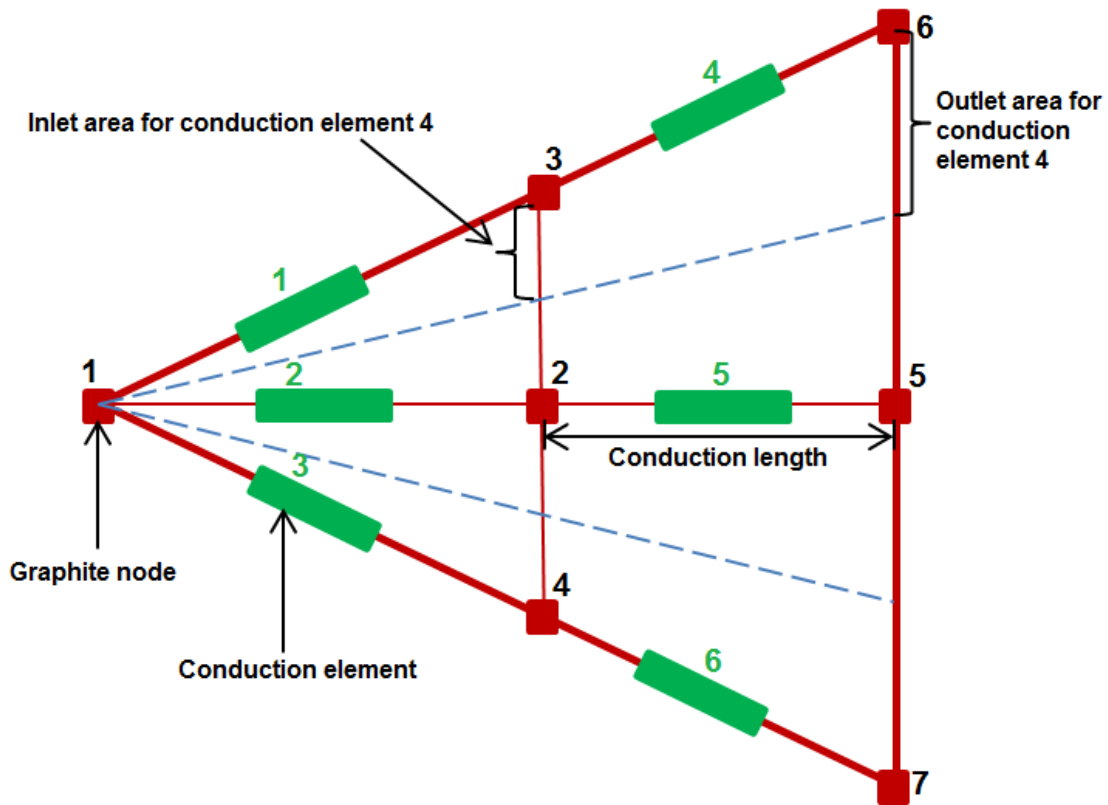


**Figure C4-3: Schematic illustrating graphite nodes, conduction distance, and inlet and outlet area.**

$$\underline{\text{Inlet area for conduction element 1}} = 0 \text{ cm}^2 \quad (\text{C4-77})$$

$$\underline{\text{Inlet area for conduction element 2}} = 0 \text{ cm}^2 \quad (\text{C4-78})$$

$$\underline{\text{Inlet area for conduction element 3}} = 0 \text{ cm}^2 \quad (\text{C4-79})$$

$$\begin{aligned} \text{Inlet area for conduction element 4} & \quad (\text{C4-80}) \\ & = ((2 \times \text{Width of segment} \\ & \quad \times \tan 30^\circ) - (2 \times \text{Width of segment} \times \tan 15^\circ)) * \text{Height} \end{aligned}$$

Inlet area for conduction element 4

$$= ((2 \times 4.5 \times \tan 30^\circ) - (2 \times 4.5 \times \tan 15^\circ)) \times 79.3$$

$$\underline{\text{Inlet area for conduction element 4} = 220.82 \text{ cm}^2}$$

Inlet area for conduction element 5

$$= (2 \times \text{Width of segment} \times \tan 15^\circ \times 2) \times \text{Height}$$

**(C4-81)**

$$\text{Inlet area for conduction element 5} = (2 \times 4.5 \times \tan 15^\circ \times 2) \times 79.3$$

$$\underline{\text{Inlet area for conduction element 5} = 382.47 \text{ cm}^2}$$

Inlet area for conduction element 6

$$= ((2 \times \text{Width of segment} \times \tan 30^\circ) - (2 \times \text{Width of segment} \times \tan 15^\circ)) * \text{Height}$$

**(C4-82)**

Inlet area for conduction element 6

$$= ((2 \times 4.5 \times \tan 30^\circ) - (2 \times 4.5 \times \tan 15^\circ)) \times 79.3$$

$$\underline{\text{Inlet area for conduction element 6} = 220.82 \text{ cm}^2}$$

$$\text{Outlet area for conduction element 1} = \text{Inlet area for conduction element 4}$$

**(C4-83)**

$$\underline{\text{Outlet area for conduction element 1} = 220.82 \text{ cm}^2}$$

$$\text{Outlet area for conduction element 2} = \text{Inlet area for conduction element 5}$$

**(C4-84)**

$$\underline{\text{Outlet area for conduction element 2} = 382.47 \text{ cm}^2}$$

$$\text{Outlet area for conduction element 3} = \text{Inlet area for conduction element 6}$$

**(C4-85)**

$$\underline{\text{Outlet area for conduction element 3} = 220.82 \text{ cm}^2}$$

$$\begin{aligned}
 &\text{Outlet area for conduction element 4} \\
 &= ((4 \times \text{Width of segment} \\
 &\quad \times \tan 30^\circ) - (4 \times \text{Width of segment} \times \tan 15^\circ)) \times \text{Height}
 \end{aligned}
 \tag{C4-86}$$

$$\begin{aligned}
 &\text{Outlet area for conduction element 4} \\
 &= ((4 \times 4.5 \times \tan 30^\circ) - (4 \times 4.5 \times \tan 15^\circ)) \times 79.3
 \end{aligned}$$

$$\underline{\text{Outlet area for conduction element 4} = 441.64 \text{ cm}^2}$$

$$\begin{aligned}
 &\text{Outlet area for conduction element 5} \\
 &= (4 \times \text{Width of segment} \times \tan 15^\circ \times 2) \times \text{Height}
 \end{aligned}$$

$$\text{Outlet area for conduction element 5} = (4 \times 4.5 \times \tan 15^\circ \times 2) \times 79.3$$

$$\underline{\text{Outlet area for conduction element 5} = 764.94 \text{ cm}^2}$$

$$\begin{aligned}
 &\text{Outlet area for conduction element 6} \\
 &= ((4 \times \text{Width of segment} \\
 &\quad \times \tan 30^\circ) - (4 \times \text{Width of segment} \times \tan 15^\circ)) \times \text{Height}
 \end{aligned}$$

**(C4-88)**

$$\begin{aligned}
 &\text{Outlet area for conduction element 6} \\
 &= ((4 \times 4.5 \times \tan 30^\circ) - (4 \times 4.5 \times \tan 15^\circ)) \times 79.3
 \end{aligned}$$

$$\underline{\text{Outlet area for conduction element 6} = 441.64 \text{ cm}^2}$$

The conduction lengths for each conduction elements are indicated below.

**Table C4- 2: Conduction lengths for graphite to graphite conduction lengths.**

Conduction element	Conduction distance (cm)
1	10.39
2	9
3	10.39
4	10.39
5	9
6	10.39

The material properties for graphite were custom defined and these are indicated in **Table 5-1**.

### **Fuel to graphite conduction**

The fuels to graphite conduction elements also require the solid fraction of the material, conduction length, and the inlet and outlet areas for conduction.

The solid fraction of the fuel to graphite conduction elements are all one since all the material is solid with no perforations from the fuel surface to the graphite (see unit cell *b* in **Figure 3-5**). The inlet and outlet areas are calculated as indicated below.

Inlet or outlet areas

$$\begin{aligned}
 &= \text{Equivalent area for fuel to graphite} && \text{(C4-89)} \\
 &\times \text{total number of fuel rods in that CV} \\
 &\times \text{Total number of coolant channels surrounding each fuel rod}
 \end{aligned}$$

Three coolant channels surround each fuel rod. The equivalent area for fuel to graphite has already been calculated as indicated in equation **(A3-11)**. The total numbers of fuel rods in each CV are calculated as indicated from equation **(C4-90)** to equation **(C4-97)**.

$$\begin{aligned} \text{Total number of fuel rods in each CV} & \qquad \qquad \qquad \text{(C4-90)} \\ & = \frac{\text{Area of each combined CV}}{\text{Area of } \frac{1}{6} \text{ th prismatic block}} \times \text{Number of fuel rods} \end{aligned}$$

$$\text{Total number of fuel rods in combined CV 1} = \frac{11.69}{187.02} \times 35 \qquad \qquad \qquad \text{(C4-91)}$$

$$\underline{\text{Total number of fuel rods in combined CV 1} = 2.19}$$

$$\text{Total number of fuel rods in combined CV 2} = \frac{43.41}{187.02} \times 35 \qquad \qquad \qquad \text{(C4-92)}$$

$$\underline{\text{Total number of fuel rods in combined CV 2} = 8.12}$$

$$\text{Total number of fuel rods in combined CV 3} = \frac{25.06}{187.02} \times 35 \qquad \qquad \qquad \text{(C4-93)}$$

$$\underline{\text{Total number of fuel rods in combined CV 3} = 4.69}$$

$$\text{Total number of fuel rods in combined CV 4} = \frac{25.06}{187.02} \times 35 \qquad \qquad \qquad \text{(C4-94)}$$

$$\underline{\text{Total number of fuel rods in combined CV 4} = 4.69}$$

$$\text{Total number of fuel rods in combined CV 5} = \frac{37.98}{187.02} \times 35 \qquad \qquad \qquad \text{(C4-95)}$$

$$\underline{\text{Total number of fuel rods in combined CV 5} = 7.11}$$

$$\text{Total number of fuel rods in combined CV 6} = \frac{21.93}{187.02} \times 35 \qquad \qquad \qquad \text{(C4-96)}$$

$$\underline{\text{Total number of fuel rods in combined CV 6} = 4.10}$$

$$\text{Total number of fuel rods in combined CV 7} = \frac{21.93}{187.02} \times 35 \quad (\text{C4-97})$$

$$\underline{\text{Total number of fuel rods in combined CV 7} = 4.10}$$

The inlet or outlet areas for fuel to graphite conduction elements are calculated as follows:

$$\underline{\text{Inlet or outlet area for conduction element 1} = 0.007 \times 2.19 \times 3 = 0.046 \text{ m}^2} \quad (\text{C4-98})$$

$$\underline{\text{Inlet or outlet area for conduction element 2} = 0.007 \times 8.12 \times 3 = 0.17 \text{ m}^2} \quad (\text{C4-99})$$

$$\underline{\text{Inlet or outlet area for conduction element 3} = 0.007 \times 4.69 \times 3 = 0.10 \text{ m}^2} \quad (\text{C4-100})$$

$$\underline{\text{Inlet or outlet area for conduction element 4} = 0.007 \times 4.69 \times 3 = 0.10 \text{ m}^2} \quad (\text{C4-101})$$

$$\underline{\text{Inlet or outlet area for conduction element 5} = 0.007 \times 7.11 \times 3 = 0.15 \text{ m}^2} \quad (\text{C4-102})$$

$$\underline{\text{Inlet or outlet area for conduction element 6} = 0.007 \times 4.10 \times 3 = 0.09 \text{ m}^2} \quad (\text{C4-103})$$

The conduction lengths are all the same as indicated in equation (A3-7).

### Graphite to coolant Conduction

The graphite to coolant conduction elements also requires the solid fraction of the material, conduction length, and the inlet and outlet areas for conduction.

The solid fraction of the fuel to graphite conduction elements are also all one since all the material is solid with no perforations from the fuel surface to the graphite (see unit cell *b* in **Figure 3-5**). The inlet and outlet areas are calculated as indicated below.

$$\begin{aligned} \text{Inlet or outlet areas} & \\ &= \text{Equivalent area for graphite to coolant} \quad (\text{C4-104}) \\ &\times \text{total number of coolant channels in that CV} \\ &\times \text{Total number of fuel rods surrounding each coolant channel} \end{aligned}$$

Six fuel rods surround each coolant channel. The equivalent area for graphite to coolant has already been calculated as indicated in equation (A3-12). The total numbers of coolant channels in each combined CV has already been calculated as indicated from equation (C4-44) to equation (C4-50).

The inlet and outlet areas for graphite to coolant conduction elements are calculated as follows:

$$\underline{\text{Inlet or outlet area for conduction element 1}} = 0.007 \times 1.13 \times 6 = 0.047 \text{ m}^2 \quad \text{(C4-105)}$$

$$\underline{\text{Inlet or outlet area for conduction element 2}} = 0.007 \times 4.18 \times 6 = 0.18 \text{ m}^2 \quad \text{(C4-106)}$$

$$\underline{\text{Inlet or outlet area for conduction element 3}} = 0.007 \times 2.41 \times 6 = 0.10 \text{ m}^2 \quad \text{(C4-107)}$$

$$\underline{\text{Inlet or outlet area for conduction element 4}} = 0.007 \times 2.41 \times 6 = 0.10 \text{ m}^2 \quad \text{(C4-108)}$$

$$\underline{\text{Inlet or outlet area for conduction element 5}} = 0.007 \times 3.66 \times 6 = 0.15 \text{ m}^2 \quad \text{(C4-109)}$$

$$\underline{\text{Inlet or outlet area for conduction element 6}} = 0.007 \times 2.11 \times 6 = 0.089 \text{ m}^2 \quad \text{(C4-110)}$$

$$\underline{\text{Inlet or outlet area for conduction element 1}} = 0.007 \times 2.11 \times 6 = 0.089 \text{ m}^2 \quad \text{(C4-111)}$$

### Fuel nodes

The heat input to the 1/6<sup>th</sup> block was applied to the fuel nodes. The heat input was distributed uniformly throughout the 1/6<sup>th</sup> block. The fuel nodes are clearly indicated in **Figure 5-7** and are also numbered similarly to the graphite nodes indicated in **Figure C4-3**. The heat input for each

$$\text{Heat input for each node} = \frac{\text{Area of each combined CV}}{\text{Area of } \frac{1}{6} \text{ th prismatic block}} \times \text{Total heat Input} \quad \text{(C4-112)}$$

fuel node is calculated as indicated in equation **(C4-112)**.

$$\text{Heat Input for node 1} = \frac{11.69}{187.02} \times 98 \quad \text{(C4-113)}$$

$$\underline{\text{Heat input for node 1} = 6.13 \text{ kW}}$$

$$\text{Heat Input for node 2} = \frac{43.41}{187.02} \times 98 \quad \text{(C4-114)}$$

$$\underline{\text{Heat input for node 2} = 22.75 \text{ kW}}$$

$$\text{Heat Input for node 3} = \frac{25.06}{187.02} \times 98 \quad \text{(C4-115)}$$

$$\underline{\text{Heat input for node 3} = 13.13 \text{ kW}}$$

$$\text{Heat Input for node 4} = \frac{25.06}{187.02} \times 98 \quad \text{(C4-116)}$$

$$\underline{\text{Heat input for node 4} = 13.13 \text{ kW}}$$

$$\text{Heat Input for node 5} = \frac{37.98}{187.02} \times 98 \quad \text{(C4-117)}$$

$$\underline{\text{Heat input for node 5} = 19.90 \text{ kW}}$$

$$\text{Heat Input for node 6} = \frac{21.93}{187.02} \times 98 \quad \text{(C4-118)}$$

$$\underline{\text{Heat input for node 6} = 11.49 \text{ kW}}$$

$$\text{Heat Input for node 7} = \frac{21.93}{187.02} \times 98 \quad \text{(C4-119)}$$

$$\underline{\text{Heat input for node 7} = 11.49 \text{ kW}}$$

## Convection Elements

The convection elements are connected to the coolant wall node. The heat that is conducted from the fuel surface via the graphite to the coolant wall is transferred to the coolant through convection. The convection elements require the heat transfer area as well as the convection correlations. In Flownex either a Dittus-Boelter correlation or a constant heat transfer coefficient is applied. In this study the Dittus-Boelter correlation was used as described in section 4.3.4.1.

The heat transfer areas were calculated as follows:

$$\begin{aligned} \text{Heat transfer area} \\ = \text{circumference of the coolant channels} \times \text{height of the block} \end{aligned} \quad \text{(C4-120)}$$

The circumference of the coolant channels in each combined CV was calculated using the formula:

$$\begin{aligned} \text{Circumference} = \pi \times \text{Diameter of coolant channel} \\ \times \text{Number of coolant channels in that combined CV} \end{aligned} \quad \text{(C4-121)}$$

The circumferences for the coolant channels in the seven combined CVs are calculated as follows:

$$\underline{\text{Circumference for coolant channels for CV 1}} = \pi \times 1.59 \times 1.13 = 5.64 \text{ cm} \quad \text{(C4-122)}$$

$$\underline{\text{Circumference for coolant channels for CV 2}} = \pi \times 1.59 \times 4.18 = 20.88 \text{ cm} \quad \text{(C4-123)}$$

$$\underline{\text{Circumference for coolant channels for CV 3}} = \pi \times 1.59 \times 2.41 = 12.04 \text{ cm} \quad \text{(C4-124)}$$

$$\underline{\text{Circumference for coolant channels for CV 4}} = \pi \times 1.59 \times 2.41 = 12.04 \text{ cm} \quad \text{(C4-125)}$$

$$\underline{\text{Circumference for coolant channels for CV 5}} = \pi \times 1.59 \times 3.66 = 18.28 \text{ cm} \quad \text{(C4-126)}$$

$$\underline{\text{Circumference for coolant channels for CV 6}} = \pi \times 1.59 \times 2.11 = 10.54 \text{ cm} \quad \text{(C4-127)}$$

$$\text{Circumference for coolant channels for CV 7} = \pi \times 1.59 \times 2.11 = 10.54 \text{ cm} \quad (\text{C4-128})$$

The convection heat transfer areas are now calculated using equation (C4-120) for each combined CV as follows:

$$\text{Heat transfer area for combined CV 1} = 5.64 \times 79.3 = 447.252 \text{ cm}^2 \quad (\text{C4-129})$$

$$\text{Heat transfer area for combined CV 2} = 20.88 \times 79.3 = 1655.78 \text{ cm}^2 \quad (\text{C4-130})$$

$$\text{Heat transfer area for combined CV 3} = 12.04 \times 79.3 = 954.77 \text{ cm}^2 \quad (\text{C4-131})$$

$$\text{Heat transfer area for combined CV 4} = 12.04 \times 79.3 = 954.77 \text{ cm}^2 \quad (\text{C4-132})$$

$$\text{Heat transfer area for combined CV 5} = 18.28 \times 79.3 = 1449.6 \text{ cm}^2 \quad (\text{C4-133})$$

$$\text{Heat transfer area for combined CV 6} = 10.54 \times 79.3 = 835.82 \text{ cm}^2 \quad (\text{C4-134})$$

$$\text{Heat transfer area for combined CV 7} = 10.54 \times 79.3 = 835.82 \text{ cm}^2 \quad (\text{C4-135})$$

### Pipe elements

The convection elements are connected to the pipes which represent the coolant channels. As indicated in **Figure 5-8**, the pipe element is a flow element. In this study, helium is custom defined and the properties are indicated in **Table 5-3**. The circumferences as well as the area of the combined CVs are specified. Since a pipe element is used, a surface roughness is also specified. A surface roughness of 20  $\mu\text{m}$  (Boyce & El-Genk, 2013) was implemented. The pipe elements also have the same numbering as the graphite nodes (see **Figure C4-3**). The circumference for each pipe element has been calculated as indicated from equations (C4-122) to (C4-128).

The areas of the piping elements (representing the coolant channels in each combined CV) were calculated using equation

$$\begin{aligned}
 &\text{Total piping area (total area for coolant channels)} \\
 &= \text{Area of 1 coolant channel} && \text{(C4-136)} \\
 &\times \text{number of coolant channels in a specified combined CV}
 \end{aligned}$$

The total areas in each combined CV for the pipe element are indicated below.

$$\underline{\text{Total piping area for combined CV 2} = 1.99 \times 1.13 = 2.25 \text{ cm}^2} \quad \text{(C4-137)}$$

$$\underline{\text{Total piping area for combined CV 2} = 1.99 \times 4.18 = 8.32 \text{ cm}^2} \quad \text{(C4-138)}$$

$$\underline{\text{Total piping area for combined CV 3} = 1.99 \times 2.41 = 4.80 \text{ cm}^2} \quad \text{(C4-139)}$$

$$\underline{\text{Total piping area for combined CV 4} = 1.99 \times 2.41 = 4.80 \text{ cm}^2} \quad \text{(C4-140)}$$

$$\underline{\text{Total piping area for combined CV 5} = 1.99 \times 3.66 = 7.28 \text{ cm}^2} \quad \text{(C4-141)}$$

$$\underline{\text{Total piping area for combined CV 6} = 1.99 \times 2.11 = 4.20 \text{ cm}^2} \quad \text{(C4-142)}$$

$$\underline{\text{Total piping area for combined CV 1} = 1.99 \times 2.11 = 4.20 \text{ cm}^2} \quad \text{(C4-143)}$$

### Flow nodes

The flow elements (pipes) were also connected to flow nodes. These flow nodes represent the inlet and outlet of the prismatic block. A temperature of 490° C and a pressure of 7 MPa were specified for the inlet and a mass flow rate 0.359 kg/s was specified for the outlet.

**Figure C4-4** clearly shows the 3 × 3 model in Flownex and all its elements. The fuel, graphite and coolant nodes 1 represent the nodes at the apex as indicated in **Figure C4-3**. The other nodes were also arranged and named in the same arrangement as that in **Figure C4-3**. The convection, cross CHT and pipe elements were arranged as indicated in **Figure 5-8**. The pipe element 8 represents the bypass gap. Pipe element 8 is a combination of all the pipe elements from the convection elements 8, 9 and 10. The inlet and outlet of the coolant for the block are represented by the flow nodes A and B. Pressure, temperature and a mass flow are specified.

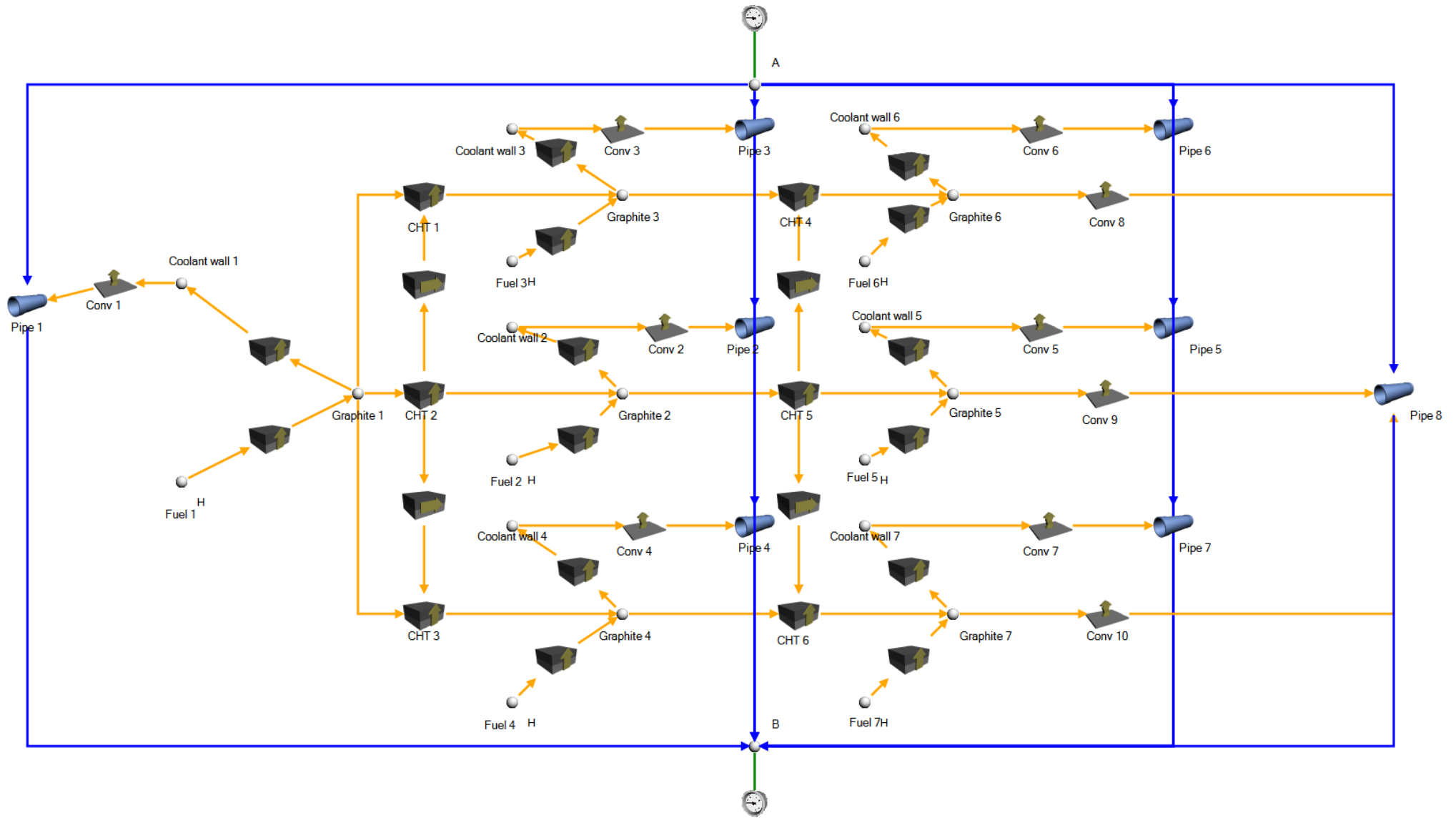


**Figure C4-4: Final 3 × 3 Flownex model with all its elements.**

## Appendix D

### D-1 Introduction

In this appendix a more detailed procedure is given for the generation of the fuel element mesh. The meshing description starts with CAD modelling.

### D-2 STAR-CCM+ Procedure

#### CAD modelling

A CAD model of a thin section of the fuel element is created. The model is shown in **Figure D2-11** below. The individual components are the graphite structure, the fuel rods, LBP rods, the cooling channels and the by-pass gap. The individual components are then exported in Parasolid format.

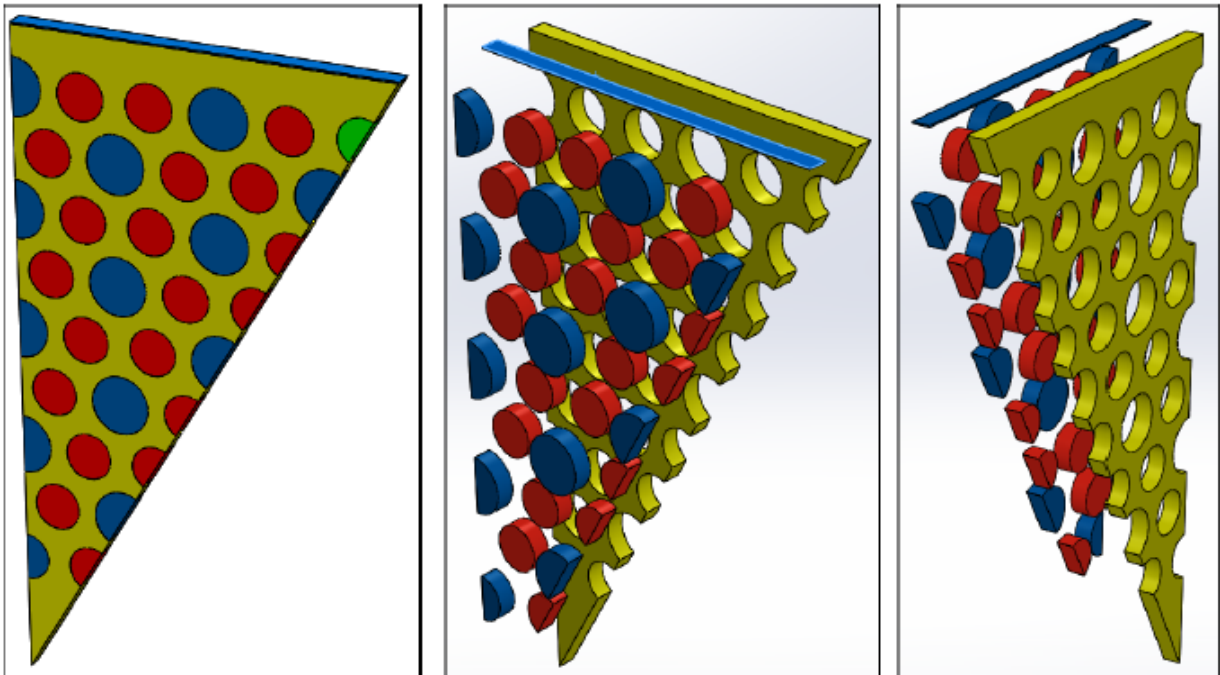


**Figure D2-1: CAD geometry of fuel rods, cooling channels, graphite, by-pass gap and LBP rods.**

#### Importation of CAD components into StarCCM+

Inside StarCCM+ the five CAD components in Parasolid format are imported as individual parts. They are renamed as Graphite, Bypass, Cool, Fuel and LBP as shown in **Figure D2-2**.

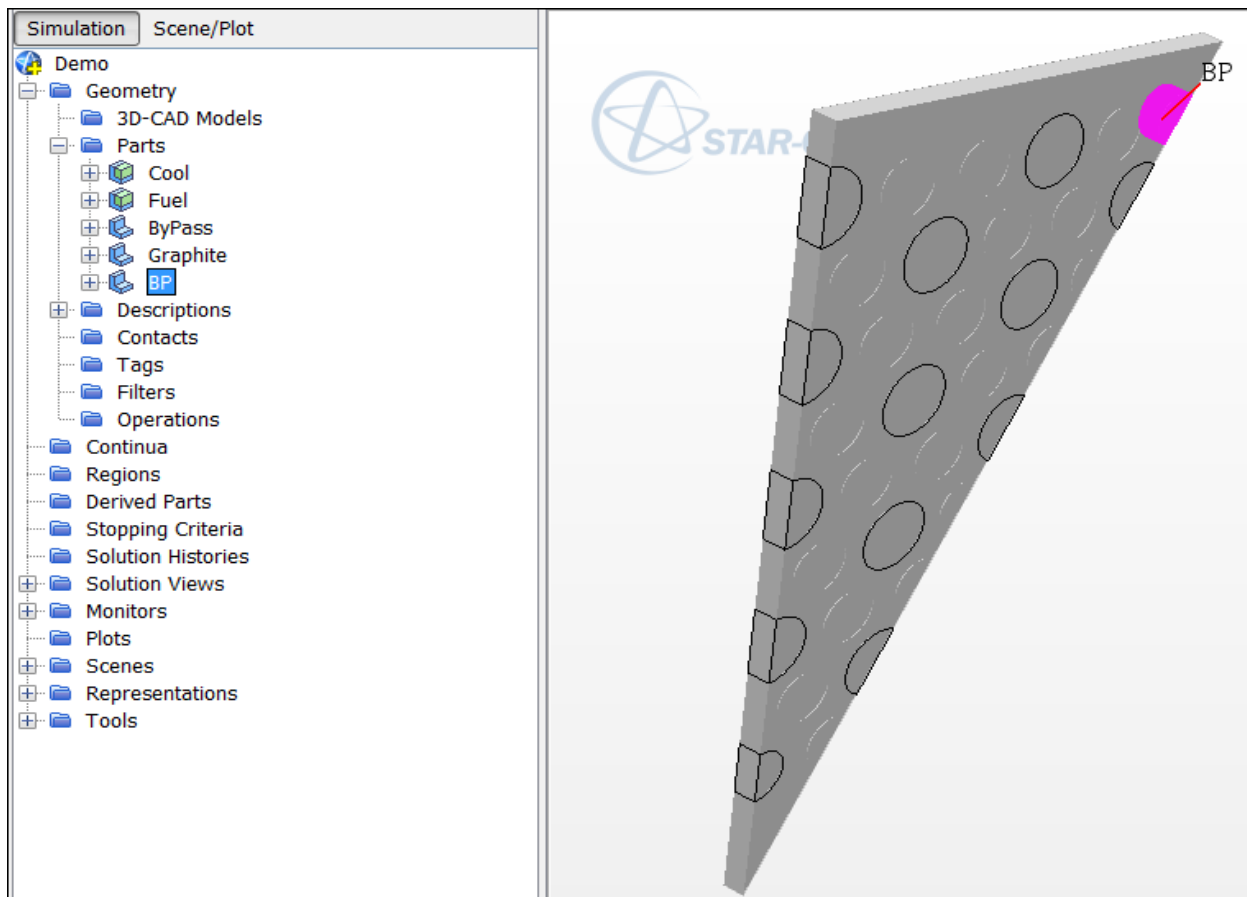


**Figure D2-2: Imported parts inside StarCCM+.**

After importing the CAD components the individual cooling channels and fuel rods will appear as separate bodies under the Cool part and Fuel part. These bodies need to be combined into a single body for the coolant and a single body for the fuel rods. Then the individual surfaces of the bodies needs to be firstly combined and then split as shown in **Figure D2-3** below.

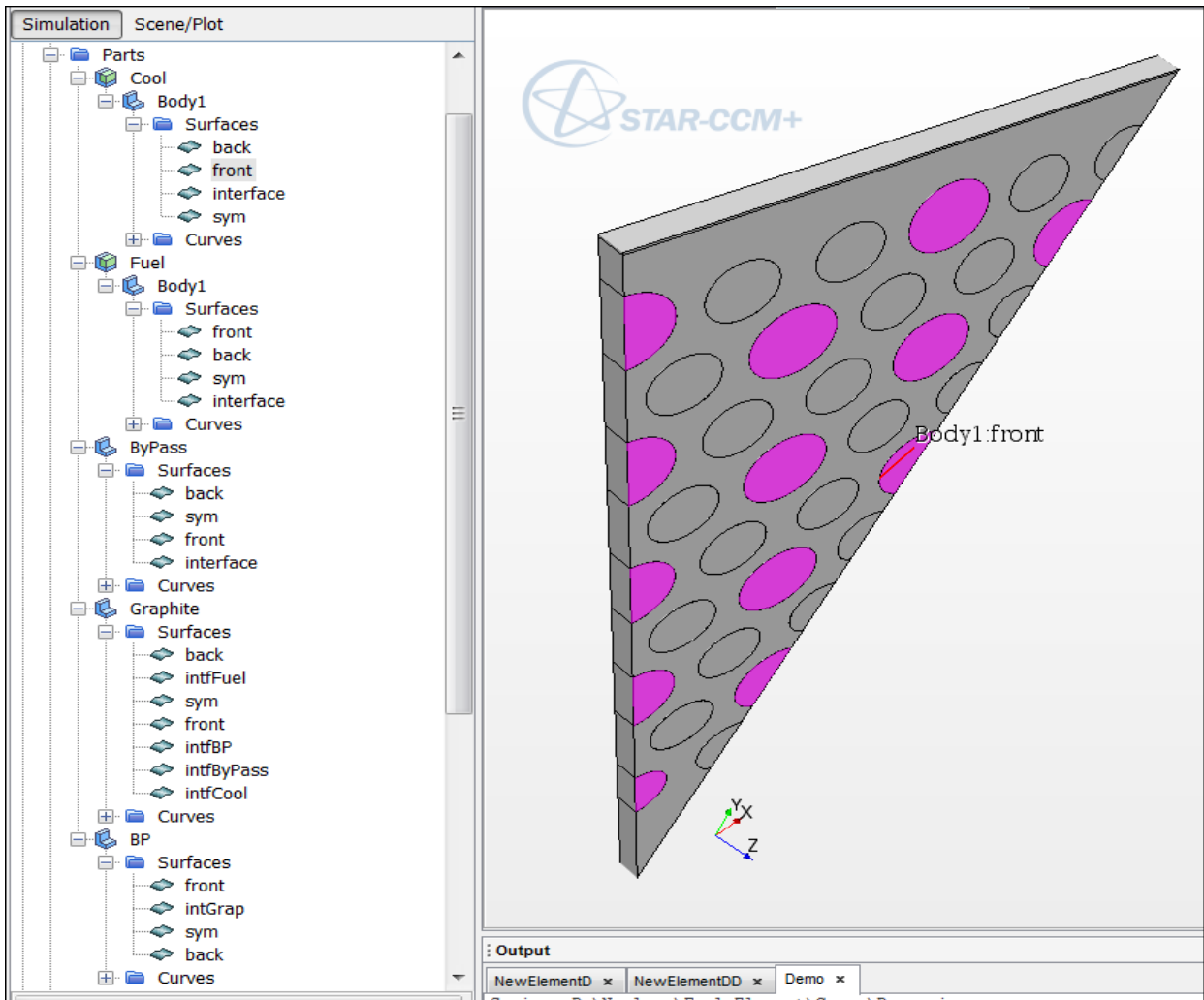


**Figure D2-3: Individual and combined surfaces of the bodies.**

The parts are now ready to be converted into regions. Select all the parts, right-click and select Convert parts to regions. Change the drop down box options so that they read as in **Figure D2-4**.

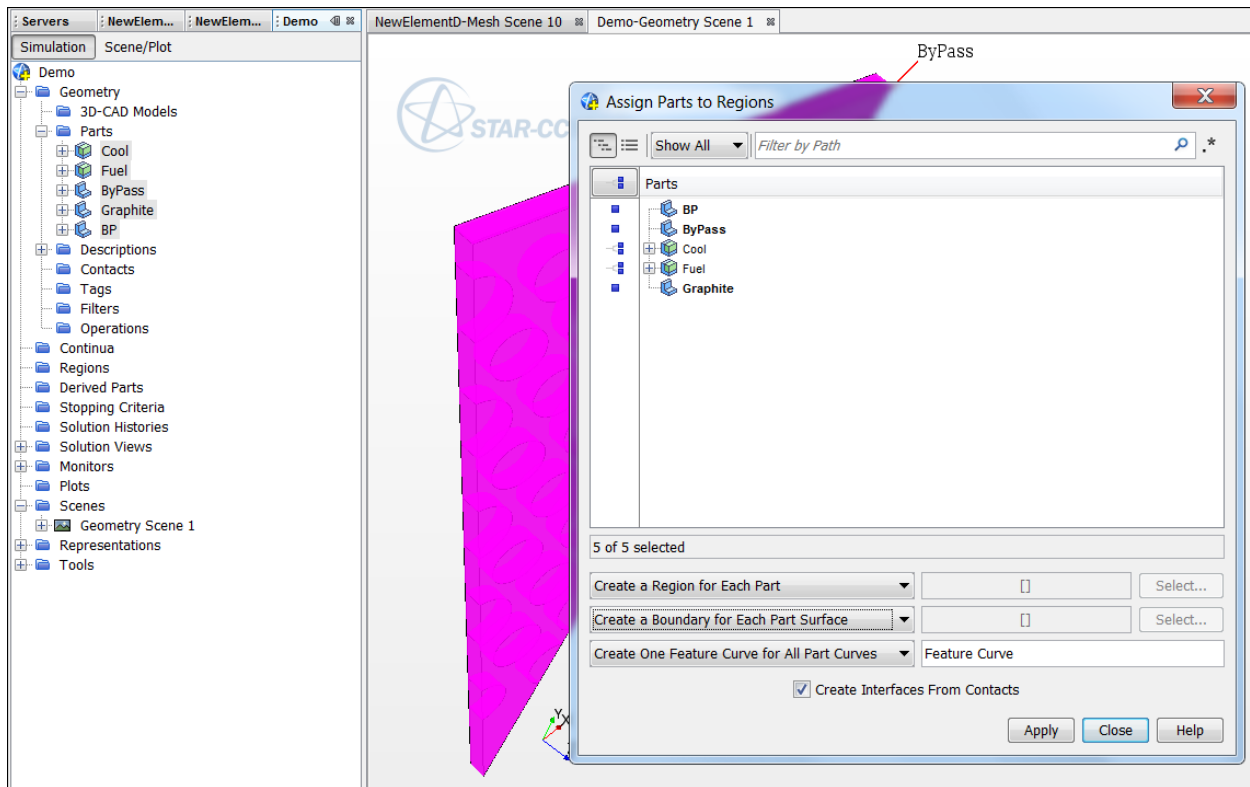


**Figure D2-4: Parts to regions dialog box.**

Create a mesh and physics continuum for each of the regions under the Continua tree item as in **Figure D2-5**.

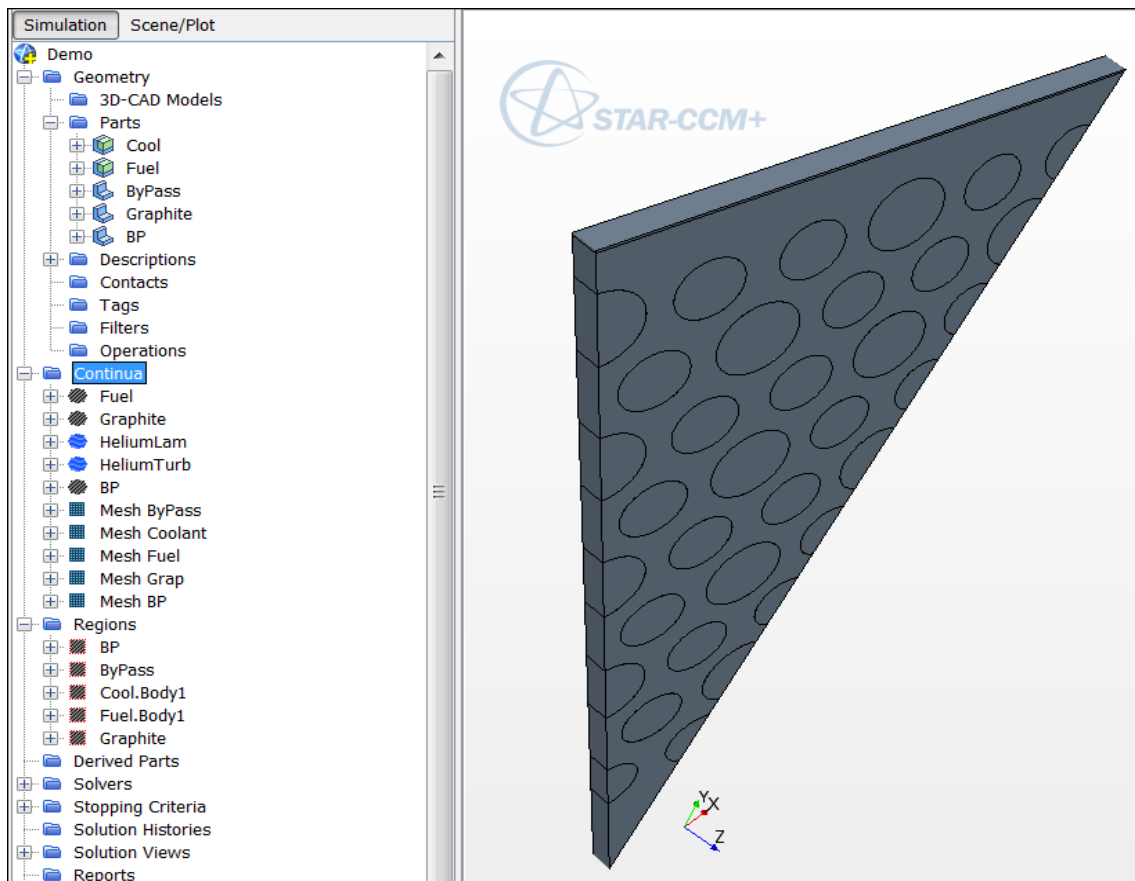


**Figure D2-5: Mesh and physics continua.**

The mesh models for each of the regions should consist of a **surface remesher**, a **polyhedral mesher** and an **extruder mesher**. The mesh models for both the coolant and the by-pass region should also include a **prism boundary layer mesher** as is shown in **Figure D2-6**.

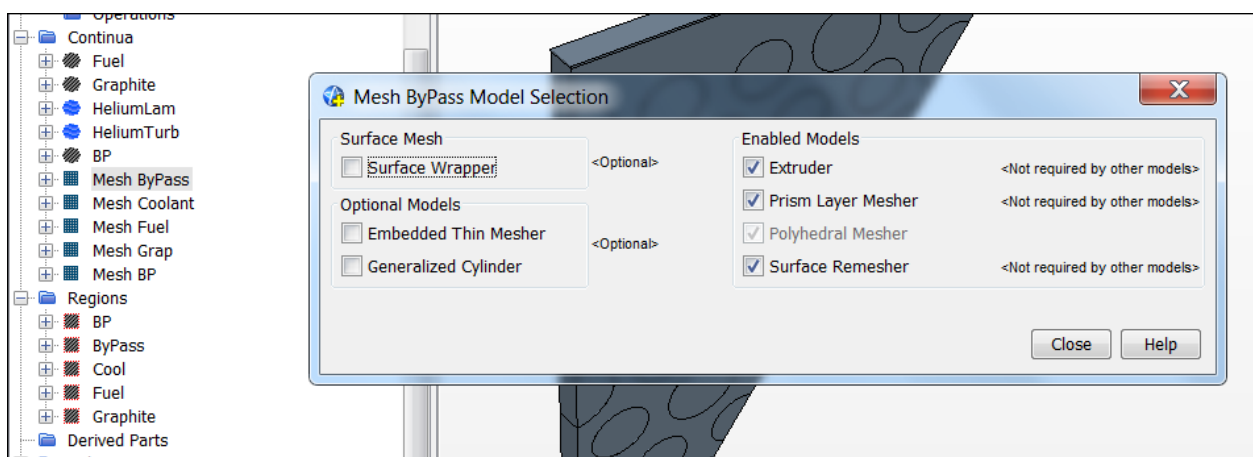


**Figure D2-6: Meshing models for the fluid regions.**

StarCCM+ requires a basic cell size for each mesh. All meshes are assigned a base size of 2 mm while the graphite mesh is assigned a base size of 4 mm. Default values are used for the rest of the meshing parameters.

The next step is to connect the different regions to mesh and material models. This is done by selecting the region and then selecting the appropriate mesh and material model from the drop down dialogs in the property window as indicated in **Figure D2-7**.

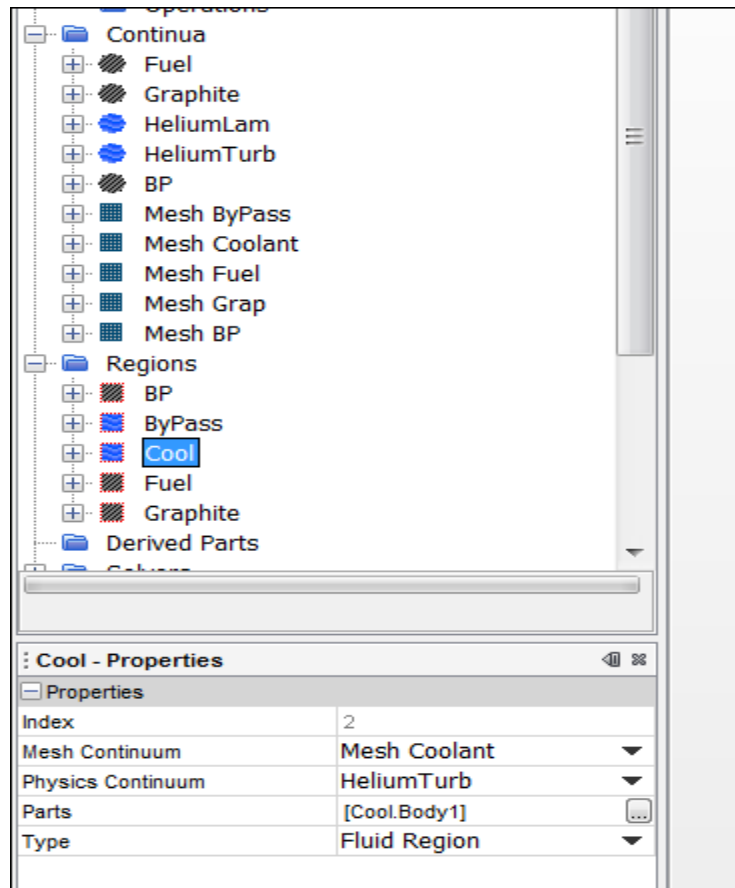


**Figure D2-7: Connecting mesh and material models to regions.**

The boundaries of the newly created regions need to be modified to enable the mesh extrusion. It is also important to create interfaces between the different materials before the extrusion is activated. Typical settings in this regard are shown in **Figure D2-8** below. A contact interface between BP and Graphite is typically created by selecting intGraph and intfBP, then right-click and then selecting the 'create interface' option from the dialog. In order to enable mesh extrusion for boundary 'front' of LBP, select 'Extrusion type' under Mesh conditions and change the option to 'constant rate'. Then fill in the extrusion parameters in the property dialog as is shown in **Figure D2-8** below. This procedure of creating solid-solid and solid-fluid interfaces as well as the mesh extrusion settings for 'front' boundaries needs to be repeated for each region.

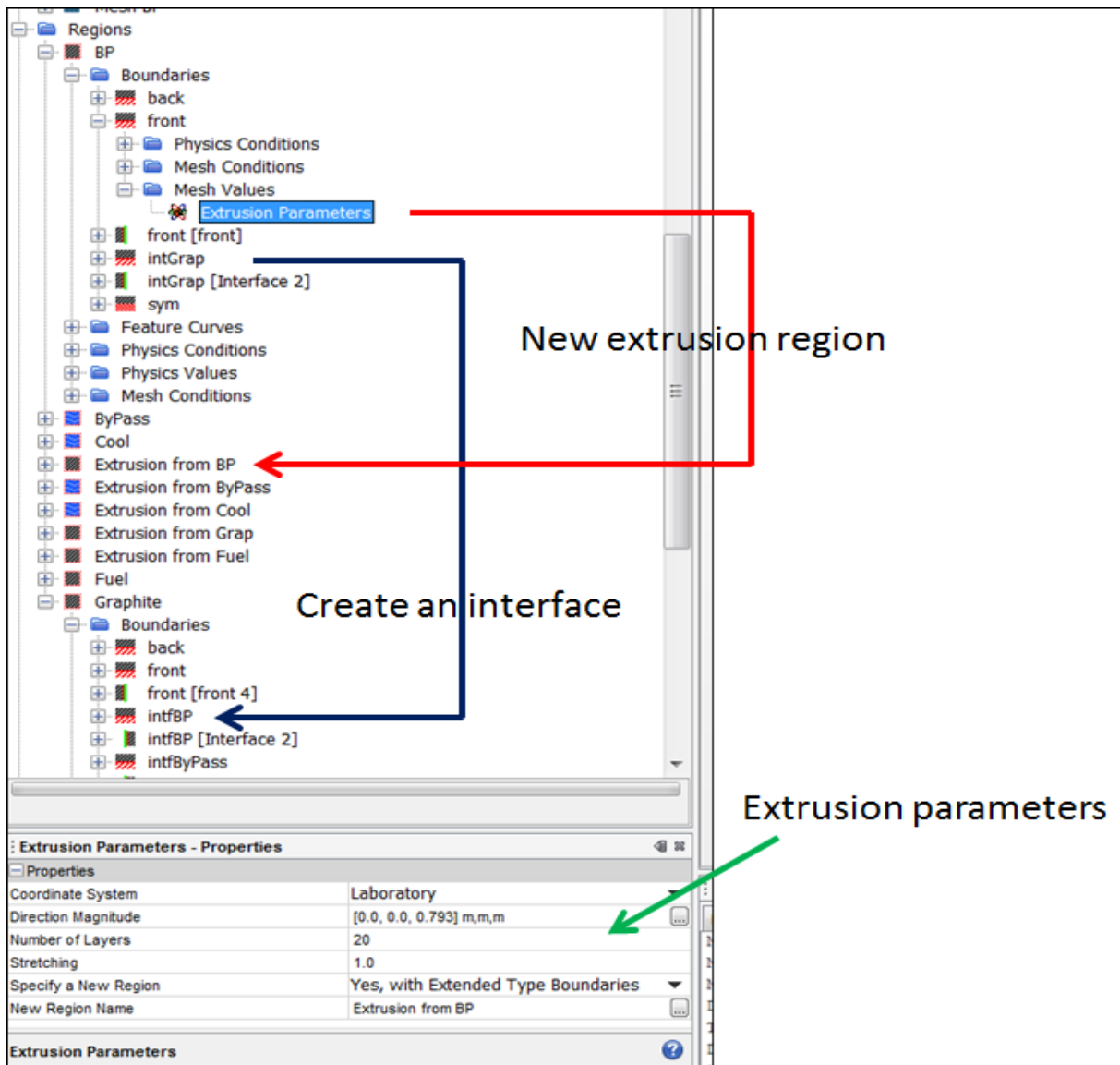


**Figure D2-8: Creating material interfaces and mesh extrusion criteria.**

At this stage it is a good idea to save the StarCCM+ case as a back-up in order to preserve the work that was done so far. In the next steps changes to the case will be made that is not recoverable. If a mistake is made then one can fall back to the original case.

Once the back-up is made the grid generation process can be activated. When the mesh generation is finished the mesh can be viewed by creating a new mesh scene as in **Figure D2-9** below.

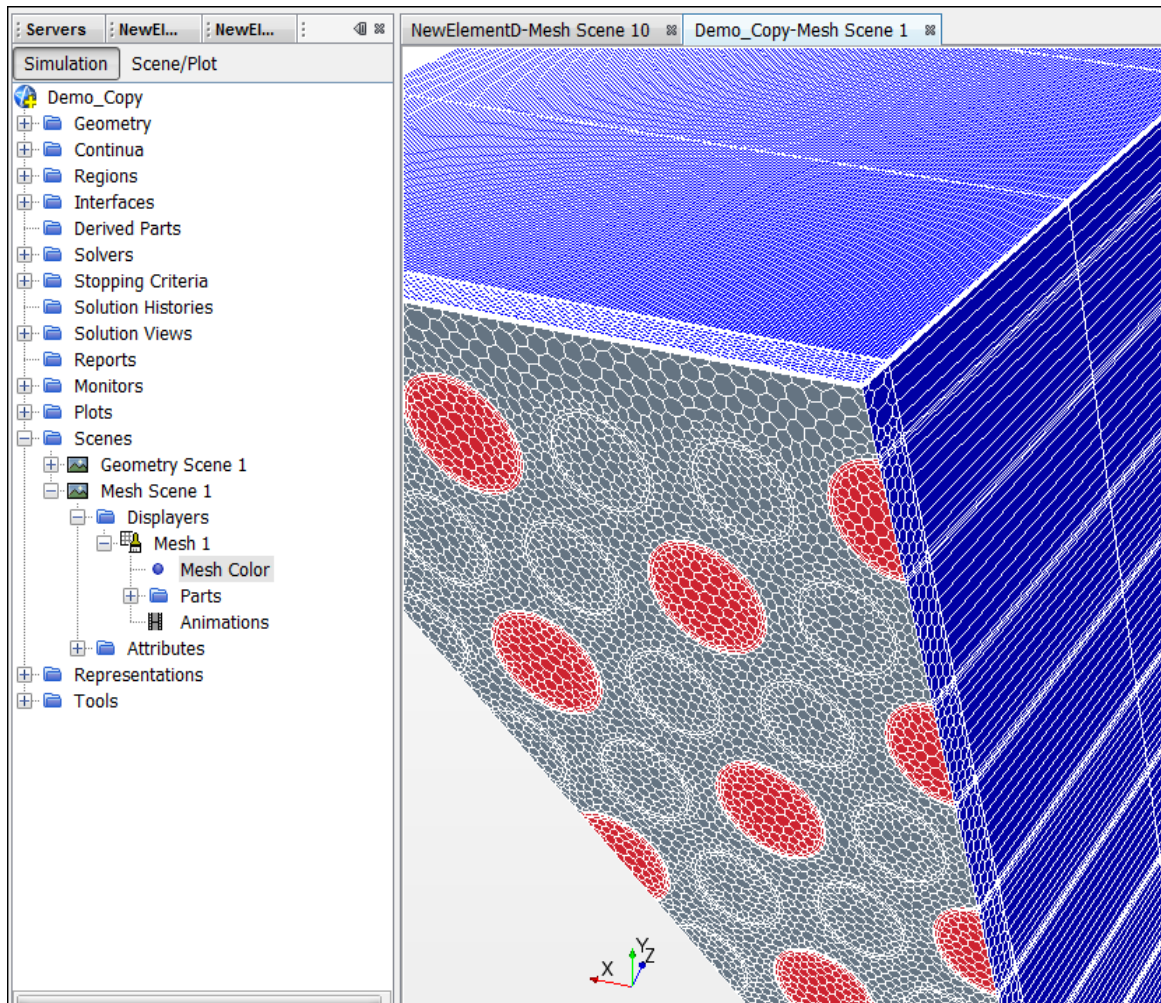


**Figure D2-9: Newly created mesh showing the original regions and the newly extruded regions.**

The original thin section of the model as well as the extruded region can be seen in **Figure D2-9**. The next step is to delete the original regions from which the extrusions were made. Once this is done the interfaces between the solid materials and between the solid and fluid materials need to be recreated. The process is shown in **Figure D2-10** below. Each interface boundary of a region is paired with an interface boundary from the graphite region. An interface is created by selecting both interface boundaries, then right-click and then select 'Create interface'.

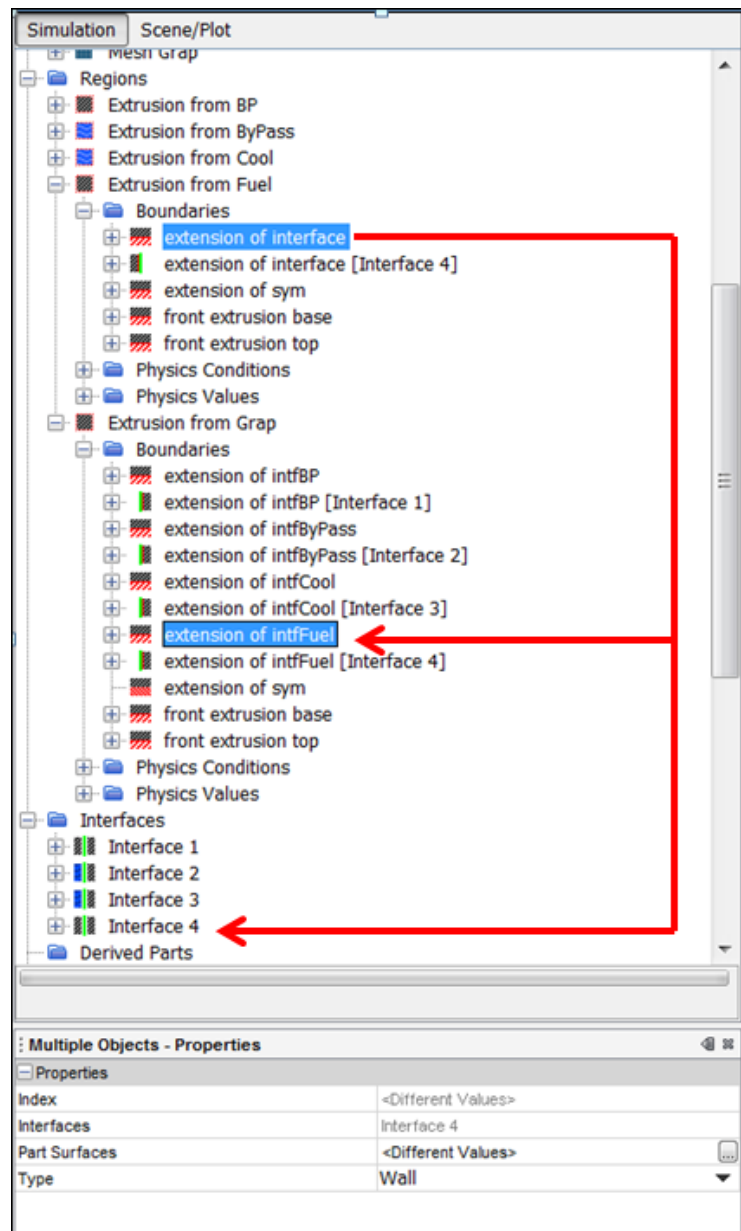


**Figure D2-10: Creating interfaces between materials.**

Create inlet boundaries for coolant channels.

Inlet velocity profiles for fully developed turbulent flow are now created at each of the coolant channels. This is a tedious task because a local reference points need to be created at the center of each of the inlets. As a first step the inlet boundary needs to be split into separate inlet boundaries. The first step is to rename the inlet boundary to 'inlet' from its typical name 'Extrusion from Cool' and also to change the type from the default 'Wall' to 'Velocity inlet'. Then select 'inlet', right-click and select 'Split Non-Contiguous'. This action will split the inlet boundary into 13 separate inlets as shown in **Figure D2-11** below. The inlets are then renumbered from 1 to 13 to conform to the numbering on the plot as indicated in **Figure D2-11**.

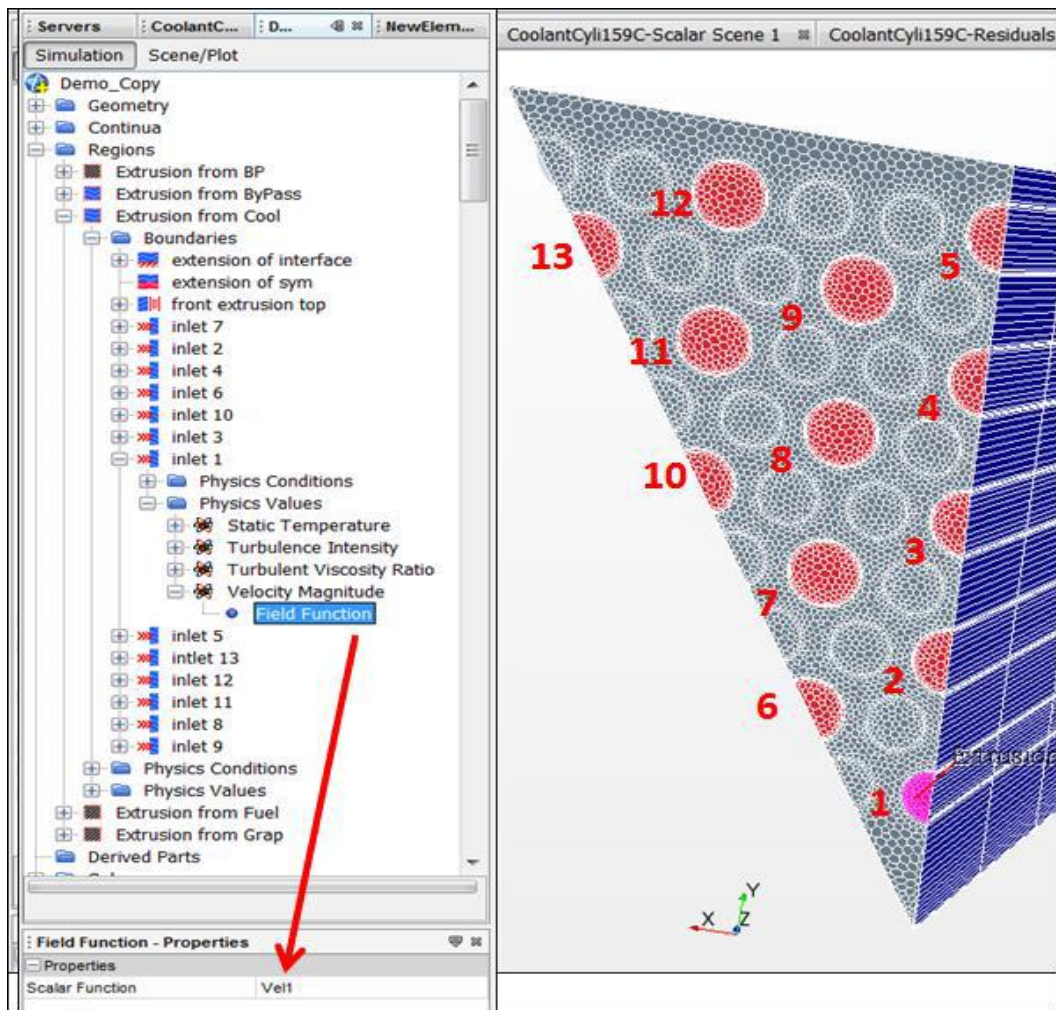


**Figure D2-11: Inlet split into 13 individual inlet boundaries.**

The turbulent velocity profile is now applied to each of the inlets by the use of field functions. A set of field functions are created to represent parameters in the power-law velocity profile used to represent the fully developed turbulent velocity profile. For example 'Vel1' in **Figure D2-12** represents the power-law velocity profile for 'inlet 1' as indicated in **Figure D2-11**.

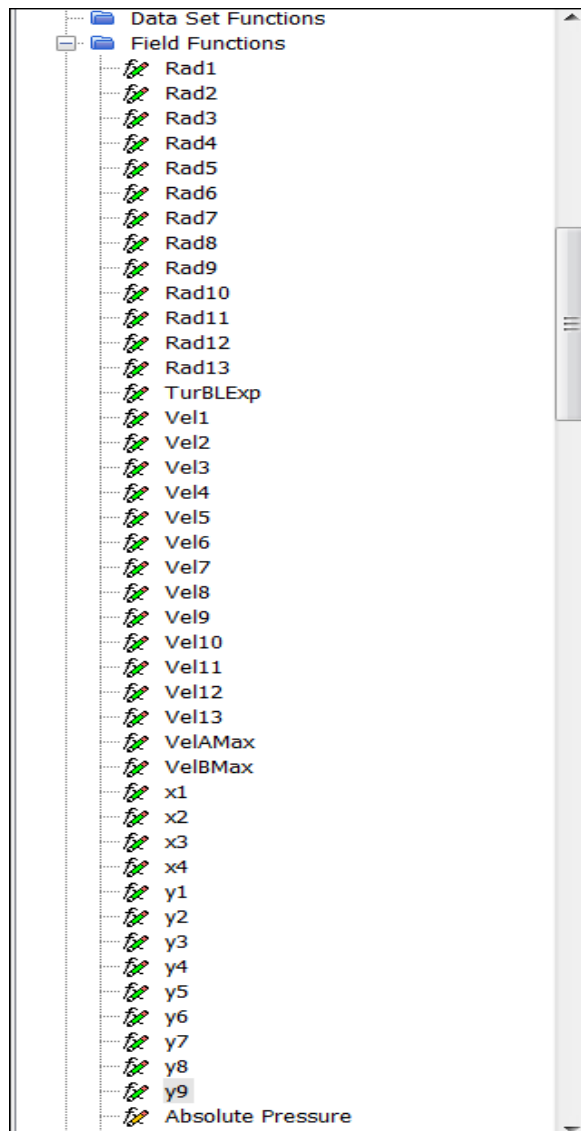


**Figure D2-12: Field functions used in the power-law velocity profile definition.**

The detail of the velocity field function is given for ‘inlet 1’, which is the smaller coolant channel. The rest are similar.

**Vel1:**

$$\text{pow}((1-\text{Rad1}/0.00635000), 1/\{\text{TurBLExp}\}) * \{\text{VelBMax}\}$$

**Rad1:**

$$\text{sqrt}((\{\text{Centroid}\}[0]-\{x1\}) * (\{\text{Centroid}\}[0]-\{x1\}) + (\{\text{Centroid}\}[1]-\{y1\}) * (\{\text{Centroid}\}[1]-\{y1\}))$$

**TurBLExp:**

**VelBMax:**

$$(0.034508198)/(3.14159265*0.0127*0.0127/4)/((100000*4)/(273.15+490)/(8314.4))$$

**X1:**

0

**Y1:**

0.03272727268

Finally the outlets of the cooling channels need to be changed to pressure outlets.